

EXTENSION OF THE ENTROPY VISCOSITY METHOD TO THE MULTI-D  
EULER EQUATIONS AND THE SEVEN-EQUATION TWO-PHASE MODEL.

A Dissertation  
by  
MARC OLIVIER GERARD DELCHINI

Submitted to the Office of Graduate and Professional Studies of  
Texas A&M University  
in partial fulfillment of the requirements for the degree of

DOCTOR OF PHILOSOPHY

Chair of Committee,	Jean Ragusa
Co-Chair of Committee,	Jean-Luc Guermond
Committee Members,	Jim Morel
	Yassin Hassan
	Ray Berry
Head of Department,	Yassin Hassan

December 2014

Major Subject: Nuclear Engineering

Copyright 2014 Marc Olivier Gerard Delchini

## ABSTRACT

The work presented in this dissertation focuses on the application of the entropy viscosity method to low-Mach single- and two-phase flow equations discretized using a continuous Galerkin finite element method with implicit time integration. The technique has been implemented and tested using the multiphysics simulation environment MOOSE.

First, the entropy viscosity method, introduced by Guermond et al., is extended to the multi-dimensional Euler equations for both subsonic (very low Mach numbers) and supersonic flows. We show that the current definition of the viscosity coefficients is not adapted to low-Mach flows and we provide a robust alternate definition valid for any Mach number value. The new definitions are derived from a low-Mach asymptotic study, is valid for a wide range of Mach numbers and no longer requires an analytical expression of the entropy function. In addition, the entropy minimum principle is used to derive the viscous regularization terms for Euler equations with variable area for nozzle flow problems and was proved valid for any equation of state with a concave entropy. The new definition of the entropy viscosity method is tested on various 1-D and 2-D numerical benchmarks employing the ideal and the stiffened gas equation of states: flow in a converging-diverging nozzle, Leblanc shock tube, slow moving shock, strong shock for liquid phase, subsonic flows around a 2-D cylinder and over a circular hump, and supersonic flow in a compression corner. Convergence studies are performed using analytical solutions in 1-D and proved the entropy viscosity method to be second-order accurate for smooth solutions.

In a second part, the entropy viscosity method is applied to the seven-equation two-phase flow model. After deriving the dissipative terms using the same procedure

as for the multi-D Euler equations, a low-Mach asymptotic study is performed in order to obtain a definition for the viscosity coefficients. Because the seven-equation model is derived by assuming that each phase obeys the Euler equations, the dissipative terms and the definition of the viscosity coefficients are analogous to the ones obtained for the single-phase system of equations. Then, 1-D numerical tests were performed to demonstrate that the entropy viscosity method properly stabilizes the flow simulations based on the seven-equation model.

Another focus of this work was to investigate the impact of source terms (gravity, friction, etc) onto the entropy viscosity method. The theoretical approach adopted here consists of deriving the entropy residual when accounting for the source terms and investigate the sign of the new terms in order to adapt the definition of the viscosity coefficients. Numerical 1-D tests are performed to validate this approach for both single- and two-phase flow models.

In the last part of this dissertation, the entropy viscosity method is applied to the 1-D grey radiation-hydrodynamic equations where the 1-D Euler equations are coupled to a radiation diffusion equation through relaxation terms. The method of manufactured solutions was used to prove second-order accuracy of the numerical stabilization method and also show that the entropy viscosity method yields the correct asymptotic diffusion limit. 1-D tests for inlet Mach number ranging from 1.2 to 50 are presented and show good agreement with semi-analytical solutions.

## DEDICATION

In memory of my grand-fathers, Francis Collet and Roger Delchini.

## ACKNOWLEDGEMENTS

This research project would not have been possible without the support of many people. First of all, I wish to express my gratitude to my advisor, Dr. Jean C. Ragusa, who was abundantly helpful and offered invaluable assistance, support and guidance.

I would like to sincerely thank my co-advisor Dr. Jean-Luc Guermond for giving me valuable ideas. I cannot forget to thank Dr. Ray Berry for his most appreciated collaboration and useful suggestions.

I would like to express my special thanks to the MOOSE community, especially the MOOSE team, for replying to all my requests.

I am forever indebted to my father Gerard Delchini and my mother Nicole Delchini for their love, understanding, endless patience and encouragement when it was most required. Finally, yet importandly, I would like to express my heartfelt thanks to my beloved wife Emmanuelle for her love, support and encouragement during the entire period of this work.

## NOMENCLATURE

P	Pressure
T	Temperature
$\vec{u}$	vector velocity
$\rho$	density
E	specific total energy
e	specific internal energy
c	speed of sound
H	total enthalpy
Z	acoustic impedance
$\eta$	mathematical entropy
s	physical entropy
A	cross section
$A_{int}$	interfacial area
$\Gamma$	mass transfer
$P_I$	interfacial pressure
$\vec{u}_I$	interfacial velocity
$\mu$	viscosity coefficient
$\kappa$	viscosity coefficient
$\beta$	viscosity coefficient
$\alpha$	void fraction
$\partial_t$	partial time derivative
$\nabla$	gradient
$\nabla \cdot$	divergence

eos	equation of state
PWR	Pressurized Water Reactor
EVM	Entropy Viscosity Method
EV	Entropy Viscosity
FO	First Order
eos	equation of state
$h_t$	heat-transfer coefficient
$h_I$	interfacial heat-transfer coefficient
$T_w$	wall temperature
$P_w$	wall-heated perimeter
$\kappa$	viscosity coefficient

## TABLE OF CONTENTS

	Page
ABSTRACT . . . . .	ii
DEDICATION . . . . .	iv
ACKNOWLEDGEMENTS . . . . .	v
NOMENCLATURE . . . . .	vi
TABLE OF CONTENTS . . . . .	viii
LIST OF FIGURES . . . . .	xii
LIST OF TABLES . . . . .	xix
1. INTRODUCTION . . . . .	1
2. HYPERBOLIC CONSERVATION LAWS . . . . .	7
2.1 Hyperbolic scalar equations . . . . .	7
2.1.1 Eigenvalue and characteristic curves . . . . .	7
2.1.2 Shocks formation and vanishing viscosity equation/solution .	10
2.1.3 Weak solution and entropy condition . . . . .	18
2.1.4 Entropy Viscosity Method (EVM) and hyperbolic scalar equations . . . . .	25
2.2 Hyperbolic system of equations . . . . .	30
3. DISCRETIZATION METHOD AND IMPLEMENTATION DETAILS OF THE ENTROPY VISCOSITY METHOD . . . . .	37
3.1 Spatial and temporal discretizations . . . . .	37
3.1.1 Spatial discretization algorithm . . . . .	37
3.1.2 Implicit time integration methods . . . . .	41
3.1.3 Jacobian-Free Newton Krylov solver . . . . .	44
3.2 Implementation of the Entropy Viscosity Method (EVM) with continuous Galerkin finite element method . . . . .	46

4. APPLICATION OF THE ENTROPY VISCOSITY METHOD TO THE MULTI-D BURGER'S EQUATION . . . . .	53
4.1 The multi-D Burger's equation . . . . .	53
4.2 Numerical results . . . . .	55
4.2.1 1-D numerical result . . . . .	55
4.2.2 2-D Riemann problem . . . . .	59
5. APPLICATION OF THE ENTROPY VISCOSITY METHOD TO THE MULTI-D EULER EQUATIONS WITH VARIABLE AREA . . . . .	64
5.1 The Entropy Viscosity Method . . . . .	66
5.1.1 Background . . . . .	66
5.1.2 Issues in the low-mach regime . . . . .	70
5.2 An all-speed reformulation of the Entropy Viscosity Method . . . . .	71
5.2.1 New definition of the entropy production residual . . . . .	71
5.2.2 Asymptotic study in the low-mach regime . . . . .	72
5.2.3 Scaling of $Re_\infty$ and $Pé_\infty$ for non-isentropic flows . . . . .	77
5.2.4 New normalization for the entropy residual . . . . .	78
5.3 Extension of the entropy viscosity technique Euler equations with vari- able area . . . . .	80
5.4 Entropy-viscosity method and source terms . . . . .	81
5.5 Boundary conditions . . . . .	83
5.5.1 Flow inlet boundary conditions . . . . .	89
5.5.2 Flow outlet boundary conditions . . . . .	91
5.5.3 Free-slip wall boundary conditions . . . . .	92
5.6 Numerical results . . . . .	93
5.6.1 Liquid water in a 1-D converging-diverging nozzle . . . . .	96
5.6.2 Steam in a 1-D converging-diverging nozzle . . . . .	99
5.6.3 Leblanc shock tube . . . . .	103
5.6.4 1-D shock tube with a liquid phase . . . . .	107
5.6.5 1-D slow moving shock . . . . .	110
5.6.6 1-D numerical results for flows with source terms . . . . .	112
5.6.7 Vapor flow in a straight pipe with wall-friction force . . . . .	113
5.6.8 Liquid water flow in a straight pipe with wall-friction force . . . . .	115
5.6.9 Vapor and liquid water flows in a straight pipe with wall- friction and wall-heat source . . . . .	116
5.6.10 1-D Pressurized Water Reactor (PWR) . . . . .	119
5.7 2-D numerical results for supersonic flows . . . . .	124
5.7.1 Supersonic 2-D flow over a forward facing step . . . . .	125
5.7.2 2-D circular explosion . . . . .	135
5.7.3 Supersonic flow in a compression corner . . . . .	137
5.7.4 Supersonic flow over a 5° double-wedge obstruction . . . . .	147

5.8	2-D numerical results for subsonic flows . . . . .	150
5.8.1	Subsonic flow over a 2-D cylinder . . . . .	150
5.8.2	Subsonic flow over a 2-D hump . . . . .	157
6.	APPLICATION OF THE ENTROPY VISCOSITY METHOD TO THE SEVEN-EQUATION MODEL . . . . .	161
6.1	Descriptions of the multi-D seven-equation model . . . . .	162
6.1.1	The system of equations for the liquid and vapor phases . . . . .	163
6.1.2	The source terms . . . . .	166
6.2	A viscous regularization for the multi-D seven-equation model . . . . .	177
6.3	Low-mach asymptotic limit and viscosity coefficients . . . . .	187
6.3.1	Definition of the viscosity coefficients . . . . .	187
6.3.2	Low-mach asymptotic limit of the seven-equation model . . . . .	190
6.4	Numerical results . . . . .	194
6.4.1	1-D advection test: uniform velocity and pressure flow with a volume fraction discontinuity . . . . .	194
6.4.2	1-D shock tube for two independent fluids . . . . .	197
6.4.3	1-D shock tube for two fluids with pressure and velocity relaxation terms . . . . .	205
6.4.4	1-D converging-diverging nozzle test . . . . .	212
6.4.5	1-D straight pipe with wall-friction force, wall heat source and exchange terms (mass and energy) . . . . .	229
7.	APPLICATION OF THE ENTROPY VISCOSITY METHOD TO THE 1-D GREY RADIATION-HYDRODYNAMIC EQUATIONS . . . . .	236
7.1	Backgrounds . . . . .	236
7.2	The Entropy Viscosity Method applied to the 1-D radiation-hydrodynamic equations . . . . .	238
7.3	Numerical results . . . . .	245
7.3.1	Space/time accuracy . . . . .	245
7.3.2	Radiation shock simulations . . . . .	250
8.	CONCLUSIONS . . . . .	271
	REFERENCES . . . . .	275
	APPENDIX A. DERIVATION OF THE DISSIPATIVE TERMS FOR THE EULER EQUATIONS WITH VARIABLE AREA USING THE ENTROPY MINIMUM PRINCIPLE . . . . .	283
	APPENDIX B. DERIVATION OF THE ENTROPY RESIDUAL AS A FUNCTION OF DENSITY, PRESSURE AND SPEED OF SOUND . . . . .	287

APPENDIX C. ENTROPY RESIDUAL FOR AN ISENTROPIC FLOW . . .	289
APPENDIX D. PROOF OF THE ENTROPY MINIMUM PRINCIPLE FOR THE RADIATION-HYDRODYNAMIC EQUATIONS WITH DISSIPATIVE TERMS . . . . .	290
APPENDIX E. ENTROPY EQUATION FOR THE MULTI-D SEVEN EQUA- TION MODEL WITHOUT VISCOUS REGULARIZATION . . . . .	296

## LIST OF FIGURES

FIGURE	Page
1.1 Marco's zoo (this is not a food chain). . . . .	6
2.1 Characteristic curves for the linear advection equation [39]. . . . .	11
2.2 Characteristic curves for the 1-D Burger's equation [39]. . . . .	12
2.3 Example of a triple-valued situation [39]. . . . .	14
2.4 Influence of the viscosity coefficient $\epsilon$ on the numerical solution stiffness [39]. . . . .	16
4.1 1-D Burger's equation: solution profile without stabilization at $t = 0.2$ s. . . . .	56
4.2 1-D Burger's equation: solution profile with first-order viscosity at $t = 0.2$ s. . . . .	57
4.3 1-D Burger's equation: solution profile with the EVM at $t = 0.2$ s. . . . .	58
4.4 1-D Burger's equation: viscosity coefficient profiles at $t = 0.2$ s. . . . .	58
4.5 2-D Burger's equation: solution profile at $t = 0.2$ s. . . . .	60
4.6 2-D Burger's equation: viscosity profile at $t = 0.2$ s. . . . .	61
4.7 2-D Burger's equation: solution profile at $t = 0.5$ s. . . . .	62
4.8 2-D Burger's equation: viscosity profile at $t = 0.5$ s. . . . .	63
5.1 Subsonic (left) and supersonic (right) flow inlets with $u_\eta = \mathbf{u} \cdot \boldsymbol{\eta}$ [46]. . . . .	87
5.2 Subsonic (left) and supersonic (right) flow outlets with $u_\eta = \mathbf{u} \cdot \boldsymbol{\eta}$ [46]. . . . .	87
5.3 Free-slip wall boundary. with $u_\eta = \mathbf{u} \cdot \boldsymbol{\eta}$ [46]. . . . .	88
5.4 Steady-state solution for a liquid flowing through a 1-D converging-diverging nozzle. . . . .	97

5.5	Steady-state solution for vapor phase flowing in a 1-D converging-diverging nozzle. . . . .	100
5.6	Exact and numerical solutions for the 1-D Leblanc shock tube at $t = 4\text{ s}$	104
5.7	Numerical solution for the 1-D liquid shock tube at at $t_{\text{final}} = 7\text{ }10^{-5}\text{ s}$ .	109
5.8	Slow moving shock profiles at $t = 1.1\text{ s}$ . . . . .	111
5.9	Steady-state profiles of a vapor flow with friction force in a straight pipe. . . . .	114
5.10	Steady-state profiles of a liquid water flow with friction force in a straight pipe. . . . .	115
5.11	Steady-state profiles of a vapor flow with friction force and wall-heat source in a straight pipe. . . . .	117
5.12	Steady-state profiles of a liquid water flow with friction force and wall-heat source in a straight pipe. . . . .	118
5.13	PWR test case: axial pressure profile . . . . .	120
5.14	PWR test case: axial temperature profile . . . . .	121
5.15	PWR test case: axial velocity profile . . . . .	122
5.16	PWR test case: axial viscosity profile . . . . .	123
5.17	PWR test case: axial mass flux (or momentum) profile . . . . .	124
5.18	Supersonic 2-D flow over a forward facing step: density solution at $t = 0.314\text{ s}$ . . . . .	127
5.19	Supersonic 2-D flow over a forward facing step: viscosity coefficient solution at $t = 0.314\text{ s}$ . . . . .	128
5.20	Supersonic 2-D flow over a forward facing step: density solution at $t = 0.664\text{ s}$ . . . . .	129
5.21	Supersonic 2-D flow over a forward facing step: viscosity coefficient solution at $t = 0.664\text{ s}$ . . . . .	130
5.22	Supersonic 2-D flow over a forward facing step: density solution at $t = 1.514\text{ s}$ . . . . .	131

5.23 Supersonic 2-D flow over a forward facing step: viscosity coefficient solution at $t = 1.514$ s. . . . .	132
5.24 Supersonic 2-D flow over a forward facing step: density solution at $t = 4$ s. . . . .	133
5.25 Supersonic 2-D flow over a forward facing step: viscosity coefficient solution at $t = 4$ s. . . . .	134
5.26 2-D circular explosion: density solution at $t = 0.2$ s. . . . .	136
5.27 2-D circular explosion: viscosity coefficient solution at $t = 0.2$ s. . . . .	137
5.28 Supersonic flow in a compression corner: pressure solution at $t = 5.5 \times 10^{-4}$ . . . . .	139
5.29 Supersonic flow in a compression corner: viscosity coefficient at $t = 5.5 \times 10^{-4}$ . . . . .	140
5.30 Supersonic flow in a compression corner: pressure solution at $t = 1.15 \times 10^{-3}$ . . . . .	141
5.31 Supersonic flow in a compression corner: viscosity coefficient at $t = 1.15 \times 10^{-3}$ . . . . .	142
5.32 Supersonic flow in a compression corner: pressure solution at steady-state. . . . .	143
5.33 Supersonic flow in a compression corner: viscosity coefficient at steady-state. . . . .	144
5.34 Supersonic flow in a compression corner: pressure and mach number profiles at steady-state . . . . .	145
5.35 Supersonic flow in a compression corner: difference between inlet and outlet mass flow rates as a function of time. . . . .	146
5.36 Supersonic flow over a $5^\circ$ double-wedge obstruction: pressure solution at steady-state. . . . .	148
5.37 Supersonic flow over a $5^\circ$ double-wedge obstruction: viscosity coefficient at steady-state. . . . .	149
5.38 Subsonic flow over a 2-D cylinder: $M_{\text{inlet}} = 10^{-3}$ . . . . .	151

5.39	Subsonic flow over a 2-D cylinder: $M_{\text{inlet}} = 10^{-4}$	152
5.40	Subsonic flow over a 2-D cylinder: $M_{\text{inlet}} = 10^{-5}$	153
5.41	Subsonic flow over a 2-D cylinder: $M_{\text{inlet}} = 10^{-6}$	154
5.42	Subsonic flow over a 2-D cylinder: $M_{\text{inlet}} = 10^{-7}$	155
5.43	Log-log plot of the pressure and velocity fluctuations as a function of the far-field Mach number.	157
5.44	Subsonic flow over a 2-D hump: mach 0.7	158
5.45	Subsonic flow over a 2-D hump: mach $10^{-2}$	159
5.46	Subsonic flow over a 2-D hump: mach $10^{-5}$	159
5.47	Subsonic flow over a 2-D hump: mach $10^{-7}$	160
6.1	Interface control volume (top); $T$ - $p$ state space around saturation line, $T_{\text{liq}} < T_{\text{vap}}$ , (bottom) [55].	170
6.2	Vaporization and condensation at a liquid-vapor interface (after Moody [47]).	172
6.3	1-D advection test: volume fraction (left) and viscosity coefficients for volume fraction equation (right) of phase 1	195
6.4	1-D advection test:: pressure profiles of phase 1 (left) and 2 (right)	195
6.5	1-D advection test:: velocity profiles of phase 1 (left) and 2 (right)	196
6.6	1-D advection test: viscosity coefficient profiles of phase 1 (left) and 2 (right)	196
6.7	1-D shock tube for two independent fluids: pressure profiles at $t = 305 \mu s$ .	198
6.8	1-D shock tube for two independent fluids: velocity profiles at $t = 305 \mu s$ .	199
6.9	1-D shock tube for two independent fluids: density profiles at $t = 305 \mu s$ .	200
6.10	1-D shock tube for two independent fluids: volume fraction profiles at $t = 305 \mu s$ .	201

6.11 1-D shock tube for two independent fluids: viscosity coefficient profiles for phase 2 at $t = 305 \mu s$ . . . . .	202
6.12 1-D shock tube for two independent fluids: viscosity coefficient profiles for phase 1 at $t = 305 \mu s$ . . . . .	203
6.13 1-D shock tube for two independent fluids: viscosity coefficient profiles for volume fraction equation of phase 1 at $t = 305 \mu s$ . . . . .	204
6.14 1-D shock tube for two fluids with relaxation terms: pressure profiles at $t = 305 \mu s$ . . . . .	206
6.15 1-D shock tube for two fluids with relaxation terms: velocity profiles at $t = 305 \mu s$ . . . . .	207
6.16 1-D shock tube for two fluids with relaxation terms: density profiles at $t = 305 \mu s$ . . . . .	208
6.17 1-D shock tube for two fluids with relaxation terms: volume fraction profiles at $t = 305 \mu s$ . . . . .	209
6.18 1-D shock tube for two fluids with relaxation terms: viscosity coefficient profiles for phase 1 at $t = 305 \mu s$ . . . . .	210
6.19 1-D shock tube for two fluids with relaxation terms: viscosity coefficient profiles for phase 2 at $t = 305 \mu s$ . . . . .	211
6.20 1-D shock tube for two fluids with relaxation terms: viscosity coefficient profiles for volume fraction equation of phase 1 at $t = 305 \mu s$ . . . . .	212
6.21 1-D converging-diverging nozzle test: pressure profiles at steady state with $A_{int,max} = 10^2$ . . . . .	214
6.22 1-D converging-diverging nozzle test: pressure profiles at steady state with $A_{int,max} = 10^3$ . . . . .	215
6.23 1-D converging-diverging nozzle test: pressure profiles at steady state with $A_{int,max} = 10^4$ . . . . .	216
6.24 1-D converging-diverging nozzle test: velocity profiles at steady state. . . . .	217
6.25 1-D converging-diverging nozzle test: density profiles at steady state. . . . .	218
6.26 1-D converging-diverging nozzle test: volume fraction profiles at steady state. . . . .	219

6.27 1-D converging-diverging nozzle test: viscosity coefficients profiles for liquid phase at steady state. . . . .	220
6.28 1-D converging-diverging nozzle test: viscosity coefficients profiles for vapor phase at steady state. . . . .	221
6.29 1-D converging-diverging nozzle test: viscosity coefficients profiles for liquid volume fraction phase at steady state. . . . .	222
6.30 1-D converging-diverging nozzle test: pressure profiles at steady state with thermodynamic relaxations and mass and heat exchange terms. . . . .	223
6.31 1-D converging-diverging nozzle test: velocity profiles at steady state with thermodynamic relaxations and mass and heat exchange terms. . . . .	224
6.32 1-D converging-diverging nozzle test: density profiles at steady state with thermodynamic relaxations and mass and heat exchange terms . . . . .	225
6.33 1-D converging-diverging nozzle test: volume fraction profiles at steady state with thermodynamic relaxations and mass and heat exchange terms. . . . .	226
6.34 1-D converging-diverging nozzle test: viscosity coefficients profiles for liquid phase at steady state with thermodynamic relaxations and mass and heat exchange terms. . . . .	227
6.35 1-D converging-diverging nozzle test: viscosity coefficients profiles for vapor phase at steady state with thermodynamic relaxations and mass and heat exchange terms. . . . .	228
6.36 1-D converging-diverging nozzle test: viscosity coefficients profiles for liquid volume fraction at steady state with thermodynamic relaxations and mass and heat exchange terms. . . . .	229
6.37 1-D straight pipe with source terms: pressure profiles at steady-state . . . . .	231
6.38 1-D straight pipe with source terms: temperature profiles at steady-state . . . . .	232
6.39 1-D straight pipe with source terms: velocity profiles at steady-state . . . . .	233
6.40 1-D straight pipe with source terms: volume fraction profiles at steady-state . . . . .	234
6.41 1-D straight pipe with source terms: viscosity coefficients profiles at steady-state . . . . .	235

7.1	Material and radiation temperature profiles at steady state for Mach 1.05 test. . . . .	252
7.2	Material density profile at steady state for Mach 1.05 test. . . . .	253
7.3	First-order viscosity $\kappa_{max}$ and second-order viscosity $\kappa$ profiles at steady state for Mach 1.05 test (logarithm scale). . . . .	254
7.4	Material and radiation temperature profiles at steady state for Mach 1.2 test. . . . .	256
7.5	Material density profile at steady state for Mach 1.2 test. . . . .	257
7.6	First-order viscosity $\kappa_{max}$ and second-order viscosity $\kappa$ profiles at steady state for Mach 1.2 test (logarithm scale). . . . .	258
7.7	Material and radiation temperature profiles at steady-state for Mach 2 test. . . . .	259
7.8	Material density profile at steady-state for Mach 2 test. . . . .	261
7.9	First-order viscosity $\kappa_{max}$ and second-order viscosity $\kappa$ profiles at steady state for Mach 2 test. . . . .	262
7.10	Comprarison between the material density and temperature profiles run with the high-order and first-order viscosity coefficients. . . . .	263
7.11	Material and radiation temperature profiles at steady state for Mach 5 test. Zoom at the location go the peak using different mesh resolutions. . . . .	264
7.12	Material temperature profiles at steady state for the Mach 5 test in the neighborhood spike. . . . .	265
7.13	Material density profile at steady state for Mach 5 test. . . . .	266
7.14	First-order viscosity $\kappa_{max}$ and second-order viscosity $\kappa$ profiles at steady state for Mach 5 test. . . . .	267
7.15	Material and radiation temperature profiles at steady state for Mach 50 test. . . . .	268
7.16	Material density profile at steady-state for Mach 50 test. . . . .	269
7.17	First-order viscosity $\kappa_{max}$ and second-order viscosity $\kappa$ profiles at steady-state for Mach 50 test. . . . .	270

## LIST OF TABLES

TABLE	Page
5.1 Subsonic flow inlet boundary conditions. . . . .	90
5.2 Subsonic flow outlet boundary conditions. . . . .	92
5.3 Initial conditions for the 1-D shock tube tests. . . . .	94
5.4 Stiffened Gas Equation of State (SGEOS) parameters for steam and liquid water. . . . .	95
5.5 $L_1$ norm of the error for the liquid phase in a 1-D converging-diverging nozzle at steady state. . . . .	98
5.6 $L_2$ norm of the error for the liquid phase in a 1-D converging-diverging nozzle at steady state. . . . .	99
5.7 $L_1$ norm of the error for the vapor phase in a 1-D converging-diverging nozzle at steady state. . . . .	102
5.8 $L_2$ norm of the error for the vapor phase in a 1-D converging-diverging nozzle at steady state. . . . .	103
5.9 $L_1$ norm of the error for the 1-D Leblanc test at $t = 4$ s. . . . .	106
5.10 $L_2$ norm of the error for the 1-D Leblanc test at $t = 4$ s. . . . .	107
5.11 Stiffened Gas Equation of State parameters for steam and liquid water used to solve the 1-D Euler equations with source terms. . . . .	112
5.12 Initial conditions for a 2-D supersonic flow past a forward-facing step. .	126
5.13 Initial conditions for a 2-D explosion. . . . .	135
5.14 Analytical solution for a mach 2.5 supersonic flow on an edge at $15^\circ$ .	138
5.15 Velocity ratio for different mach numbers. . . . .	156
6.1 Stiffened Gas Equation of State (SGEOS) parameters for steam and liquid water. . . . .	213

7.1	$L_2$ norms of the error for for the equilibrium diffusion limit case using a manufactured solution. . . . .	247
7.2	$L_2$ norms of the error for for the streaming limit case using a manufactured solution. . . . .	249
7.3	Initial conditions for mach 1.05. . . . .	251
7.4	Initial conditions for mach 1.2. . . . .	255
7.5	Initial conditions for mach 2. . . . .	259
7.6	Initial conditions for mach 5. . . . .	264
7.7	Initial conditions for mach 50. . . . .	268

## 1. INTRODUCTION

Hyperbolic systems of equations are encountered in various engineering fields (extraction of oil, turbine technology, nuclear reactors, etc). Improving numerical solution techniques for such equations is an ongoing topic of research. This is obviously the case for fluid equations. Being able to accurately solve and predict the behavior of a fluid in a turbine or in a reactor, for example, may lead to a safe decrease in conservative safety margins, which translates into a decrease in production cost. Thus, we can see the importance of having a good understanding of the mathematical theory behind these wave-dominated systems of equations and also the importance of developing robust and accurate numerical methods.

A large number of theoretical studies has shown the role played by characteristic equations and the corresponding eigenvalues on how and at what speed the physical information propagates: physical shocks or discontinuities can form, leading to unphysical instabilities and oscillations that pollute the numerical solution due to entropy production [65]. Naturally, the following question arises: how to accurately detect and resolve shocks as well as conserve the physical solution at the same time? Numerous works are available in the literature and include Riemann solvers, Godunov-type fluxes, flux limiters, and artificial viscosity methods. Toro's book [65] provides a good overview of the theory related to hyperbolic systems of equations and focuses on Riemann solvers and Godunov-type fluxes that can be used with discontinuous spatial discretizations: finite volume (FV) and discontinuous Galerkin finite element method (DGFEM). Flux limiters [13, 15] can achieve high-order accuracy with DGFEM [14] but suffer from some drawbacks: difficulties reaching steady-state solutions were found when using time-stepping schemes, and generalization to

unstructured grids is not obvious [12]. The artificial viscosity method was first introduced by Neumann and Richtmeyer [70] but was found to be over-dissipative and, thus, abandoned. Later, with the development of high-order schemes, that artificial viscosity methods have regained interest: Lapidus [35, 20] developed a high-order viscosity method by making the viscosity coefficient proportional to the gradient of the velocity in 1-D. Lohner et al. [44] extended this concept to multi-dimensions by introducing a vector that will measure the direction of maximum change in the absolute value of the velocity norm so that shear layers are not smeared. Pressure-based viscosities were also studied [43] where the viscosity coefficient is set proportional to the Laplacian of pressure, allowing the detection of curvature changes in the pressure profile. Since pressure is often nearly constant except in shock regions, the Laplacian of pressure is a good indicator of the presence of a shock wave. Recently, Reisner et al. [57] introduced the C-method for the compressible Euler equations with artificial dissipative terms: instead of computing the viscosity coefficient on the fly as for Lapidus and pressure-based methods, a partial differential equation (PDE) is added to the original system of equations. This additional PDE is solved for the viscosity coefficient and contains a source term that is function of the gradient of velocity. Numerical results presented using the C-method indicate it yields satisfactory results in 1-D for a wide range of test cases. Guermond et al. [29, 30, 23] proposed an entropy-based viscosity method for conservative hyperbolic systems of equations. In their technique, artificial dissipative terms are added to the system of equations with a viscosity coefficient modulated by the entropy production that is known to be large in shocks and small everywhere else. The method was successfully applied using various spatial discretizations [30, 23, 69] and showed high-order convergence with smooth solutions. Results using the ideal gas equation of state were run for a 1-D Sod shock tube and showed good agreement with the exact solutions. 2-D tests

were also performed on unstructured grids and the method behaved very satisfactorily [29, 69]. The method is fairly simple to implement and is consistent with the entropy minimum principle.

The objective of this dissertation is to solve hyperbolic system of equations using a *continuous* Galerkin finite element method (CGFEM) with an implicit temporal discretization within the Idaho National Laboratory (INL) MOOSE framework [17]. We are particularly interested in simulating flow behaviors occurring in nuclear reactors. The set of equations that will be considered are the multi-dimensional Euler equations with variable area [65] and the seven-equation model for two-phase fluids [55]. These systems of equations are hyperbolic and well defined in a sense that they possess real eigenvalues. To numerically solve these equations, we need to rely on a numerical method that can resolve shocks and other discontinuities that may form. Furthermore, a method is needed that is accurate for a wide range of Mach numbers and is not restricted to any particular equation of state. These requirements may be hard to fulfill. Numerical methods are often tested with the ideal gas equation of state which can not describe the behavior of a compressible liquid. Another difficulty deals with devising a numerical method that is valid for *all speeds*, that is, a method that is required to work satisfactorily in the low-Mach regime while remaining accurate for shock problems. Specifically, a compressible fluid model is employed to simulate flows in the incompressible limit. Recent publications [25, 68] highlights the difficulties related to employing compressible flow solvers in the low-Mach limit: asymptotic studies have shown that some of the numerical methods become ill-scaled in the low-Mach limit, making the numerical solution unphysical. For example, the Roe scheme requires a fix in the low-Mach limit while conserving its accuracy when shocks are present [41].

We propose to extend the entropy viscosity method (EVM) introduced by Guer-

mond et al. to compressible fluid flow equations for reactor applications. The technique is relatively simple to implement and can be used with various spatial discretizations using unstructured grids; furthermore, its dissipative terms are consistent with the entropy minimum principle and are proven to be valid for any equation of state under certain conditions [24]. However, several questions remain: the low-Mach limit has not been investigated, and the current definition of the entropy viscosity coefficients requires an analytical expression of the entropy which can be difficult to obtain for some equations of state. These two issues will be addressed. Particular attention will be given to the low-Mach problem and the available literature related to the asymptotic limit of the Navier-Stokes [48] and Euler equations [25, 68], which, should provide great insight in order to understand how the dissipative terms behave. The effect of the source terms (friction, gravity, heat source) will be also investigated in the prospective of using the entropy viscosity method for nuclear reactor applications. Finally, we also extend the technique to Euler equations with *variable* area.

In addition, we propose to investigate how the entropy viscosity method can be applied to the multi-D radiation-hydrodynamic equations [56]. These equations are known to develop solutions with shocks [7]. They consist of coupling the multi-D Euler equations with a radiation-diffusion equation through source terms. Most of the current solvers are based on Riemann-type solvers [54]. Flux-limiter techniques [28] are also used and suffer from the same drawbacks as for the pure multi-D Euler equations. Therefore, it is valuable to assess how the entropy viscosity method can be adapted to this multi-physics systems. If successful, it will offer an alternative to current numerical methods.

This Dissertation is organized as follows: in Section 2, a brief background is given on the mathematical properties of an hyperbolic scalar equation; the origin of the

entropy viscosity method developed by Guermond et al. [29] is presented. Then, a generalization of the method to hyperbolic systems of equations is provided. In Section 3, the temporal and spatial discretizations employed in the INL MOOSE framework [17] are described and details regarding the implementation of the EVM within a CGFEM discretization are also provided. Then, the multi-D Burger's equation is solved, in order to illustrate the main features of the EVM, and computational results are presented in Section 4. Section 5 and Section 6 are dedicated to the application of the EVM to the multi-D Euler equations with variable area and the 1-D seven-equation two-phase model, respectively. A low-Mach asymptotic limit is performed and the effect of source terms on the EVM are also investigated. Various numerical results are presented in order to validate our approach. Finally, the extension of the EVM to the 1-D radiation-hydrodynamic equation is discussed in Section 7. Lastly, conclusions are given in Section 8.

All of the numerical results are obtained from codes developed using the INL MOOSE framework [17] and their various code names are given in Fig. 1.1.

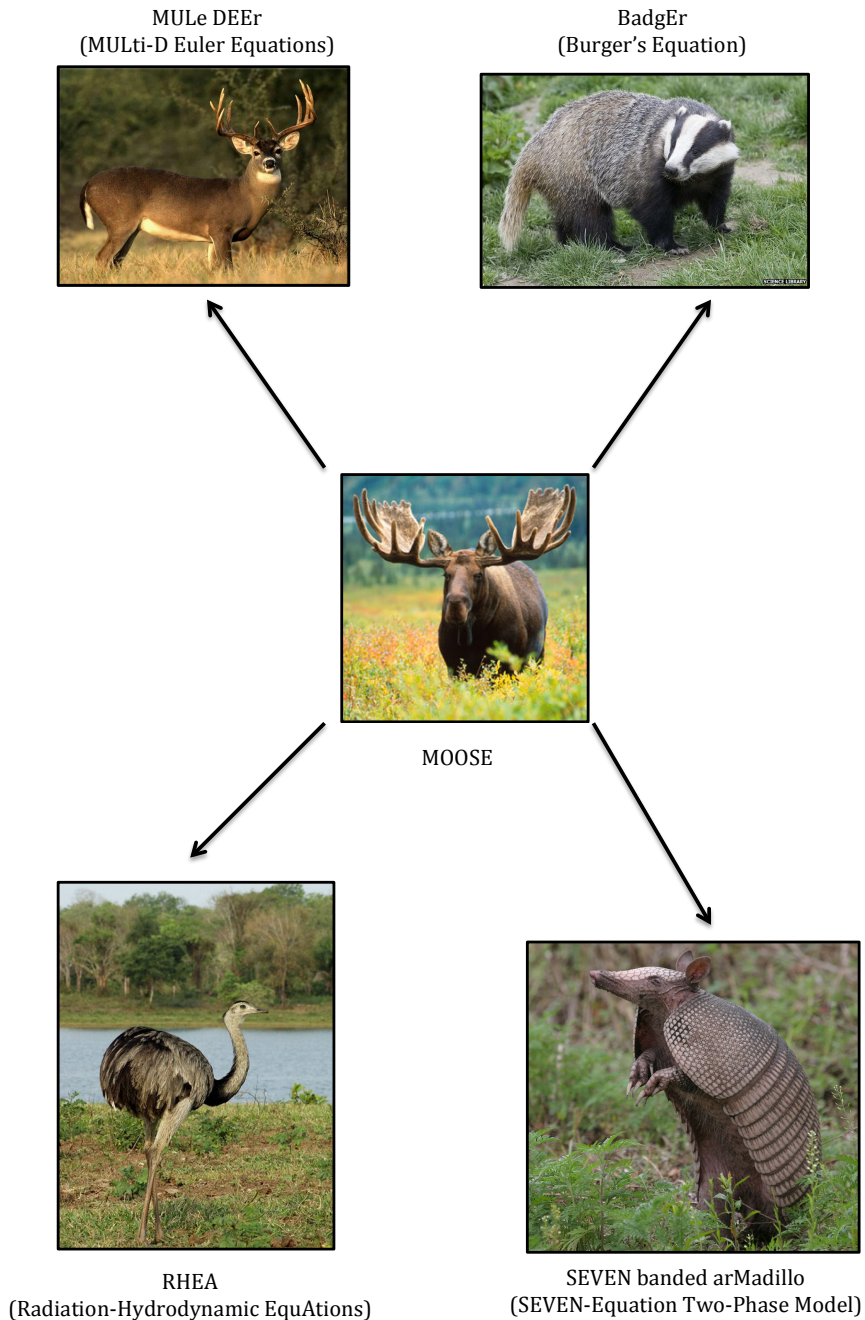


Figure 1.1: Marco's zoo (this is not a food chain).

## 2. HYPERBOLIC CONSERVATION LAWS

In this chapter, some key properties of hyperbolic conservation laws are recalled. The objective is to introduce the reader to the notion of shocks, weak solutions, and entropy conditions by first studying a simple hyperbolic scalar equation. The mathematical properties of the hyperbolic scalar equation are studied, including the derivation of the Jacobian eigenvalues and the characteristic equations. Then, we explain how a shock is formed which leads to a discussion of solution non-uniqueness and weak solutions. We explained how the entropy condition is used to ensure uniqueness of the weak solution and, finally, we discuss convergence of the numerical solution to the physical one. In the last section of this chapter, the notions introduced for the hyperbolic scalar equation are generalized to hyperbolic systems of equations.

### 2.1 Hyperbolic scalar equations

The study of a hyperbolic scalar equation is first given in order to provide the reader with an understanding of the mathematical properties that are needed to aid in the comprehension of shock formation, among other topics.

#### 2.1.1 *Eigenvalue and characteristic curves*

Consider a simple hyperbolic scalar equation with initial and boundary conditions to form what is called an *Initial Boundary Value Problem* (IBVP), as shown in Eq. (2.1). We denote the computational domain by  $\Omega$  of dimension  $d$ , bounded by the boundary  $\Gamma$  of dimension  $d - 1$ . Each variable is assumed to be a function of

space,  $\mathbf{r} \in R^d$ , and time  $t \in \mathbb{R}_+$ .

$$\begin{cases} \partial_t u(\mathbf{r}, t) + \nabla \cdot \mathbf{f}(u) = 0, \quad (\mathbf{r}, t) \in R^d \times R_+ \\ u(\mathbf{r}, 0) = u_0(\mathbf{r}) \end{cases} \quad (2.1)$$

where  $u$  and  $\mathbf{f}(u)$  are the solution and the inviscid flux, respectively. The inviscid flux  $\mathbf{f}(u)$  is assumed to be a differentiable function of the solution  $u$ . Two definitions of the inviscid flux will be considered in this chapter in order to illustrate the differences between linear and non-linear hyperbolic scalar systems: a linear flux  $\mathbf{f}_1$  and a non-linear flux  $\mathbf{f}_2$ , as shown in Eq. (2.2) and Eq. (2.2a).

$$\partial_t u + \nabla \cdot \mathbf{f}_1(u) = \partial_t u(\mathbf{r}, t) + \nabla \cdot (u \hat{\mathbf{n}}) = 0 \quad (2.2a)$$

$$\partial_t u + \nabla \cdot \mathbf{f}_2(u) = \partial_t u(\mathbf{r}, t) + \nabla \cdot \left( \frac{u^2}{2} \hat{\mathbf{n}} \right) = 0 \quad (2.2b)$$

Eq. (2.2a) and Eq. (2.2b) are respectively known as the linear advection and Burger's equations. They have been widely studied in the literature and are well understood [65, 39]. The definition of the vector  $\hat{\mathbf{n}}$  depends on the dimension of the geometry as follows:  $\hat{\mathbf{n}} = (1, 0, 0)$  in 1-D,  $\hat{\mathbf{n}} = (1, 1, 0)$  in 2-D and  $\hat{\mathbf{n}} = (1, 1, 1)$  in 3-D.

The eigenvalue, denoted by  $\lambda$ , of the hyperbolic equation is obtained from the Jacobian of the inviscid flux,  $\mathbf{f}(u)$ , with respect to the solution  $u$ , and corresponds to the wave propagation speed. When considering the fluxes  $\mathbf{f}_1$  and  $\mathbf{f}_2$ , it is found that their eigenvalues are  $\lambda_1 = \|\mathbf{a}\|$  and  $\lambda_2 = u$ , respectively. For the linear advection equation, the wave speed is a constant throughout the computational domain (provided that  $a$  is not a function of space). On the other hand, the wave speed for Burger's equation is a function of space and time since it is equal to the solution itself.

Once the eigenvalues are determined, the next step consists of deriving the characteristic equation and the characteristic curves. For 1-D analysis, the phase space is limited to the  $x - t$  plane. Under this assumption, characteristic curves are defined as curves  $x = x(t)$  and the PDE transforms into an ODE [65] along these curves. To determine the characteristic curves, Eq. (2.1) is recast as a function of the eigenvalue,  $\lambda$ , by using the chain rule as shown in Eq. (2.3).

$$\begin{aligned} \partial_t u + \frac{df}{du} \partial_x u &= 0 \\ \partial_t u + \lambda \partial_x u &= 0 \\ \frac{Du}{Dt} = \partial_t u + \frac{dx}{dt} \partial_x u &= 0 \text{ along } \frac{dx}{dt} = f'(u) = \lambda \end{aligned} \quad (2.3)$$

Eq. (2.3) represents the rate of change of the solution  $u$  along the curve  $\frac{dx}{dt} = f'(u) = \lambda$  that is an ODE. It states that the solution  $u$  is constant along the curve  $\frac{dx}{dt} = \lambda$  because its rate of change is zero. The eigenvalue is the inverse slope of the characteristic curve and is referred to as the characteristic speed. For a given characteristic curve, the characteristic speed is a constant, since the solution  $u$  is constant as well, and given by the initial condition,  $f'(u(x, 0)) = f'(u_0)$  which allows us to integrate to obtain an analytical expression for  $x(t)$ :

$$\begin{aligned} \frac{dx}{dt} &= f'(u_0) \\ \Leftrightarrow x(t) &= x_0 + f'(u_0)t \end{aligned} \quad (2.4)$$

where setting  $x(t = 0) = x_0$  is the initial position of a particle traveling along the characteristic curve. It is common to represent the characteristic curves in a  $x - t$  plane and examples will be given for the linear advection equation and for Burger's equation. Eq. (2.4) informs us of the position  $x$  of a particle carrying the initial value

$u_0$  at each time value  $t$ . Assuming that the initial value of the solution is  $u_0(x_0)$  along the characteristic curve passing through the point  $x_0$  given by Eq. (2.4), the solution  $u(x, t)$  at position  $x$  and time  $t$  can be expressed as follows:

$$u(x, t) = u_0(x_0) = u_0(x - f'(u_0)t). \quad (2.5)$$

Eq. (2.5) can be seen as an analytical solution of the hyperbolic scalar equation (Eq. (2.1)). It is also understood that the derivative of the flux, that corresponds to the eigenvalue of the scalar system, has direct consequence on the behavior of the solution, as will be explained in the next Section.

### 2.1.2 Shocks formation and vanishing viscosity equation/solution

Nonlinear hyperbolic scalar equations are known to develop shocks, even with a smooth initial condition. This section aims at detailing how shocks form based on the mathematical properties introduced in Section 2.1.1 and the two examples of Eq. (2.2a) and Eq. (2.2b), i.e., the 1-D linear advection and Burger's equations.

When considering the 1-D linear advection equation (with the flux  $f_1(u) = au$ ), the eigenvalue is found equal to  $\lambda_1 = a$  and is constant. Thus, the slope of the characteristic curve remains constant and each particle travels at the same velocity through the computational domain. In other word, the initial profile  $u_0(x)$  of the solution is simply translated at speed  $a$  to the right if  $a \geq 0$  or to the left if  $a \leq 0$ . Obviously, if  $a = 0$ , the flux is also null and the solution does not evolve in time. A representation of the characteristic curve for the linear advection equation, Eq. (2.2a), is given in Fig. 2.1 in the  $x - t$  plane: all of the characteristic curves are parallel since their slope is given by the eigenvalue  $\lambda_1 = a$  that is constant.

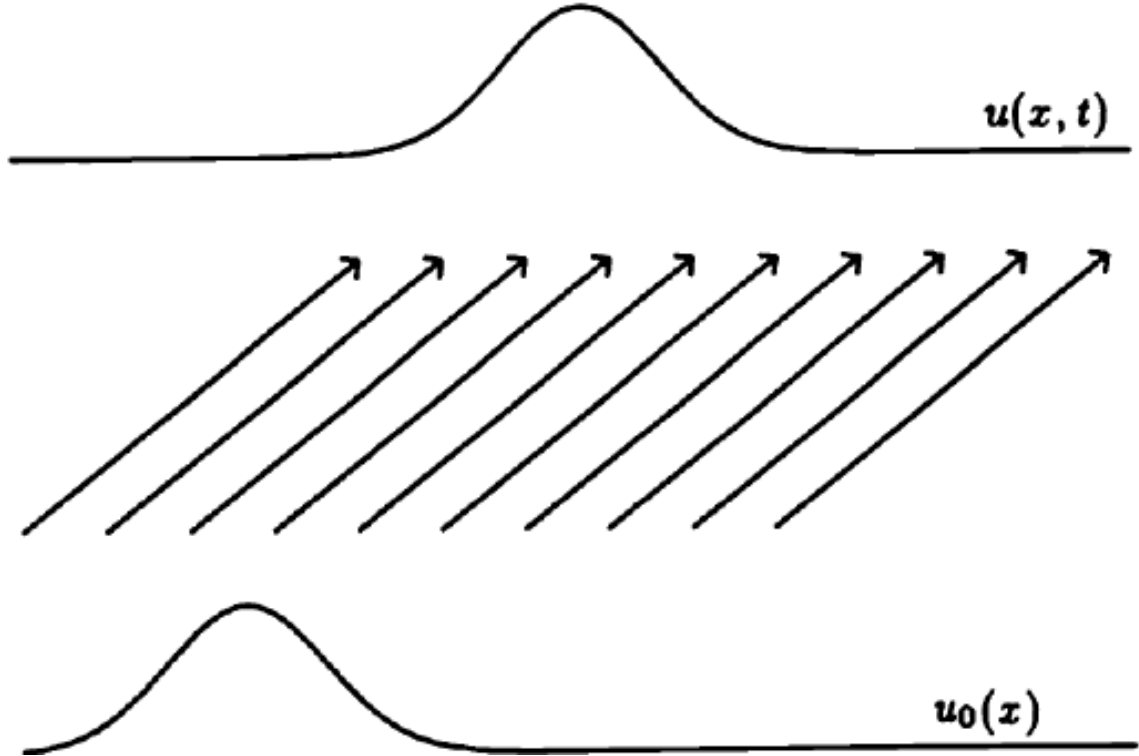


Figure 2.1: Characteristic curves for the linear advection equation [39].

In the case of the 1-D Burger's equation, the eigenvalue is no longer constant and is equal to the solution itself  $\lambda_2 = u(x, t)$ . The slope of the characteristic curve is now a function of space and more precisely of the initial solution  $u_0$  which requires us to analyze two distinct cases: a constant and a non-constant initial solution. In the former case, the slope of the characteristic is constant which is the same situation as with the linear advection equation previously discussed. In the latter case, the characteristic curves will not have the same slope and thus, may intersect. When two characteristic curves intersect, it means that, at a given time and position, two values of the solution are allowed (each characteristic curve carries different initial values of the solution): the solution displays an infinite gradient also called shock wave as shown in Fig. 2.2.

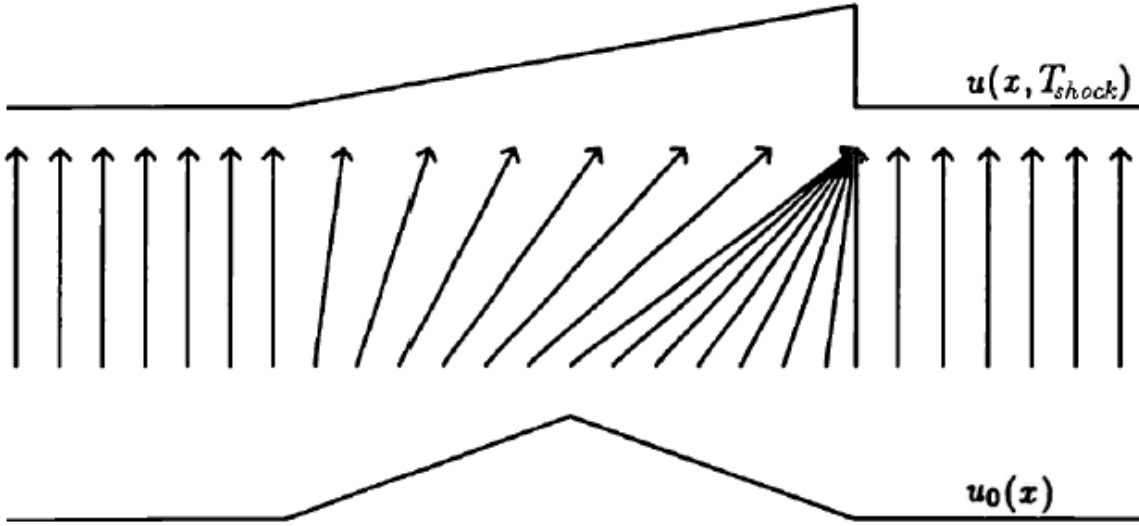


Figure 2.2: Characteristic curves for the 1-D Burger's equation [39].

The time  $T_{shock}$  at which the shock occurs can be analytically determined. Consider a 1-D non-linear flux  $f(u)$  and two characteristic curves originating from the position  $x_0$  and  $x_0 + dx$  carrying the initial values  $u_0(x_0)$  and  $u_0(x_0 + dx)$ , respectively. The characteristic curves are:

$$\begin{aligned} x_1(t) &= x_0 + f'(u_0(x_0))t \\ x_2(t) &= (x_0 + dx) + f'(u_0(x_0 + dx))t. \end{aligned} \quad (2.6)$$

Now assume that the two characteristic curves intersect at time  $T_{shock}$ , which implies  $x_1(T_{shock}) = x_2(T_{shock})$ . Using Eq. (2.6) yields:

$$x_0 + f'(u_0(x_0))T_{shock} = (x_0 + dx) + f'(u_0(x_0 + dx))T_{shock} \quad (2.7)$$

From Eq. (2.7), after a few lines of algebra, an expression for  $T_{\text{shock}}$  can be obtained:

$$T_{\text{shock}} = \frac{-dx}{f'(u_0(x_0 + dx)) - f'(u_0(x_0))} \quad (2.8)$$

Taking the limit  $dx \rightarrow 0$  and using the definition of the derivative, Eq. (2.8) becomes:

$$T_{\text{shock}} = \frac{-1}{f''(u_0)u'_0(x_0)}, \quad (2.9)$$

The trivial case  $f''(u_0) = 0$  implies two options. The first case verifying  $f''(u_0) = 0$  corresponds to a linear-flux which is ruled out since we assumed a non-linear flux. When taking the limit of Eq. (2.9), it yields  $T_{\text{shock}} \rightarrow \infty$ , which means that a shock wave never forms. This result is consistent with the conclusion made earlier in this section when studying the linear advection equation. The second case corresponds to a non-linear flux whose second-order derivative is locally zero: at this particular point, a shock wave cannot form. From Eq. (2.9), it is understood that the convexity of the flux will determine whether or not a shock wave can form. If  $f(u)$  is a convex function, such that  $f''(u) \leq 0$  for all  $u$ , a shock wave will form where the slope of the initial solution  $u'_0$  is negative. On the other hand, when assuming a concave flux, i.e.  $f''(u) \geq 0$ , the initial data must have points where the slope is positive. By minimizing the denominator of Eq. (2.9), the time the wave will brake at, is obtained:

$$T_{\text{shock}} = \frac{-1}{\min(f''(u_0)u'_0(x_0))} \quad (2.10)$$

Once the shock is formed, at a time  $t \geq T_{\text{shock}}$ , more than two characteristic curves may intersect leading to a triple-valued situation as shown in Fig. 2.3.

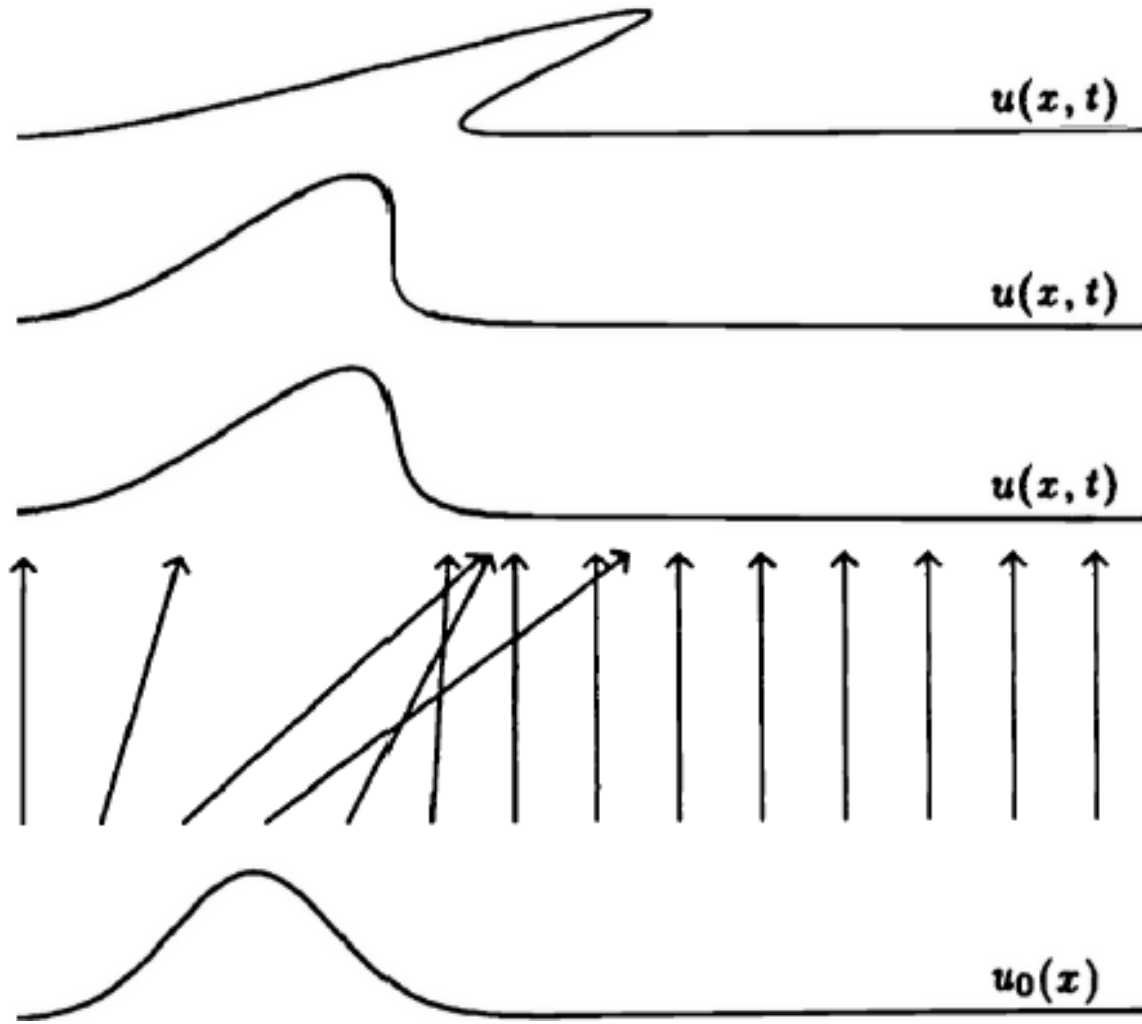


Figure 2.3: Example of a triple-valued situation [39].

In this case, uniqueness of the solution is not ensured since for a given position and time the solution admits three values. This particular phenomenon makes sense when solving the 3-D shallow-water equations that are used to model a breaking wave on a sloping beach. However, when considering gas flows, uniqueness of the thermodynamic properties is required to ensure a point-wise single-valued density. From the last example, we understand that preventing the tripled-value situation from forming may be the key to obtaining the correct physical behavior when solving hyperbolic

scalar equations and hyperbolic systems of equations (e.g., Euler equations). A solution to this problem could come from the study of an advection-diffusion equation type that is used, for instance, to model the propagation of particles in a material by both advection and diffusion phenomena. This type of equation is known to have unconditionally *smooth solution* for all time and spatial location. A 1-D generic form is given in Eq. (2.11).

$$\partial_t u + \partial_x f(u) = \epsilon \partial_{xx} u, \quad (2.11)$$

where  $\epsilon$  is a diffusion coefficient that can be solution-dependent in theory but is assumed constant for the purpose of this section. Since the main difference between the hyperbolic problem given in Eq. (2.1) and Eq. (2.11) lies in the diffusion term  $\epsilon \partial_x x u(x, t)$ , it is proposed to investigate its effect on the numerical solution. If the solution  $u(x, t)$  is smooth, the diffusion term  $\epsilon \partial_{xx} u(x, t)$  in Eq. (2.11) is negligible and the numerical solution is driven by the advection term  $\partial_x f(u(x, t))$  so that Eq. (2.11) and Eq. (2.1) have similar behaviors. As the solution becomes steeper, the diffusion terms becomes large enough to influence the behavior of the numerical solution and will prevent the wave from breaking as it happens in hyperbolic problems. In other terms, the diffusion term, by monitoring the change of curvature in the numerical solution, locally affects the numerical solution where needed. The diffusion coefficient  $\epsilon$  can be seen as a tuning coefficient that will also affect the smoothness of the numerical solution as shown in Fig. 2.4. As  $\epsilon$  goes to zero, the numerical solution becomes sharper and tends to the solution obtained when solving the hyperbolic problem given in Eq. (2.11). On the opposite, with a very large diffusion (viscosity) coefficient, the shock is smoothed out.

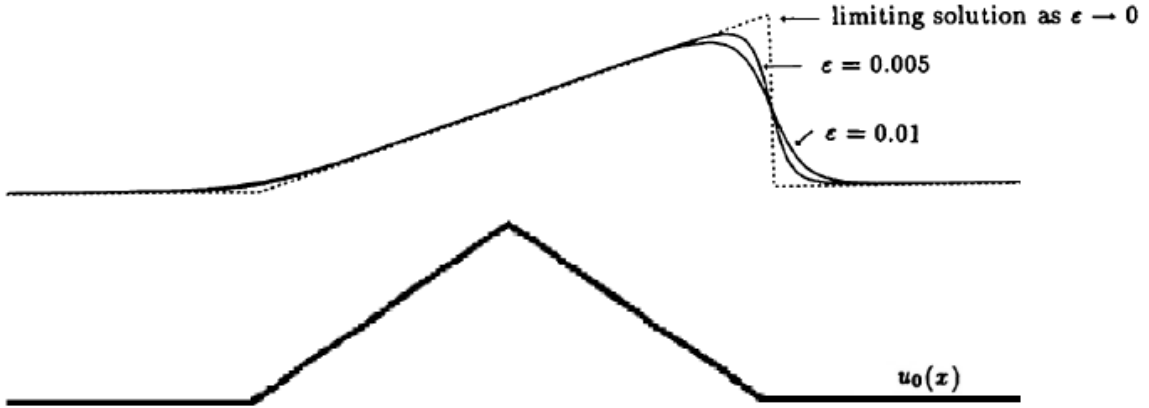


Figure 2.4: Influence of the viscosity coefficient  $\epsilon$  on the numerical solution stiffness [39].

Thus, by adding a diffusion term, also called viscosity term, the numerical solution remains smooth and single valued, and should allow us to retrieve the correct physical behavior of a hyperbolic problem in the limit  $\epsilon \rightarrow 0$ . This approach is referred to as a *vanishing viscosity method* and the numerical solution obtained with this method is denoted by  $u^\epsilon(x, t)$  and called *vanishing viscosity solution*. We can now define the notion of *generalized solution*.

**Definition 2.1.** *A generalized definition  $u$  of a hyperbolic scalar equation conservation law*

$$\partial_t u + \nabla \cdot \mathbf{f}(u) = 0,$$

*is called an admissible vanishing viscosity solution if there is a sequence of smooth unique solutions  $u^\epsilon$  to the parabolic equation*

$$\partial_t u^\epsilon + \nabla f(u^\epsilon) = \epsilon \nabla u^\epsilon,$$

*that converges to  $u$  as  $\epsilon \rightarrow 0$ .*

It is now clear that by adding a viscosity term to an hyperbolic equation as previously explained, a generalized solution can be obtained with the vanishing viscosity approach. We will see in Section 2.1.3 that a generalized solution can be also defined by the use of a mathematical technique resulting in a weak formulation of the hyperbolic scalar equation. Before doing so, it is proposed to investigate one more property of a shock wave: its speed. Knowing the breaking time  $T_{\text{shock}}$  and position is not sufficient information to track a shock wave once it has formed. An useful information will be to derive an expression that provides us with the speed of the shock. One of the reasons for deriving such an expression is to obtain an analytical solution that can be used for comparison against numerical solutions in order to assess their accuracy. To do so, we consider, again, a general 1-D hyperbolic scalar equation for simplicity, as shown in Eq. (2.12):

$$\partial_t u(x, t) + \partial_x f(u(x, t)) = 0 \quad (2.12)$$

We assume that the position of the shock is given by a function of time denoted by  $s(t)$  and that the associated speed is  $S = \frac{ds}{dt}$ . At this particular position, the derivatives of the solution  $u$  and the flux  $f(u)$  are no longer continuous. We also define a control volume  $[x_1; x_2]$  that contains the shock wave so that  $x_1 \leq s(t) \leq x_2$ .

Eq. (2.12) is integrated over the control volume as shown in Eq. (2.13):

$$\frac{d}{dt} \int_{x_1}^{s(t)} u(x, t) dx + \frac{d}{dt} \int_{s(t)}^{x_2} u(x, t) dx + f(x_2, t) - f(x_1, t) = 0 \quad (2.13)$$

The first two integrals can be recast by using the Leibnitz Rule:

$$\frac{d}{dt} \int_{y_1(t)}^{y_2(t)} g(y, t) dy = \int_{y_1(t)}^{y_2(t)} \frac{\partial g(y, t)}{\partial y} dy + g(y_2, t) \frac{dy_2(t)}{dt} - g(y_1, t) \frac{dy_1(t)}{dt}. \quad (2.14)$$

By noticing that  $x_1$  and  $x_2$  are fixed and thus not functions of time, we obtain:

$$\int_{x_1}^{s(t)} \partial_t u(x, t) dx - \int_{s(t)}^{x_2} \partial_t u(x, t) dx + (u(s^-(t)) - u(s^+(t))) S + f(x_2, t) - f(x_1, t) = 0, \quad (2.15)$$

where  $u(s^-(t), t)$  and  $u(s^+(t), t)$  are the values of the solution  $u$  before and after the shock position, respectively. Assuming that the  $x_1$  and  $x_2$  approach the shock position  $s(t)$  from the left and right, respectively, and that  $\partial_t u$  is bounded, the two integrals vanish to yield the following expression for the shock speed  $S$ :

$$S = \frac{f(x_2, t) - f(x_1, t)}{u(s^-(t)) - u(s^+(t))} = \frac{\Delta f}{\Delta u}. \quad (2.16)$$

The above expression for the speed of shock (Eq. (2.16)) is known as the Rankine-Hugoniot jump condition. The hyperbolic scalar equation given Eq. (2.12) is only valid in smooth parts of the solution, and thus, require the use of the Rankine-Hugoniot jump condition in order to solve for the shock region.

### 2.1.3 Weak solution and entropy condition

As mentioned in Section 2.1.2, another way to define a generalized solution is to use a mathematical technique that consists of multiplying the hyperbolic scalar equation by a smooth test function that is continuously differentiable within a compact support. Then, integration per parts is performed in order to transfer the derivative from the solution  $u$  and onto the test function. The resulting equation involves fewer derivatives on  $u$  and, hence, requires less smoothness. It is assumed that the test functions are only non-zero and continuously differentiable within a bounded set such as:  $\phi(\mathbf{r}, t) \in C_0^1(\mathbb{R}^d \times \mathbb{R}^+)$ . Following the method detailed in Leveque's book [39] (page 27), the 1-D conservation law  $\partial_t u + \partial_x f(u) = 0$  is multiplied by a test function

$\phi(x, t)$  and integrated over space and time to yield:

$$\int_0^{+\infty} dt \int_{-\infty}^{+\infty} dx [\partial_t u(x, t) + \partial_x f(u)] \phi(x, t) = 0. \quad (2.17)$$

Eq. (2.17) is integrating by parts to obtain:

$$\begin{aligned} & \int_0^{+\infty} dt \int_{-\infty}^{+\infty} dx [u(x, t) \partial_t \phi(x, t) + f(u) \partial_x \phi(x, t)] = \\ & - \int_{-\infty}^{+\infty} dx \phi(x, t) u(x, t) \Big|_0^{+\infty} - \int_0^{+\infty} dt \phi(x, t) f(u(x, t)) \Big|_{-\infty}^{+\infty} \end{aligned} \quad (2.18)$$

where the two integrals on the right-hand-side of Eq. (2.18) correspond to the boundary terms. Recalling that the test function is identically zero outside a bounded set which means  $\phi(x, t) \rightarrow 0$  as  $x \rightarrow \pm\infty$  and  $t \rightarrow +\infty$ , all of the boundary terms vanish but for  $t = 0$ . The resulting equation contains only one boundary term that is a function of the initial condition as shown in Eq. (2.19).

$$\begin{aligned} & \int_0^{+\infty} dt \int_{-\infty}^{+\infty} dx [u(x, t) \partial_t \phi(x, t) + f(u) \partial_x \phi(x, t)] = \\ & - \int_{-\infty}^{+\infty} dx \phi(x, 0) u_0(x). \end{aligned} \quad (2.19)$$

Eq. (2.19) is used in the definition of a weak solution as follows:

**Definition 2.2.** *The function  $u(x, t)$  is called a weak solution of the conservative law*

$$\partial_t u + \partial_x f(u) = 0,$$

*if Eq. (2.19) holds for all test functions  $\phi(\mathbf{r}, t) \in C_0^1(\mathbb{R}^d \times \mathbb{R}^+)$ .*

The formulation obtained in Eq. (2.19) presents some similarities with the 1-D

conservation law when integrated over a rectangle  $[x_1, x_2] \times [t_1, t_2]$ :

$$\begin{aligned} \partial_t u(x, t) + \partial_x f(u) = 0 \rightarrow \\ \int_{x_1}^{x_2} [x(x, t_2) - u(x, t_1)] dx + \int_{t_1}^{t_2} [f(u(x_2, t)) - f(u(x_1, t))] dt = 0 \end{aligned} \quad (2.20)$$

As a matter of fact, we can show that Eq. (2.19) and Eq. (2.20) are equivalent. To do so, we consider a test function  $\phi(x, t)$  with the following properties:

$$\phi(x, t) = \begin{cases} 1 & \text{for } (x, t) \in [x_1, x_2] \times [t_1, t_2] \\ 0 & \text{for } (x, t) \notin [x_1 - \delta, x_2 + \delta] \times [t_1 - \delta, t_2 + \delta] \end{cases} \quad (2.21)$$

where  $\delta$  is the width of the intermediate strip. Since the test function  $\phi$  verifying Eq. (2.21) vanish as  $x \rightarrow \pm\infty$  and  $t \rightarrow \infty$ , Eq. (2.19) is still valid. The temporal and spatial derivatives of the test function  $\phi(x, t)$  are zero everywhere but in the intermediate strip, and approach delta function as  $\delta \rightarrow 0$ . Thus, in the limit  $\delta \rightarrow 0$ , Eq. (2.19) is shown to be equivalent to the integral form of the conservation law given in Eq. (2.20). A direct consequence of this result is that the weak solution in the sense of Eq. (2.19) includes the solution of the hyperbolic conservation law we are seeking and also the vanishing viscosity generalized solution. However, uniqueness of the weak solution is not ensured by Eq. (2.19) and can be demonstrated by considering a 1-D Riemann problem for a hyperbolic conservation law. The reader is referred to [65] and [39] for additional details. The question arising from the previous statement is: how to identify the correct weak solution that corresponds to the physically vanishing viscosity solution? The answer lies in the entropy condition that is defined by analogy to the gas dynamics case. Mathematically, the entropy condition can be defined in multiple ways using either the speed of shock  $S$  (see page 37 in [39]) or an entropy

function that will be further detailed next. Because our focus is on hyperbolic system of equations, we have chosen to define the entropy condition through the derivation of an entropy residual for an hyperbolic conservation law.

Before detailing the steps employed to obtain an entropy residual, we recall the meaning of the entropy condition for gas dynamics. In gas dynamics, the physical entropy is constant along a smooth path flow but experiences a jump to a higher value across a shock wave. Thus, the physical entropy is expected to increase if the flow contains a shock wave, which gives us a condition in order to pick out the correct weak solution. It remains to translate this condition into a mathematical statement. Before doing so, we want to emphasize the difference between the mathematical and physical entropies in order to clear any confusion. The physical entropy (from an engineering point of view) is by definition positive and increases as a function of time to reach a maximum value at steady-state. The mathematical entropy is defined convex and decreases as a function of time. In order to avoid any confusion, the mathematical and physical entropies will be referred to as  $\eta$  and  $s$ , respectively. These two entropies are related to each other by the following relation:

$$s(u) = -\eta(u) + \eta_0, \quad (2.22)$$

where  $\eta_0$  is taken larger than the maximum of the absolute value of the mathematical entropy  $\eta$  in order to ensure positivity of the physical entropy  $s$ . Of course, with such relation, convexity of  $\eta$  implies that  $s$  is concave. It is customary to work with the mathematical entropy when dealing with hyperbolic scalar equations, whereas the physical entropy is preferred for hyperbolic systems of equations such as the Euler equations.

We now derive the entropy condition for a hyperbolic scalar conservation law of

the generic form:

$$\partial_t u(\mathbf{r}, t) + \boldsymbol{\nabla} \cdot \mathbf{f}(u) = 0. \quad (2.23)$$

We assume the existence of an entropy function  $\eta(u)$  for which a conservation law to be determined holds. We first consider the case of a smooth flow and multiply Eq. (2.23) by the derivative of  $\eta$  with respect to  $u$ , denoted by  $\eta_u$ :

$$\eta_u \partial_t u(\mathbf{r}, t) + \eta_u \boldsymbol{\nabla} \cdot \mathbf{f}(u) = 0. \quad (2.24a)$$

Using the chain rule, one obtains

$$\eta_u \partial_t u(\mathbf{r}, t) + \eta_u \mathbf{f}'(u) \cdot \boldsymbol{\nabla} u = 0, \quad (2.24b)$$

which can be simplified to

$$\partial_t \eta(u) + \mathbf{f}'(u) \cdot \boldsymbol{\nabla} \eta(u) = 0. \quad (2.24c)$$

The relation given in Eq. (2.24c) is a conservation law for  $\eta$  which means that the mathematic entropy is conserved in a smooth flow. The entropy conservation law can also be recast as a function of the entropy flux  $\psi$  by setting  $\psi'(u) = \eta_u \mathbf{f}'(u)$ , which yields<sup>1</sup>:

$$\partial_t \eta(u) + \boldsymbol{\nabla} \cdot \psi(u) = 0. \quad (2.25)$$

The set  $(\eta, \psi)$  is called an entropy pair. The corresponding physical entropy pair is  $(s, -\psi)$  since  $\psi'(u) = \eta_u \mathbf{f}'(u)$ .

We now consider a solution that presents one or more regions with a discontinuity or shock. The manipulations performed above are no longer valid since the

---

<sup>1</sup>here,  $\eta$  depends only on  $u$ , so we could have written  $\psi'(u) = \eta'(u) \mathbf{f}'(u)$

solution is not smooth. Instead, it is proposed to look at the vanishing viscosity equation introduced in Eq. (2.11) and investigate the behavior of the weak solution as the viscosity coefficient tends to zero. Applying the vanishing viscosity method to Eq. (2.24) yields

$$\partial_t u(\mathbf{r}, t) + \nabla \cdot \mathbf{f}(u) = \nabla \cdot (\mu(\nabla u(\mathbf{r}, t))) , \quad (2.26)$$

where  $\mu(\mathbf{r}, t)$  is a positive viscosity coefficient that is typically spatially dependent in general. Because of the presence of the viscous term in Eq. (2.26), the solution remains smooth which allows us to perform the same manipulations as in Eq. (2.24). Hence, we obtain (the notation  $(\mathbf{r}, t)$  is dropped to simplify the derivation):

$$\partial_t \eta(u) + \nabla \cdot \psi(u) = \eta_u \nabla \cdot (\mu \nabla u) , \quad (2.27)$$

By integrating per parts the right-hand-side of Eq. (2.27), one obtains:

$$\partial_t \eta(u) + \nabla \cdot \psi(u) = \nabla \cdot (\eta_u \mu \nabla u) - \mu(\nabla u \cdot \nabla \eta_u) . \quad (2.28)$$

Since we are interested in the weak solution, Eq. (2.28) is integrated over the space-time domain  $\Theta = [\mathbf{r}_1, \mathbf{r}_2] \times [t_1, t_2]$  on the same model as in Eq. (2.20). It is also assumed that the shock remains within  $\Theta$  for all time  $t \in [t_1, t_2]$  and away from the boundaries. Thus, Eq. (2.28) becomes:

$$\begin{aligned} \int_{\mathbf{r}_1}^{\mathbf{r}_2} d\mathbf{r} \int_{t_1}^{t_2} dt [\partial_t \eta(u) + \nabla \cdot \psi(u)] &= \int_{\mathbf{r}_1}^{\mathbf{r}_2} d\mathbf{r} \int_{t_1}^{t_2} dt \nabla \cdot (\eta_u \mu \nabla u) \\ &- \int_{\mathbf{r}_1}^{\mathbf{r}_2} d\mathbf{r} \int_{t_1}^{t_2} dt \mu \nabla u \cdot \nabla \eta_u . \end{aligned} \quad (2.29)$$

The first term in the right-hand-side of Eq. (2.29) can be recast as follows:

$$\int_{\mathbf{r}_1}^{\mathbf{r}_2} d\mathbf{r} \int_{t_1}^{t_2} dt \nabla \cdot (\eta_u \mu \nabla u) = \int_{t_1}^{t_2} dt [\eta_u \mu(\mathbf{r}_2, t) d\mathbf{r} \nabla u(\mathbf{r}_2, t) - \eta_u \mu(\mathbf{r}_1, t) \nabla u(\mathbf{r}_1, t)]. \quad (2.30)$$

Since the shock position cannot be confounded with the boundary of the domain by assumption, the gradient of the solution at the points  $\mathbf{r}_1$  and  $\mathbf{r}_2$  remains bounded as  $\mu \rightarrow 0$ . Then, as the viscosity coefficient tends to zero, the whole integral vanishes. The second term in the right-hand-side of Eq. (2.29) is more complex to deal with. First, the integral is recast by applying the chain rule to  $\nabla \eta_u$ :

$$\int_{\mathbf{r}_1}^{\mathbf{r}_2} d\mathbf{r} \int_{t_1}^{t_2} dt \mu \nabla u \cdot \nabla \eta_u = \int_{\mathbf{r}_1}^{\mathbf{r}_2} d\mathbf{r} \int_{t_1}^{t_2} dt \mu \eta_{uu} \nabla u \cdot \nabla u, \quad (2.31)$$

where  $\eta_{uu}$  denotes the second derivative of  $\eta$  with respect to  $u$ . As  $\mu \rightarrow 0$ , the integral does not vanish because of the terms  $\nabla u \cdot \nabla u$  that will become larger and larger at the location of the discontinuity. However, by assuming that the entropy function is convex, i.e.,  $\eta_{uu} \geq 0$  and noticing that  $\nabla u \cdot \nabla u \geq 0$  and  $\mu \geq 0$ , the sign of Eq. (2.31) is found to be positive. Using the above results, we conclude that the vanishing viscosity weak solution satisfies the inequality:

$$\int_{\mathbf{r}_1}^{\mathbf{r}_2} d\mathbf{r} \int_{t_1}^{t_2} dt [\partial_t \eta(u) + \nabla \cdot \psi(u)] \leq 0, \quad (2.32)$$

for both smooth and discontinuous solutions. Since the inequality given in Eq. (2.32) holds for any  $\Theta$ , it can be simplified to

$$\partial_t \eta(u) + \nabla \cdot \psi(u) \leq 0 \quad (2.33)$$

in the weak sense and is known as the *entropy inequality*.

**Definition 2.3.** *The function  $u(\mathbf{r}, t)$  is the entropy solution of the hyperbolic conservation law*

$$\partial_t u(\mathbf{r}, t) + \nabla \cdot \mathbf{f}(u) = 0$$

*if for all convex entropy pair  $(\eta, \psi)$ , the inequality*

$$\partial_t \eta(u) + \nabla \cdot \psi(u) \leq 0$$

*is satisfied in a weak sense.*

The entropy inequality is used to analyze numerical methods in order to demonstrate that the numerical solution converges to the entropy solution. It is now proposed to see how the entropy inequality is used in the theoretical derivation of the entropy viscosity method for an hyperbolic scalar equation.

#### 2.1.4 Entropy Viscosity Method (EVM) and hyperbolic scalar equations

This section aims at making the link between the theoretical results presented from Section 2.1.1 through Section 2.1.3 and the entropy viscosity method (EVM) that is the focus of this dissertation. The results presented in this section rely on the work by Guermond et al. [29, 30, 23, 69] and are used to familiarize the reader with the EVM.

In Section 2.1.2 and Section 2.1.3, we emphasized on the importance of ensuring uniqueness of the weak solution: this is achieved (i) by adding a viscosity term to the hyperbolic scalar equation in order to prevent triple-value points from forming and (ii) by using the entropy inequality (Eq. (2.33)), which is mathematically equivalent to:

$$\partial_t u + \nabla \cdot \mathbf{f}(u) = \nabla \cdot (\mu \nabla u) \quad (2.34a)$$

$$R(\mathbf{r}, t) = \partial_t \eta(\mathbf{r}, t) + \nabla \cdot \psi(\mathbf{r}, t) \leq 0, \quad (2.34b)$$

where  $\mu(\mathbf{r}, t)$  is a spatially dependent viscosity coefficient and  $R(\mathbf{r}, t)$  denotes the entropy residual. Assuming that  $\mu$  is constant, Eq. (2.11) is retrieved. All of the other variables in Eq. (2.34) were defined previously. It was shown in Section 2.1.3 that the sign of the entropy residual,  $R$ , is related to the convexity of the mathematical entropy function  $\eta$  and to the positivity of the viscosity coefficient  $\mu(\mathbf{r}, t)$ , when using the vanishing viscosity equation Eq. (2.34a). Instead of taking a viscous flux of the form  $\mu(\mathbf{r}, t) \nabla u(\mathbf{r}, t)$  in Eq. (2.34a), a more generic expression could have been assumed:

$$\partial_t u + \nabla \cdot \mathbf{f}(u) = \nabla \cdot \mathbf{g}(\mu, u),$$

where  $\mathbf{g}(\mu, u)$  is a viscous flux that will have to be determined such that  $R$  is negative. In other words, the entropy condition could be used to derive the proper viscous terms that will ensure the correct sign for the entropy residual in the shock region. In the case of the hyperbolic scalar equations, the choice of the viscous term is obvious and probably unique. However, when considering hyperbolic systems of equations (e.g., Euler equations), deriving the viscous terms consistent with the entropy condition may no longer be evident. This aspect of the method is detailed in Section 2.2.

Once the viscous term is derived and known to be consistent with the entropy condition, it remains to define the positive viscosity coefficient  $\mu(\mathbf{r}, t)$ . This step is crucial and should not be underestimated since it will determine the accuracy of the numerical method. We require the viscosity coefficient to be smooth: in [8], it is shown that a discontinuous viscosity coefficient could yield instabilities in the numerical solution. Such a behavior can be easily understood by considering the following example. Let us assume that the viscosity coefficient jumps from zero to a large value in the vicinity of the shock region. Because the dissipative term

is conservative, the gradient of the solution,  $\nabla u$ , will have to experience the same discontinuity as the viscosity coefficient, thus, yielding the same type of behavior in the solution itself. Going back to the definition of the  $\mu$ , the simplest definition we can think of is to set  $\mu$  equal to a constant value. By doing so, dissipation will be added to the shock region, preventing the waves from breaking, but also to the smooth regions of the solution that do not need dissipation. Such a behavior is not ideal as it is over-dissipative. Another option would be to track the shock position in order to only add a significant amount of dissipation in the shock region. Defining a viscosity function capable of detecting and tracking shocks is not straightforward and needs to rely on a good understanding of the theory related to the formation of shocks. For example, we can think of monitoring the gradient of the solution itself that will become large in the shock region. Following this reasoning, a possible definition (in 1-D) would be to have  $\mu(x, t) \propto |\partial_x u(x, t)|$ . Another approach consists of using the entropy residual  $R$  derived in Section 2.1.3. The entropy residual was initially studied to ensure uniqueness of the weak solution, but its variations are intimately related to the solution:  $R$  is small as the solution is smooth and  $R$  becomes large (in absolute value) in the shock region. Thus, by monitoring the variation of the entropy residual, the shock can be detected and also tracked. This approach was used by Guermond et al. [29, 30, 23] to solve for hyperbolic scalar equations such as the multi-D Burger's equation. Their method has been coined as the "Entropy Viscosity Method" (EVM). It requires the definition of three viscosity coefficients: a high-order viscosity coefficient,  $\mu_e(\mathbf{r}, t)$ , that is defined to be proportional to the absolute value of the entropy residual  $|R|$ , a first-order viscosity coefficient, denoted by  $\mu_{max}(\mathbf{r}, t)$  and set proportional to the local maximum eigenvalue of  $\mathbf{f}(u)$ , and the final viscosity coefficient  $\mu(\mathbf{r}, t)$  taken to be the minimum of the previous two coefficients, i.e.,  $\mu(\mathbf{r}, t) = \min(\mu_{max}(\mathbf{r}, t), \mu_e(\mathbf{r}, t))$ . The coefficient  $\mu$  is the one

actually used in the dissipative term  $\nabla \cdot (\mu(\mathbf{r}, t) \nabla u(\mathbf{r}, t))$ . The idea is to detect the entropy production characteristic of a shock wave. By defining  $\mu_e(\mathbf{r}, t)$  proportional to  $|R|$ , the high-order viscosity will be large in the shock region and small elsewhere. The first-order viscosity serves as an upper bound for  $\mu(\mathbf{r}, t)$  and its definition meets two criteria:

1. the definition of  $\mu_{max}(\mathbf{r}, t)$  is determined so that the viscous regularization in Eq. (2.34a) is equivalent to the upwind-scheme when employing  $\mu(\mathbf{r}, t) = \mu_{max}(\mathbf{r}, t) := \frac{h}{2}f'(u(\mathbf{r}, t))$  ( $h$  being the local grid size). The derivation of the expression for  $\mu_{max}$  can be found in [24] and is easily demonstrated in 1-D when discretizing Eq. (2.34) with a finite difference method (or equivalently with a continuous FEM methods with trapezoidal quadrature rules).
2. the first-order viscosity coefficient is related to the Courant-Friedrichs-Lowy number (CFL) and more precisely to the stability of the numerical solution when using temporal explicit schemes.

Based on the definition of the high- and first-order viscosity coefficients, the values taken by  $\mu(\mathbf{r}, t)$  are as follows: when the solution is smooth, the entropy production measured by the entropy residual  $R$  is small and thus  $\mu(\mathbf{r}, t) = \mu_e(\mathbf{r}, t)$  is also small. In the shock region, the entropy residual is peaked and the high-order viscosity coefficient is expected to saturate to the first-order viscosity coefficient that is known to be over-dissipative since it is equivalent to the upwind scheme. With such definitions, the viscosity coefficient  $\mu(\mathbf{r}, t)$  is peaked in the shock region and small elsewhere, while experiencing a continuous spatial variation.

The definition of the high-order viscosity coefficient,  $\mu_e$ , is not complete yet. A dimensional analysis of Eq. (2.34) shows that the viscosity coefficients have the units

of  $m^2 \cdot s^{-1}$ , which yield the following definition for  $\mu_e$ :

$$\mu_e(\mathbf{r}, t) = h^2 \frac{|R(\mathbf{r}, t)|}{\text{norm}(s)}$$

where  $\text{norm}(s)$  is a normalization function of the same unit as the entropy  $s$ . Guermond et al. proposed in [30] to use  $\text{norm}(s) = \|s - \bar{s}\|_\infty$  where  $\bar{s}$  is the average value of the entropy function over the entire computational domain and  $\|\cdot\|_\infty$  denotes the infinity norm. With such a normalization,  $\mu_e$  was found to behave well in their numerical tests. Their definition of the EVM, when applied to hyperbolic scalar equation, is the following:

$$\partial_t u + \nabla \cdot \mathbf{f}(u) = \nabla \cdot (\mu \nabla u) \quad (2.35a)$$

$$R = \partial_t \eta + \nabla \cdot \psi \quad (2.35b)$$

$$\begin{cases} \mu(\mathbf{r}, t) = \min(\mu_e(\mathbf{r}, t), \mu_{\max}(\mathbf{r}, t)) \\ \mu_{\max}(\mathbf{r}, t) = \frac{h}{2} |f'(u(\mathbf{r}, t))| \\ \mu_e(\mathbf{r}, t) = h^2 \frac{\max(|R(\mathbf{r}, t), J|)}{\|s - \bar{s}\|_\infty} \end{cases} \quad (2.35c)$$

The jump of the entropy flux  $\psi$ , denoted by  $J$ , is included in the definition of the high-order viscosity coefficient since it is also a good indicator of entropy production. Information relative to the computation of the jump with a continuous Galerkin finite element method (CGFEM) discretization will be detailed in Section 3.1.1. In the case of discontinuous schemes, the reader is referred to [69]. Numerical results for the multi-D Burger's equation solved with the EVM and discretized using the CGFEM are presented in Section 4.1.

**Remark.** *The definition of the viscosity coefficients given in Eq. (2.35c) requires an isotropic mesh in order to be able to define the grid size  $h$ . An alternative definition*

without  $h$  is under investigation for the case of hyperbolic scalar equations.

## 2.2 Hyperbolic system of equations

In this section, the entropy viscosity method is applied to non-linear hyperbolic systems of equations. The reader can refer to [65] and [39] for an extension of the theoretical notions (eigenvalues, characteristic curves, ...) in the case of non-linear hyperbolic conservation laws. The objective of this section is to provide the reader with a methodology on how to apply the EVM to any hyperbolic system of equations. For academic purpose, we will rely on the latest published version of the EVM [69] for the multi-D Euler equations in order to understand the main steps of the method. Other more recent publications will be also used. [24, 30] are good prerequisites to [69] to observe the evolution of the EVM in the recent years. For hyperbolic system of equation, it is customary to work with the physical entropy  $s$  that is of opposite sign of the mathematical entropy  $\eta$ .

To the best of our knowledge, the EVM was successfully applied to one hyperbolic system of equation: the multi-D Euler equations with the ideal gas equation of state [24, 69]. Good agreements with the exact solutions were obtained in 1- and 2-D results when using discontinuous schemes (finite volume and discontinuous Galerkin finite element methods), spectral and Fourier methods. We now recall the details of the latest version of the method [69] and remind the reader that this version will be used as a starting point and modified during this dissertation. The viscous regularization derived from the entropy condition for the multi-D Euler equations with the ideal gas equation of state is as follows:

$$\partial_t \rho + \nabla \cdot (\rho \mathbf{u}) = \nabla \cdot (\mu \nabla \rho) \quad (2.36a)$$

$$\partial_t (\rho \mathbf{u}) + \nabla (\rho \mathbf{u} \otimes \mathbf{u}) + \nabla P = \nabla \cdot (\rho \mu \nabla^s \mathbf{u}) \quad (2.36b)$$

$$\partial_t (\rho E) + \nabla \cdot [\mathbf{u} (\rho E + P)] = \nabla \cdot (\kappa \mathbf{u} \nabla^s \mathbf{u} + \kappa \nabla T) \quad (2.36c)$$

$$P = (\gamma - 1) \rho e = (\gamma - 1) C_v \rho T \quad (2.36d)$$

where  $\rho$ ,  $\rho \mathbf{u}$  and  $\rho E$  are the fluid density, momentum and total energy, respectively, and will be referred to as the conservative variables. The pressure  $P$  and the temperature  $T$  are computed from the Ideal Gas equation of state (IGEOS) recalled in Eq. (2.36d) which is a function of the density  $\rho$  and the specific internal energy  $e$ . The heat capacity  $C_v$  is constant by definition. The viscosity coefficients  $\mu$  and  $\kappa$  are space- and time-dependent and are taken proportional to an entropy residual  $R$  as follows:

$$\begin{cases} \mu(\mathbf{r}, t) = \min(\mu_e(\mathbf{r}, t), \mu_{max}(\mathbf{r}, t)) \\ \kappa(\mathbf{r}, t) = \frac{\gamma_{-1}^{\text{Pr}}}{\gamma - 1} \mu(\mathbf{r}, t), \end{cases} \quad (2.37a)$$

and

$$\begin{aligned} \mu_{max}(\mathbf{r}, t) &= \frac{h}{2} (||\mathbf{u}(\mathbf{r}, t)|| + c(\mathbf{r}, t)) \\ \mu_e(\mathbf{r}, t) &= C_E h^2 \frac{\max(||R(\mathbf{r}, t)||, J)}{||s(\mathbf{r}, t) - \bar{s}(t)||_\infty} \\ R(\mathbf{r}, t) &= \partial_t s(\mathbf{r}, t) + \mathbf{u} \cdot \nabla s(\mathbf{r}, t), \end{aligned} \quad (2.37b)$$

where  $C_E$  is a constant coefficient of order one,  $h$  is the grid size,  $c = \sqrt{\gamma P / \rho}$  is the speed of sound and  $\text{Pr}$  is a Prandtl number taken in the interval  $\in [0; \frac{1}{4}]$ . The variable  $J$  denotes the jump of the entropy flux  $\mathbf{u} s$ , is cell-wise constant, and is computed at the interfaces between a cell and its direct neighbors [69]. The entropy  $s$  is function of the density and the pressure:

$$s(\rho, P) = C_v \ln \left( \frac{P}{\rho^\gamma} \right), \quad (2.38)$$

but can also be recast as a function of the density and the internal energy using the IGEOS. The symmetric gradient  $\nabla^s \mathbf{u}$  is defined with the following entries  $\nabla^s \mathbf{u}_{i,j} = \frac{1}{2} \left( \frac{\partial u_i}{\partial x_j} + \frac{\partial u_j}{\partial x_i} \right)$ . The current definition of the EVM suffers from a few theoretical gaps. The normalization parameters  $\|s(\mathbf{r}, t) - \bar{s}(t)\|_\infty$  used in the definition of the high-order viscosity coefficient  $\mu_e$  in Eq. (2.37b) does not currently have a theoretical justification beyond a dimensionality argument. The same remark can be made for the Prandtl number that is set by the user based on testing and experience. Moreover, the viscous regularization given in Eq. (2.36) depends on the equation of state and, as given here, is only valid for the IGEOS. However, new developments in the theory extended the validity of the method for the multi-D Euler equations to any equation of state [24] and hence makes it a good candidate for nuclear reactor applications, for instance. Thus, based on the work done in [24] and with the experience gained from [30, 69] the following methodology is proposed. We consider the generic non-linear hyperbolic system in order to explain the methodology:

$$\partial_t \mathbf{U} + \nabla \cdot \mathbf{F}(\mathbf{U}) = 0, \quad (2.39)$$

where  $\mathbf{U} = (U_1, \dots, U_n)$  is the solution vector and  $\mathbf{F}(\mathbf{U}) = (F_1, \dots, F_n)$  is a hyperbolic flux whose eigenvalues are denoted by  $(\lambda_1, \dots, \lambda_n)$ .

1. The first step consists of deriving a conservation law for an entropy function denoted by  $s(\mathbf{U})$  of the form:

$$R(\mathbf{U}) = \partial_t s(\mathbf{U}) + \mathbf{F}_U \cdot \nabla s(\mathbf{U}) = 0, \quad (2.40)$$

where  $\mathbf{F}_U = \frac{\partial \mathbf{F}}{\partial \mathbf{U}}$  is the jacobian matrix of the hyperbolic flux  $\mathbf{F}(\mathbf{U})$ . This entropy equation/residual is obtained from the hyperbolic system of equation

given in Eq. (2.39) either by multiplying by the matrix  $s_{\mathbf{U}} = \frac{\partial s(\mathbf{U})}{\partial \mathbf{U}}$  and using the chain rule, or by doing combination of the equations of the hyperbolic system. This step is well documented for the multi-D Euler equation [65]. The objective is to understand the steps that lead to the derivation of the entropy equations since the same steps will be used to obtain the viscous terms.

2. We now want to derive the viscous terms consistent with the entropy condition. The method is inspired of what is done for the multi-D Euler equations in [24]. To do so, we first modify Eq. (2.39) by adding a viscous flux  $\mathbf{G}(\mathbf{U})$  that we want to determine by invoking the entropy inequality:

$$\partial_t \mathbf{U}(\mathbf{r}, t) + \nabla \cdot \mathbf{F}(\mathbf{U}) = \nabla \cdot \mathbf{G}(\mathbf{U}), \quad (2.41)$$

Then, the entropy residual is derived again:

$$\begin{aligned} R(\mathbf{U}) &= \partial_t s(\mathbf{U}) + \mathbf{F}_{\mathbf{U}} \cdot \nabla s(\mathbf{U}) = s_{\mathbf{U}} \nabla \cdot \mathbf{G}(\mathbf{U}) \\ R(\mathbf{U}) &= \partial_t s(\mathbf{U}) + \mathbf{F}_{\mathbf{U}} \cdot \nabla s(\mathbf{U}) = \\ &\quad \nabla \cdot (s_{\mathbf{U}} \mathbf{G}(\mathbf{U})) - \mathbf{G}(\mathbf{U}) \cdot \nabla s_{\mathbf{U}}. \end{aligned} \quad (2.42)$$

To prove that the entropy residual  $R$  remains positive, the non-conservative terms of the right hand-side have to be positive. Thus, positivity of the entropy residual is tied to the definition of the viscous term  $\mathbf{G}(\mathbf{U})$  and the entropy function  $s$ . For the multi-D Euler equation, Guermond et al. [24] proved that the entropy function  $s$  needs to be concave ( $-s$  is convex) in order to ensure positivity of the entropy residual for any equation of state. This condition is tied to a particular choice of the dissipative terms that will be detailed in Section 5.1 and to the positivity of the viscosity coefficients. In the general

case, the parabolic regularization [51] can be used and consists of dissipating on the solution itself  $\mathbf{U}$  as shown in Eq. (2.43):

$$\partial_t \mathbf{U}(\mathbf{r}, t) + \nabla \cdot \mathbf{F}(\mathbf{U}) = \nabla \cdot (\mu \nabla(\mathbf{U})), \quad (2.43)$$

where  $\mu$  is a positive viscosity coefficient. Eq. (2.43) obeys to the entropy condition under the condition of having a concave entropy  $s$  [51]. Using the entropy condition, other viscous regularizations can be found with multiple viscosity coefficients (see [24] for Euler equations). However, it is expected that they all degenerate to the parabolic regularization when assuming that all viscosity coefficients are equal to each other. Furthermore, for consistency with the parabolic regularization [51], the entropy function  $s$  is required to be concave. In other terms, the parabolic regularization can be used as a hint in order to derive a viscous regularization with multiple viscosity coefficients. We will see in Section 5.2.2 that having a viscous regularization with two viscosity coefficients is required for the multi-D Euler equation in order to have well-scaled viscous terms in the non-isentropic low-Mach limit. Before moving forward to the next step, we recast the entropy residual  $R$  as a function of the conservative variables. This step is justified by the difficulty encountered in obtaining an analytical expression for the entropy function. This is particularly true for Euler equations when dealing with equation of states. We assume that the entropy residual was successfully recast as a function of the conservative variables and that the new entropy residual is denoted by  $\tilde{R}$ . The reader is referred to Section 5.2.1 for an example.

3. Once the entropy residual is proven to be positive, it remains to define the viscosity coefficient(s). Assuming that a viscous regularization was derived

in step 2 with  $n$  viscosity coefficients denoted by  $\mu_i$ ,  $i \in [1, \dots, n]$ , a general definition can be given in the form:

$$\begin{cases} \mu_i(\mathbf{r}, t) = \max(\mu_{i,e}(\mathbf{r}, t), \mu_{max}(\mathbf{r}, t)) \\ \mu_{max}(\mathbf{r}, t) = \frac{h}{2} \max_{i \in [1, n]} |\lambda_i(\mathbf{r}, t)| \\ \mu_{i,e}(\mathbf{r}, t) = h^2 \frac{\max(\tilde{R}(\mathbf{r}, t), J)}{norm_i(\mathbf{r}, t)}, \end{cases}$$

where  $\mu_{e,i}$  and  $\mu_{max}$  are the high- and first-order viscosity coefficients, respectively. The high-order viscosity coefficient  $\mu_{e,i}$  is defined proportional to the local entropy residual  $R(\mathbf{r}, t)$  and also function of a normalization parameter  $norm_i(\mathbf{r}, t)$  that will be explained further. The first-order viscosity coefficient  $\mu_{max}(\mathbf{r}, t)$  is set proportional to the maximum eigenvalue and is unique for all viscosity coefficients  $\mu_i(\mathbf{r}, t)$ .  $h$  still denotes the local grid size. In order to have a complete definition for the  $\mu_e(\mathbf{r}, t)$ , the normalization parameter  $norm_i(\mathbf{r}, t)$  needs to be defined. It is well known that hyperbolic system of equations suffer from ill-scaled dissipative term in some particular asymptotic limit. This is particularly true for the stabilization methods used for the multi-D Euler equations, that require a fix in the low Mach asymptotic limit in order to yield the correct asymptotic behavior [25, 68]. Thus, by non-dimensionalizing the equations, the normalization parameter  $norm_i(\mathbf{r}, t)$  may be determined for each viscosity coefficients  $\mu_i(\mathbf{r}, t)$  to ensure well-scaled dissipative terms.

This three-step process is applied to the multi-D Euler equations with variable area in Section 5, to the seven-equation model in Section 6 and to the radiation-hydrodynamic equations in Section 7 to determine the viscous terms and to define the viscosity coefficients. Details about the implementation of the EVM with continuous Galerkin finite element method are provided in Section 3.1.1. The jump  $J$

is given on a case by case basis since its definition depends on the variables involved in the expression of the new entropy residual  $\tilde{R}$ .

### 3. DISCRETIZATION METHOD AND IMPLEMENTATION DETAILS OF THE ENTROPY VISCOSITY METHOD

This chapter is organized in two mains sections. In Section 3.1, the spatial and temporal discretization methods are detailed for a generic hyperbolic system of equations. Then, the implementation of the EVM is explained in Section 3.2 using an hyperbolic scalar equation as an example.

#### 3.1 Spatial and temporal discretizations

##### 3.1.1 *Spatial discretization algorithm*

The continuous Galerkin finite element method is employed via the INL MOOSE framework. This section focuses on the weak statement associated with the strong form of a generic hyperbolic system of equations with source terms of the form:

$$\partial_t \mathbf{U}(\mathbf{r}, t) + \nabla \cdot \mathbf{F}(\mathbf{U}(\mathbf{r}, t)) = \mathbf{S}(\mathbf{U}(\mathbf{r}, t)) \quad (3.1)$$

where the solution and flux are defined by

$$\mathbf{U}(\mathbf{r}, t) \equiv \begin{bmatrix} U_1(\mathbf{r}, t) \\ \vdots \\ U_i(\mathbf{r}, t) \\ \vdots \\ U_n(\mathbf{r}, t) \end{bmatrix}, \quad \mathbf{F} \equiv \begin{bmatrix} \mathbf{F}_1(\mathbf{U}(\mathbf{r}, t)) \\ \vdots \\ \mathbf{F}_i(\mathbf{U}(\mathbf{r}, t)) \\ \vdots \\ \mathbf{F}_n(\mathbf{U}(\mathbf{r}, t)) \end{bmatrix} \quad (3.2)$$

and  $\mathbf{S}(\mathbf{U}(\mathbf{r}, t))$  consists of the source terms. The weak form of Eq. (3.1) is obtained by multiplying by an “admissible” vector of test functions  $\mathbf{W}$  (more details will be

given shortly) and integrating over the domain  $\Omega$  with boundary  $\Gamma$  as follows:

$$\int_{\Omega} [\partial_t \mathbf{U}(\mathbf{r}, t) + \boldsymbol{\nabla} \cdot \mathbf{F}(\mathbf{U}(\mathbf{r}, t))] \mathbf{W} = \int_{\Omega} \mathbf{S}(\mathbf{U}(\mathbf{r}, t)) \mathbf{W}. \quad (3.3)$$

Eq. (3.3) is recast by integrating per parts the second term of the left-hand-side to yield:

$$\int_{\Omega} \partial_t \mathbf{U}(\mathbf{r}, t) \mathbf{W} - \int_{\Omega} \mathbf{F}(\mathbf{U}(\mathbf{r}, t)) \cdot \boldsymbol{\nabla} \mathbf{W} + \int_{\Gamma} (\mathbf{F}(\mathbf{U}(\mathbf{r}, t)) \mathbf{W}) \cdot \mathbf{n} = \int_{\Omega} \mathbf{S}(\mathbf{U}(\mathbf{r}, t)) \mathbf{W}, \quad (3.4)$$

where  $\mathbf{n}$  denotes the outward normal to the boundary  $\Gamma$ . We note the difference with a discontinuous approach where the integrals are first split over each element of the computational mesh before integrating by parts.

By integrating by parts, a boundary term appears in Eq. (3.4) and will require boundary conditions in order to compute the flux vector  $\mathbf{F}(\mathbf{U}(\mathbf{r}, t))$  at the boundaries. Because of the special nature of hyperbolic system of equation, a generic treatment of the boundary terms is not suitable. Instead, a case by case approach is chosen and boundary conditions will be specified further for each system of equations studied in this Dissertation.

The test function  $\mathbf{W}$  is not chosen arbitrarily. In particular, it is required that

$\mathbf{W}$  comes from the space of vector functions

$$\mathbf{W} \in \left\{ \begin{bmatrix} w \\ 0 \\ 0 \\ 0 \\ \vdots \\ 0 \end{bmatrix}, \begin{bmatrix} 0 \\ w \\ 0 \\ 0 \\ \vdots \\ 0 \end{bmatrix}, \dots, \begin{bmatrix} 0 \\ \vdots \\ 0 \\ w \\ 0 \\ \vdots \\ 0 \end{bmatrix}, \dots, \begin{bmatrix} 0 \\ 0 \\ 0 \\ 0 \\ \vdots \\ 0 \end{bmatrix}, \begin{bmatrix} 0 \\ 0 \\ 0 \\ 0 \\ \vdots \\ w \end{bmatrix}, \dots, \begin{bmatrix} 0 \\ 0 \\ 0 \\ 0 \\ \vdots \\ 0 \end{bmatrix} \right\} \quad (3.5)$$

where  $w \in \mathcal{W}$  is a scalar test function. In the present work, and in general practice, the space  $\mathcal{W}$  is taken to be (a subspace of) the Hilbert space  $H^1(\Omega)$ . This choice, for instance, guarantees enough smoothness so that Eq. (3.3) makes sense. The approximate problem then proceeds by selecting only test functions from a finite-dimensional subspace of  $\mathcal{W}$ , denoted by  $\mathcal{W}^h$ , which is spanned by the basis  $\{\phi_k\}$ ,  $k = 1, \dots, N$ . We then seek  $\mathbf{U}^h$  with components in the same space as  $\mathcal{W}^h$ , satisfying the boundary conditions, and such that

$$\int_{\Omega} \partial_t \mathbf{U}^h \mathbf{W} - \int_{\Omega} \mathbf{F}(\mathbf{U}^h) \cdot \nabla \mathbf{W}^h + \int_{\Gamma} (\mathbf{F}(\mathbf{U}^h) \mathbf{W}^h) \cdot \mathbf{n} = \int_{\Omega} \mathbf{S}(\mathbf{U}^h) \mathbf{W}^h, \quad (3.6)$$

holds for all  $\mathbf{W}^h$  defined analogously to Eq. (3.5), with components in  $\mathcal{W}^h$ . Note that Eq. (3.6) has been placed in a “continuous” setting, that is, a mesh and finite element discretization has been introduced requiring a continuous solution. Eq. (3.6) is a “weak” statement of the “strong” Eq. (3.1) in the sense that derivatives of the solution and its flux need not be continuous. As an example, the first equation of

Eq. (3.6) would yield:

$$\int_{\Omega} \partial_t U_1^h \phi_k - \int_{\Omega} \mathbf{F}_1(\mathbf{U}^h) \cdot \nabla \phi_k + \int_{\Gamma} (\mathbf{F}_1(\mathbf{U}^h) \phi_k) \cdot \mathbf{n} = \int_{\Omega} S_1(\mathbf{U}^h) \phi_k, \quad (3.7)$$

and must hold for  $k = 1, \dots, N$ . Note that the flux  $\mathbf{F}_1$  and the source term  $S_1$  are not necessarily only functions of  $U_1$ . As mentioned, a continuous Galerkin formulation is employed and, therefore, the unknowns are expressed in the same basis used for the test functions, i.e.,

$$U_1^h(\mathbf{r}, t) = \sum_{j=0}^N (U_1)_j(t) \phi_j(\mathbf{r}) \quad (3.8)$$

⋮

$$U_i^h(\mathbf{r}, t) = \sum_{j=0}^N (U_i)_j(t) \phi_j(\mathbf{r}) \quad (3.9)$$

⋮

$$U_n^h(\mathbf{r}, t) = \sum_{j=0}^N (U_n)_j(t) \phi_j(\mathbf{r}) \quad (3.10)$$

where the coefficients  $(U_i)_j$  correspond to the  $j^{th}$  nodal values of the  $i^{th}$  component of the vector solution  $\mathbf{U}$  and vary in time. The spatial dependence is carried by the test function  $\phi_k$ . Eq. (3.6) is numerically evaluated by splitting the integrals over the elements  $e$  of the mesh, and then by using a quadrature rule denoted by  $\mathcal{Q} = \{\mathbf{r}_q\}$  as follows:

$$\int_{\Omega} \mathbf{F}(\mathbf{U}(\mathbf{r}, t)^h) \cdot \nabla \mathbf{W}^h(\mathbf{r}, t) = \sum_e \sum_q \mathbf{F}(\mathbf{U}(\mathbf{r}_q, t)^h) \cdot \nabla \cdot \mathbf{W}^h(\mathbf{r}_q, t), \quad (3.11)$$

where the values of the vector solution at the quadrature points are obtained from Eq. (3.8). The number of elements can vary and depends on how fine the mesh is.

The quadrature rule sets the number of quadrature points and is usually taken large enough to exactly integrate the test function  $\phi_k$ . The other integrals in Eq. (3.6) are treated on the same model as Eq. (3.11). Note that the first term in the left-hand-side of Eq. (3.6) contains a time derivative that has not been discretized yet. Under this form Eq. (3.6) is referred to as a semi-discrete equation. Discretization of the time dependent term for a temporal implicit scheme is detailed in Section 3.1.2. Furthermore, it is well-known that a continuous Galerkin discretization of this set of hyperbolic equations is equivalent to a central difference method for a certain choice of integration rule and, therefore, will exhibit oscillatory instabilities unless some artificial diffusion is added to stabilize the method. The EVM will be used to stabilize the scheme and details of its implementation are given in Section 3.2.

### 3.1.2 Implicit time integration methods

The MOOSE framework offers both first- and second-order implicit temporal integrators: Backward Euler and BDF2.

#### 3.1.2.1 Backward Euler

The backward Euler method [10] is a well-known, first-order, A-stable implicit time integration method. Given a generic semi-discrete equation in a form similar to Eq. (3.7) (the upper-script  $h$  is dropped in order to simplify the notation),

$$\int_{\Omega} \left( \frac{\partial U_1(\mathbf{r}, t)}{\partial t} + \mathbf{G}_1(\mathbf{U}(\mathbf{r}, t)) \right) \phi_k \, d\Omega = 0 \quad (3.12)$$

where  $\mathbf{G}(\mathbf{U}^h)$  denotes the steady-state residual, the backward Euler method results in the temporal discretization

$$\int_{\Omega} \left( \frac{U_1^{n+1}(\mathbf{r}) - U_1^n(\mathbf{r})}{\Delta t} + \mathbf{G}_1(\mathbf{U}^{n+1}(\mathbf{r})) \right) \phi_k \, d\Omega = 0 \quad (3.13)$$

where  $\Delta t$  is the timestep,  $t^{n+1} = t^n + \Delta t$ , and  $U_1(\mathbf{r}, t^n) \equiv U_1^n(\mathbf{r})$  is a shorthand notation used to refer to the finite element solution at time level  $n$ . Equation (3.13) is a fully-discrete (possibly nonlinear) equation which must be satisfied for each test function  $k$ .

We study the truncation error of the backward Euler method on a simple linear convection equation

$$\frac{\partial u}{\partial t} + a \frac{\partial u}{\partial x} = 0. \quad (3.14)$$

Using a Taylor expansion in time, an expression for the continuous time derivative is obtained:

$$\frac{\partial u}{\partial t} \Big|_{t^{n+1}} = \frac{u^{n+1} - u^n}{\Delta t} + \frac{\Delta t}{2} \frac{\partial^2 u}{\partial t^2} \Big|_{t^{n+1}} + \mathcal{O}(\Delta t^2), \quad (3.15)$$

which can be recast as

$$\frac{\partial u}{\partial t} \Big|_{t^{n+1}} = \frac{u^{n+1} - u^n}{\Delta t} + \frac{a^2 \Delta t}{2} \frac{\partial^2 u}{\partial x^2} \Big|_{t^{n+1}} + \mathcal{O}(\Delta t^2), \quad (3.16)$$

by differentiating the continuous equation Eq. (3.14) with respect to time:

$$\frac{\partial^2 u}{\partial t^2} = -a \frac{\partial}{\partial t} \left( \frac{\partial u}{\partial x} \right) = -a \frac{\partial}{\partial x} \left( \frac{\partial u}{\partial t} \right) = -a \frac{\partial}{\partial x} \left( -a \frac{\partial u}{\partial x} \right) = a^2 \frac{\partial^2 u}{\partial x^2}. \quad (3.17)$$

Rearranging terms in Eq. (3.16) and adding  $a \frac{\partial u}{\partial x}$  to both sides allows us to write

$$\frac{u^{n+1} - u^n}{\Delta t} + a \frac{\partial u}{\partial x} = \frac{\partial u}{\partial t} + a \frac{\partial u}{\partial x} - \frac{a^2 \Delta t}{2} \frac{\partial^2 u}{\partial x^2} + \mathcal{O}(\Delta t^2) \quad (3.18)$$

where all the continuous derivatives are assumed to be evaluated at time level  $t^{n+1}$ .

Thus, the semi-discrete form of the linear convection on the left-hand side of (3.18) is equal to the continuous parabolic partial differential equation on the right-hand side, which includes “artificial” diffusion or viscosity of  $\mathcal{O}(\frac{a^2 \Delta t}{2})$ , to within  $\mathcal{O}(\Delta t^2)$ . For this reason, we often say that the backward Euler time discretization is inherently stabilizing for the hyperbolic equation (3.14). Obviously, the artificial viscosity for the complete scheme is a composite of the artificial viscosity of both the time and spatial discretization.

The backward Euler time integration method may generate excessive artificial viscosity and should, therefore, only be used for transients as an initial scoping calculation or if only the steady-state solution is of interest. For accurate transient solutions, the BDF2 time integration method, described next, is highly recommended because it is a second-order (in time) discretization.

### 3.1.2.2 BDF2

The backward differentiation formula (BDF) is a family of implicit methods for numerically integrating ordinary differential equations. Some notable members of this family include BDF1, which is equivalent to the backward Euler [6] method discussed in Section 3.1.2.1, and BDF2, which is the highest-order BDF method that is still A-stable. We consider again the example from Section 3.1.2.1:

$$\int_{\Omega} \left( \frac{\partial U_1(\mathbf{r}, t)}{\partial t} + \mathbf{G}_1(\mathbf{U}(\mathbf{r}, t)) \right) \phi_k \, d\Omega = 0. \quad (3.19)$$

Considering three consecutive solutions  $U_1(\mathbf{r}, t^{n+1}) = U_1^{n+1}(\mathbf{r})$ ,  $U_1(\mathbf{r}, t^n) = U_1^n(\mathbf{r})$  and  $U_1(\mathbf{r}, t^{n-1}) = U_1^{n-1}(\mathbf{r})$ , the update step is:

$$\int_{\Omega} \left( \omega_0 U_1^{n+1}(\mathbf{r}) + \omega_1 U_1^n(\mathbf{r}) + \omega_2 U_1^{n-1}(\mathbf{r}) + \mathbf{G}_1(\mathbf{U}^{n+1}(\mathbf{r}, t)) \right) \phi_k \, d\Omega = 0. \quad (3.20)$$

with

$$\omega_0 = \frac{2\Delta t^{n+1} + \Delta t^n}{\Delta t^{n+1}(\Delta t^{n+1} + \Delta t^n)}, \quad \omega_1 = -\frac{\Delta t^{n+1} + \Delta t^n}{\Delta t^{n+1}\Delta t^n}$$

$$\text{, and } \omega_2 = \frac{\Delta t^{n+1}}{\Delta t^n(\Delta t^{n+1} + \Delta t^n)}$$

where  $\Delta t^n = t^n - t^{n-1}$  and  $\Delta t^{n+1} = t^{n+1} - t^n$ . Since BDF2 requires two old time-steps, the method must be “bootstrapped” by either a lower-order method, such as backward Euler, or a second-order method, such as Crank-Nicholson. This means that a much smaller time step size should be used for start-up at the beginning of a transient. The BDF2 method is recommended for most transient simulations.

### 3.1.3 Jacobian-Free Newton Krylov solver

The Moose framework allows coupled multi-physics problems to be solved using the Jacobian-free Newton Krylov (JFNK) approach. The JFNK method is a fully-coupled method for solving large systems of nonlinear equations. In general, it consists of at least two levels: the outer Newton loop for the nonlinear solve and the inner Krylov loop for the linear systems of equations associated with each Newton iteration. The JFNK method has become an increasingly popular option for solving large nonlinear equation systems arising from multi-physics problems over the last 20 years, and has been incorporated into a number of different disciplines [33].

In what follows, a brief description of the JFNK method is given. The FEM-discretized equations are first written as

$$\mathcal{R}(\mathbf{U}) = \partial_t \mathbf{U}(\mathbf{r}, t) + \nabla \cdot \mathbf{F}(\mathbf{U}(\mathbf{r}, t)) - \mathbf{S}(\mathbf{U}(\mathbf{r}, t)) = \mathbf{0} \quad (3.21)$$

where  $\mathcal{R}$  represents the nonlinear residual and  $\mathbf{U}$  is the solution vector. Newton’s

method requires an initial guess,  $\mathbf{U}^0$ , to start the iteration process. For the transient problems of interest here, the solution at a previous time step is generally used as the initial guess for the method. At the  $\ell^{th}$  iteration, the residual vector is defined as

$$\mathbf{r}^\ell \equiv \mathcal{R}(\mathbf{U}^\ell). \quad (3.22)$$

Clearly if  $\mathbf{U}^\ell$  satisfies Eq. (3.21) *exactly*, the  $k^{th}$  residual will be zero. To update the solution vector, the following equation is solved for the update vector,  $\delta\mathbf{U}^{k+1}$ :

$$J(\mathbf{U}^\ell)\delta\mathbf{U}^{k+1} = -\mathbf{r}^\ell \quad (3.23)$$

where  $J(\mathbf{U}^\ell)$  is the Jacobian matrix of the residual  $\mathcal{R}$  evaluated at  $\mathbf{U}^\ell$ . In index notation, the entries of the Jacobian matrix are:

$$J_{ij} \equiv \frac{\partial \mathcal{R}_i}{\partial U_j}. \quad (3.24)$$

After  $\delta\mathbf{U}^{k+1}$  is obtained, the  $(k+1)^{st}$  solution iterate is computed by

$$\mathbf{U}^{k+1} = \mathbf{U}^k + \delta\mathbf{U}^{k+1}. \quad (3.25)$$

The Newton iteration is terminated when one of the following conditions is met:

1. The residual vector norm,  $|\mathbf{r}^\ell|$ , is sufficiently small.
2. The relative residual vector norm  $\frac{|\mathbf{r}^\ell|}{|\mathbf{r}^0|}$  is sufficiently small.
3. The step size norm,  $|\delta\mathbf{U}^{k+1}|$  is sufficiently small.

Note that (3.23) represents a large linear system of equations. In the JFNK

method, we need not explicitly to form the matrix  $J$ : only its action on a vector is required. Specifically, given a Krylov vector  $v$ , the solution subspace construction requires to compute  $Jv$ . The Jacobian-free approach performs this using a finite difference approach

$$J^\ell v \approx \frac{\mathcal{R}(\mathbf{U}^\ell + \epsilon v) - \mathcal{R}(\mathbf{U}^\ell)}{\epsilon} \quad (3.26)$$

where  $\epsilon$  is a perturbation parameter (choices for  $\epsilon$  can be discussed in [33], for instance).

Effective preconditioning is generally required for Krylov subspace methods to be efficient, i.e., for the method to converge in a reasonable number of linear iterations. A preconditioned version of equation (3.23) can be expressed as (using right preconditioning),

$$J^\ell P^{-1} (P \delta \mathbf{U}^{k+1}) = -\mathbf{r}^\ell \quad (3.27)$$

where  $P$  is the preconditioning matrix. For 1-D simulations, the Jacobian matrix is numerically computed by finite difference (FDP) according to Eq. (3.24), and passed to the underlying numerical solver library as the matrix  $P$  for preconditioning purposes. For multi-D simulations, the same method would be very slow and inefficient since the FDP is even used to compute the zero entries of the Jacobian matrix. Instead, an expression of the Jacobian matrix is derived by hand and hard coded in the code. This process is significantly faster than the FDP method since the entries of the Jacobian matrix are simply evaluated.

### 3.2 Implementation of the Entropy Viscosity Method (EVM) with continuous Galerkin finite element method

After describing the theoretical approach that leads to the derivation of the dissipative terms consistent with the entropy minimum principle and the definition of the viscosity coefficient in Section 2, this section focuses on the implementation of

the method in a continuous Galerkin finite element setting. Details are given on how to implement and compute the jump, the entropy residual and the dissipative terms, for instance. Special attention is required for the jump since their definition is spatial discretization-dependent. A non-uniform 2-D mesh family  $\Omega$  is considered. Each member of this family is called element,  $e$ , and the set of its faces is denoted by  $\delta e = \{\delta e_f\}$ , where  $f$  is the number of faces. To integrate the integral over each element  $e$  and the boundaries  $\delta e$ , a quadrature rule,  $\mathcal{Q} = \{q\}$  is used.

For academic purpose, the multi-D Burger's equation is considered and recalled here along with the definition of the viscosity coefficients based on Section 2.1.4:

$$\partial_t u + \nabla \cdot \left[ \hat{\mathbf{n}} \frac{u^2}{2} \right] = \nabla \cdot (\mu \nabla u) = \nabla \cdot \mathbf{g} \quad (3.28a)$$

$$R(\mathbf{r}, t) = \partial_t (\eta(\mathbf{r}, t)) + \nabla \cdot (\hat{\mathbf{n}} \psi(\mathbf{r}, t)) \leq 0 \quad (3.28b)$$

$$\mu(\mathbf{r}, t) = \max(\mu_e(\mathbf{r}, t), \mu_{max}(\mathbf{r}, t)) \quad (3.28c)$$

$$\mu_{max}(\mathbf{r}, t) = \frac{h}{2} |u(\mathbf{r}, t)| \quad (3.28d)$$

$$\mu_e(\mathbf{r}, t) = h^2 \frac{\max(R(\mathbf{r}, t), J)}{\|\eta - \bar{\eta}\|_\infty} \quad (3.28e)$$

where  $u(\mathbf{r}, t)$  is a conservative variable that depends on both space and time. The entropy function  $\eta$  and the conservative flux in the entropy residual  $R$  are defined as  $\eta(\mathbf{r}, t) = \frac{u(\mathbf{r}, t)^2}{2}$  and  $\psi = \frac{u(\mathbf{r}, t)^3}{3}$ , respectively. It is also interesting to note that the corresponding physical entropy  $s$  is  $s(\mathbf{r}, t) = -\frac{u(\mathbf{r}, t)^2}{2} + \max(\eta(\mathbf{r}, t))$  and that it is concave. The Burger's equation is known to admit an unique eigenvalue  $\lambda = u(\mathbf{r}, t)$ .

The vector  $\hat{\mathbf{n}}$  is defined as follows:

$$\hat{\mathbf{n}} = (1, 0, 0) \text{ in 1-D}$$

$$\hat{\mathbf{n}} = (1, 1, 0) \text{ in 2-D}$$

$$\hat{\mathbf{n}} = (1, 1, 1) \text{ in 3-D}$$

The jump  $J$  is assumed piecewise constant and details regarding its evaluation will be given next. The normalization parameter  $\|\eta - \bar{\eta}\|_\infty$  used in Eq. (3.28e) denotes the infinite norm over the entire computational domain of the quantity  $\eta - \bar{\eta}$  where  $\bar{\eta}$  is the average entropy over the computational domain as well.

The first step in the implementation of the EVM is the integration of the dissipative terms over each element of the mesh. The continuous finite element approach consists of multiplying each term by a test function and then integrating over the computational domain. Since the dissipative terms are second-order spatial derivatives, an integration per part is performed leading to:

$$\nabla \cdot \mathbf{g} \rightarrow \int_{\Omega} \nabla \cdot \mathbf{g}^h \phi_k d\Omega = - \int_{\Omega} \mathbf{g}^h \cdot \nabla \phi_k d\Omega + \int_{\Gamma} \mathbf{n} \cdot \mathbf{g}^h \phi_k d\Gamma \quad (3.29)$$

In Eq. (3.29), the integral over the domain  $\Omega$  is transformed into a sum over the elements and evaluated by using a quadrature rule. The other term, consists of an integral over the boundary of the computational domain  $\Gamma$  and is neglected by assuming that the viscosity coefficient  $\mu$  is zero at the boundaries. We are now left with:

$$\nabla \cdot \mathbf{g} \rightarrow \int_{\Omega} \nabla \cdot \mathbf{g}^h \phi_k d\Omega = - \int_{\Omega} \nabla \phi_k \cdot \mathbf{g}^h d\Omega. \quad (3.30)$$

The dissipative term  $\mathbf{g}^h$  is function of the viscosity coefficient and the derivative of the conservative variable  $u$  that need to be evaluated at quadrature points. Obtain-

ing the derivative values at the quadrature points with a continuous finite element discretization type is straightforward by using the test function:

$$\nabla u(\mathbf{r}, t) = \sum_j u_j(t) \nabla \phi_j(\mathbf{r}) \quad (3.31)$$

On the other hand, computing the viscosity coefficient at the same quadrature points require a little bit more of computational work and is explained in the following.

The next step consists of determining the viscosity coefficient  $\mu$  that is not obtained by solving a PDE but computed on the fly from the definition recalled in Eq. (3.28c). The definition of the viscosity coefficient  $\mu(\mathbf{r}, t)$  involves two other viscosity coefficients: a first-order viscosity coefficient  $\mu_{max}(\mathbf{r}, t)$  that is an upper bound and a high-order viscosity coefficient often also called entropy-viscosity coefficient that is denoted by  $\mu_e(\mathbf{r}, t)$ . A common element to the definition of  $\mu_{max}(\mathbf{r}, t)$  and  $\mu_e(\mathbf{r}, t)$  is the mesh size  $h$  that can vary through the computational domain and is defined as the shortest distance between two nodes of an element. Thus, when considering a 1-D mesh with linear test function, the local mesh size is simply  $\Delta x$ . For a shape regular mesh, the mesh size is finite and usually available through a function call. For instance, when using libMesh, a function can be called in order to get the mesh size or diameter of the cell under consideration. Once the mesh size  $h$  is available, it remains to compute the local maximum eigenvalue, the entropy residual  $R$  and the jump  $J$ .

The maximum eigenvalue is involved in the definition of the first-order viscosity coefficient. For a given quadrature point  $q$  in a element  $e$  of the mesh, the first-order viscosity coefficient  $\mu_{max}^{e,q}$ , is given by  $\mu_{max}^{e,q} = \frac{h^e}{2} |u^{e,q}|$  where  $u^{e,q}(\mathbf{r}, t) = \sum_j u_j(t) \phi_j(\mathbf{r}_q)$ . The high-order viscosity coefficient is more involved to compute since it necessitates the evaluation of the entropy residual  $R$  at the quadrature points

and the jumps  $J$  at the interface between cells. The entropy residual  $R$  is a PDE but is not discretized in a finite element sense. Instead, each term of the entropy residual is locally computed using the test functions but without integration over the computational domain as follows:

$$R_e^{q,n} = w_0 s^{n,e,q} + w_1 s^{n-1,e,q} + w_2 s^{n-2,e,q} + \hat{\mathbf{n}} \cdot \sum_j s_j^e \nabla \phi_j^{e,q} \quad (3.32)$$

when considering three successive entropy values  $s^{n,e,q}$ ,  $s^{n-1,e,q}$  and  $s^{n-2,e,q}$  in time. The BDF2 weights  $w_0$ ,  $w_1$  and  $w_2$  were defined in Section 3.1.2.2. The values of the entropy function  $s$  at the quadrature points is computed using test functions:  $s^{e,q} = \sum_j s_j^e \phi_j^q = \sum_j \frac{(u_j^e)^2}{2} \phi_j^q$ , which requires to access the values of solution  $u$  at the nodes  $j$  and the test functions at quadrature points. The same method is used for the entropy flux  $\psi$ . It is noted that the entropy residual can be recast under a non-conservative form as shown in Eq. (3.33) that can be easier to evaluate depending on what is available to the user.

$$R(\mathbf{r}, t) = \partial_t \left( \frac{u(\mathbf{r}, t)^2}{2} \right) + u(\mathbf{r}, t)^2 \nabla \cdot (\hat{\mathbf{n}} u(\mathbf{r}, t)) \quad (3.33)$$

It remains, now, to compute the jump  $J$  that is set constant in each element. In continuous Galerkin finite elements, the variables are continuous at the faces, but their derivative are discontinuous. Thus, the jump of the gradient of a variable to choose, seems to be a good entropy production indicator since it will inform us on the presence of a sharp discontinuity. In the remaining of this section, a generic method is detailed to compute the jump of the gradient of a variable when using a continuous Galerkin finite element method. Then, the jump used in the definition of the viscosity coefficient for solving Burger's equation is given.

To be more specific, let us consider an element  $e$  and its set of  $n$  boundaries  $\delta k = \{\delta e_1, \dots, \delta e_n\}$ . We also assume that the outward normal  $\mathbf{n}_i$  to each boundary  $\delta e_i$  is available to us. The objective is to compute the jump  $J_e$  of the gradient of the variable  $v(\mathbf{r}, t)$  for the element  $e$ . Since an element  $e$  shares boundaries with  $n$  other elements of the computational domain, a jump  $J_{e,i}$  can be computed for each boundary  $\delta e_i$  and is defined as follows:

$$J_{e,i} = \left| \left( \nabla v(\mathbf{r}, t)_i^e - \nabla v(\mathbf{r}, t)_i^{neighbor} \right) \cdot \mathbf{n}_i \right| \quad (3.34)$$

where the quantity  $\nabla v(\mathbf{r}, t)_{neighbor,i}$  denotes the gradient of  $v(\mathbf{r}, t)$  in the neighbor cell to the element  $e$  sharing the interface  $\delta e_i$ . The difference of gradients between the two elements sharing the interface  $\delta e_i$  is multiplied by the outward normal vector  $\mathbf{n}_i$  to obtain the jump normal to the interface. Once all the jumps  $J_i^e$  are computed for each face  $i$  of the element  $e$  (a loop over the faces  $i$  of element  $e$  applies), the jump  $J^e$  is computed by choosing the maximum over the  $J_i^e$ :

$$J^e = \max_i (J_i^e) \quad (3.35)$$

With the definition given in Eq. (3.35), the jump  $J^e$  is constant in each element  $e$  of the computational domain  $\Omega$ . From this point, the entropy residual  $R$  and the jump  $J$  are known in the element  $e$ , at a given time  $t^n$  and at every quadrature points  $q$ . It remains to compute the normalization parameters  $\|s - \bar{s}\|_\infty$  that is obtained from a post processing for every new non-linear iteration of the solver and thus is a function of time. The average value of the entropy function of the computational domain is

computed from an integral as follows:

$$\bar{\eta} = \frac{1}{\Omega} \int_{\Omega} \eta(\mathbf{r}, t) d\Omega \quad (3.36)$$

The high-order viscosity coefficient  $\mu_e^{n,e,q}$  can now be computed at a given quadrature points  $q$  and given time  $t^n$ :

$$\mu_e^{n,e,q} = (h^e)^2 \frac{\max(R^{n,e,q}, J^{n,e})}{\|\eta - \bar{\eta}\|_{\infty}^n} \quad (3.37)$$

The definition of the viscosity coefficient  $\mu$  from Eq. (3.38) follows:

$$\mu_e^{n,e,q} = \min(\mu_e^{n,e,q}, \mu_{max}^{n,e,q}) \quad (3.38)$$

At this stage, all of the variables required to compute the integral of the dissipative term  $\int_e \mu \nabla u \nabla \phi = \sum_q \mu^{n,e,q} \nabla u^{n,e,q} \nabla \phi^q$ , are known.

## 4. APPLICATION OF THE ENTROPY VISCOSITY METHOD TO THE MULTI-D BURGER'S EQUATION

The multi-D Burger's equation is solved using the entropy viscosity method described in Section 2.1.4. The equation with the viscous regularization and the definition of the viscosity coefficients are recalled, and the treatment of the boundary condition is also explained in Section 4.1. 1- and 2-D numerical results are presented in Section 4.2. The objective of this section is to present numerical results obtained with the entropy viscosity method for the simple hyperbolic scalar Burger's equation before dealing with hyperbolic system of equations. The multi-physics framework MOOSE [17] was used to implement the multi-D Burger's equation. The code name is Badger.

### 4.1 The multi-D Burger's equation

We recall the multi-D Burger's equation (Eq. (4.1a)) with the viscous regularization and the definition of the viscosity coefficient (Eq. (4.1b)).

$$\partial_t u(\mathbf{r}, t) + \nabla \cdot \left( \frac{u(\mathbf{r}, t)^2}{2} \hat{\mathbf{n}} \right) = \nabla \cdot (\mu(\mathbf{r}, t) \nabla u(\mathbf{r}, t)) \quad (4.1a)$$

$$\begin{cases} \mu(\mathbf{r}, t) = \min(\mu_{max}(\mathbf{r}, t), \mu_e(\mathbf{r}, t)) \\ \mu_{max}(\mathbf{r}, t) = \frac{h}{2} |u(\mathbf{r}, t)| \\ \mu_e(\mathbf{r}, t) = h^2 \frac{\max(R_e(\mathbf{r}, t), J)}{\|s(\mathbf{r}, t) - \bar{s}(t)\|_\infty} \end{cases} \quad (4.1b)$$

$$\begin{cases} R_e(\mathbf{r}, t) = \partial_t s(\mathbf{r}, t) + \nabla (u(\mathbf{r}, t) s(\mathbf{r}, t)) \\ J = [u(\mathbf{r}, t) s(\mathbf{r}, t)] \end{cases} \quad (4.1c)$$

where  $\hat{\mathbf{n}}$  was previously defined in Section 2.1.1 as:  $\hat{\mathbf{n}} = (1, 0, 0)$  in 1-D,  $\hat{\mathbf{n}} = (1, 1, 0)$  in 2-D and  $\hat{\mathbf{n}} = (1, 1, 1)$  in 3-D. The entropy function is denoted by  $\eta$  and is taken equal to the convex function  $\eta(\mathbf{r}, t) = u(\mathbf{r}, t)^2/2$  for the two examples presented in Section 4.2. The continuous Galerkin finite element method described in Section 3 along with the second-order implicit itemporal integrator BDF2 are used to discretize Eq. (4.1a). Such discretization requires to compute the flux at the boundary of the computational domain Eq. (3.11). Our implementation of the boundary condition for Burger's equation is based on the sign of the dot product  $u(\mathbf{r}, t)\hat{\mathbf{n}} \cdot \mathbf{n}$  at the boundary, where  $\mathbf{n}$  is the outward normal to the boundary. For Burger's equation it was demonstrated in Section 2.1.1 that the eigenvalue is the solution itself  $\lambda = u$ . Being at the boundary, two cases have to be distinguished:

- $u(\mathbf{r}, t)$  is negative: the wave enters the computational domain and thus, information needs to be supplied to the code. This boundary condition can be enforced either weakly or strongly. In the former case, the boundary value is specified in the input file, for instance, and used to compute the flux at the boundary. In the later case, the boundary value is still specified but strongly enforced with a Dirichlet boundary condition. This approach is valid for both implicit and explicit temporal integrators.
- $u(\mathbf{r}, t)$  is positive: the wave exits the computational domain. The flux is computed with the value of the solution from the last Krylov iteration supplied by the temporal implicit solver. Because of the iterative process, the information normally carried by the waves is transmitted to the boundary. This approach is only valid with an implicit solver. When using an explicit solver, the solution at the new time on the boundary is obtained from the characteristic equation that is integrated over the first cell in.

## 4.2 Numerical results

Two typical numerical tests are presented in order to illustrate the main features of the entropy viscosity method when applied to the multi-D Burger's equation.

### 4.2.1 1-D numerical result

We consider a 1-D computational domain of length  $L = 1\text{ m}$  discretized by an uniform mesh of 100 elements. The initial condition consists of a smooth sinusoidal function  $u(x, 0) = \sin(2\pi x)$ . The values at the left and right boundaries are set to zero and enforced by Dirichlet conditions. The numerical solution is run until  $t = 0.2\text{ s}$  with a *CFL* of one. In order to investigate the effect of the entropy viscosity method onto the numerical solution, three tests are performed. In the first test, the numerical solution is run with first-order viscosity coefficient which implies  $\mu(x, t) = \mu_{max}(x, t)$  at all point of the computational domain and for all time. Then, the same run is performed using the definition of  $\mu(x, t)$  recalled in Eq. (4.1b). Lastly, the code is run without stabilization,  $\mu(x, t) = 0$ . The objective of running these three cases is to demonstrate the usefulness of the stabilization method and also to show the gain in accuracy when a high-order stabilization method is utilized. Numerical results are shown in Fig. 4.1 through Fig. 4.4.

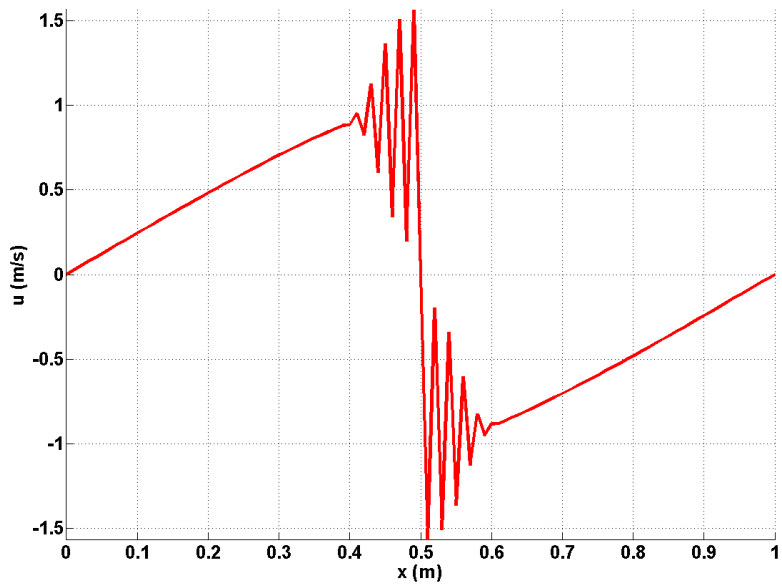


Figure 4.1: 1-D Burger's equation: solution profile without stabilization at  $t = 0.2$  s.

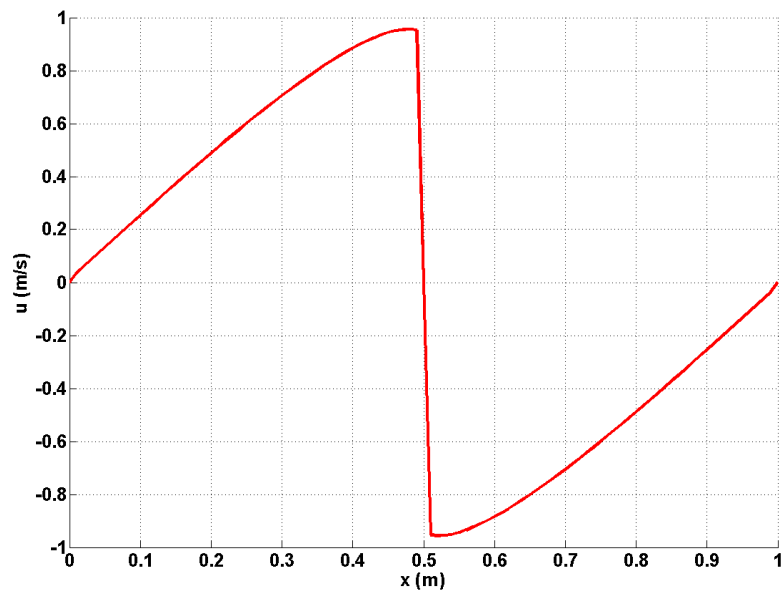


Figure 4.2: 1-D Burger's equation: solution profile with first-order viscosity at  $t = 0.2$  s.

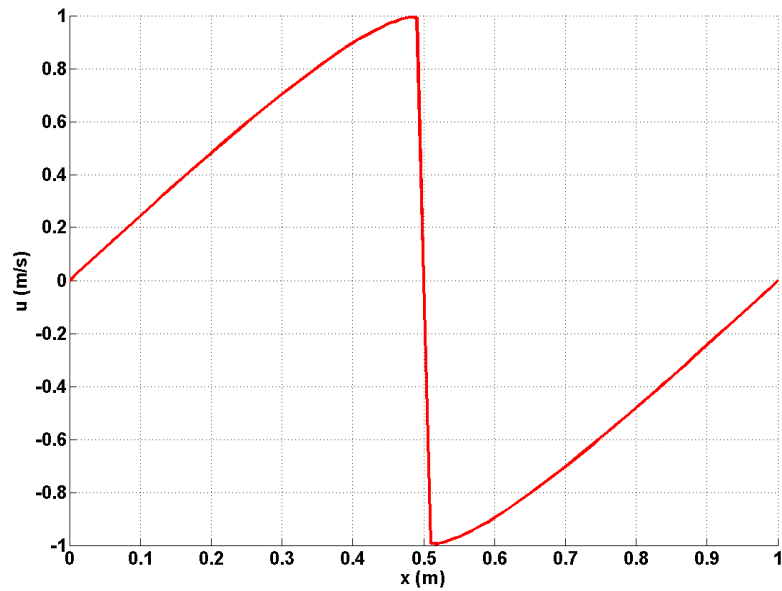


Figure 4.3: 1-D Burger's equation: solution profile with the EVM at  $t = 0.2 \text{ s}$ .

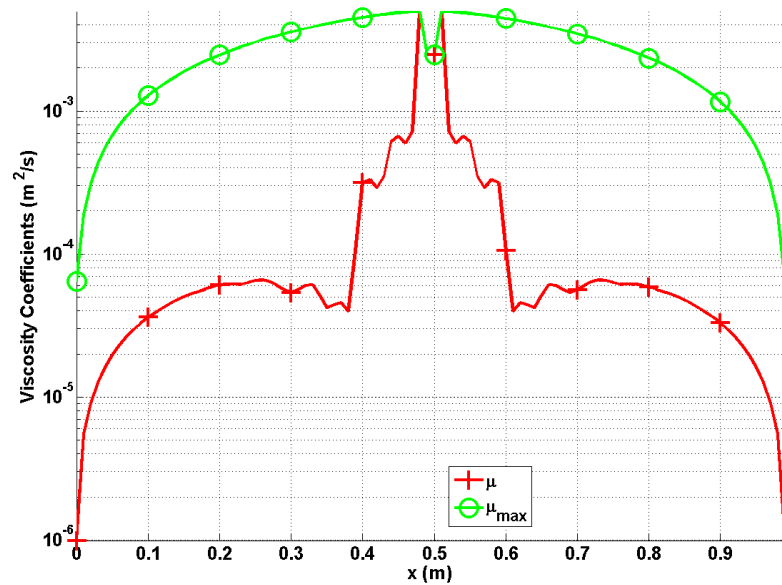


Figure 4.4: 1-D Burger's equation: viscosity coefficient profiles at  $t = 0.2 \text{ s}$ .

In Fig. 4.1, no stabilization is used and numerical instabilities are observed in the shock region. When run with the over-dissipative first-order viscosity coefficient, the solution does not display any instabilities but the shock amplitude is smoothed as shown in Fig. 4.2. Lastly, the numerical solution obtained with the EVM in Fig. 4.3 is very close to the exact solution: the shock amplitude is preserved and the solution is stable. The viscosity coefficients are shown in Fig. 4.4 on a log-scale: the high-order viscosity coefficient  $\mu_e$  is peaked in the shock region and is small anywhere else. This behavior is expected and corresponds to the theoretical approach detailed in Section 2.1.4. It was demonstrated in [69] that high-order accuracy is preserved with the EVM when the solution is smooth (i.e. away from the shock region). It is also noticed in Fig. 4.4 the difference of order of magnitude between the high- and first-order viscosity coefficients away from the shock region.

#### 4.2.2 2-D Riemann problem

We now consider a typical 2-D benchmark problem known as Riemann problem. The computational domain consists of a  $1 \times 1$  square and the following initial conditions are used:

$$u(\mathbf{r}, 0) = u_0 = \begin{cases} +0.5 & \text{for } x \leq 0.5 \text{ and } y \leq 0.5 \\ +0.8 & \text{for } x \geq 0.5 \text{ and } y \leq 0.5 \\ -0.2 & \text{for } x \leq 0.5 \text{ and } y \geq 0.5 \\ -1. & \text{for } x \geq 0.5 \text{ and } y \geq 0.5 \end{cases}$$

An uniform mesh of  $100 \times 100$  elements is used. The solution is run until  $t = 0.5$  s with a *CFL* of 0.5. The numerical solution and the viscosity coefficient profiles are given next.

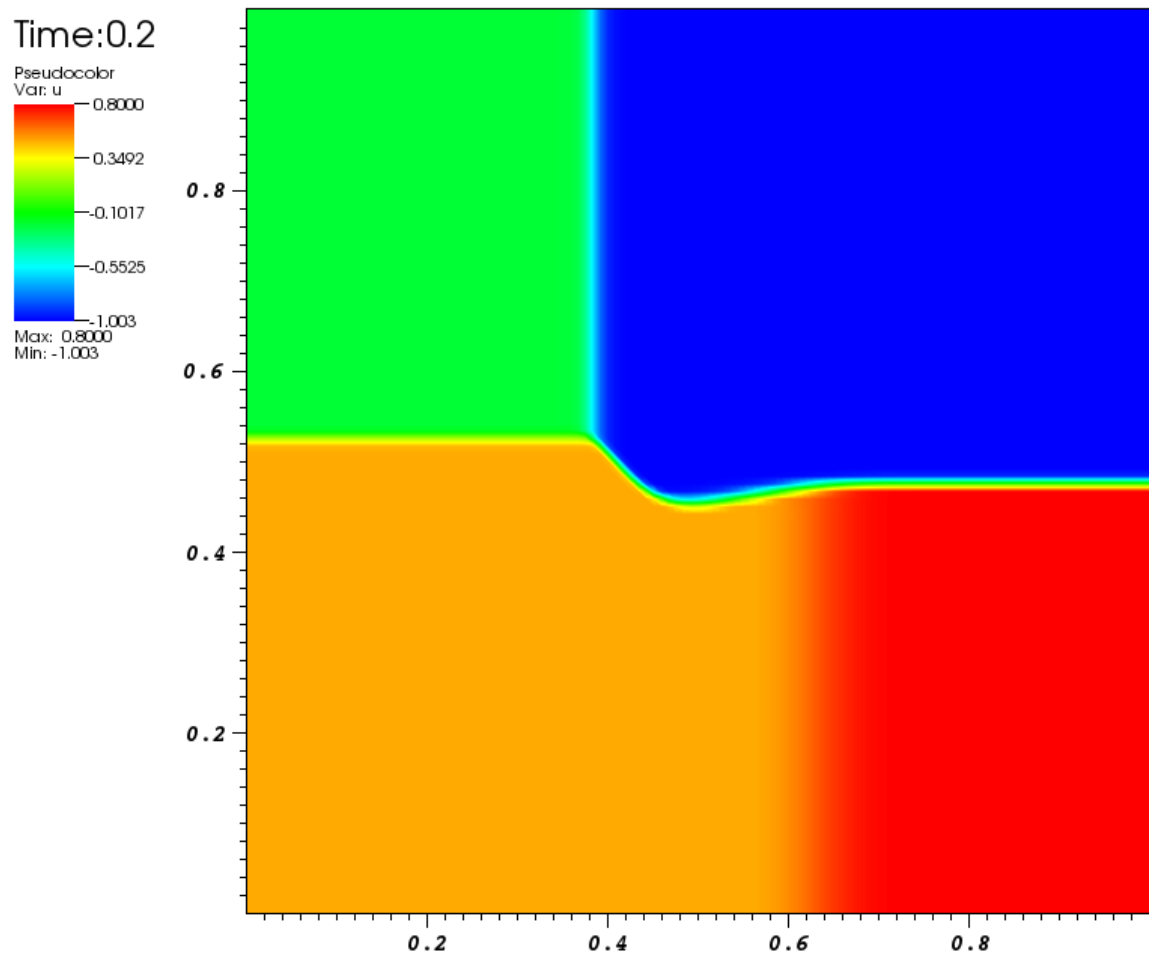


Figure 4.5: 2-D Burger's equation: solution profile at  $t = 0.2$  s.

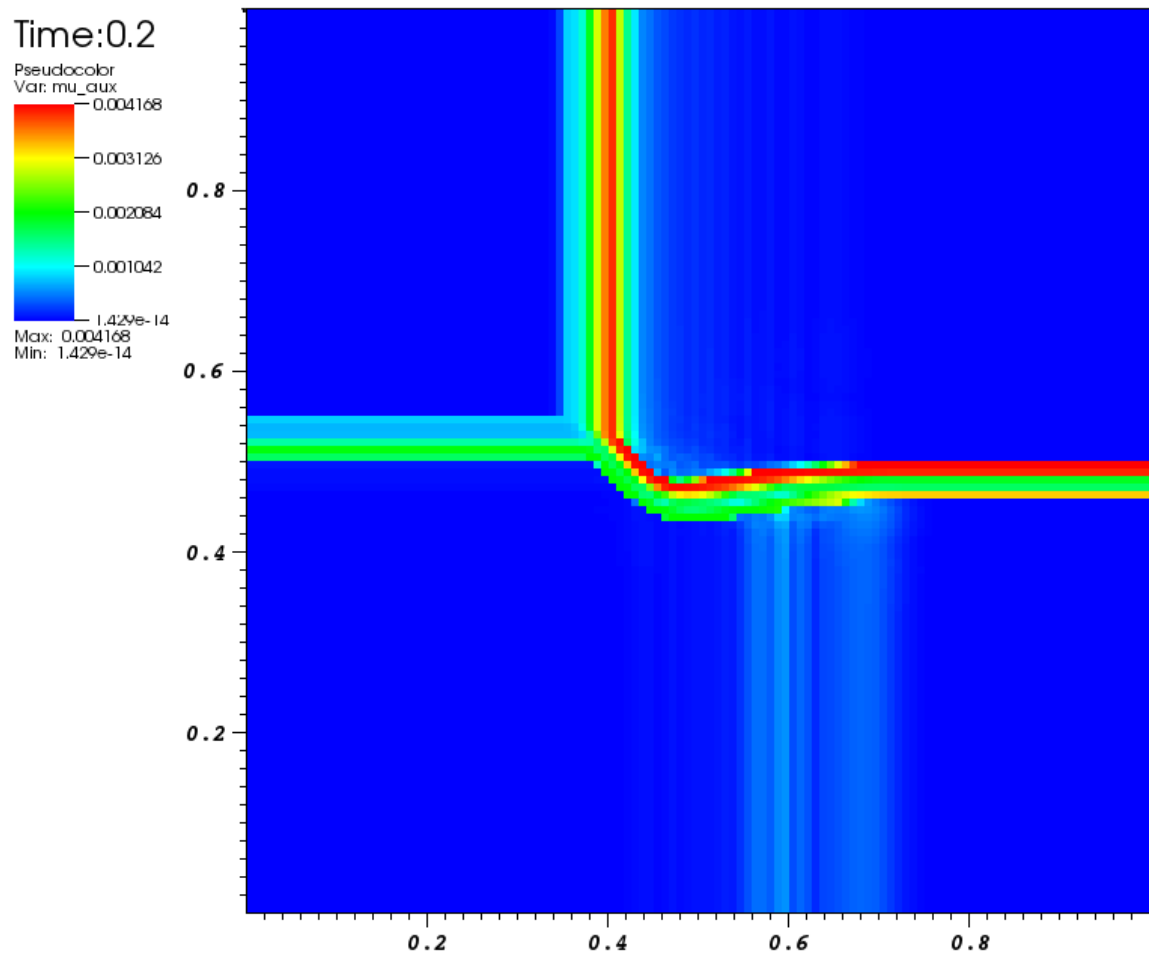


Figure 4.6: 2-D Burger's equation: viscosity profile at  $t = 0.2$  s.

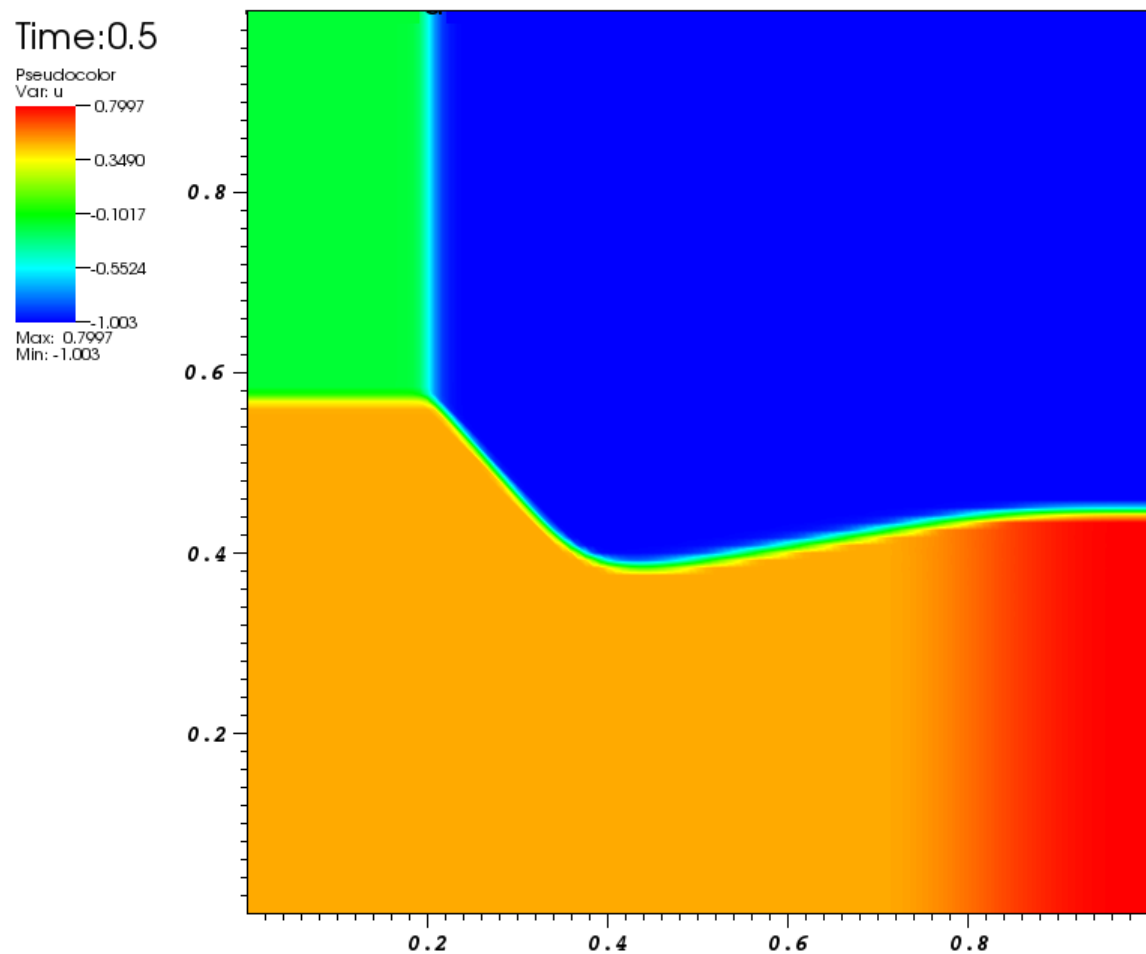


Figure 4.7: 2-D Burger's equation: solution profile at  $t = 0.5$  s.

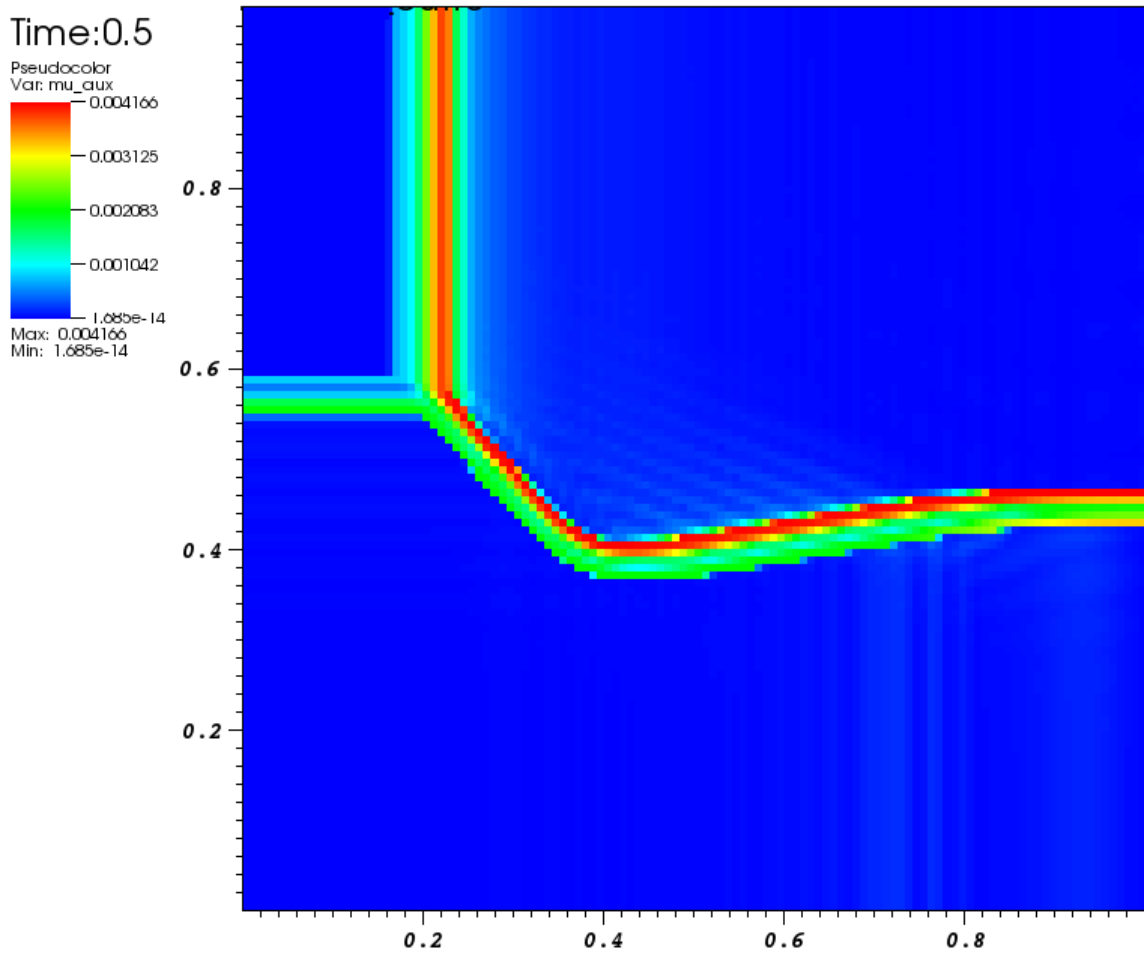


Figure 4.8: 2-D Burger's equation: viscosity profile at  $t = 0.5$  s.

The numerical solution is plotted in Fig. 4.5 and Fig. 4.7 at  $t = 0.2$  and  $t = 0.5$  s, respectively. The numerical solution does not display any oscillations and the shocks are well resolved. The high-order viscosity coefficient is showed in Fig. 4.6 and Fig. 4.8: the shock is well tracked by the EVM and sufficient dissipation is only added in the shock regions, where saturation to the first-order viscosity is achieved.

The above examples were simple illustrations of the capabilities of the EVM when applied to hyperbolic scalar equations. We now focus our attention to the application of the EVM to various hyperbolic systems of equations.

## 5. APPLICATION OF THE ENTROPY VISCOSITY METHOD TO THE MULTI-D EULER EQUATIONS WITH VARIABLE AREA

Over the past years an increasing interest has been raised for computational methods that can solve both compressible and incompressible flows. In engineering applications, there is often the need to solve for complex flows where a near incompressible regime or low Mach flow coexists with a supersonic flow domain. For example, such flows are encountered in aerodynamics in the study of airships. In the nuclear industry, flows are nearly in the incompressible regime but compressible effects cannot be neglected because of the heat source and because of postulated accident scenarios, and thus needs to be accurately resolved.

When solving the multi-D Euler equations for a wide range of Mach numbers, multiple problems must be addressed: stability, accuracy and acceleration of the convergence in the low Mach regime. Because of the hyperbolic nature of the equations, shocks can form during transonic and supersonic flows, and require the use of numerical methods in order to stabilize the scheme and correctly resolve the discontinuities. The literature offers a wide range of stabilization methods: flux-limiter [13, 14], pressure-based viscosity method ([43]), Lapidus method ([35, 44, 20]), and the entropy-viscosity method([29, 30]) among others. These numerical methods are usually developed using simple equations of state and tested for transonic and supersonic flows where the disparity between the acoustic wave speed and the fluid speed is not large because the Mach number is of order one. This approach, however, leads to a well-known accuracy problem in the low Mach regime where the fluid velocity is smaller than the speed of sound by multiple orders of magnitude. The numerical dissipative terms become ill-scaled in the low Mach regime and lead to the wrong

numerical solution by changing the nature of the equations solved. This behavior is well documented in the literature [25, 68, 34] and often treated by performing a low Mach asymptotic study of the multi-D Euler equation. This method was originally used [25] to show convergence of the compressible multi-D Euler equations to the incompressible ones. Thus, by using the same method, the effect of the dissipative terms in the low Mach regime, can be understood and, when needed, a fix is developed in order to ensure the convergence of the equations to the correct physical solution. This approach was used as a "fixing" method for multiple well known stabilization methods alike Roe scheme ([41]) and SUPG [34] while preserving the original stabilization properties of shocks for supersonic flows. Furthermore, it is also of common knowledge that low-Mach steady-state solutions can be difficult to obtain with a temporal explicit solver. For stability purpose, the time step must be chosen inversely proportional to the largest eigenvalue of the system which is approximately the speed of sound,  $c$ , for slow flows. However, other waves are convected at the fluid speed, which is much slower. Hence, these waves do not change very much over a time step. Thus, thousands of time steps are required to reach a steady state. Acceleration techniques were developed and proved efficient [68], but require the modification of the temporal derivatives of the equation and thus, can only be used for steady-state flows. To avoid modifying the temporal derivatives, the temporal implicit capabilities of the MOOSE multiphysics framework [17] is used. Such a choice should allow us to quickly obtain low-Mach steady-state solutions, while preserving the accuracy of the transient solution; but it also requires a preconditioner.

We propose in this chapter to investigate how the entropy viscosity method, when applied to the multi-D Euler equations with variable area, behaves in the low Mach regime. This method was initially introduced by Guermond et al. to solve for the hyperbolic systems and has shown good results when used for solving the multi-

D Euler equations for supersonic flows with various discretization schemes. More importantly, it is simple to implement, can be used with unstructured grids, and its dissipative terms are consistent with the entropy minimum principle and it has proven valid for any equation of state under certain conditions [24].

In Section 5.1 the current definition of the entropy viscosity method is recalled, and inconsistency with the low Mach regime is pointed out. Since our interest is in the variable area version of the multi-D Euler equation, the reader is guided through the steps leading to the derivation of the dissipative terms on the model of [24]. Then in Section 5.2, a new definition of the viscosity coefficient is introduced and derived from a low Mach asymptotic study. 1-D and 2-D numerical results are presented in Section 5.6 for a wide range of Mach numbers: low Mach flow over a cylinder and a circular bump, and supersonic flows over various geometries. Convergence studies are performed in 1-D, in order to demonstrate the accuracy of the solution.

## 5.1 The Entropy Viscosity Method

### 5.1.1 Background

The Euler equations are given by

$$\partial_t \rho + \nabla \cdot (\rho \mathbf{u}) = 0 \quad (5.1a)$$

$$\partial_t (\rho \mathbf{u}) + \nabla \cdot (\rho \mathbf{u} \otimes \mathbf{u} + P \mathbb{I}) = 0 \quad (5.1b)$$

$$\partial_t (\rho E) + \nabla \cdot [\mathbf{u} (\rho E + P)] = 0 \quad (5.1c)$$

where  $\rho$ ,  $\rho \mathbf{u}$  and  $\rho E$  are the density, the momentum and the total energy, respectively, and will be referred to as the conservative variables.  $\mathbf{u}$  is the fluid velocity and its specific internal energy is denoted by  $e = E - \frac{u^2}{2}$ . An equation of state, dependent

upon  $\rho$  and  $e$ , is used to compute the pressure  $P$ . The tensor product  $\mathbf{a} \otimes \mathbf{b}$  is such that  $(\mathbf{a} \otimes \mathbf{b})_{i,j} = a_i b_j$ . The identity tensor is denoted by  $\mathbb{I}$ .

Next, the entropy viscosity method [29, 30, 23, 69] applied to Eq. (5.1) is recalled. The derivation of the viscous regularization (or dissipative terms) is carried out to be consistent with the entropy minimum principle; details and proofs of the derivation can be found in [24]. The viscous regularization thus obtained is valid for any equation of state as long as the physical entropy function  $s$  is concave (or  $-s$  is a convex function) with respect to the internal energy  $e$  and the specific volume  $1/\rho$ . The Euler equations with viscous regularization become:

$$\partial_t \rho + \nabla \cdot (\rho \mathbf{u}) = \nabla \cdot (\kappa \nabla \rho) \quad (5.2a)$$

$$\partial_t (\rho \mathbf{u}) + \nabla \cdot (\rho \mathbf{u} \otimes \mathbf{u} + P \mathbf{I}) = \nabla \cdot (\mu \rho \nabla^s \mathbf{u} + \kappa \mathbf{u} \otimes \nabla \rho) \quad (5.2b)$$

$$\partial_t (\rho E) + \nabla \cdot [\mathbf{u} (\rho E + P)] = \nabla \cdot \left( \kappa \nabla (\rho e) + \frac{1}{2} \|\mathbf{u}\|^2 \kappa \nabla \rho + \rho \mu \mathbf{u} \nabla \mathbf{u} \right) \quad (5.2c)$$

where  $\kappa$  and  $\mu$  are positive viscosity coefficients.  $\nabla^s \mathbf{u}$  denotes the symmetric gradient operator that guarantees the method to be rotationally invariant [24]. The viscosity coefficients are key ingredients in the viscous regularization of Eq. (5.2). Other stabilization approaches have been proposed in the literature, for instance, the Lapidus method [20, 35] or pressure-based viscosity methods [43]. Here, we follow the work of Guermond et al. and define the viscosity coefficients,  $\kappa$  and  $\mu$ , based on the local entropy production. These coefficients are numerically evaluated using the local entropy residual  $R(\mathbf{r}, t)$  defined in Eq. (5.3);  $R(\mathbf{r}, t)$  is known to be peaked in shocks and vanishingly small elsewhere [65].

$$R(\mathbf{r}, t) := \partial_t s + \mathbf{u} \cdot \nabla s \quad (5.3)$$

In the current version of the method, the ratio of  $\kappa$  to  $\mu$  is defined through a numerical Prandlt number,  $\text{Pr} = \kappa/\mu$ .  $\text{Pr}$  is a user-defined parameter and is usually taken in the range  $[0.001; 1]$ . Since the entropy residual  $R(\mathbf{r}, t)$  may be extremely large in shocks, the definition of the viscosity coefficients also includes a first-order viscosity coefficient that serves as an upper bound for the entropy-based viscosity coefficients. The first-order viscosity coefficients, denoted by  $\mu_{\max}$  and  $\kappa_{\max}$ , are chosen so that the numerical scheme becomes equivalent to an one-wave (maximum local eigenvalue) upwind scheme when the first-order coefficients are employed. The upwind scheme is known to be over-dissipative but guarantees monotonicity [65]. In practice, the viscosity coefficients only saturate to the first-order viscosity coefficients in shocks and are much smaller elsewhere, hence avoiding the over-dissipation of the upwind method. The first-order viscosity coefficients  $\mu_{\max}$  and  $\kappa_{\max}$  are equal and set proportional to the largest local eigenvalue  $\|\mathbf{u}\| + c$ :

$$\mu_{\max}(\mathbf{r}, t) = \kappa_{\max}(\mathbf{r}, t) = \frac{h}{2} (\|\mathbf{u}(\mathbf{r}, t)\| + c(\mathbf{r}, t)), \quad (5.4)$$

where  $h$  denotes the local grid size (for higher than linear finite element representations,  $h$  is defined as the ratio of the grid size to the polynomial order of the test functions used, see Eq. 2.4 in [69]). For simplicity, the first-order viscosity coefficients will only be referred to as the  $\kappa_{\max}(\mathbf{r}, t)$ . In practice, these quantities are evaluated within a given cell  $K$  at quadrature points:

$$\kappa_{\max}^e(\mathbf{r}_q, t) = \frac{h^e}{2} (\|\mathbf{u}(\mathbf{r}_q, t)\| + c(\mathbf{r}_q, t)), \quad (5.5)$$

where  $\mathbf{r}_q$  denotes the position of a quadrature point. As stated earlier, the entropy viscosity coefficients, which we denote by  $\kappa_e$  and  $\mu_e$ , are set proportional to the

entropy production evaluated by computing the local entropy residual  $R$ . The definitions also include the inter-element jump  $J[s]$  of the entropy flux, allowing for the detection of discontinuities other than shocks (e.g., contact).

$$\mu_e^e(\mathbf{r}_q, t) = (h^e)^2 \frac{\max(|R^e(\mathbf{r}_q, t)|, J^e[s](t))}{\|s - \bar{s}\|_\infty} \quad (5.6a)$$

$$\kappa_e^e(\mathbf{r}_q, t) = \frac{\gamma}{\gamma - 1} \text{Pr} \mu_e^e(\mathbf{r}_q, t) \quad (5.6b)$$

where  $\|\cdot\|_\infty$  and  $\bar{\cdot}$  denote the  $L_\infty$ -norm and the average operator over the entire computational domain, respectively. The definition of the entropy jump  $J[s]$  is spatial discretization-dependent and examples of definitions can be found in [69] for discontinuous Galerkin discretization. For continuous finite element methods (FEM), the jump of a given quantity is defined as the change of its normal derivative ( $\partial_n(\cdot) = \nabla(\cdot) \cdot \mathbf{n}$ ) across the common face separating the two elements, and will be further referred to as the inter-element jump. We take the largest value over all faces  $f$  present on the boundary  $\partial e$  of element  $e$ :

$$J^e[s](t) = \max_{f \in \partial e} \max_{\mathbf{r}_q \in f} (||\mathbf{u}|| \llbracket \nabla s(\mathbf{r}_q, t) \cdot \mathbf{n}(\mathbf{r}_q) \rrbracket_f) , \quad (5.7)$$

where  $\llbracket a(\mathbf{r}_q) \rrbracket_f$  denotes the inter-element jump in  $a(\mathbf{r})$  at quadrature point  $\mathbf{r}_q$  on face  $f$  (the quadrature points  $\mathbf{r}_q$  are taken on the faces  $f$  of the element  $e$ ). With the definition given in Eq. (5.7), the jump is constant over each element  $e$  of the computational domain. The denominator  $\|s - \bar{s}\|_\infty$  is used for dimensionality purposes. Currently, there is no theoretical justification for choosing the denominator beyond

a dimensionality argument. Finally, the viscosity coefficients  $\mu$  and  $\kappa$  are as follows:

$$\mu(\mathbf{r}, t) = \min \left( \mu_e(\mathbf{r}, t), \mu_{\max}(\mathbf{r}, t) \right) \quad \text{and} \quad \kappa(\mathbf{r}, t) = \min \left( \kappa_e(\mathbf{r}, t), \kappa_{\max}(\mathbf{r}, t) \right). \quad (5.8)$$

Given these definitions, we have the following properties. In shock regions, the entropy viscosity coefficients will experience a peak because of entropy production and thus will saturate to the first-order viscosity. The first-order coefficients are known to be over-dissipative and will smooth out any oscillatory behavior. Elsewhere in the domain, entropy production will be small and the viscosity coefficients  $\mu$  and  $\kappa$  will remain small. High-order accuracy for entropy-based viscous stabilization has been demonstrated using several 1-D shock tube examples and various 2-D tests [29, 30, 69].

### 5.1.2 Issues in the low-mach regime

In the low-Mach Regime, a smooth flow is known to approach the isentropic limit, resulting in very little entropy production. Since the entropy viscosity method is directly based on the evaluation of the evaluation of the local entropy production, it is of interest to study how the entropy viscosity coefficients  $\mu_e$  and  $\kappa_e$  scale in the low-Mach regime. In practice, the entropy residual  $R$  will be very small in that regime and so will be the denominator  $\|s - \bar{s}\|_\infty$ , thus making the definition of the viscosity coefficients in Eq. (5.6) undetermined and likely ill-scaled. One possible approach would consist of expanding the numerator and denominator in terms of the Mach number and deriving its limit when the Mach number goes to zero. Such derivation may not be straightforward, especially for general equations of state. However, this can be avoided by noting that the entropy residual  $R$  can be recast as a function of pressure, density, velocity, and speed of sound as will be shown in Eq. (5.9) of

Section 5.2.1. This alternate entropy residual definition is the basis for the low-Mach analysis carried out in this paper and possesses several advantages that are detailed next.

## 5.2 An all-speed reformulation of the Entropy Viscosity Method

In this section, the entropy residual  $R$  is recast as a function of pressure, density, velocity and speed of sound. Then, an isentropic low-Mach asymptotic study is carried out for the Euler equations with viscous regularization in order to derive an appropriate normalization parameter that is valid in the isentropic low-Mach regime as well as for transonic and supersonic flows.

### 5.2.1 New definition of the entropy production residual

The first step in defining viscosity coefficients that behave well in the low-Mach limit is to recast the entropy residual in terms of thermodynamic variables. This provides physical insight on possible normalization choices that can be valid in both low-Mach and transonic flows. The alternate definition of the entropy residual, the derivation of which is given in Appendix A, is given

$$R(\mathbf{r}, t) := \partial_t s + \mathbf{u} \cdot \nabla s = \frac{Ds}{Dt} = \frac{s_e}{P_e} \left( \underbrace{\frac{DP}{Dt} - c^2 \frac{D\rho}{Dt}}_{\tilde{R}(\mathbf{r}, t)} \right), \quad (5.9)$$

where  $\frac{D}{Dt}$  denotes the material derivative ( $\frac{D}{Dt} := \frac{\partial}{\partial t} + \mathbf{u} \cdot \nabla$ ), and  $x_y$  is the standard shorthand notation for the partial derivative of  $x$  with respect to  $y$ , e.g.,  $P_e := \frac{\partial P}{\partial e}$ . The entropy residuals  $R$  and  $\tilde{R}$  are proportional to one another and will experience similar variations in space and time. Thus, one may elect to employ  $\tilde{R}$  instead of  $R$  for the evaluation of the local entropy residual. The new expression presents several advantages which includes:

- An analytical expression of the entropy function  $s$  is no longer needed: the residual  $\tilde{R}$  is evaluated using the local values of pressure, density, velocity and speed of sound. Deriving an entropy function for some complex equations of state may be difficult;
- Suitable normalizations for the residual  $\tilde{R}$  can be devised. Examples include the pressure itself or combinations of the density, the speed of sound and the norm of the velocity, i.e.,  $\rho c^2$ ,  $\rho c\|\mathbf{u}\|$  or  $\rho\|\mathbf{u}\|^2$ .

Denoting the normalization of  $\tilde{R}$  by  $\text{norm}_P$ , the entropy-based viscosity coefficients  $\mu_e$  and  $\kappa_e$  can be re-defined as follows:

$$\mu_e^e(\mathbf{r}, t) = (h^e)^2 \frac{\max \left( |\tilde{R}^e(\mathbf{r}_q, t)|, \|\mathbf{u}(\mathbf{r}_q, t)\| J^e[P](t), \|\mathbf{u}(\mathbf{r}_q, t) c^2(\mathbf{r}_q, t)\| J^e[\rho](t) \right)}{\text{norm}_P^\mu}, \quad (5.10a)$$

and

$$\kappa_e^e(\mathbf{r}, t) = (h^e)^2 \frac{\max \left( |\tilde{R}^e(\mathbf{r}_q, t)|, \|\mathbf{u}(\mathbf{r}_q, t)\| J^e[P](t), \|\mathbf{u}(\mathbf{r}_q, t) c^2(\mathbf{r}_q, t)\| J^e[\rho](t) \right)}{\text{norm}_P^\kappa}. \quad (5.10b)$$

Note that now the jump operator acts on the variables appearing in  $\tilde{R}$ , namely, pressure and density. The  $\mu$  and  $\kappa$  coefficients are kinematic viscosities (units of  $m^2/s$ ); the normalization parameters  $\text{norm}_P$  are thus in units of pressure, hence the use of the subscript  $P$ . Note also that we are not requiring the same normalization for both  $\mu_e$  and  $\kappa_e$  so the entropy viscosity coefficients can be different. The isentropic low-Mach asymptotic study presented next will determine the proper normalization.

### 5.2.2 Asymptotic study in the low-mach regime

The Euler equations with viscous stabilization, Eq. (5.6), bear some similarities with the Navier-Stokes equations in the sense that dissipative terms (containing

second-order spatial derivatives) are present in both sets of equations. An abundant literature exists regarding the low-Mach asymptotics of the Navier-Stokes equations [25, 68, 34, 48]. The asymptotic study presented here is inspired by the work of Muller et al. [48] where an asymptotic derivation for the Navier-Stokes was presented. We remind the reader that the objective is to determine appropriate scaling for the entropy viscosity coefficients so that the dissipative terms remain well-scaled for two limit cases: (i) the isentropic limit where Euler equations degenerate to an incompressible system of equations in the low-Mach limit and (ii) the non-isentropic limit with formation of shocks. The isentropic limit of the Euler equations with viscous regularization should yield incompressible fluid flow solutions in the low-Mach limit, namely, that the pressure fluctuations are of the order  $M^2$  and that the velocity satisfies the divergence constraint  $\nabla \cdot \mathbf{u}_0 = 0$  [25, 68, 34]. For non-isentropic situations, shocks may form for any value of Mach number and the minimum entropy principle should still be satisfied so that numerical oscillations, if any, be controlled by the entropy viscosity method independently of the value of the Mach number. Our objective is to determine the appropriate scaling for the Reynolds and Péclet numbers,  $\text{Re}_\infty$  and  $\text{Pé}_\infty$ , in these two limit cases.

In this Section, we are interested in the isentropic limit; the non-isentropic case is treated later. The first step in the study of the limit cases (i) and (ii) is to rewrite Eq. (5.2) in a non-dimensional manner. To do so, the following variables are introduced:

$$\begin{aligned} \rho^* &= \frac{\rho}{\rho_\infty}, \quad u^* = \frac{u}{u_\infty}, \quad P^* = \frac{P}{\rho_\infty c_\infty^2}, \quad E^* = \frac{E}{c_\infty^2}, \\ x^* &= \frac{x}{L_\infty}, \quad t^* = \frac{t}{L_\infty/u_\infty}, \quad \mu^* = \frac{\mu}{\mu_\infty}, \quad \kappa^* = \frac{\kappa}{\kappa_\infty}, \end{aligned} \quad (5.11)$$

where the subscript  $\infty$  denote the far-field or stagnation quantities and the super-script  $*$  stands for the non-dimensional variables. The far-field reference quantities are chosen such that the dimensionless flow quantities are of order 1. The reference Mach number is given by

$$M_\infty = \frac{u_\infty}{c_\infty}, \quad (5.12)$$

where  $c_\infty$  is a reference value for the speed of sound. Then, the scaled Euler equations with viscous regularization are:

$$\partial_{t^*} \rho^* + \nabla^* \cdot (\rho^* \mathbf{u}^*) = \frac{1}{\text{P\'{e}}_\infty} \nabla^* \cdot (\kappa^* \vec{\nabla}^* \rho^*) \quad (5.13a)$$

$$\begin{aligned} \partial_{t^*} (\rho^* \mathbf{u}^*) + \nabla^* \cdot (\rho^* \mathbf{u}^* \otimes \mathbf{u}^*) + \frac{1}{M_\infty^2} \vec{\nabla}^* P^* &= \frac{1}{\text{Re}_\infty} \nabla^* \cdot \left( \rho^* \mu^* \vec{\nabla}^{s,*} \mathbf{u}^* \right) \\ &+ \frac{1}{\text{P\'{e}}_\infty} \nabla^* \cdot \left( \mathbf{u}^* \otimes \kappa^* \vec{\nabla}^* \rho^* \right) \end{aligned} \quad (5.13b)$$

$$\begin{aligned} \partial_{t^*} (\rho^* E^*) + \nabla^* \cdot [\mathbf{u}^* (\rho^* E^* + P^*)] &= \frac{1}{\text{P\'{e}}_\infty} \nabla^* \cdot \left( \kappa^* \vec{\nabla}^* (\rho^* e^*) \right) \\ &+ \frac{M_\infty^2}{\text{Re}_\infty} \nabla^* \cdot \left( \mathbf{u}^* \rho^* \mu^* \vec{\nabla}^{s,*} \mathbf{u}^* \right) + \frac{M_\infty^2}{2\text{P\'{e}}_\infty} \nabla^* \cdot \left( \kappa^* (u^*)^2 \vec{\nabla}^* \rho^* \right), \end{aligned} \quad (5.13c)$$

where the numerical Reynolds ( $\text{Re}_\infty$ ) and P\'{e}clet ( $\text{P\'{e}}_\infty$ ) numbers are defined as:

$$\text{Re}_\infty = \frac{u_\infty L_\infty}{\mu_\infty} \text{ and } \text{P\'{e}}_\infty = \frac{u_\infty L_\infty}{\kappa_\infty}. \quad (5.14)$$

Note that the Prandlt number used in the original version of the entropy viscosity method is simply given by

$$\text{Pr}_\infty = \text{P\'{e}}_\infty / \text{Re}_\infty. \quad (5.15)$$

The numerical Reynolds and Péclet numbers defined in Eq. (5.14) are related to the entropy viscosity coefficients  $\mu_\infty$  and  $\kappa_\infty$ . Thus, once a scaling (in powers of  $M_\infty$ ) is obtained for  $\text{Re}_\infty$  and  $\text{Pé}_\infty$ , the corresponding normalization parameters  $\text{norm}_P^\mu$  and  $\text{norm}_P^\kappa$  will automatically be set. For simplicity, we use here the ideal gas equation of state; its non-dimensionalized expression is given by

$$P^* = (\gamma - 1) \rho^* \left( E^* - \frac{1}{2} M_\infty^2 (u^*)^2 \right) = (\gamma - 1) \rho^* e^*. \quad (5.16)$$

For brevity, the superscripts  $*$  are omitted in the remainder of this section. In the low-Mach isentropic limit, shocks cannot form and the compressible Euler equations are known to converge to the incompressible equations when the Mach number tends to zero. When adding dissipative terms, as is the case with the entropy viscosity method, the main properties of the low-Mach asymptotic limit must be preserved. We begin by expanding each variable in powers of the Mach number. As an example, the expansion for the pressure is given by:

$$P(\mathbf{r}, t) = P_0(\mathbf{r}, t) + P_1(\mathbf{r}, t) M_\infty + P_2(\mathbf{r}, t) M_\infty^2 + \dots \quad (5.17)$$

By studying the resulting momentum equations for various powers of  $M_\infty$ , it is observed that the leading order and first-order pressure terms,  $P_0$  and  $P_1$ , are spatially constant if and only if  $\text{Re}_\infty = \text{Pé}_\infty = 1$ . In this case, at order  $M_\infty^{-2}$ :

$$\nabla P_0 = 0 \quad (5.18a)$$

and, at order  $M_\infty^{-1}$ ,

$$\nabla P_1 = 0. \quad (5.18b)$$

Using the scaling  $\text{Re}_\infty = \text{Pé}_\infty = 1$ , the leading-order (order 1) expressions for the continuity, momentum, and energy equations are:

$$\partial_t \rho_0 + \nabla \cdot (\rho \mathbf{u})_0 = \nabla \cdot (\kappa \nabla \rho)_0 \quad (5.19a)$$

$$\partial_t (\rho \mathbf{u})_0 + \nabla \cdot (\rho \mathbf{u} \otimes \mathbf{u})_0 + \nabla P_2 = \nabla \cdot (\rho \mu \nabla^s \mathbf{u} + \kappa \mathbf{u} \otimes \nabla \rho)_0 \quad (5.19b)$$

$$\partial_t (\rho E)_0 + \nabla \cdot [\mathbf{u}(\rho E + P)]_0 = \nabla \cdot (\kappa \nabla (\rho e))_0 \quad (5.19c)$$

where the notation  $(fg)_0$  means that we only keep the 0<sup>th</sup> order terms in the product  $fg$ . The leading-order of the equation of state is given by

$$P_0 = (\gamma - 1)(\rho E)_0. \quad (5.20)$$

Using Eq. (5.20), the energy equation can be recast as a function of the leading-order pressure,  $P_0$ , as follows:

$$\partial_t P_0 + \gamma \nabla \cdot (\mathbf{u} P)_0 = \nabla \cdot (\kappa \nabla (P))_0 \quad (5.21)$$

From Eq. (5.18a), we infer that  $P_0$  is spatially constant. Thus, Eq. (5.21) becomes

$$\frac{1}{\gamma P_0} \frac{dP_0}{dt} = -\nabla \cdot \mathbf{u}_0 \quad (5.22)$$

and, at steady state, we have

$$\nabla \cdot \mathbf{u}_0 = 0. \quad (5.23)$$

That is, the leading-order of velocity is divergence-free. The same reasoning can be applied to the leading-order of the continuity equation (Eq. (5.19a)) to show that

the material derivative of the density is zero:

$$\frac{D\rho_0}{Dt} := \partial_t \rho_0 + \mathbf{u}_0 \cdot \nabla \cdot \rho_0 = 0. \quad (5.24)$$

Therefore, we conclude that by setting the Reynolds and Péclet numbers to one, the incompressible fluid results are retrieved in the isentropic low-Mach limit when employing the compressible Euler equations with viscous regularization terms present. In addition, the scaling of the Prandtl number can also be obtained using Eq. (5.15), hence clarifying the use of the numerical Prandtl in the original entropy viscosity method [29].

### 5.2.3 Scaling of $Re_\infty$ and $Pé_\infty$ for non-isentropic flows

Next, we consider the non-isentropic case. Recall that even subsonic flows can present shocks (for instance, a step initial condition in the pressure will trigger shock formation, independently of the Mach number). The non-dimensional form of the Euler equations given in Eq. (5.13) provides some insight on the dominant terms as a function of the Mach number. This is particularly obvious in the momentum equation, Eq. (5.13b), where the gradient of pressure is scaled by  $1/M_\infty^2$ . In the non-isentropic case, we no longer have  $\frac{\nabla P}{M_2} = \nabla P_2$  and this pressure gradient term may need to be stabilized by some dissipative terms of the same scaling so as to prevent spurious oscillations from forming. This leads to the following three possible requirements regarding the non-dimensionalized Reynolds and Péclet numbers for non-isentropic flows: (a)  $Re_\infty = M_\infty^2$  and  $Pé_\infty = 1$ , (b)  $Re_\infty = 1$  and  $Pé_\infty = M_\infty^2$ , or (c)  $Re_\infty = Pé_\infty = M_\infty^2$ . Any of these choices will also affect the stabilization of the continuity and energy equations. For instance, using a Péclet number equal to  $M_\infty^2$  may effectively stabilize the continuity equation in the shock region but this may also add an excessive amount of dissipation for subsonic flows at the location

of the contact wave. Such a behavior may not be suitable for accuracy purpose, making options (b) and (c) inappropriate. The same reasoning, left to the reader, can be carried out for the energy equation (Eq. (5.13c)) and results in the same conclusion. The remaining choice, option (a), has the proper scaling: in this case, only the dissipation terms involving  $\vec{\nabla}^{s,*} \mathbf{u}^*$  scale as  $1/M_\infty^2$  since  $\text{Re}_\infty = M_\infty^2$ , leaving the regularization of the continuity equation unaffected because  $\text{P\'{e}}_\infty = 1$ .

#### 5.2.4 New normalization for the entropy residual

The study of the above limit cases yields two different possible scalings for the Reynolds number:  $\text{Re}_\infty = 1$  in the isentropic case and  $\text{Re}_\infty = M_\infty^2$  for non-isentropic case, whereas the numerical P\'{e}clet number always scales as one. In order to have a stabilization method valid for a wide range of Mach numbers, including situations with shocks, these two scalings should be combined in a unique definition.

We begin with the normalization parameter  $\text{norm}_P^\kappa$ . Using the definition of the viscosity coefficients given in Eq. (5.10) and the scaling of Eq. (5.11), it can be shown that:

$$\kappa_\infty = \frac{\rho_\infty c_\infty^2 u_\infty L}{\text{norm}_{P,\infty}^\kappa}, \quad (5.25)$$

where  $\text{norm}_{P,\infty}$  is the reference far-field quantity for the normalization parameter  $\text{norm}_P$ . Substituting Eq. (5.25) into Eq. (5.14) and recalling that the numerical P\'{e}clet number scales as unity, we obtain:

$$\text{norm}_{P,\infty}^\kappa = \text{P\'{e}}_\infty \rho_\infty c_\infty^2 = \rho_\infty c_\infty^2. \quad (5.26)$$

Eq. (5.26) provides a proper normalization factor to define the  $\kappa$  viscosity coefficient.

The derivation for  $\text{norm}_P^\mu$  is similar and yields

$$\text{norm}_P^\mu = \text{Re}_\infty \rho_\infty c_\infty^2 = \begin{cases} \rho \|\mathbf{u}\|^2 & \text{for non-isentropic flows} \\ \rho c^2 = \text{norm}_P^\kappa & \text{for isentropic low-Mach flows} \end{cases} . \quad (5.27)$$

A smooth function to transition between these two states is as follows:

$$\sigma(M) = \frac{\tanh(a(M - M^{\text{thresh}})) + |\tanh(a(M - M^{\text{thresh}}))|}{2}, \quad (5.28)$$

where  $M^{\text{thresh}}$  is a threshold Mach number value beyond which the flow is no longer considered to be low-Mach (we use  $M^{\text{thresh}} = 0.05$ ),  $M$  is the local Mach number, and the scalar  $a$  determines how rapid the transition from  $\text{norm}_P^\mu = \rho c^2$  to  $\text{norm}_P^\mu = \rho \|\mathbf{u}\|^2$  occurs in the vicinity of  $M^{\text{thresh}}$  (we use  $a = 3$ ). It is easy to verify that

$$\text{norm}_P^\mu = (1 - \sigma(M))\rho c^2 + \sigma(M)\rho \|\mathbf{u}\|^2 \quad (5.29)$$

satisfies Eq. (5.27).

Finally, we summarize the definition of the viscosity coefficients  $\mu$  and  $\kappa$  for completeness:

$$\kappa(\mathbf{r}, t) = \min \left( \mu_{\max}(\mathbf{r}, t), \kappa_e(\mathbf{r}, t) \right), \quad (5.30a)$$

$$\mu(\mathbf{r}, t) = \min \left( \mu_{\max}(\mathbf{r}, t), \mu_e(\mathbf{r}, t) \right), \quad (5.30b)$$

where the first-order viscosity is given by

$$\kappa_{\max}(\mathbf{r}, t) = \mu_{\max}(\mathbf{r}, t) = \frac{h}{2} \left( \|\mathbf{u}\| + c \right) \quad (5.30c)$$

and the entropy viscosity coefficients by

$$\kappa_e(\mathbf{r}, t) = \frac{h^2 \max(\tilde{R}, J)}{\rho c^2} \text{ and } \mu_e(\mathbf{r}, t) = \frac{h^2 \max(\tilde{R}, J)}{\text{norm}_P^\mu} \quad (5.30d)$$

with the jumps given by

$$J = \max \left( \|\mathbf{u}\| [[\nabla P \cdot \mathbf{n}]], \|\mathbf{u}\| c^2 [[\nabla \rho \cdot \mathbf{n}]] \right) \quad (5.30e)$$

where  $\text{norm}_P^\kappa$  is computed from Eq. (5.29). The jump  $J$  is a function of the jump of pressure and density gradients across the face with respect to its normal vector  $\mathbf{n}$ . Then, the largest value over all faces is determined and used in the definition of the viscosity coefficients. With the definition of the viscosity coefficients  $\mu$  and  $\kappa$  proposed in Eq. (5.30), the dissipative terms are expected to scale appropriately for very low-Mach regimes as well for transonic and supersonic flows.

### 5.3 Extension of the entropy viscosity technique Euler equations with variable area

Fluid flows in nozzles and in pipes of varying cross-sectional area can be modeled using the variable-area variant of the Euler equations, where the conservative variables are now multiplied by the area  $A$ . In addition, these equations differ from the standard Euler equations in that the momentum equation Eq. (5.31b) contains a non-conservative term proportional to the area gradient. For the purpose of this paper, the variable area is assumed to be a smooth function of space only.

$$\partial_t (\rho A) + \nabla \cdot (\rho \mathbf{u} A) = 0 \quad (5.31a)$$

$$\partial_t (\rho \mathbf{u} A) + \nabla \cdot [A (\rho \mathbf{u} \otimes \mathbf{u} + P \mathbb{I})] = P \nabla A \quad (5.31b)$$

$$\partial_t (\rho E A) + \nabla \cdot [\mathbf{u} A (\rho E + P)] = 0 \quad (5.31c)$$

The application of the entropy viscosity method to the Euler equations with variable area is not fundamentally different to its application to the standard Euler equations. However, we need to derive the associated dissipative terms and verify that the entropy minimum principle is still satisfied. The variable-area Euler equations with viscous regularization are given below; details of the derivation are provided in Appendix A.

$$\partial_t (\rho A) + \nabla \cdot (\rho \mathbf{u} A) = \nabla \cdot (A \kappa \nabla \rho) \quad (5.32a)$$

$$\partial_t (\rho \mathbf{u} A) + \nabla \cdot [A (\rho \mathbf{u} \otimes \mathbf{u} + P \mathbf{I})] = P \nabla A + \nabla \cdot [A (\mu \rho \nabla^s \mathbf{u} + \kappa \mathbf{u} \otimes \nabla \rho)] \quad (5.32b)$$

$$\partial_t (\rho A E) + \nabla \cdot [\mathbf{u} A (\rho E + P)] = \nabla \cdot \left[ A \left( \kappa \nabla (\rho e) + \frac{1}{2} \|\mathbf{u}\|^2 \kappa \nabla \rho + \rho \mu \mathbf{u} \nabla^s \mathbf{u} \right) \right] \quad (5.32c)$$

The dissipative terms are quite similar to the ones obtained for the standard Euler equations: each dissipative flux is simply multiplied by the variable area  $A$  in order to ensure conservation of the dissipative flux. When assuming a constant area, Eq. (5.2) are recovered.

A low-Mach asymptotic limit of the multi-D Euler equations with variable area on the same model as in Section 5.2.2 will lead to the divergence constraint  $\nabla \cdot (\mathbf{u} A) = 0$  that can be recast as  $\nabla \cdot \mathbf{u} = -\mathbf{u} \cdot \nabla A/A$ . The gradient of the area acts as a source term and will force the fluid to accelerate or decelerate, depending on its sign.

#### 5.4 Entropy-viscosity method and source terms

In this section, we investigate the effect of the source terms on the EVM with the aim of using the EVM to solve for complex flows involved in engineering applications such as modeling the coolant in nuclear reactors. Since the EVM relies on the entropy minimum principle and the positivity of the entropy residual, our approach consists

of starting with the 1-D Euler equation with source terms in both the momentum and energy equation but without the viscous regularization (the dissipative terms were derived using the entropy minimum principle and should not be affected by the addition of source terms), and then, derive the entropy residual in order to study how the source terms affect its sign.

We start with the 1-D Euler equations with variables area and multiple source terms in the momentum and energy equations as follow:

$$\partial_t (\rho A) + \partial_x (\rho u A) = 0 \quad (5.33a)$$

$$\partial_t (\rho u A) + \partial_x [A (\rho u^2 + P)] = P \partial_x A + f_s + f_v A \quad (5.33b)$$

$$\partial_t (\rho E A) + \partial_x [u A (\rho E + P)] = f_v u A + q \quad (5.33c)$$

where  $f_s$  is a surface force and does not necessarily have an associated work in the energy equation (an example will be given in later in this section). The body forces (such as gravity force) are denoted by  $f_v$ . The last source term  $q$  consists of either a heat source if it is positive, or a heat sink if it is negative. As mentioned earlier in this section, the dissipative terms are ignored to simplify the derivations, but also because their impact on the sign of the residual is already known. Derivation of the entropy residual follows the same steps as in Section 5.3: the internal energy equation is obtained by combining the momentum and total energy equations. Then, using the continuity and internal energy equations, the 1-D entropy equation is obtained and yields:

$$\rho A \frac{Ds}{Dt} = \rho A [\partial_t s + u \partial_x s] = s_e (-f_s u + q), \quad (5.34)$$

where  $s_e$  was determined to be the inverse of the temperature and thus is positive. We note that the body forces do not affect the entropy residual. Using the result from Eq. (5.9), Eq. (5.34) is recast as follows:

$$\rho \tilde{R} = \rho \left( \frac{DP}{Dt} - c^2 \frac{D\rho}{Dt} \right) = P_e (-f_s u + q). \quad (5.35)$$

The sign of  $\tilde{R}$  is given by the right hand-side of Eq. (5.35) which is function of the surface force  $f_s$ , the fluid velocity  $u$  and the heat source term  $q$ . Let us assume that  $q$  is a large heat sink ( $q \leq 0$ ) such as  $|q| \geq -f_s u$ . Under this assumption,  $\tilde{R}$  becomes negative and violates the entropy inequality. On the other hand, if  $q$  is positive, the entropy residual remains positive and does not violate the entropy inequality. This example illustrates the fact that source terms can affect the sign of the entropy residual in both ways. Thus, in order to be consistent with the entropy inequality, it is proposed to include the right hand-side of Eq. (5.35) in the definition of the entropy residual such as:

$$\tilde{R}^{source} = \tilde{R} - \frac{P_e}{\rho} (-f_s u + q) \geq 0 \quad (5.36)$$

The sign of  $\tilde{R}^{source}$  remains positive since it is given by the viscous terms that were omitted in Eq. (5.33). The initial definition of the viscosity coefficients given in Eq. (5.30) is modified by simply substituting  $\tilde{R}$  into  $\tilde{R}^{source}$  and also keeping the same normalization parameters.

## 5.5 Boundary conditions

Because we cannot consider infinitely large domain, the computational domain needs to be truncated at some particular points (or on particular surfaces). These particular points are referred to as boundaries and are present in the weak form of

the equation to solve as shown in Section 3, under the form of an integral as follows:

$$\int_{\Gamma} (\mathbf{F}(\mathbf{U}(\mathbf{r}, t)) \phi_k) \cdot \mathbf{n}. \quad (5.37)$$

Computing the integral given in Eq. (5.37) requires the determination of the flux at the boundary  $\Gamma$ , which is the focus of this section for the case of the multi-D Euler equation with variable area. Treatment of the boundary conditions require great care and must be based on the study of the mathematical properties of the system of equations under consideration, in order to preserve the physical solution. An error in the treatment of the boundary conditions can lead to inaccurate transient and steady-state numerical solutions and also to numerical instabilities.

The multi-D Euler equations given in Eq. (5.32) are discretized using a continuous Galerkin finite element method and high-order temporal integrators provided by the MOOSE framework and detailed in Section 3. The discretization scheme requires the computation of two fluxes at the boundaries as it was shown in Eq. (3.4): the first boundary term comes from the integration by parts of the dissipative flux which vanishes by assuming that the viscosity coefficients are zero. The second boundary term is due to the integration by parts of the hyperbolic terms (inviscid flux) and is recalled in Eq. (5.38), when considering a 2-D computational domain  $\Omega$  of boundaries  $\Gamma$  for generality:

$$\mathbf{F}(\mathbf{U}(\mathbf{r}, t)) \cdot \mathbf{n} = \begin{bmatrix} \rho \mathbf{u} \cdot \mathbf{n} \\ \rho u \mathbf{u} \cdot \mathbf{n} + P n_x \\ \rho v \mathbf{u} \cdot \mathbf{n} + P n_y \\ \mathbf{u} \cdot \mathbf{n} (\rho E + P) \end{bmatrix} \quad (5.38)$$

where  $\mathbf{u} = (u, v)$  and  $\mathbf{n} = (n_x, n_y)$ . As mentioned earlier, the mathematical properties of the multi-D Euler equations with variable area are studied in order to under-

stand how the physical information travels inside the computational domain and at the boundaries. Similarity to the multi-D Burger's equation described in Section 2 and Section 4, the eigenvalues can be derived [65] and are recalled,

$$\left\{ \begin{array}{l} \lambda_1 = \mathbf{u} \cdot \mathbf{n} - c \\ \lambda_{2,3} = \mathbf{u} \cdot \mathbf{n} \\ \lambda_4 = \mathbf{u} \cdot \mathbf{n} + c \end{array} \right. , \quad (5.39)$$

with the corresponding characteristic equations,

$$\partial_t \omega_i + \lambda_i \mathbf{n} \cdot \nabla \omega_i = 0 \text{ where } \left\{ \begin{array}{l} \partial \omega_1 = -\partial(\mathbf{u} \cdot \mathbf{n}) + \frac{\partial P}{\rho c} \\ \partial \omega_2 = \partial \rho - \frac{\partial P}{c^2} \\ \partial \omega_3 = -\partial(\mathbf{u} \cdot \boldsymbol{\tau}) \\ \partial \omega_4 = \partial(\mathbf{u} \cdot \mathbf{n}) + \frac{\partial P}{\rho c} \end{array} \right. \quad (5.40)$$

where  $\boldsymbol{\omega} = (\omega_1, \omega_2, \omega_3, \omega_4)$  are the characteristic variables and  $\boldsymbol{\tau} = (\tau_x, \tau_y) = (-\eta_y, \eta_x)$  is the tangential vector to the boundary. From a theoretical point of view, the eigenvalues are derived by assuming the existence of an unit vector that is taken, here, equal to the outwards normal vector to the boundary since this is a direction of interest. Each of the characteristic equations given in Eq. (5.40) corresponds to the propagation of a particular wave. The characteristic equations for  $i = 1, 4$  are associated with the propagation of acoustic waves or pressure variations through the domain. The entropy wave is described by the second characteristic equation ( $i = 2$ ). The remaining characteristic equation,  $i = 3$ , corresponds to the change in the tangential velocity and represents the propagation of the vorticity waves. It is common to recast the characteristic equations in the form  $\frac{D\omega_i}{Dt} = 0$  along  $\frac{d\mathbf{r}}{dt} \cdot \mathbf{n} = \lambda_i$ , which is analogous to what was done for the hyperbolic scalar equations in Section 2. Based

on the study of the sign of the eigenvalues at the boundary relative to its outward normal, we determine which quantity enters or exits the computational domain. We consider the entropy wave in order to illustrate the methodology. We first assume that the eigenvalue,  $\lambda_2$ , associated with the entropy characteristic variable  $\omega_2$ , is negative. Thus, the entropy wave carrying  $\omega_2$  travels from the boundary into the domain and its value must be specified. On the other hand, if  $\lambda_2$  is positive, the wave travels in the opposite direction and the variable  $\omega_2$  is solved numerically by using the associated characteristic equation. For this simple example, we generalize the process and use the following rule: *the characteristic equations with negative eigenvalues (when assuming an outward normal vector to the boundary) are computed from the boundary conditions that are provided to the code, whereas characteristic equations with positive eigenvalues are numerically solved in order to get a value for the corresponding characteristic variable.* The boundary conditions denote, here, the set of values that are specified for a given boundary and the number of values required is determined by the sign of the eigenvalues. Furthermore, for a given flow, the sign of the eigenvalues associated with the pressure waves can change depending on how the flow speed compares with the speed of sound, which is measured by the Mach number, but also depends upon whether the flow is entering or exiting the domain. In other words, a distinction needs to be made between subsonic boundary, supersonic boundary, flow inlet and flow outlet. Thus, in the remaining of this section, we will look at three different boundary types: subsonic and supersonic flow inlet, subsonic and supersonic flow outlet and free-slip wall boundary, that are illustrated in Fig. 5.1, Fig. 5.2 and Fig. 5.3, respectively.

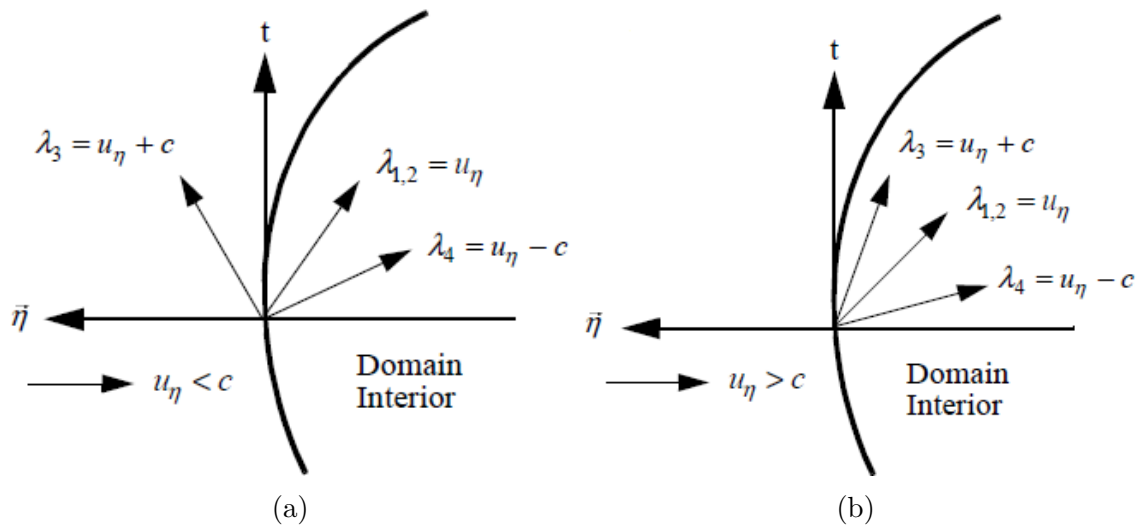


Figure 5.1: Subsonic (left) and supersonic (right) flow inlets with  $u_\eta = \mathbf{u} \cdot \boldsymbol{\eta}$  [46]

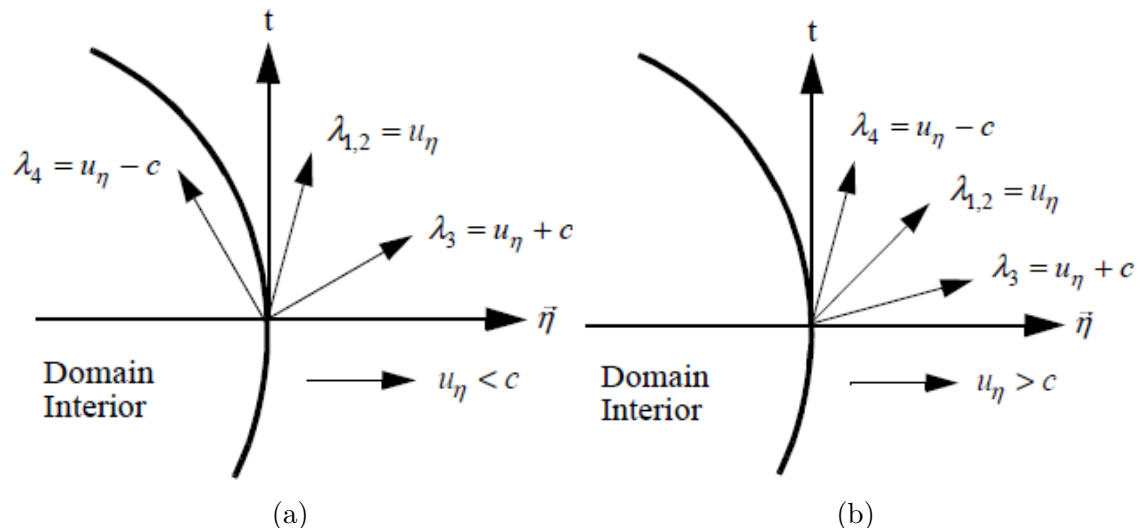


Figure 5.2: Subsonic (left) and supersonic (right) flow outlets with  $u_\eta = \mathbf{u} \cdot \boldsymbol{\eta}$  [46]

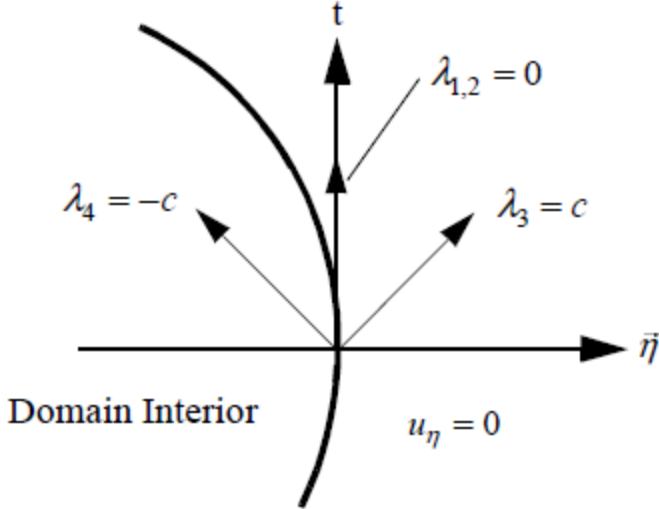


Figure 5.3: Free-slip wall boundary. with  $u_\eta = \mathbf{u} \cdot \boldsymbol{\eta}$  [46]

As mentioned earlier, discretization of the characteristic equations depends on the numerical scheme used and has to be consistent with the rest of the computational domain in order to maintain accuracy of the method. Moreover, a distinction must be made between explicit and implicit temporal integrators. Because an implicit solver has been chosen to update the solution at each time step, a few words about the method to follow with an explicit temporal integrator are given for completeness.

When using an explicit temporal integrator, the new time values are computed from the old time ones. The flux at the boundary, Eq. (5.38), is computed from the characteristic variables  $\boldsymbol{\omega}$  that are obtained from the boundary conditions and the discretization of some of the characteristic equations. For example, when considering a 2-D subsonic flow inlet boundary (Fig. 5.1a), three boundary values have to be specified since three waves enter the domain. To have a well-posed system, a fourth value is computed by using the characteristic equation corresponding to the wave exiting the domain ( $\lambda_4$ ). The characteristic equation is discretized over the first

interior cell and the boundary of the computational domain which can require a ghost cell. From this point, the details of the method depends on the scheme used. The reader can refer to [46] or [55] for examples with finite element and finite volume, respectively.

Implementation of the boundary conditions with an implicit temporal integrator is now detailed.

### 5.5.1 Flow inlet boundary conditions

Flow inlet boundary can be split into two categories: subsonic and supersonic.

#### 5.5.1.1 Subsonic flow inlet boundary condition

In the case of subsonic flow inlet, three waves enter the domain and only one exits it, as shown in Fig. 5.1a. In order to ensure a well-posed system at the boundary, three boundary values need to be supplied to the code, since three waves enter the domain. The fourth value is usually computed from the characteristic equation associated with the wave exiting the domain at the boundary, and the three boundary values. In the case of an implicit temporal integrator, the solver iterates over the solution until convergence is reached. Thus, it is proposed to take advantage of the solver in order to compute the boundary values as follows. We assume that a set three boundary values are known at the inlet  $(U_1^{bc}, U_2^{bc}, U_3^{bc})$ . The fourth value,  $U_4$  is chosen so that the set of four values can be used to retrieve any other variables, e.g. the fluxes, which ensures the system to be well-posed. At a given time and for a given iteration  $\ell$ , the solver iterates over the entire solution vector and  $U_4^k$  is updated whereas the three other values do not vary since they are given. The set of four values is used to compute the flux at the boundary given in Eq. (5.38) which will be also updated at every iteration. Because of the iterative process, information from inside the computational domain is transmitted to the boundary until the solution reaches

convergence: the solver substitutes itself for the characteristic equation associated to the wave exiting the domain. Using this method, various boundary conditions are implemented and detailed in Table 5.1:

Table 5.1: Subsonic flow inlet boundary conditions.

boundary type	$U_1^{bc}$	$U_2^{bc}$	$U_3^{bc}$	$U_4^\ell$
static pressure	$P$	$T$	$\theta$	$u$
mass flow rate	$\rho \ \mathbf{u}\ $	$h$	$\theta$	$u$
stagnation pressure	$P_0$	$T_0$	$\theta$	$u$

where the vector velocity is of the form  $\mathbf{u} = (u, v)$ ,  $\theta$  is defined as the angle between the outward normal to the boundary and the velocity vector ( $\mathbf{u} \cdot \mathbf{n} = \|\mathbf{u}\| \cos \theta$ ) and  $h = E + P/\rho$  is the fluid enthalpy. The stagnation pressure  $P_0$  and temperature  $T_0$  are function of the Mach number  $M$  and the static pressure  $P$  and temperature  $T$ . An analytical expression can be derived from the equation of state. For example, when considering the SGEOS, the stagnation variables are given for isentropic flows in Eq. (5.41) [55]:

$$P_0 + P_\infty = (P + P_\infty) \left( 1 + \frac{\gamma - 1}{2} M^2 \right) \quad (5.41)$$

$$T_0 = T \left( 1 + \frac{\gamma - 1}{2} M^2 \right)^{\frac{\gamma - 1}{\gamma}} \quad (5.42)$$

### 5.5.1.2 Supersonic flow inlet boundary condition

For a supersonic flow inlet boundary, the implementation is very straightforward since all the waves enter the computational domain. Thus, in 2-D, four boundary values  $(U_1^{bc}, U_2^{bc}, U_3^{bc}, U_4^{bc})$  need to be supplied for the system to be well-posed. Using these four values and the equation of state, the flux at the boundary, given in Eq. (5.38), can be computed and used to weakly impose the boundary conditions. An alternative idea consists of using Dirichlet method to strongly impose the boundary values: assuming that a set of four boundary values is supplied, the values of the conservative variables of the Euler equations at the boundary are computed and strongly imposed.

## 5.5.2 Flow outlet boundary conditions

Once again, implementation of subsonic and supersonic boundary conditions is investigated.

### 5.5.2.1 Subsonic flow outlet boundary condition

In the case of a subsonic outlet boundary, three waves exit the domain and one wave enters it, as shown in Fig. 5.2a. This is the opposite situation as the subsonic inlet boundary described in Section 5.5.1.1. Thus, following the same reasoning as before, only one boundary value needs to be supplied to the code that we denote by  $U_4^{bc}$ , whereas the other boundary values are given by the solver:  $(U_1^\ell, U_2^\ell, U_3^\ell)$ . The most common subsonic outlet boundary condition is the static pressure boundary. It consists of supplying the code with a background static pressure  $P_b$ . Details of the implementation relative to the implicit scheme are given in Table 5.2.

Table 5.2: Subsonic flow outlet boundary conditions.

boundary type	$U_1^\ell$	$U_2^\ell$	$U_3^\ell$	$U_4^{bc}$
background pressure	$\rho$	$u$	$v$	$P_b$

### 5.5.2.2 Supersonic flow outlet boundary condition

At a supersonic flow outlet boundary (Fig. 5.2b), all of the waves exit the computational domain. Thus, the code does not need to be provided with any boundary value. The flux is computed with the values given from the solver at the latest iteration for each time step and updated until convergence is reached.

### 5.5.3 Free-slip wall boundary conditions

The free-slip wall boundary condition consists of an impenetrable wall with no boundary layer since the fluid is assumed inviscid. The boundary condition used in the case of free-slip wall is  $\mathbf{u} \cdot \mathbf{n} = 0$ . Thus, at the wall, the eigenvalues  $\lambda_2$  and  $\lambda_3$  are zero, whereas the eigenvalues associated with the acoustic waves are equal to  $\pm c$  as shown in Fig. 5.3. The flux at the boundary can be simplified using the physical boundary condition  $\mathbf{u} \cdot \mathbf{n} = 0$  and expressed only as a function of the pressure as follows:

$$\mathbf{F}(\mathbf{U}(\mathbf{r}, t)) \cdot \mathbf{n} = \begin{bmatrix} 0 \\ Pn_x \\ Pn_y \\ 0 \end{bmatrix}. \quad (5.43)$$

Computing the pressure can be achieved by integrating the characteristic equations associated to the acoustic waves ( $i = 1, 4$ ) over the first cell in. Alternatively, we

take advantage of the non-linear solver and update the pressure and then the flux at each iteration. Then, the flux at a free-slip boundary condition is simply:

$$\mathbf{F}(\mathbf{U}(\mathbf{r}, t)^\ell) \cdot \mathbf{n} = \begin{bmatrix} 0 \\ P^\ell n_x \\ P^\ell n_y \\ 0 \end{bmatrix}. \quad (5.44)$$

## 5.6 Numerical results

1-D and 2-D numerical solutions for the Euler equations with viscous regularization using the entropy viscosity method are presented here. Our results validate the chosen definitions for the viscosity coefficients in the low-Mach limit and verify that the new definitions resolve shocks appropriately.

The first set of 1-D simulations consists of liquid water and steam flowing in a converging-diverging nozzle. This test is of interest for multiple reasons: (a) a steady state can be reached (some stabilization methods are known to have difficulties reaching a steady state, [13, 14]), (b) an analytical solution is available and a space-time convergence study can be performed, (c) it can be performed for liquid and gas phases, wherein the gas phase simulation presents a shock while the liquid-phase simulation has a significantly lower Mach number. Next, a 1-D shock tube test (in a straight pipe), taken from the Leblanc test-case suite [45], is performed. This test is known to be more challenging than Sod shock tubes and the fluid's Mach number varies spatially between 0 and 5. A convergence study is also performed to demonstrate convergence of the numerical solution to the exact solution. A slow moving shock is also investigated [52]. This test helps in assessing the ability of the method to damp the post-shock low frequency noise (oscillations). Then, a strong

shock for a liquid phase is also investigated[2]. Finally, numerical tests with source terms are performed in order to test our approach detailed in Section 5.4.

The initial conditions (density in  $kg.m^{-3}$ , velocity in  $m.s^{-1}$ , pressure in  $Pa$ ) for the afore mentioned 1-D shock tubes are given in Table 5.3.

Table 5.3: Initial conditions for the 1-D shock tube tests.

$\rho_{\text{left}}$	$u_{\text{left}}$	$P_{\text{left}}$	$\rho_{\text{right}}$	$u_{\text{right}}$	$P_{\text{right}}$
Leblanc shock tube (Section 5.6.3)					
1	0	$4 \cdot 10^{-2}$	$10^{-3}$	0	$4 \cdot 10^{-11}$
Strong shock for liquid phase (Section 5.6.4)					
1000	0	$10^9$	1000	0	$10^5$
Slow moving shock (Section 5.6.5)					
1	-0.81	1	3.86	-3.44	10.33

2-D simulations are presented next. First, results for 2-D supersonic flows are presented including flow over a forward facing step [64], a circular explosion [65], Liska and Wendroff's Riemann problem number 12 [42], flow in a compression corner [5] and over a  $5^\circ$  double wedge [46].

Then, 2-D subsonic flows around a cylinder [34] and over a Gaussian hump [18] are presented for various far-field Mach numbers (as low of  $10^{-7}$ ). Convergence studies are performed when analytical solutions are available.

For each simulation, data relative to the boundary conditions, the Courant-Friedrichs-Lowy number ( $CFL$ ), mesh and equation of state are provided. All of

the numerical solutions presented are obtained using BDF2 as temporal integrator and linear (1-D mesh),  $\mathbb{P}_1$  (2-D triangular mesh) or  $\mathbb{Q}_1$  (2-D quadrangular mesh) finite elements. The spatial integrals are numerically computed using a second-order Gauss quadrature rule. The steady-state solution is detected from the transient by monitoring the norm of the total residual (including all of the equations) and noting when the norm of the total residual falls below  $10^{-6}$ . The ideal gas [50] or stiffened gas equations of state [38] are used; a generic expression is given in Eq. (5.45).

$$P = (\gamma - 1)\rho(e - q) - \gamma P_\infty \quad (5.45)$$

where the parameters  $\gamma$ ,  $q$ , and  $P_\infty$  are fluid-dependent and are given in Table 5.4. The ideal gas equation of state is recovered by setting  $q = P_\infty = 0$  in Eq. (5.45).

Table 5.4: Stiffened Gas Equation of State (SGEOS) parameters for steam and liquid water.

fluid	$\gamma$	$C_v$ ( $J.kg^{-1}.K^{-1}$ )	$P_\infty$ (Pa)	$q$ ( $J.kg^{-1}$ )
liquid water (Section 5.6.1)	2.35	1816	$10^9$	$-1167 \cdot 10^3$
steam (Section 5.6.2)	1.43	1040	0	$2030 \cdot 10^3$
liquid water (Section 5.6.4)	4.4	1000	$6 \cdot 10^8$	0

The entropy function for the stiffened gas equation of state is convex and given by

$$s = C_v \ln \left( \frac{P + P_\infty}{\rho^{\gamma-1}} \right),$$

where  $C_v$  is the heat capacity at constant volume.

Finally, the convergence rates are computed using the following relation

$$\text{rate}_h = \ln \left( \frac{\|U_{2h} - U_{\text{exact}}\|}{\|U_h - U_{\text{exact}}\|} \right) / \ln 2 \quad (5.46)$$

where  $\|\cdot\|$  denotes either the  $L_1$  or  $L_2$  norms and  $h$  is the characteristic grid size.

### 5.6.1 Liquid water in a 1-D converging-diverging nozzle

This simulation uses the Euler equations to solve liquid water flowing through a 1-D converging-diverging nozzle of length  $L = 1m$  and  $A(x) = 1 + 0.5 \cos(2\pi x/L)$ . At the inlet, the stagnation pressure and temperature are set to  $P_0 = 1MPa$  and  $T_0 = 453K$ , respectively. At the outlet, only the static pressure is specified:  $P_s = 0.5MPa$ . Initially, the liquid is at rest, the temperature is uniform and equal to the stagnation temperature and the pressure linearly decreases from the stagnation pressure inlet value to the static pressure outlet value. The stiffened gas equation of state is used to model the liquid water with the parameters provided in Table 5.4. Because of the low pressure difference between the inlet and the outlet, the smooth initial conditions, and the large value of  $P_\infty$ , the flow remains subsonic and thus displays no shock. A detailed derivation of the exact steady-state solution can be found in [37]. A uniform mesh of 50 cells was used to obtain the numerical solution and the time step size was computed using a  $CFL$  number of 750. Plots of the Mach number, density, and pressure are given at steady-state in Fig. 5.4 for the numerical and exact solutions. The viscosity coefficients are also graphed in Fig. 5.4d.

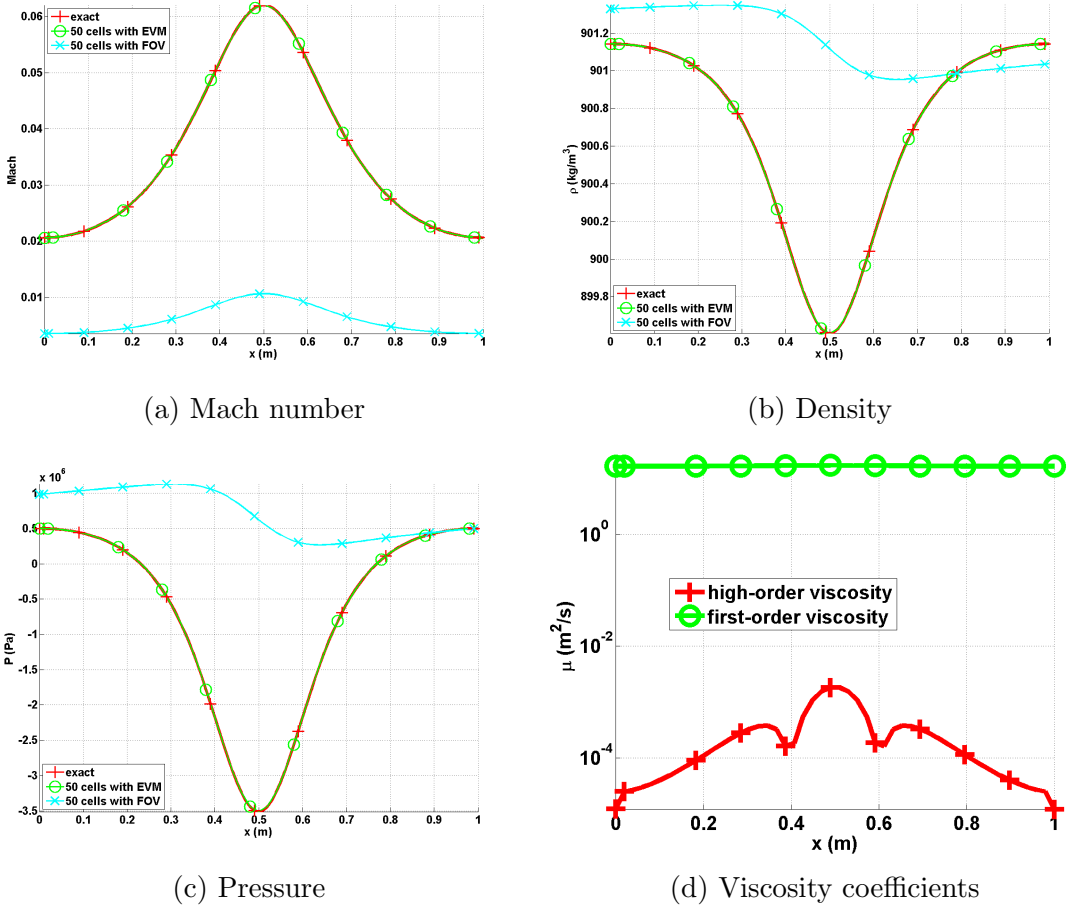


Figure 5.4: Steady-state solution for a liquid flowing through a 1-D converging-diverging nozzle.

In Fig. 5.4, the numerical solutions obtained using the first-order viscosity (FOV) and the entropy viscosity method (EVM) are plotted against the exact solution. The numerical solution obtained with the EVM and the exact solution overlap, even for a fairly coarse mesh (50 cells). On the other hand, the numerical solution obtained with the FOV does not give the correct steady state: this is an illustration of the effect of ill-scaled dissipative terms. Note that the entropy viscosity coefficient is very small compared to the first-order one (Fig. 5.4d): (i) the numerical solution is smooth

as shown in Fig. 5.4, and (ii) the flow is in a low-Mach regime and thus isentropic. A convergence study was performed using the exact solution as a reference: the  $L_1$  and  $L_2$  norms of the error and the corresponding convergence rates are computed at steady state on various uniform mesh from 4 to 256 cells. Spatial convergence results using linear finite elements are reported in these two norms in Table 5.5 and Table 5.6 for the primitive variables: density, velocity and pressure.

Table 5.5:  $L_1$  norm of the error for the liquid phase in a 1-D converging-diverging nozzle at steady state.

cells	density	rate	pressure	rate	velocity	rate
4	$2.8037 \cdot 10^{-1}$	—	$8.4705 \cdot 10^5$	—	7.2737	—
8	$1.3343 \cdot 10^{-1}$	1.07	$4.7893 \cdot 10^5$	0.82	6.1493	0.24
16	$2.9373 \cdot 10^{-2}$	2.18	$1.0613 \cdot 10^5$	2.17	1.2275	2.32
32	$5.1120 \cdot 10^{-3}$	2.52	$1.8446 \cdot 10^4$	2.52	$1.8943 \cdot 10^{-1}$	2.69
64	$1.0558 \cdot 10^{-3}$	2.28	$3.7938 \cdot 10^3$	2.28	$3.7919 \cdot 10^{-2}$	2.32
128	$2.3712 \cdot 10^{-4}$	2.15	$8.4471 \cdot 10^2$	2.17	$8.5517 \cdot 10^{-3}$	2.15
256	$5.6058 \cdot 10^{-5}$	2.08	$1.9839 \cdot 10^2$	2.09	$2.0475 \cdot 10^{-3}$	2.06
512	$1.3278 \cdot 10^{-5}$	2.08	$4.6622 \cdot 10^1$	2.09	$4.9516 \cdot 10^{-4}$	2.04
1024	$3.1193 \cdot 10^{-6}$	2.08	$1.1755 \cdot 10^1$	1.99	$1.2379 \cdot 10^{-4}$	2.00

Table 5.6:  $L_2$  norm of the error for the liquid phase in a 1-D converging-diverging nozzle at steady state.

cells	density	rate	pressure	rate	velocity	rate
4	$3.106397 \cdot 10^{-1}$	—	$5.254445 \cdot 10^5$	—	3.288543	—
8	$7.491623 \cdot 10^{-2}$	2.05	$1.636966 \cdot 10^5$	1.68	1.823880	0.85
16	$2.079858 \cdot 10^{-2}$	1.85	$4.627338 \cdot 10^4$	1.49	$4.990605 \cdot 10^{-1}$	0.87
32	$5.329627 \cdot 10^{-3}$	1.96	$1.180287 \cdot 10^4$	1.97	$1.261018 \cdot 10^{-1}$	1.98
64	$1.341583 \cdot 10^{-3}$	1.99	$2.967104 \cdot 10^3$	1.99	$3.160914 \cdot 10^{-2}$	1.99
128	$3.359766 \cdot 10^{-4}$	1.99	$7.428087 \cdot 10^2$	1.99	$7.907499 \cdot 10^{-3}$	1.99
256	$8.403859 \cdot 10^{-5}$	1.99	$1.857861 \cdot 10^2$	1.99	$1.977292 \cdot 10^{-3}$	1.99
512	$2.10075 \cdot 10^{-5}$	2.00	$4.7024 \cdot 10^1$	1.98	$4.9516 \cdot 10^{-4}$	1.99

It is observed that the convergence rate for the  $L_1$  and  $L_2$  norm of the error is 2; the entropy viscosity method preserves the high-order accuracy when the numerical solution is smooth, and the new definition of the entropy viscosity coefficient behaves appropriately in the low-Mach limit.

### 5.6.2 Steam in a 1-D converging-diverging nozzle

We use the same nozzle geometry, initial conditions and boundary conditions as in the previously example but replace liquid water with steam and use the steam parameters of the stiffened gas equation of state, Table 5.4. In this example, compressible effects will become dominant. The pressure difference between the inlet and outlet is large enough to accelerate the steam through the nozzle, leading to the formation of a shock in the diverging portion of the nozzle. The behavior is different from that observed for the liquid water phase in Section 5.6.1 because of the liquid to

gas density ratio is about 1,000. An exact solution at steady state is available for the gas phase [37]. The aim of this section is to show that when using the new definitions of the viscosity coefficients (Eq. (5.30)), the shock can be correctly resolved without spurious oscillations. The steady-state numerical solution, obtained using a uniform mesh with 1600 cells, is shown in Fig. 5.5. The *CFL* was set to 80 (a high *CFL* value can be used because the shock is stationary).

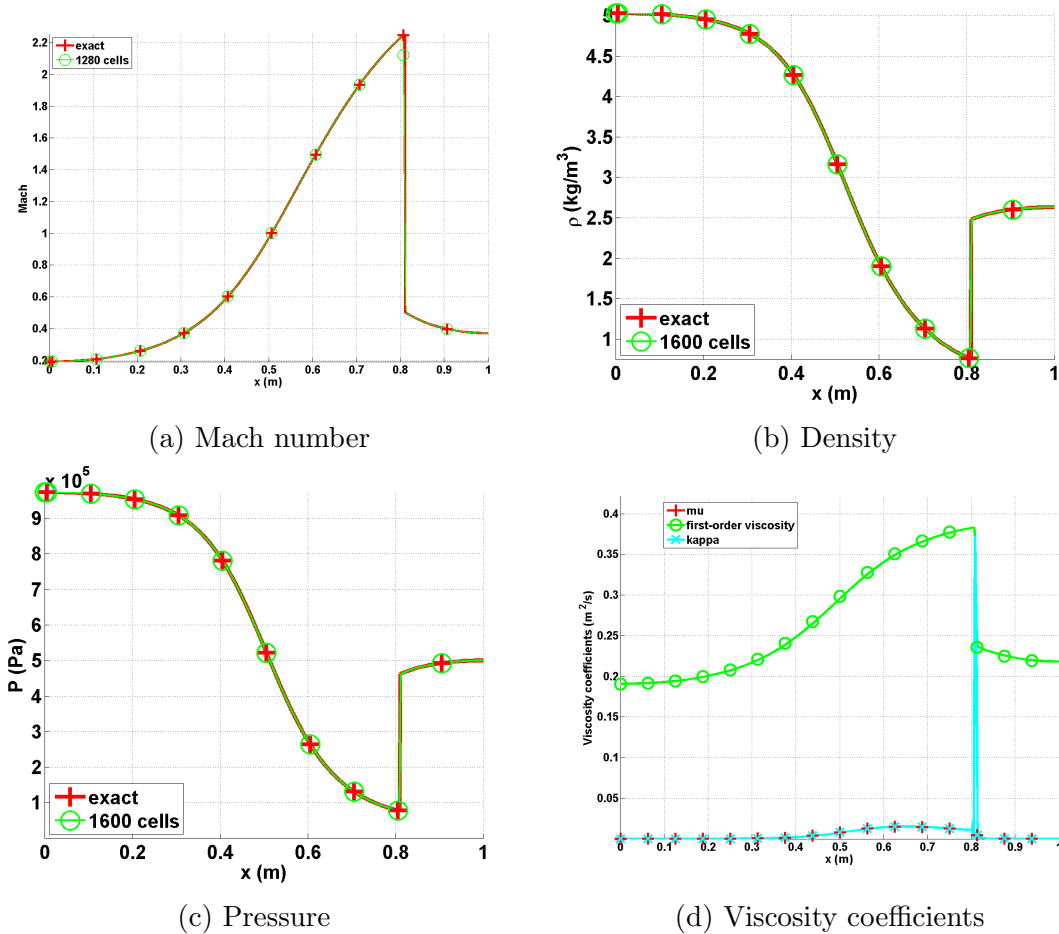


Figure 5.5: Steady-state solution for vapor phase flowing in a 1-D converging-diverging nozzle.

The steady-state solution of the density, Mach number and pressure are given in Fig. 5.5. The steady-solution exhibits a shock around  $x = 0.8m$  and matches the exact solution. In Fig. 5.5d, the first-order and entropy viscosity coefficients are plotted at steady-state (on a log scale): the entropy viscosity coefficient is peaked in the shock region around  $x = 0.8m$  as expected where it saturates to the first-order viscosity coefficient. The graph also presents another peak at  $x = 0.5m$  corresponding to the position of the sonic point for a 1-D converging-diverging nozzle. This particular point is known to exhibit small instabilities that are detected when computing the jumps of the pressure and density gradients. Everywhere else, the entropy viscosity coefficient is small. In order to prove convergence of the numerical solution to the exact solution, a convergence study is performed. Because of the presence of a shock, second-order accuracy is not expected and the convergence rate of a numerical solution should be 1 and  $1/2$  when measured in the  $L_1$  and  $L_2$  norms, respectively (see Theorem 9.3 in [19]). Results are reported in Table 5.7 and Table 5.8 for the primitive variables: density, velocity and pressure. The convergence rates for the  $L_1$  and  $L_2$  norms of the error computed using Eq. (5.46) are in good agreement with the theoretical values.

Table 5.7:  $L_1$  norm of the error for the vapor phase in a 1-D converging-diverging nozzle at steady state.

cells	density	rate	pressure	rate	velocity	rate
5	$0.72562 \cdot 10^{-1}$	—	$1.5657 \cdot 10^5$	—	173.69	—
10	$0.4165 \cdot 10^{-1}$	0.80	$9.6741 \cdot 10^4$	0.63	120.69	0.53
20	$0.20675 \cdot 10^{-1}$	1.01	$4.9193 \cdot 10^4$	0.97	72.149	0.74
40	$0.093703 \cdot 10^{-1}$	1.14	$2.0103 \cdot 10^4$	0.73	34.716	1.06
80	$0.047328 \cdot 10^{-1}$	0.99	$1.0208 \cdot 10^4$	0.98	16.082	1.11
160	$0.023965 \cdot 10^{-2}$	0.98	$5.1969 \cdot 10^3$	0.97	7.9573	1.02
320	$0.020768 \cdot 10^{-2}$	1.03	$2.5116 \cdot 10^3$	1.05	3.7812	1.07
640	$0.0059715 \cdot 10^{-2}$	0.98	$1.2754 \cdot 10^3$	0.98	1.8353	1.04

Table 5.8:  $L_2$  norm of the error for the vapor phase in a 1-D converging-diverging nozzle at steady state.

cells	density	rate	pressure	rate	velocity	rate
5	$9.7144 \cdot 10^{-1}$	—	$2.0215 \cdot 10^5$	—	236.94	—
10	$5.9718 \cdot 10^{-1}$	0.70	$1.3024 \cdot 10^5$	0.63	166.56	0.51
20	$2.9503 \cdot 10^{-1}$	1.02	$6.6503 \cdot 10^4$	0.97	103.36	0.69
40	$1.8193 \cdot 10^{-1}$	0.69	$4.0171 \cdot 10^4$	0.73	66.374	0.64
80	$1.3366 \cdot 10^{-1}$	0.44	$2.3163 \cdot 10^4$	0.44	42.981	0.63
160	$9.6638 \cdot 10^{-2}$	0.47	$1.7263 \cdot 10^4$	0.42	31.717	0.44
320	$7.0896 \cdot 10^{-2}$	0.45	$1.2763 \cdot 10^4$	0.44	23.138	0.45
640	$5.2191 \cdot 10^{-2}$	0.44	$9.4217 \cdot 10^3$	0.44	16.910	0.45

### 5.6.3 Leblanc shock tube

The 1-D Leblanc shock tube is a Riemann problem designed to test the robustness and the accuracy of stabilization methods. The initial conditions are given in Table 5.3. The ideal gas equation of state (with  $\gamma = 5/3$ ) is used to compute the pressure. This test is computationally challenging because of the large pressure ratio at the initial interface. The computational domain consists of a 1-D straight pipe of length  $L = 9m$  with the initial interface located at  $x = 2m$ . At  $t = 0.s$ , the interface is removed. The numerical solution is run until  $t = 4s$  and the density, momentum and total energy profiles are given in Fig. 5.6, along with the exact solution. The viscosity coefficients are also plotted in Fig. 5.6d. These plots were run with three different uniform meshes of 800, 3200 and 6000 cells and a constant  $CFL = 1$ .

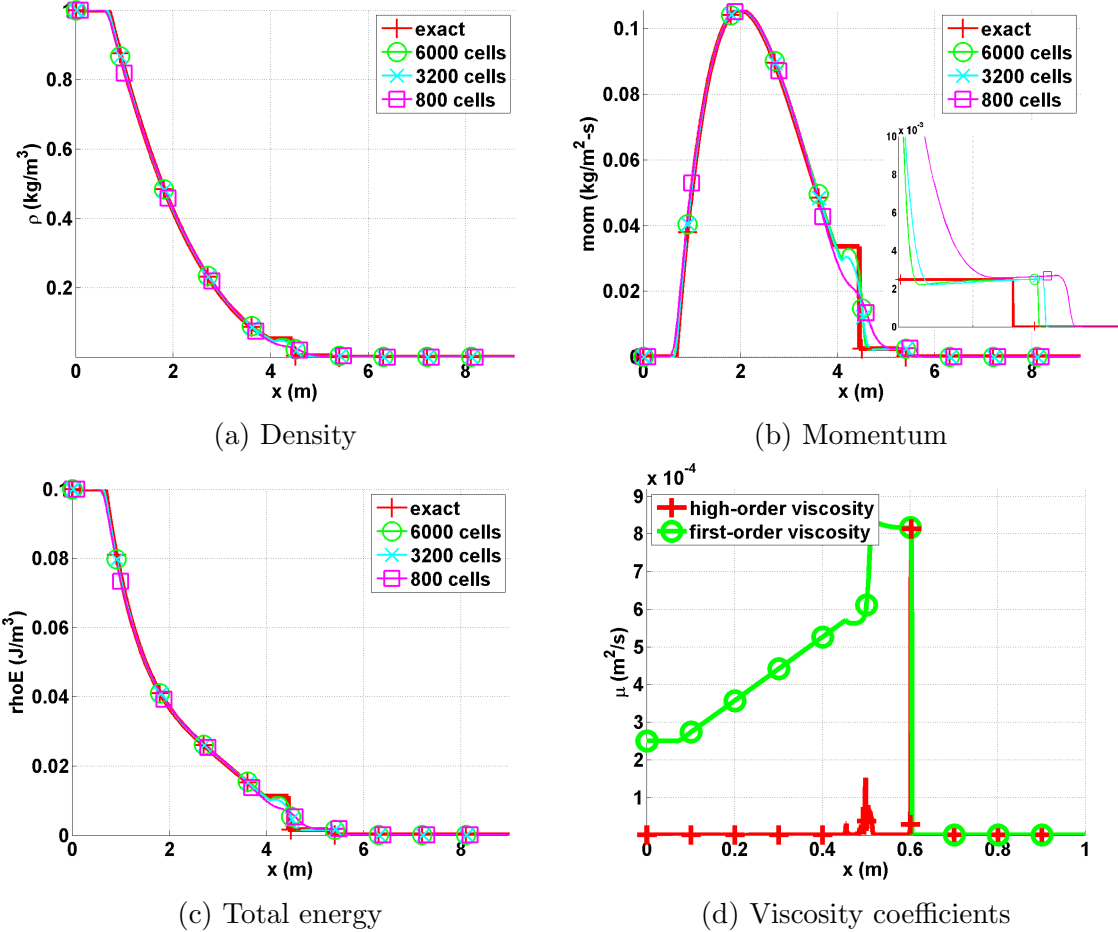


Figure 5.6: Exact and numerical solutions for the 1-D Leblanc shock tube at  $t = 4$  s

The density, momentum and total energy profiles are provided in Fig. 5.6. In Fig. 5.6b, the shock region is zoomed in for better resolution: the shock is well resolved. We also observe that the shock position computed numerically converges to the exact position under mesh refinement. The contact wave at  $x = 4.5m$  can be seen in Fig. 5.6b. The entropy viscosity coefficient profile is shown in Fig. 5.6d and behaves as expected: it saturates to the first-order viscosity in the shock region, thus preventing oscillations from forming. At the location of the contact wave, a smaller peak is observed that is due to the presence of the jumps in the definition of

the entropy viscosity coefficient (Eq. (5.30)). The Mach number, not plotted, is of the order of 1.3 just before the shock and reaches a maximum value close to 5 in the contact region.

Once again, a convergence study is performed in order to prove convergence of the numerical solution to the exact solution. As in the previous example (vapor phase in the 1-D nozzle, Section 5.6.2), the expected convergence rates in the  $L_1$  and  $L_2$  norms are 1 and  $1/2$ , respectively. The exact solution was obtained by running a 1-D Riemann solver and used as the reference solution to compute the  $L_1$  and  $L_2$ -norms that are reported in Table 5.9 and Table 5.10 for the conservative variables: density, momentum and total energy. The convergence rates are again approaching the theoretical values.

Table 5.9:  $L_1$  norm of the error for the 1-D Leblanc test at  $t = 4$  s.

cells	density	rate	momentum	rate
100	$1.0354722 \cdot 10^{-2}$	—	$3.5471714 \cdot 10^{-3}$	—
200	$7.2680512 \cdot 10^{-3}$	0.51064841	$2.5933119 \cdot 10^{-3}$	0.45187331
400	$5.0825628 \cdot 10^{-3}$	0.51601245	$2.0668092 \cdot 10^{-3}$	0.32739054
800	$3.4025056 \cdot 10^{-3}$	0.57895861	$1.4793838 \cdot 10^{-3}$	0.48240884
1600	$2.1649953 \cdot 10^{-3}$	0.65223363	$9.7152832 \cdot 10^{-4}$	0.6066684
3200	$1.2465433 \cdot 10^{-3}$	0.79643094	$5.5937409 \cdot 10^{-4}$	0.79644263
6400	$6.4476928 \cdot 10^{-4}$	0.95107804	$3.0244198 \cdot 10^{-4}$	0.88715502
12800	$3.3950948 \cdot 10^{-4}$	0.92533116	$1.5958118 \cdot 10^{-4}$	0.9223679

cells	total energy	rate
100	$1.4033046 \cdot 10^{-3}$	—
200	$9.8611746 \cdot 10^{-4}$	0.5089968
400	$7.7844421 \cdot 10^{-4}$	0.34116585
800	$5.5702549 \cdot 10^{-4}$	0.48285029
1600	$3.5720171 \cdot 10^{-4}$	0.64100438
3200	$2.0491799 \cdot 10^{-4}$	0.80169235
6400	$1.0914891 \cdot 10^{-4}$	0.90874889
12800	$5.7909794 \cdot 10^{-5}$	0.91441847

Table 5.10:  $L_2$  norm of the error for the 1-D Leblanc test at  $t = 4$  s.

cells	density	rate	momentum	rate
100	$5.7187851 \cdot 10^{-3}$	—	$1.7767236 \cdot 10^{-3}$	—
200	$3.8995238 \cdot 10^{-3}$	0.55241073	$1.4913161 \cdot 10^{-3}$	0.25263314
400	$2.8103526 \cdot 10^{-3}$	0.4725468	$1.3305301 \cdot 10^{-3}$	0.164585
800	$2.1081933 \cdot 10^{-3}$	0.41474398	$1.1398931 \cdot 10^{-3}$	0.22310254
1600	$1.5731052 \cdot 10^{-3}$	0.42239201	$9.0394227 \cdot 10^{-4}$	0.33459602
3200	$1.0610667 \cdot 10^{-3}$	0.56809979	$6.2735595 \cdot 10^{-4}$	0.52694639
6400	$7.3309974 \cdot 10^{-4}$	0.53343397	$4.4545754 \cdot 10^{-4}$	0.49399631
12800	$5.1020991 \cdot 10^{-4}$	0.52291857	$3.1266758 \cdot 10^{-4}$	0.5106583

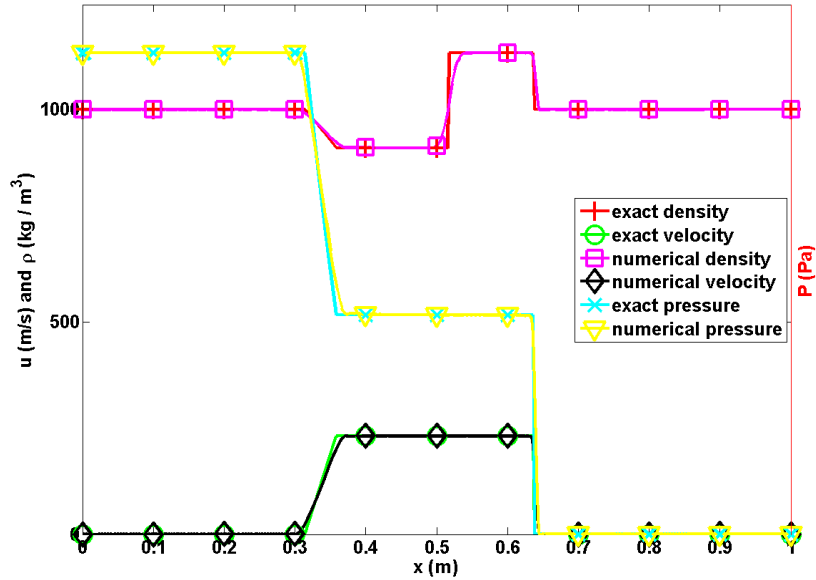
cells	total energy	rate
100	$7.6112265 \cdot 10^{-4}$	—
200	$5.5497308 \cdot 10^{-4}$	0.45571115
400	$4.6063172 \cdot 10^{-4}$	0.26880405
800	$3.7798953 \cdot 10^{-4}$	0.28526749
1600	$2.9584646 \cdot 10^{-4}$	0.35349763
3200	$2.054455 \cdot 10^{-4}$	0.52609289
6400	$1.4670834 \cdot 10^{-4}$	0.48580482
12800	$1.0299897 \cdot 10^{-5}$	0.51032105

#### 5.6.4 1-D shock tube with a liquid phase

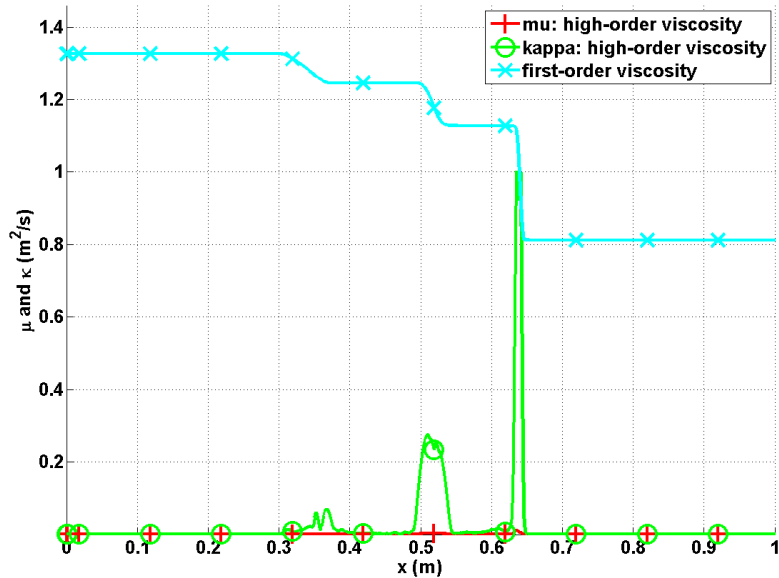
The purpose of this test is to investigate the ability of the entropy viscosity method to stabilize a strong shock with a small Mach number [2] (this reference is

for a two-phase flow model but we are only interested in the initial conditions for the liquid phase): the Mach number in the shock region is of the order of 0.1. In this case, as explained in Section 5.2.2, the viscosity coefficients are required to have different order of magnitude in order to ensure the correct scaling of the dissipative terms. The purpose of this test is to validate the approach presented in Section 5.2.2.

The stiffened gas equation of state is used to model a liquid flow with the parameters given in Table 5.4. The computational domain of length  $L = 1m$  is uniformly discretized using 500 cells. The step initial conditions are given in Table 5.3. The simulation is run with a  $CFL = 1$  until the final time  $t_{\text{final}} = 7 \cdot 10^{-5}s$ . Results for pressure, density, velocity and the viscosity coefficients are given in Fig. 5.7 along with the exact solution for comparison purposes. The numerical solution is in good agreement with exact solution in Fig. 5.7a. The viscosity coefficients  $\mu$  and  $\kappa$  are not equal in the shock because the Mach number is of order 0.1. The viscosity coefficient  $\kappa$  saturates to the first-order viscosity in the shock region around  $x = 0.65m$  and is sufficient to stabilize the numerical scheme.



(a) Density, velocity and pressure profiles.

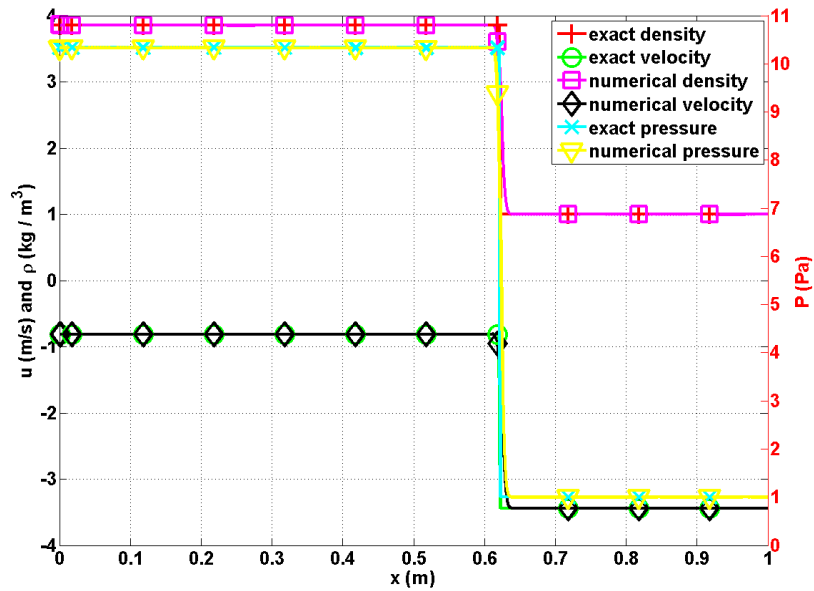


(b) Viscosity coefficients profile.

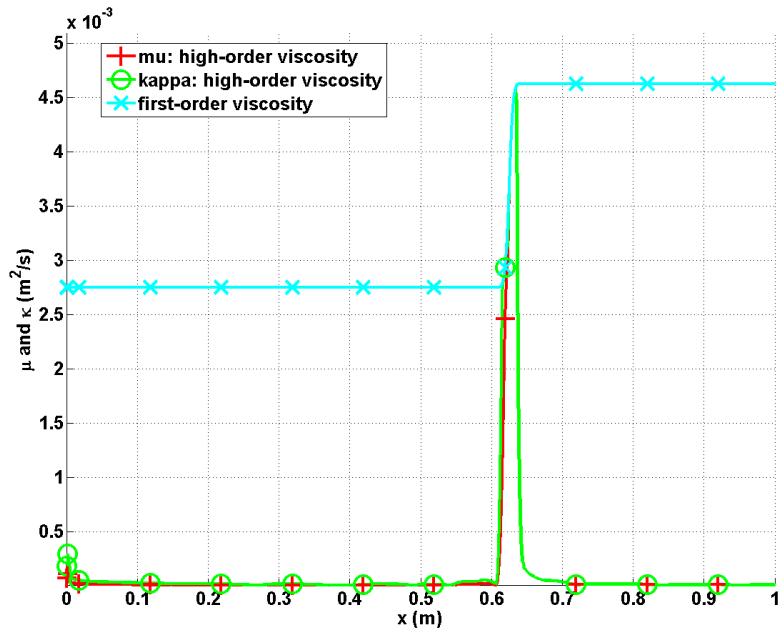
Figure 5.7: Numerical solution for the 1-D liquid shock tube at  $t_{\text{final}} = 7 \times 10^{-5} \text{ s}$ .

### 5.6.5 1-D slow moving shock

Slow moving shocks are known to produce post-shock noise of low frequency that is not damped by some numerical dissipation methods [52]. The aim of this simulation is to test the ability of the entropy viscosity method to dampen the low frequency waves. The 1-D slow moving shock consists of a shock wave moving from left to right with the initial conditions given in Table 5.3. The ideal gas equation of state is used with a heat capacity ratio  $\gamma = 1.4$ . In order to make the shock travel a significant distance, the final time is taken equal to  $t = 1.1s$ . A pressure boundary condition is used at the left boundary to let the rarefaction and contact waves exit the domain. The numerical solution, obtained with 200 equally-spaced cells, is given in Fig. 5.8 and is compared to the exact solution obtained from a Riemann solver. We use a *CFL* of 1. With this *CFL* value, it takes about 50 time steps for the shock to traverse one cell. The numerical results are in good agreement with the exact solution and do not display any post-shock noise. The rarefaction and contact waves are not visible on Fig. 5.8a since they exited the computational domain through the left pressure boundary condition earlier. As explained in [58], Godunov's type method usually fails to resolve a slow moving shock because of the nature of the stabilization method: the method scales as the eigenvalue of the appropriate field. In the case of a slow moving shock, the dissipation added to the system is under-estimated and leads to post-shock noise. In the case of the entropy viscosity method, the entropy residual detects the shock position and the viscosity coefficients saturate to the first-order viscosity values in the shock region. The main difference between a Godunov's type method and the entropy viscosity method lies in the definition of the first-order viscosity coefficients that are proportional to the *local maximum eigenvalue*  $\|\mathbf{u}\| + c$  and not to the eigenvalue of the characteristic field.



(a) Velocity, density and pressure



(b) Viscosity coefficients

Figure 5.8: Slow moving shock profiles at  $t = 1.1\text{ s}$ .

### 5.6.6 1-D numerical results for flows with source terms

This section illustrates the theoretical approach developed in Section 5.4 for solving 1-D flows with source terms using the EVM. All of the results presented in this section were obtained with the RELAP-7 code developed by Idaho National Laboratory [4]. Three source terms are considered: the wall-friction force and the wall heat source that were detailed in Section 5.4, and gravity terms, which yields the following 1-D Euler equations (assuming an upward vertical x-axis):

$$\partial_t (\rho A) + \partial_x (\rho u A) = 0 \quad (5.47a)$$

$$\partial_t (\rho u A) + \partial_x [A (\rho u^2 + P)] = P \partial_x A - \frac{f_c}{D_h} \rho u^2 - \rho g A \quad (5.47b)$$

$$\partial_t (\rho E A) + \partial_x [u A (\rho E + P)] = h_t P_w (T_w - T) - \rho g u A \quad (5.47c)$$

where  $g$  is the gravity acceleration and is equal to  $9.8 \text{ m}^2/\text{s}$ . For each of the tests, the source terms parameters, the boundary conditions and information relative to the geometry, the mesh and the time step will be given. The SGEOS is used for vapor and liquid water with the parameters of Table 5.11:

Table 5.11: Stiffened Gas Equation of State parameters for steam and liquid water used to solve the 1-D Euler equations with source terms.

fluid	$\gamma$	$C_v \text{ (J.kg}^{-1}.\text{K}^{-1}\text{)}$	$P_\infty \text{ (Pa)}$	$q \text{ (J.kg}^{-1}\text{)}$
liquid water (Section 5.6.1)	2.35	1816	$10^9$	$-1167 \text{ } 10^3$
steam (Section 5.6.2)	1.43	1040	0	$2030 \text{ } 10^3$

The first test consists of a flow with only wall-friction force. Then, a wall-heat source is added to the system and different values of the heat transfer coefficient  $h_t$  are investigated. All of the tests are performed for both vapor and liquid water phases. Lastly, a 1-D core channel component from RELAP-7 is used to model the core of a Pressurized Water Reactor (PWR) with liquid water.

### 5.6.7 *Vapor flow in a straight pipe with wall-friction force*

The geometry consists of a three 1-D straight pipes of constant area  $A = 10^{-4} m^2$  and length  $L = 1, 4$  and  $1 m$ . The source terms are only applied to the middle pipe of length 4 m. The objective is to investigate the entropy variations due to the source terms by comparing with the first and third pipes that are source-term free. The friction coefficient is set to  $f_c = 10$ . A subsonic inlet flow boundary condition is used by imposing the momentum  $\rho u_{inlet} = 52.8 \text{ kg}/(m^2 s)$  and the total enthalpy  $H_{inlet} = 2784615.9 \text{ J/kg}$ . At the outlet, the static pressure  $P_{outlet} = 6.6 \text{ MPa}$  is specified. The initial conditions are taken equal to the boundary conditions and can be computed using the SGEOS and the parameters provided in Table 5.11. The code is run until steady-state with  $CFL = 10$  and the geometry is discretized with an uniform mesh of 60 cells. Steady-state profiles of the pressure, the velocity, the density and the viscosity coefficients are given in Fig. 5.9.

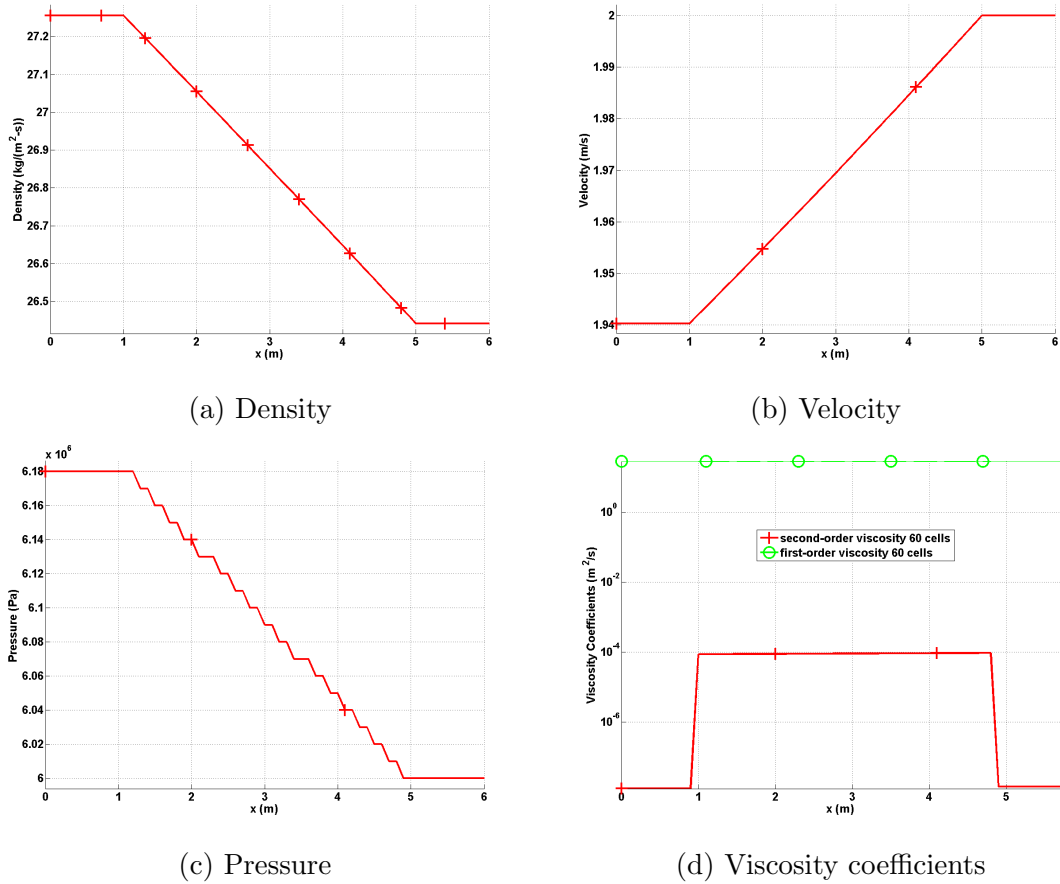


Figure 5.9: Steady-state profiles of a vapor flow with friction force in a straight pipe.

The pressure decreases in the middle pipe because of the wall-friction forces as seen in Fig. 5.9c (the staircase effect is a plotting artifact). The friction force makes the pressure drop along the pipe which also makes the density drop. In Fig. 5.9b the velocity increases through the middle pipe to ensure conservation of the mass flux through the pipe at steady state. The density variation, Fig. 5.9a, is the same as the pressure one since they are related through the equation of state. The viscosity coefficients are shown in Fig. 5.9d: because of the entropy production due to the wall-friction force, the viscosity coefficient displays a step profile. All of the variables

shown in Fig. 5.9, are constant in the first and third pipes since they are source term free.

### 5.6.8 Liquid water flow in a straight pipe with wall-friction force

The same geometry with the same temporal and spatial discretization as in Section 5.6.7 is used to simulate a liquid water flow. The boundary conditions are also the same and the following boundary values are used:  $\rho u_{inlet} = 1617.4 \text{ kg}/(\text{m}^2\text{s})$  and  $H_{inlet} = 998407.2 \text{ J/kg}$ . Steady-state numerical results are presented in Fig. 5.10.

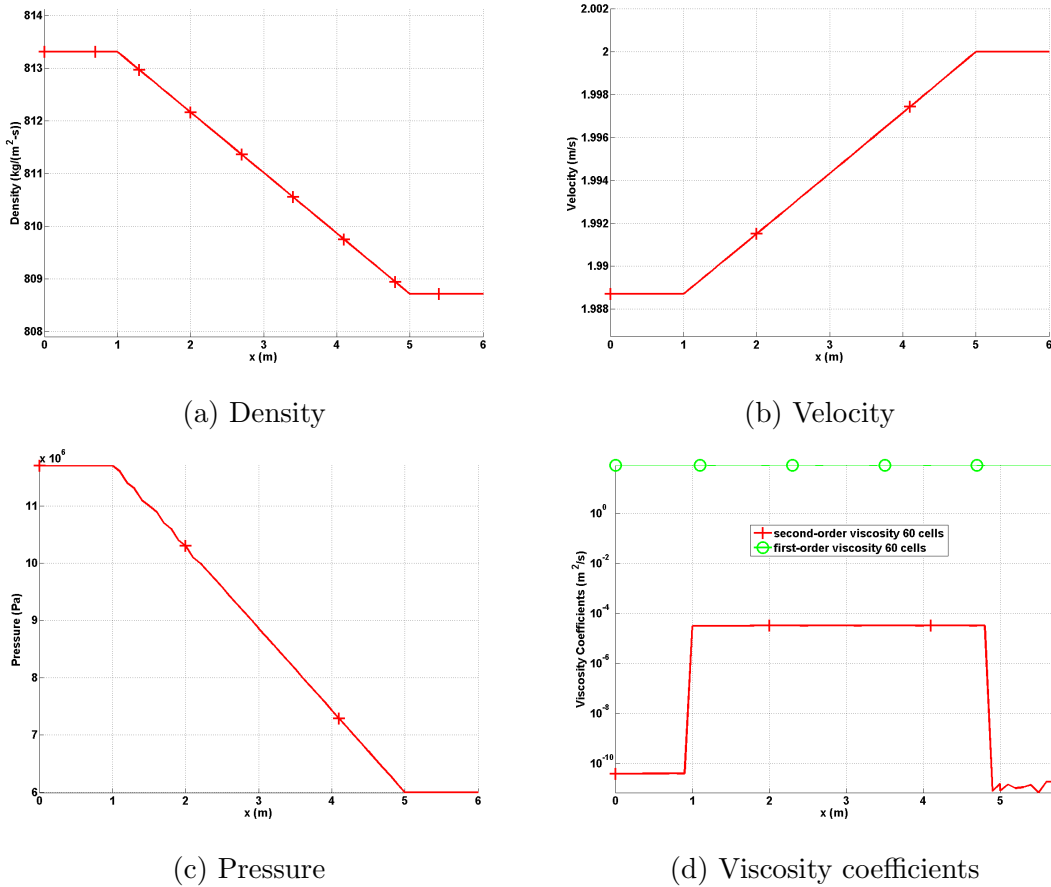
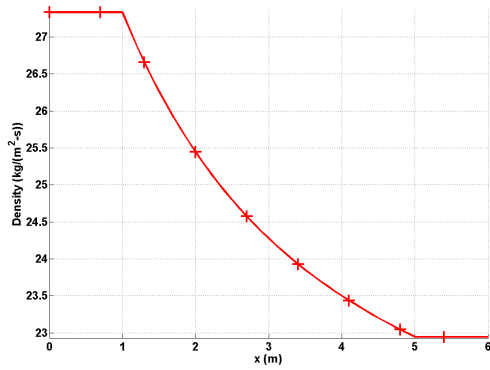


Figure 5.10: Steady-state profiles of a liquid water flow with friction force in a straight pipe.

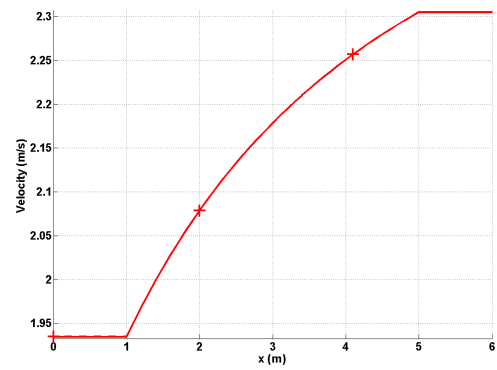
The pressure, velocity, density and viscosity coefficients profiles show similar spatial variation as the vapor phase case described in Section 5.6.7, but with different order of magnitude.

### 5.6.9 Vapor and liquid water flows in a straight pipe with wall-friction and wall-heat source

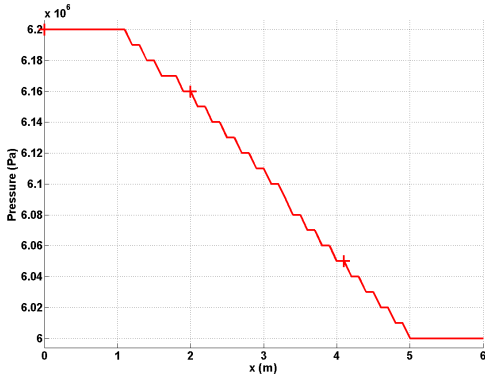
Once again, the same set up as in Section 5.6.7 and in Section 5.6.8 is used to simulate the behavior of liquid water and vapor phases with a wall-heat source. The wall temperature is assumed constant and set to  $T_w = 600\text{ K}$  for both phases. The wall heat transfer coefficients are also constant and are chosen so that a significant change in the temperature profile can be observed:  $h_t^{liquid} = 1000\text{ W/(K - m}^2\text{)}$  and  $h_t^{vapor} = 100\text{ W/(K - m}^2\text{)}$ . The wall heated perimeter  $P_w$  is the same for both phases since function of the geometry and set to  $P_w = 0.0314156\text{ m}$ . The steady-state profiles are shown in Fig. 5.12 for liquid water and in Fig. 5.11 for vapor.



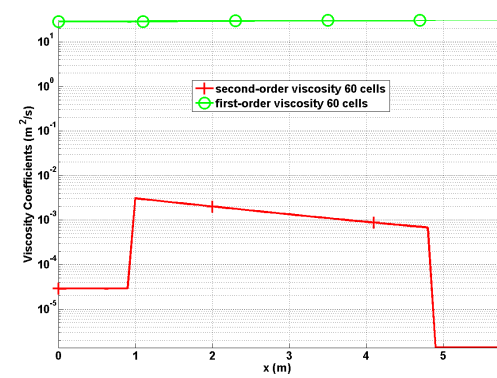
(a) Density



(b) Velocity



(c) Pressure



(d) Viscosity coefficients

Figure 5.11: Steady-state profiles of a vapor flow with friction force and wall-heat source in a straight pipe.

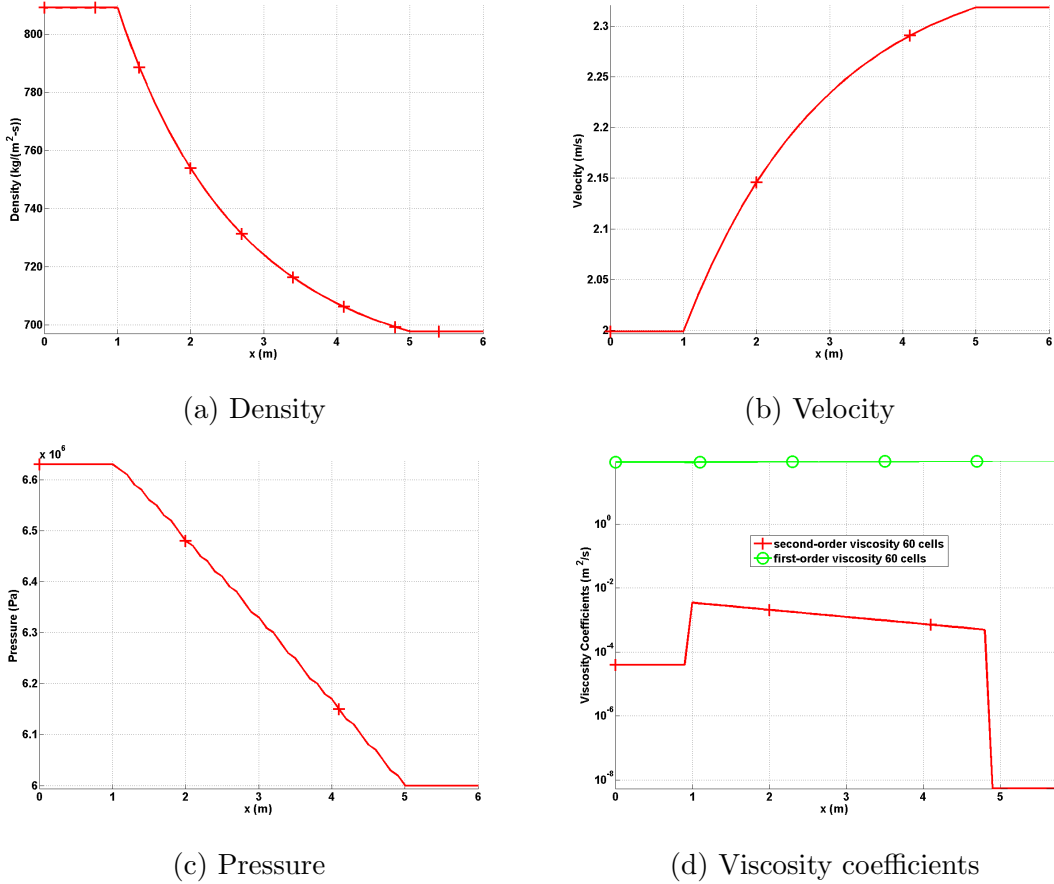


Figure 5.12: Steady-state profiles of a liquid water flow with friction force and wall-heat source in a straight pipe.

Both phases show similar spatial variations. Because of the wall heat source, the velocity increases and is curved as shown in Fig. 5.12b and Fig. 5.11b. In Fig. 5.12a and Fig. 5.11a, the density decreases through the middle pipe since heat is added to the system. The pressure profile remains the same since the pressure variations are decoupled from the rest of the system in the low Mach limit as shown in Fig. 5.12c and Fig. 5.11c. The viscosity coefficients profile is affected by the heat source (Fig. 5.12d and Fig. 5.11d) and is larger in the middle pipe than in the two other pipes. It is also noted that the high-order viscosity coefficient is several orders of magnitude

smaller than the first-order viscosity coefficient. Influence of the first-order viscosity coefficient onto the numerical solution is demonstrated in the next section.

### 5.6.10 1-D Pressurized Water Reactor (PWR)

Numerical tests are performed for a 1-D pipe of cross-section  $A = 7.854 \times 10^{-5} \text{ m}^2$  and length  $L = 3.865 \text{ m}$  with the following parameters: the heat transfer coefficient  $h_w$  is set to a constant  $5.33 \times 10^4 \text{ W/(K - m)}$ , the heated surface  $P_w$  is computed from  $A$  and  $L$  and set to  $0.0298 \text{ m}$ , and the friction factor is constant and equal to 0.01. The wall temperature  $T_w$  is no longer constant and computed using the model available in RELAP-7 for PWR [4]. For boundary conditions, we impose, at the inlet, a mass inflow ( $\rho u = 3359.62 \text{ kg/(m}^2\text{s)}$ ) and a specific enthalpy ( $H_{inlet} = 1.28 \times 10^6 \text{ J/kg}$ ) and employ a static pressure condition at the exit ( $P_s = 155 \text{ bar}$ ). The stiffened gas equation of state (SGEOS) is used [38] with the parameters given in Table 5.11 for liquid water. The steady-state is reached at around  $t = 150 \text{ sec}$  with a time step of  $\Delta t = 0.5 \text{ sec}$ . Figures 5.13 through 5.16 represent the results obtained using 20 mesh cells, using either the overly-dissipative first-order viscosity (FO), the higher-order entropy viscosity (EV), or the SUPG [21] method to stabilize the numerical scheme. From these figures, it is clear that employing the first-order viscosity leads to erroneous answers, while the entropy-viscosity results are correct and look similar to those obtained with the SUPG method. Plots obtained using a finer spatial resolution (100 cells) are also shown in these figures.

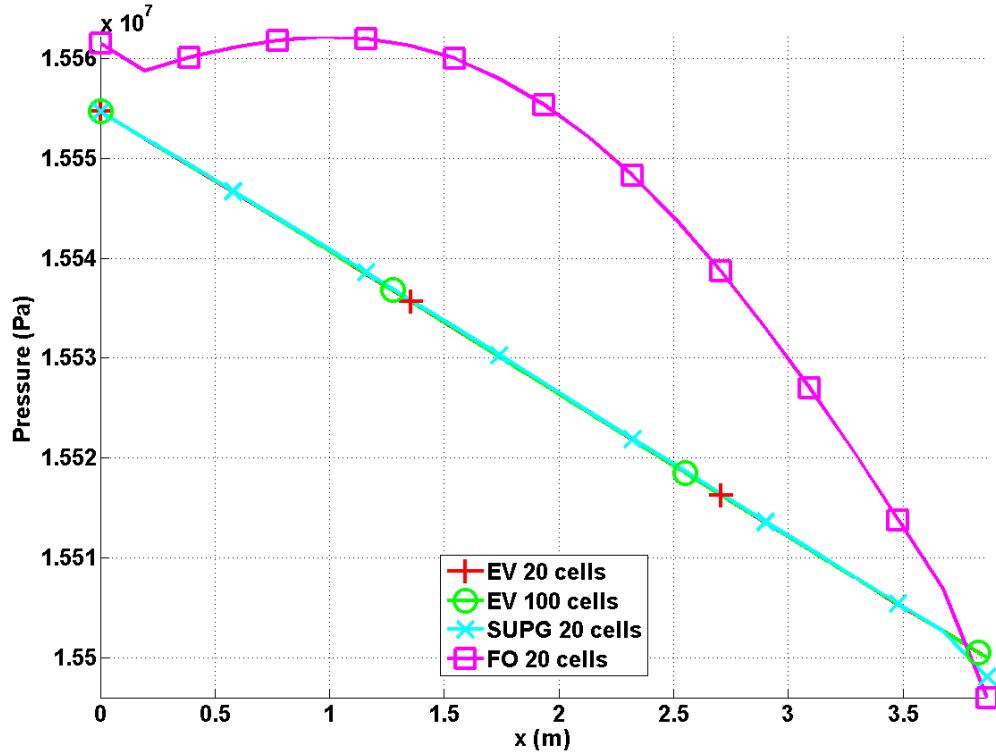


Figure 5.13: PWR test case: axial pressure profile

In Fig. 5.13, the steady-state pressure profile obtained with the SUPG method shows a small non-physical change of slope at the outlet that does not disappear under mesh refinement. This artifact is not seen when using the entropy viscosity method.

It is noted from Figures 5.13 through 5.16 that the first-order viscosity solution becomes ill-scaled. This is due to the low-Mach nature of the flow under consideration (flow speed around 5 m/s while the speed of sound is around 1,500 m/s). We carry out a low-Mach limit study for the continuity equation written with its artificial dissipative term. The same reasoning can be applied as well to the momentum and

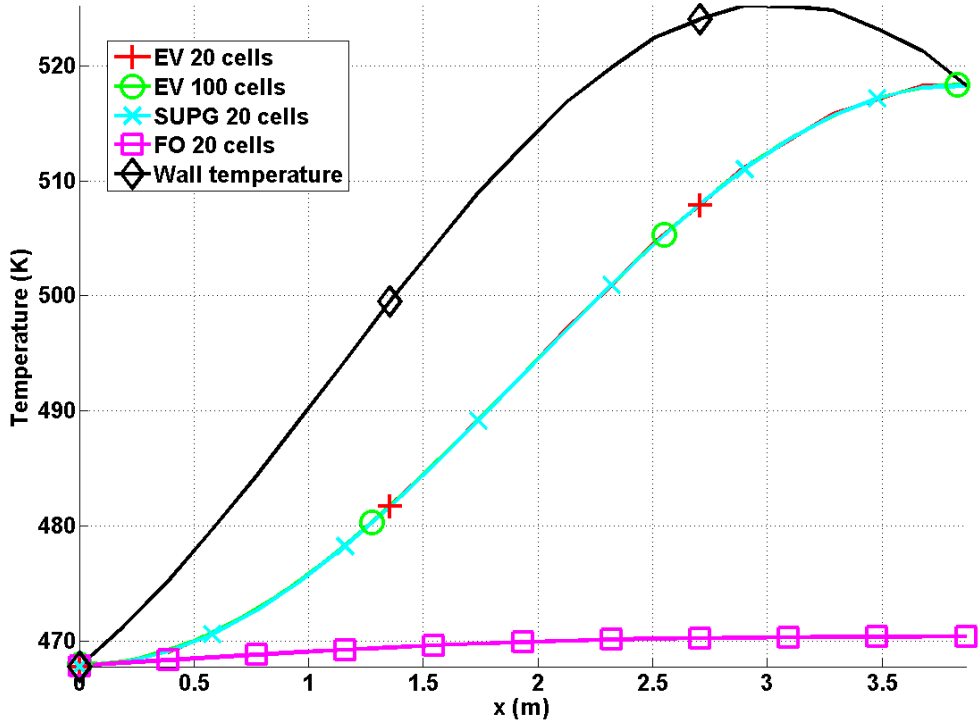


Figure 5.14: PWR test case: axial temperature profile

energy equations. Using the reference variables defined in Eq. (5.11), the continuity equation yields

$$\partial_{t^*} \rho^* + \nabla^* \cdot (\rho^* \mathbf{u}^*) = \frac{\kappa_\infty}{Lu_\infty} \nabla^* \cdot (\kappa^* \nabla^* \rho^*). \quad (5.48)$$

The coefficient  $k^*$  depends upon whether the first- or entropy-order viscosity coefficient is employed. When using the first-order viscosity, Eq. (5.4), an expression for  $\kappa_\infty$  is:  $\kappa_\infty = \frac{L}{2} (u_\infty + c_\infty)$ . By substituting this definition into Eq. (5.48), the expression obtained for the scaled continuity equation is

$$\partial_{t^*} \rho^* + \nabla^* \cdot (\rho^* \mathbf{u}^*) = \frac{1}{2} \left( 1 + \frac{1}{M_\infty} \right) \nabla^* \cdot (\kappa^* \nabla^* \rho^*), \quad (5.49)$$

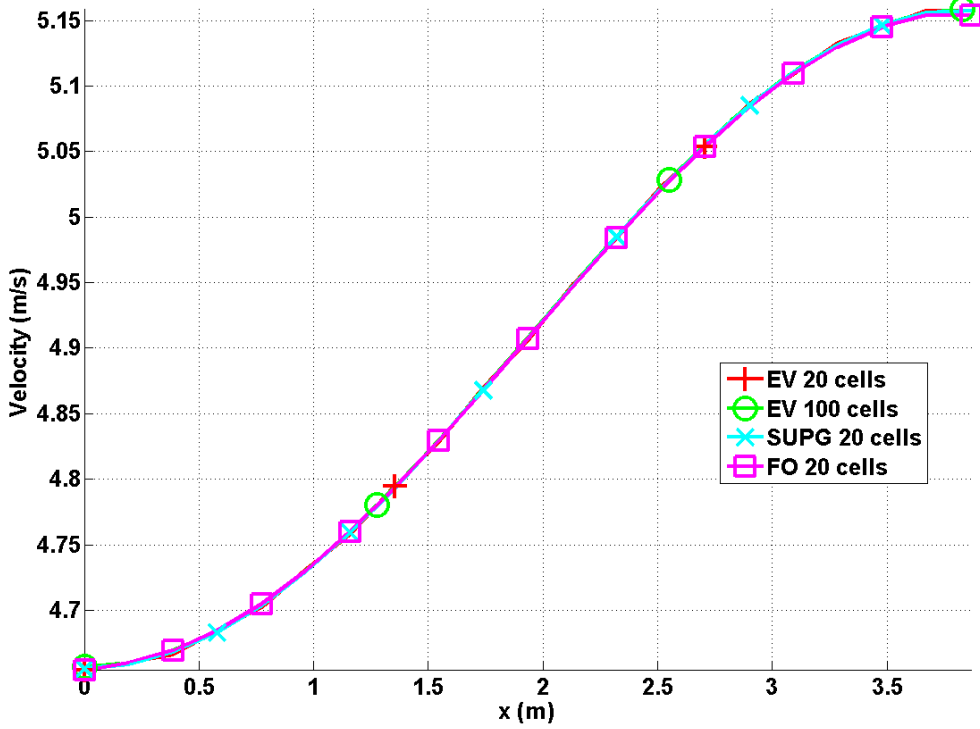


Figure 5.15: PWR test case: axial velocity profile

where  $M^*$  is a reference Mach number. Thus, for low Mach flows, the dissipative term will become ill-scaled and will alter the solution greatly when using the first-order viscosity. However, when employing the definition of the entropy-viscosity coefficient given in Eq. (5.30), it yields  $k_\infty = u_\infty L_\infty$ , and the dissipative term is well-scaled in the low Mach limit:

$$\partial_{t^*} \rho^* + \nabla^* \cdot (\rho^* \mathbf{u}^*) = \nabla^* \cdot (\kappa^* \nabla^* \rho^*). \quad (5.50)$$

Obviously, it is therefore critical to evaluate, and if needed, to adapt the definition of the viscosity coefficients employed with the dissipative terms to a wide range of flow speeds.

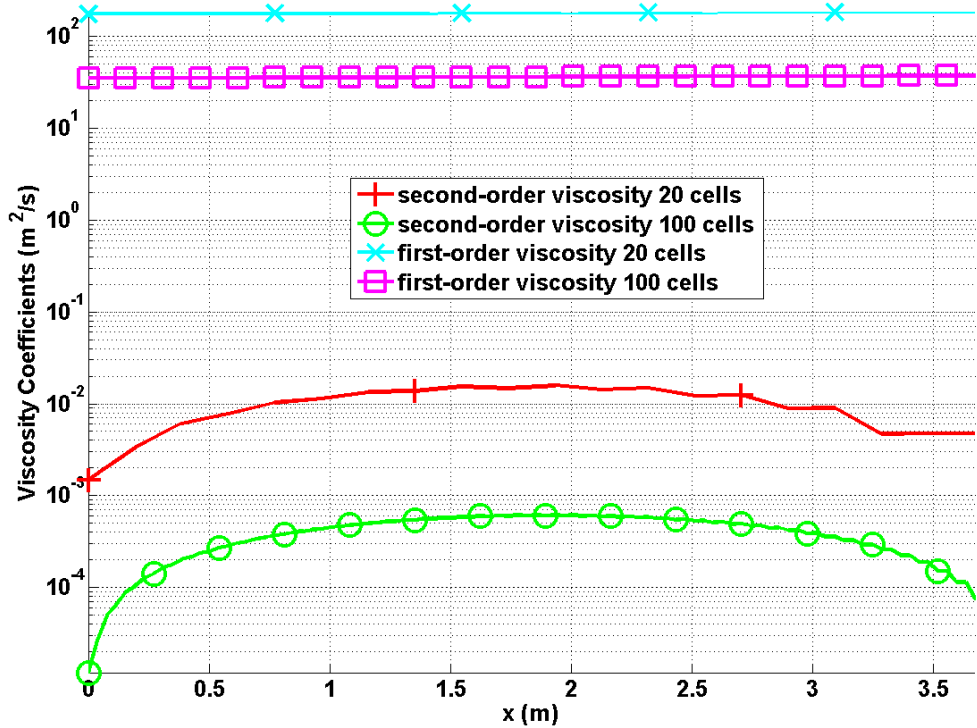


Figure 5.16: PWR test case: axial viscosity profile

A good way to assess the impact of the dissipative terms on the steady-state solution is to plot the mass flux (or momentum density) variable. It is expected to be constant in the low Mach limit, in the absence of a mass source and under the condition of having well-scaled dissipative terms, Eq. (5.49) and Eq. (5.50).

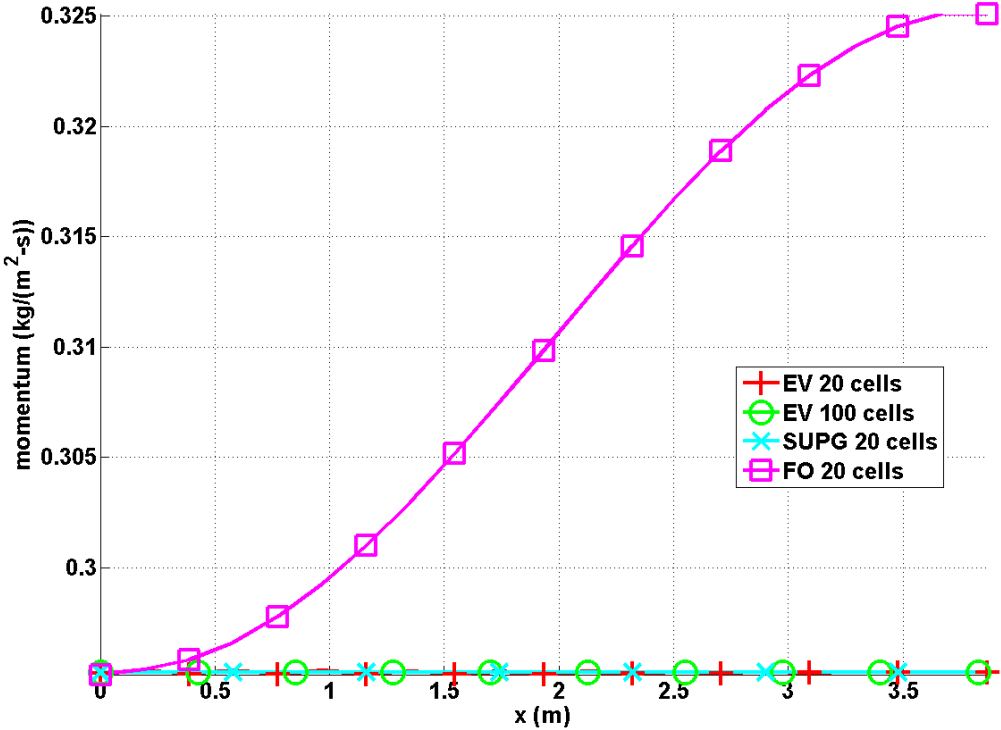


Figure 5.17: PWR test case: axial mass flux (or momentum) profile

This is shown in Fig. 5.17, where it is clear that the mass flux remains constant ( $0.2953 \text{ kg/m}^2\text{s}$ ) through the domain at steady-state when using either the entropy viscosity method or SUPG. When run with the first-order viscosity, the steady-state mass flux displays a 10% variation over the domain because of the  $\frac{1}{M_\infty}$  coefficient in the dissipative term of Eq. (5.49).

## 5.7 2-D numerical results for supersonic flows

This section focuses on demonstrating the ability of the entropy viscosity method, with the new definition of the viscosity coefficients derived in Section 5.2.2, to accurately resolve shocks occurring in transonic flows. Such tests were already performed

in [69] with the former definition of the entropy viscosity method recalled in Section 5.1.1, and using a discontinuous Galerkin finite element discretization. Our objective here, is to show that the new definition of the viscosity coefficients is still capable of resolving shocks. The numerical tests presented in this section include: flow pass a forward facing step [64], a circular explosion [65], a steady-state flow over a double wedge [46] and a steady-state flow in a compression corner [5]. The last two tests will also allow us to evaluate the ability of the method to reach a steady-state. For each numerical results presented in this section, information relative to the equation of state and its parameters, the boundary conditions, the initial conditions, the mesh and the discretization order will be provided along with the numerical results. For clarity purpose we will refer to as  $\Omega$ . Since only 2-D computational domain is considered, left, right, bottom and top boundaries are referred to as  $\delta\Omega_1$ ,  $\delta\Omega_2$ ,  $\delta\Omega_3$  and  $\delta\Omega_4$ , respectively, with  $\delta\Omega = (\delta\Omega_1, \delta\Omega_2, \delta\Omega_3, \delta\Omega_4)$ .

### 5.7.1 Supersonic 2-D flow over a forward facing step

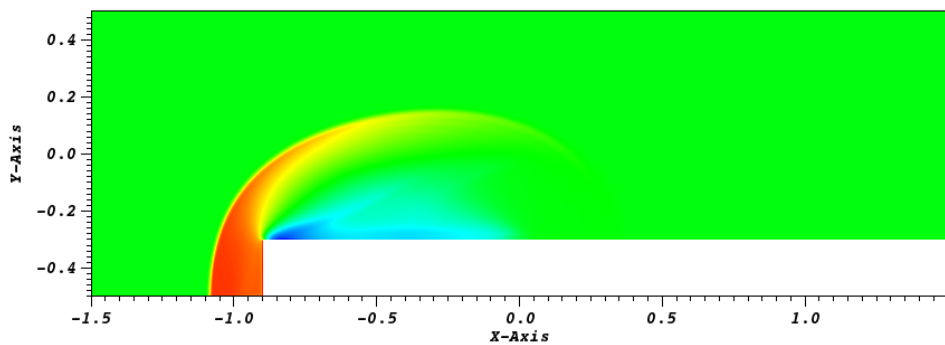
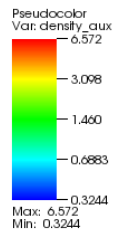
This benchmark was introduced in [64]. It consists of a Mach 3 flow past a forward-facing step in a 2-D wind tunnel. The geometry is given in (FIGURE) and was discretized with an uniform mesh of  $10^5$  cells. A supersonic inlet boundary condition is used to set the flow conditions. A slip wall boundary condition is specified at the top and bottom wall following the method explained in Section 5.5. The outflow, in  $x = 4$  is free since the flow remains supersonic at the outlet boundary. The uniform initial conditions are given in Table 5.12 for the primitive variables. The Ideal gas equation of state is used with a adiabatic gas constant  $\gamma = 1.4$ .

Table 5.12: Initial conditions for a 2-D supersonic flow past a forward-facing step.

primitive variables	$\rho$	$\mathbf{u}$	P
value	1.4	(3, 0)	1.

The numerical solution was obtained with a  $\mathbb{Q}_1$  continuous Galerkin finite element method and the second-order temporal integrator *BDF2*. The solution was run until  $t = 0.25s$  with a *CFL* of 2. The density and the viscosity coefficients profiles are given in Fig. 5.18-Fig. 5.25. It was chosen to show the numerical solution at times  $t = 0.314$ ,  $t = 0.664$ ,  $t = 1.551$  and  $t = 4$  s to illustrate the ability of the entropy viscosity method to detect shocks and discontinuities during a transient, and add significant dissipation only in their close neighborhood.

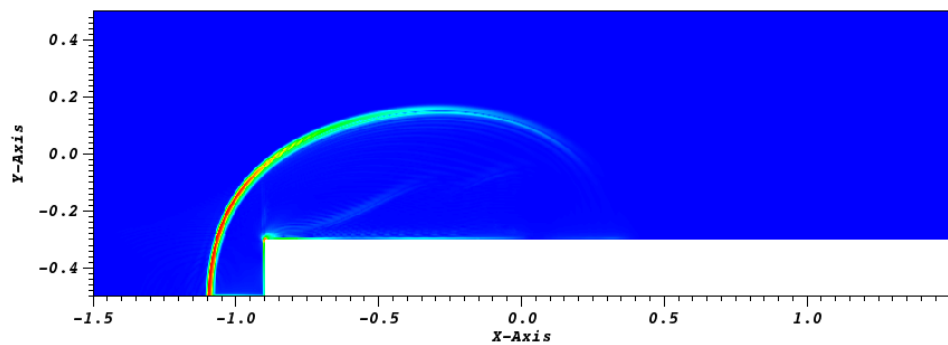
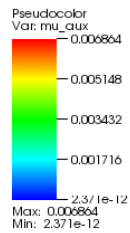
DB: ForwardFacingStep\_out\_save.e  
Time: 0.314



user: delchini  
Wed May 14 15:59:30 2014

Figure 5.18: Supersonic 2-D flow over a forward facing step: density solution at  $t = 0.314$  s.

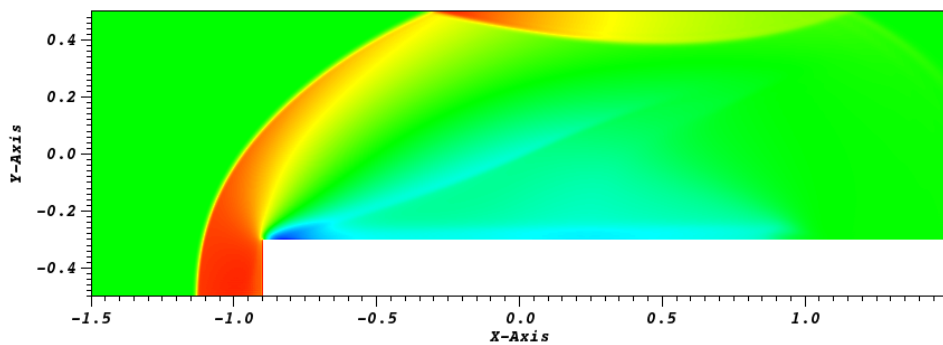
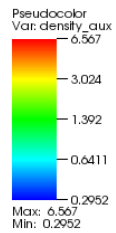
DB: ForwardFacingStep\_out\_save.e  
Time: 0.314



user: delchini  
Wed May 14 15:51:08 2014

Figure 5.19: Supersonic 2-D flow over a forward facing step: viscosity coefficient solution at  $t = 0.314$  s.

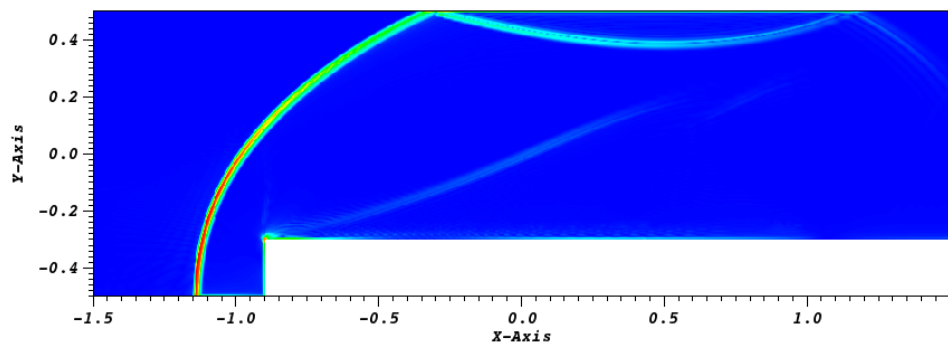
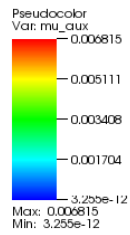
DB: ForwardFacingStep\_out\_save.e  
Time: 0.664



user: delchini  
Wed May 14 15:54:46 2014

Figure 5.20: Supersonic 2-D flow over a forward facing step: density solution at  $t = 0.664$  s.

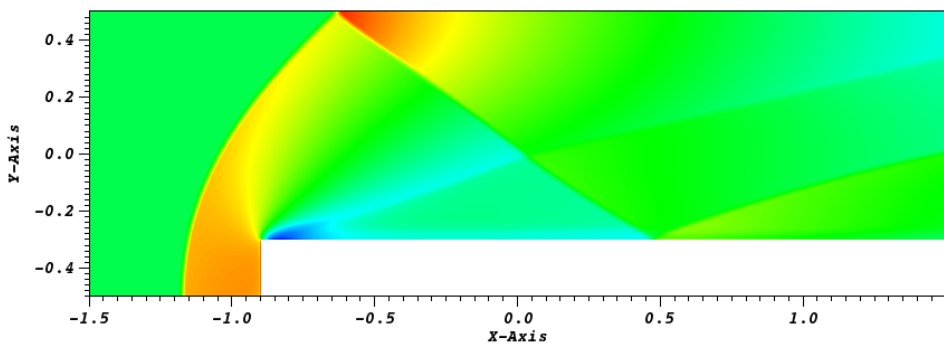
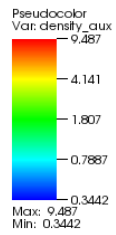
DB: ForwardFacingStep\_out\_save.e  
Time: 0.664



user: delchini  
Wed May 14 15:53:35 2014

Figure 5.21: Supersonic 2-D flow over a forward facing step: viscosity coefficient solution at  $t = 0.664$  s.

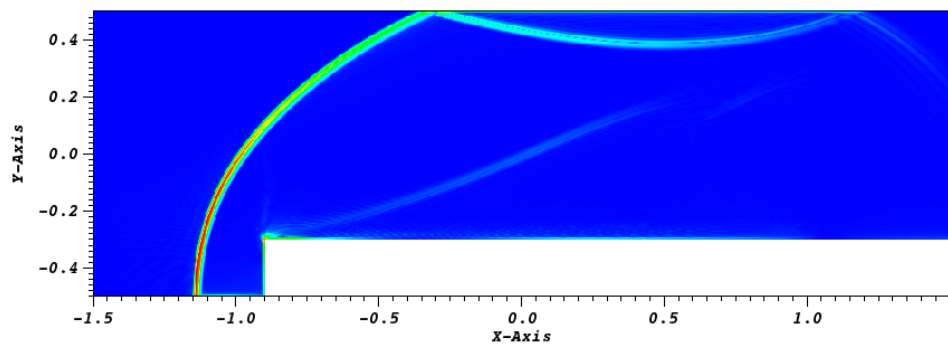
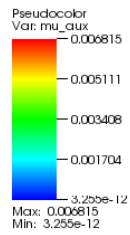
DB: ForwardFacingStep\_out\_save.e  
Time: 1.514



user: delchini  
Wed May 14 15:56:46 2014

Figure 5.22: Supersonic 2-D flow over a forward facing step: density solution at  $t = 1.514$  s.

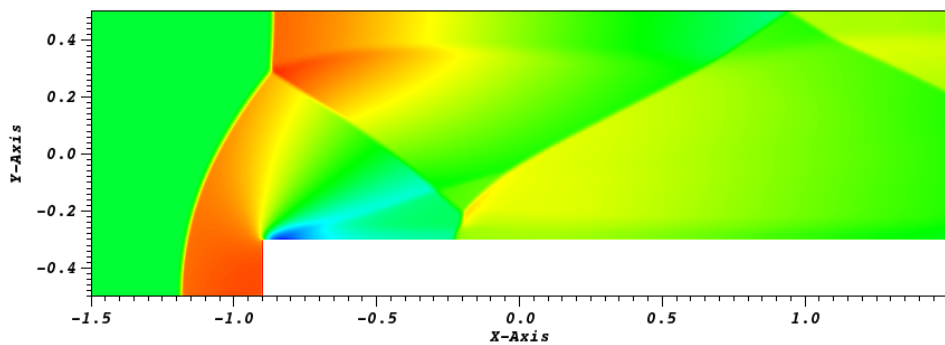
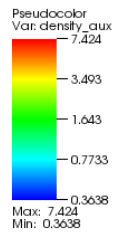
DB: ForwardFacingStep\_out\_save.e  
Time: 0.664



user: delchini  
Wed May 14 15:53:35 2014

Figure 5.23: Supersonic 2-D flow over a forward facing step: viscosity coefficient solution at  $t = 1.514$  s.

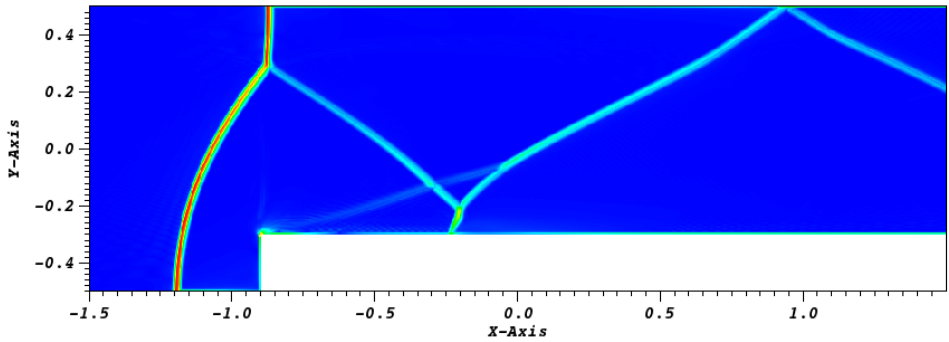
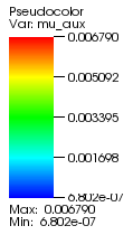
DB: ForwardFacingStep\_out\_save.e  
Time:4



user: delchini  
Wed May 14 15:58:39 2014

Figure 5.24: Supersonic 2-D flow over a forward facing step: density solution at  $t = 4$  s.

DB: ForwardFacingStep\_out\_save.e  
Time:4



user: delchini  
Wed May 14 15:58:11 2014

Figure 5.25: Supersonic 2-D flow over a forward facing step: viscosity coefficient solution at  $t = 4$  s.

The numerical solution of the density at  $t = 4$  s compares well to the ones obtained in [69], as least in a visual norm. The triple-point feature and the contact wave emerging from it are well resolved. It is also noticed that a significant amount of entropy is produced near the corner region. This is due to the corner singularity and this phenomenon is well explained in [16]. This artifact can be treated either by using special boundary condition to the corner since its normal vector is not defined, or by aggressively refining the mesh in the singularity region, or lastly, by modifying the geometry and use a round corner.

### 5.7.2 2-D circular explosion

We now consider a 2-D circular explosion [65] that is known to develop an unstable layer contact. The computational domain is a square of dimension  $\Omega = (-1, 1)^2$ . The initial conditions consist of a pressure and density step located in the center of the computational domain. The values of the initial conditions are given in Table 5.13 in function of the radius  $r^2 = x^2 + y^2$ . The Ideal gas equation of state is still used with the same parameters as in Section 5.7.1. Dirichlet boundary conditions are used to specify the values on the boundaries  $\delta\Omega$  of the computational domain  $\Omega$ , assuming that the simulation is stopped before the waves reach the boundaries.

Table 5.13: Initial conditions for a 2-D explosion.

primitive variables	$\rho$	$\mathbf{u}$	P
$r \in [0, 0.4]$	1	(0, 0)	1
$r \geq 0.4$	0.125	(0, 0)	0.1

The numerical solutions of the density and viscosity coefficient are given in Eq. (5.26) and Eq. (5.27), respectively.

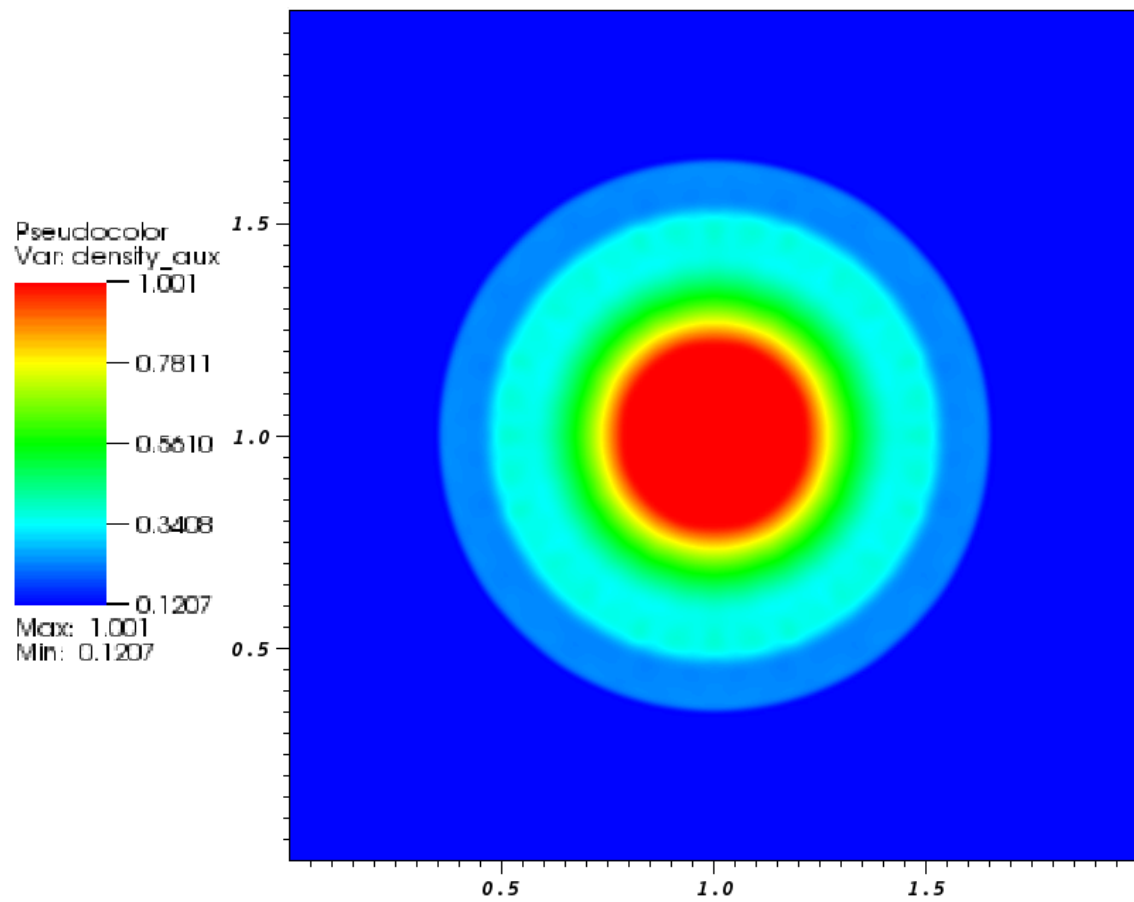


Figure 5.26: 2-D circular explosion: density solution at  $t = 0.2$  s.

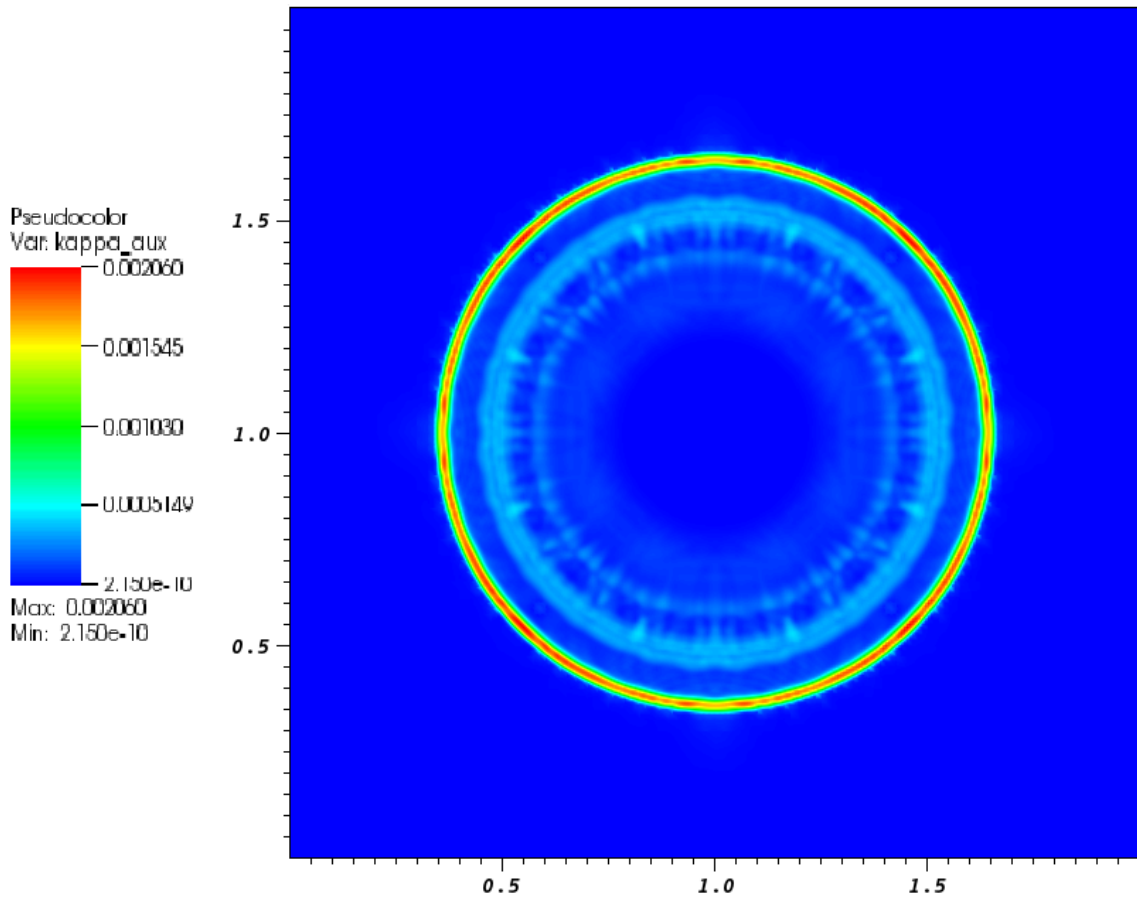


Figure 5.27: 2-D circular explosion: viscosity coefficient solution at  $t = 0.2$  s.

The density profile shown in Fig. 5.26 does not display any oscillations. The shock and the contact waves are well resolved. The viscosity coefficient reaches its maximum value in the shock region (Fig. 5.27), as expected. A smaller peak is also observed in the contact region.

### 5.7.3 Supersonic flow in a compression corner

This is an example of a supersonic flow over a wedge of angle  $15^\circ$  where an oblique shock is generated at steady-state. The Mach number upstream of the shock is fixed to  $M = 2.5$ . The initial conditions are uniform: the pressure and temperature are

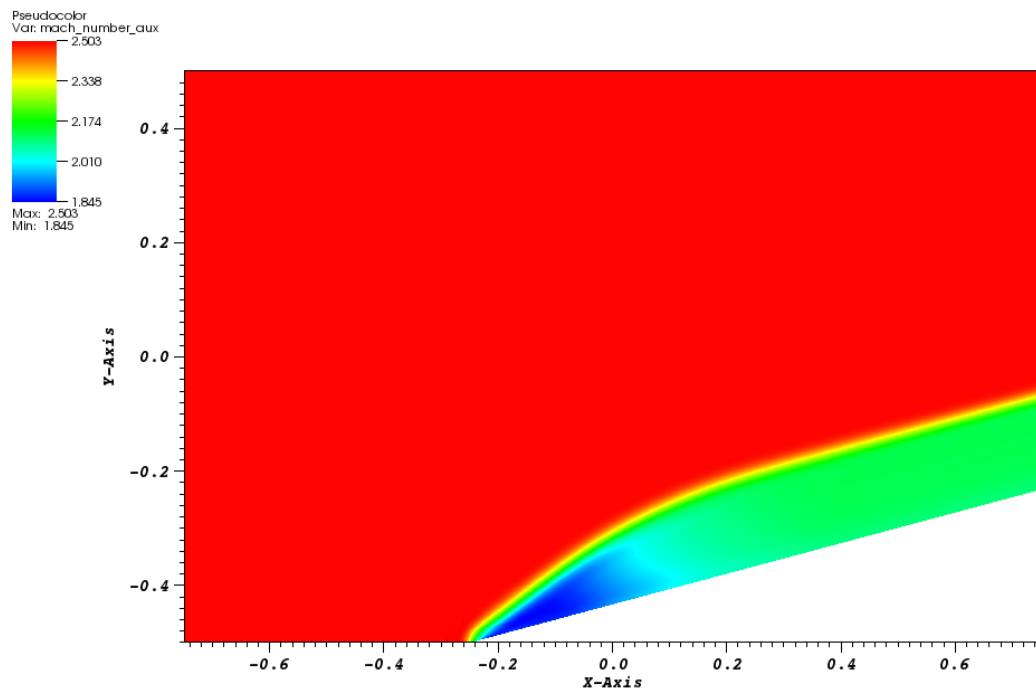
set to  $P = 101325 \text{ Pa}$  and  $T = 300 \text{ K}$ , respectively. The initial velocity is computed from the upstream Mach number and using the Ideal Gas equation of state with the same parameters as in Section 5.8.2. The code is run until steady-state. An analytical solution for this supersonic flow is available and give the downstream to upstream pressure, entropy and Mach number ratios [5]. The analytical and numerical ratios are given in see in Table 5.14, and are very close. The pressure and viscosity coefficient solution are given for different times in Fig. 5.28 - Fig. 5.33.

Table 5.14: Analytical solution for a mach 2.5 supersonic flow on an edge at  $15^\circ$

	analytical downstream to upstream ratio	numerical downstream to upstream ratio
Pressure	2.47	2.467
Mach number	0.74	0.741
Entropy	1.03	1.026

The inlet is supersonic and therefore, the pressure, temperature and velocity are specified using Dirichlet boundary conditions. The outlet is also supersonic and none of the characteristics enter the domain through this boundary: the values will be computed by the implicit solver.

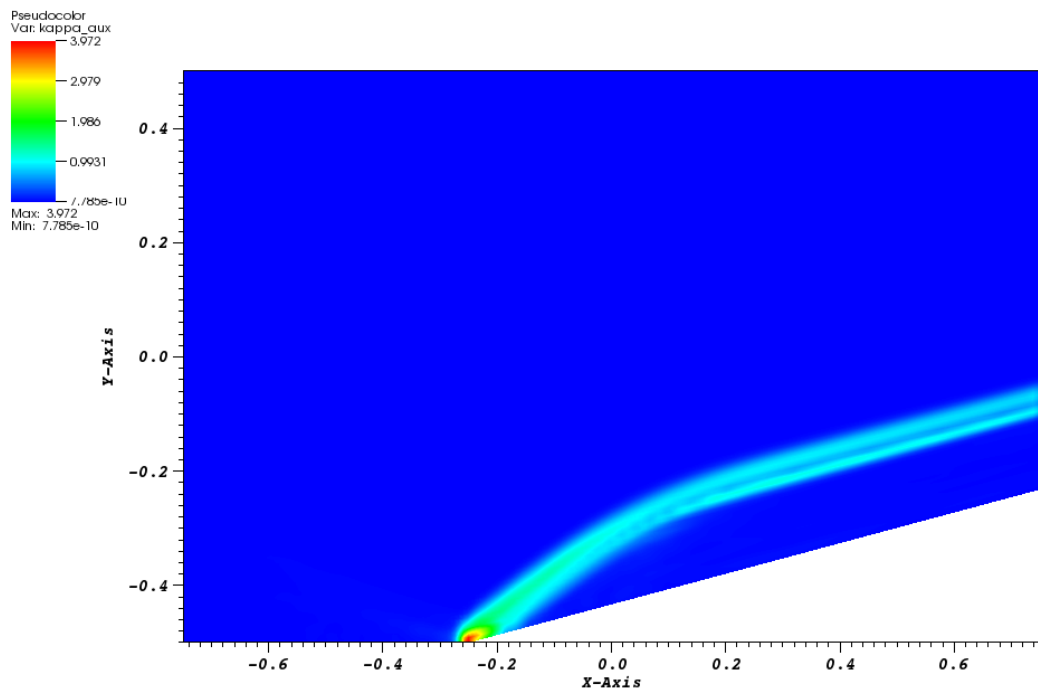
DB: CompressionCorner2DQuad\_high\_pressure\_out.e  
Time: 0.00055



user: delchini  
Wed May 14 16:42:33 2014

Figure 5.28: Supersonic flow in a compression corner: pressure solution at  $t = 5.5 \times 10^{-4}$ .

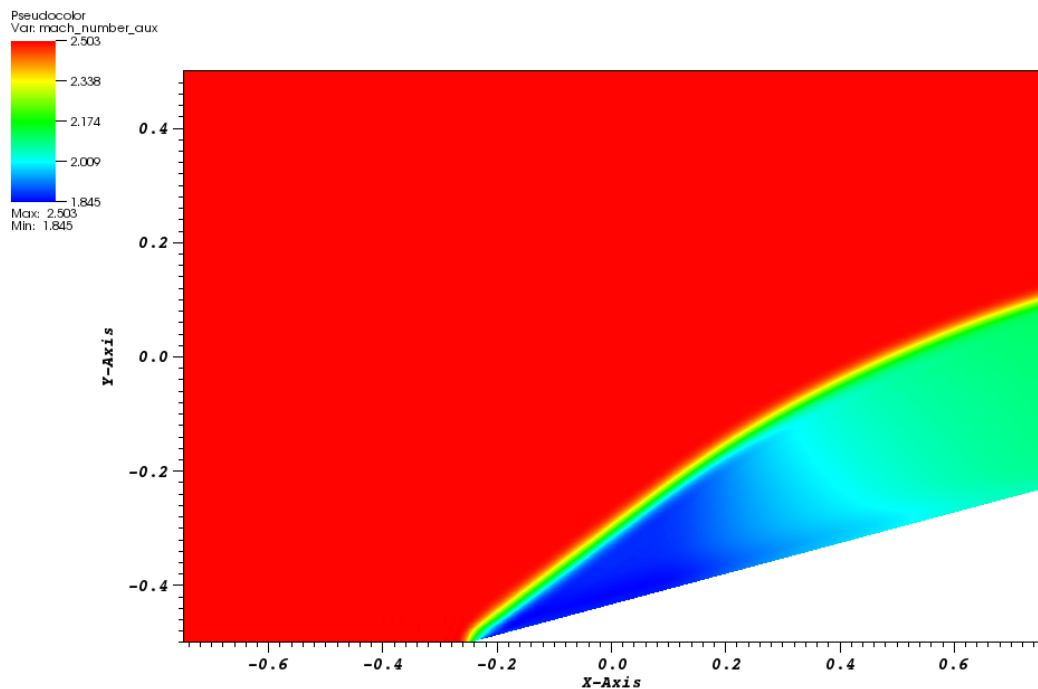
DB: CompressionCorner2DQuad\_high\_pressure\_out.e  
Time: 0.00055



user: delchini  
Wed May 14 16:43:40 2014

Figure 5.29: Supersonic flow in a compression corner: viscosity coefficient at  $t = 5.5 \times 10^{-4}$ .

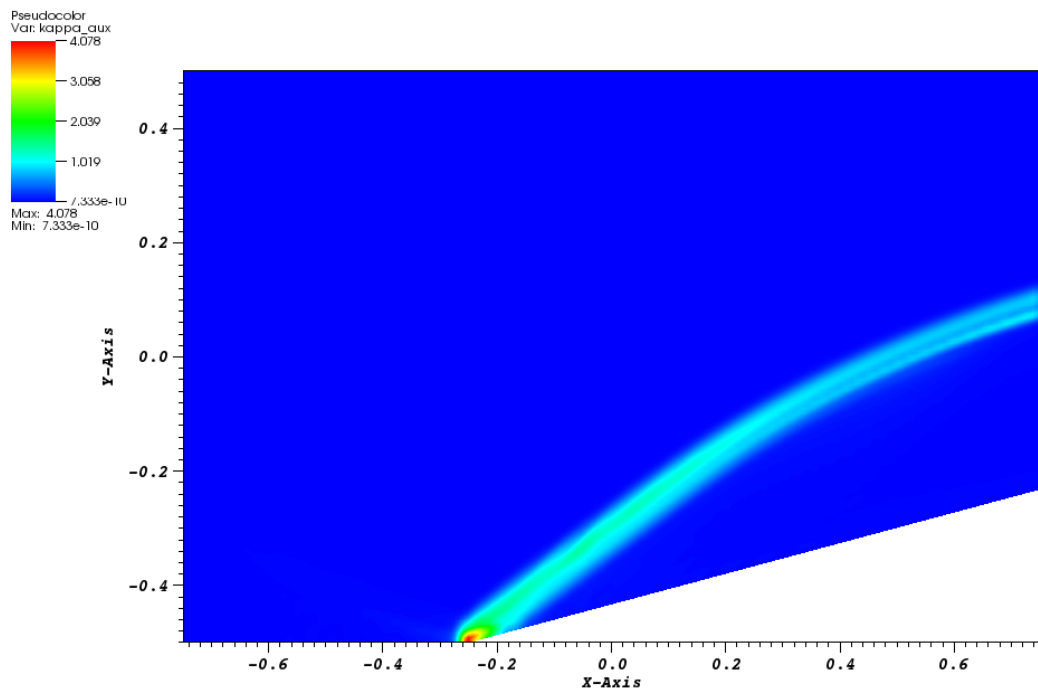
DB: CompressionCorner2DQuad\_high\_pressure\_out.e  
Time: 0.00115



user: delchini  
Wed May 14 16:44:54 2014

Figure 5.30: Supersonic flow in a compression corner: pressure solution at  $t = 1.15 \times 10^{-3}$ .

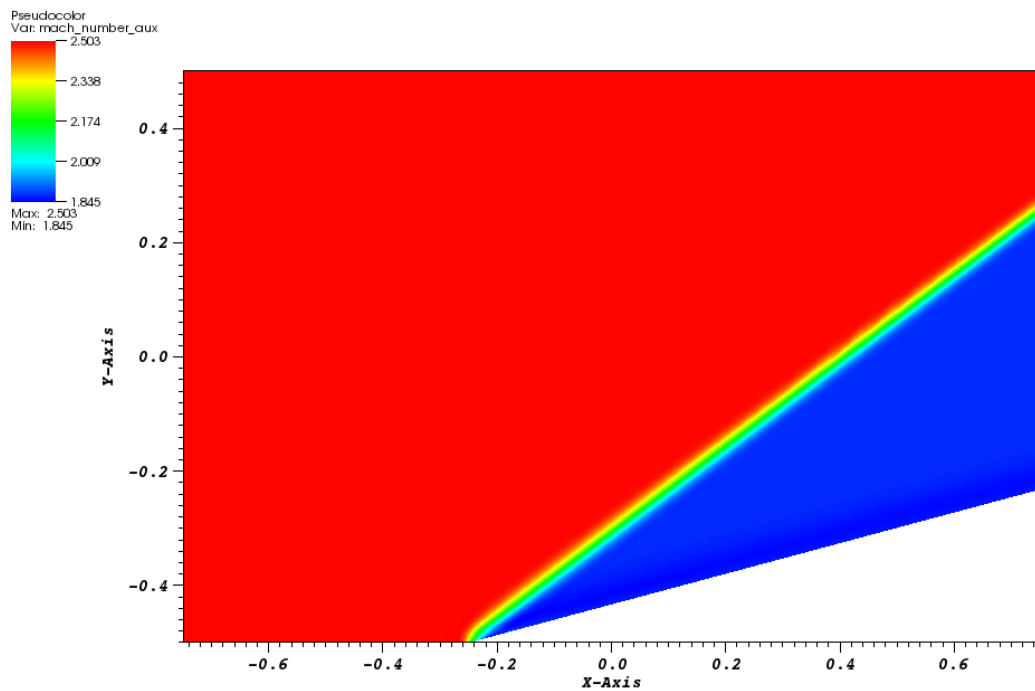
DB: CompressionCorner2DQuad\_high\_pressure\_out.e  
Time: 0.00115



user: delchini  
Wed May 14 16:44:19 2014

Figure 5.31: Supersonic flow in a compression corner: viscosity coefficient at  $t = 1.15 \times 10^{-3}$ .

DB: CompressionCorner2DQuad\_high\_pressure\_out.e  
Time: 0.005



user: delchini  
Wed May 14 16:57:07 2014

Figure 5.32: Supersonic flow in a compression corner: pressure solution at steady-state.

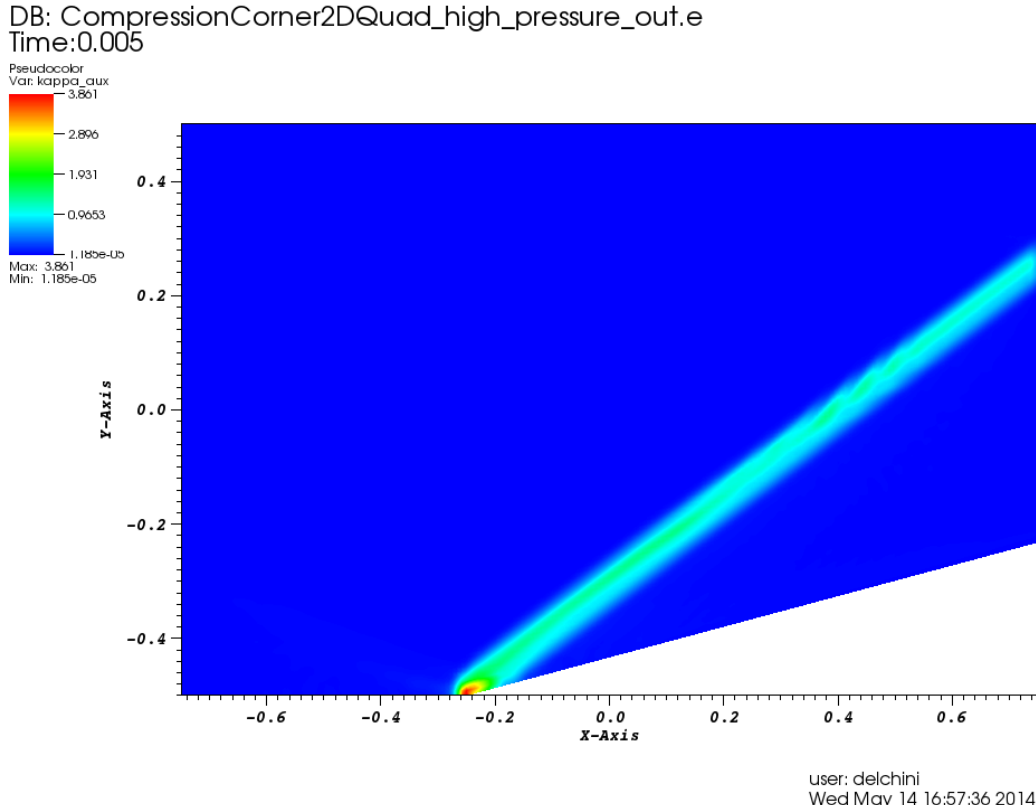


Figure 5.33: Supersonic flow in a compression corner: viscosity coefficient at steady-state.

From the above figures, it is observed that the solution is composed of two regions of constant state. During the transient, the shock moves from the bottom wall to its steady-state solution. The same variations are observed in viscosity coefficient solution. At steady-state, the viscosity coefficient is large in the shock region and small anywhere else and thus, behaves as expected. At the corner of the edge at  $x = -0.25\text{ m}$ , the viscosity coefficient is peaked because of the treatment of the wall boundary condition: at this particular node, the normal is not well defined and can cause numerical errors.

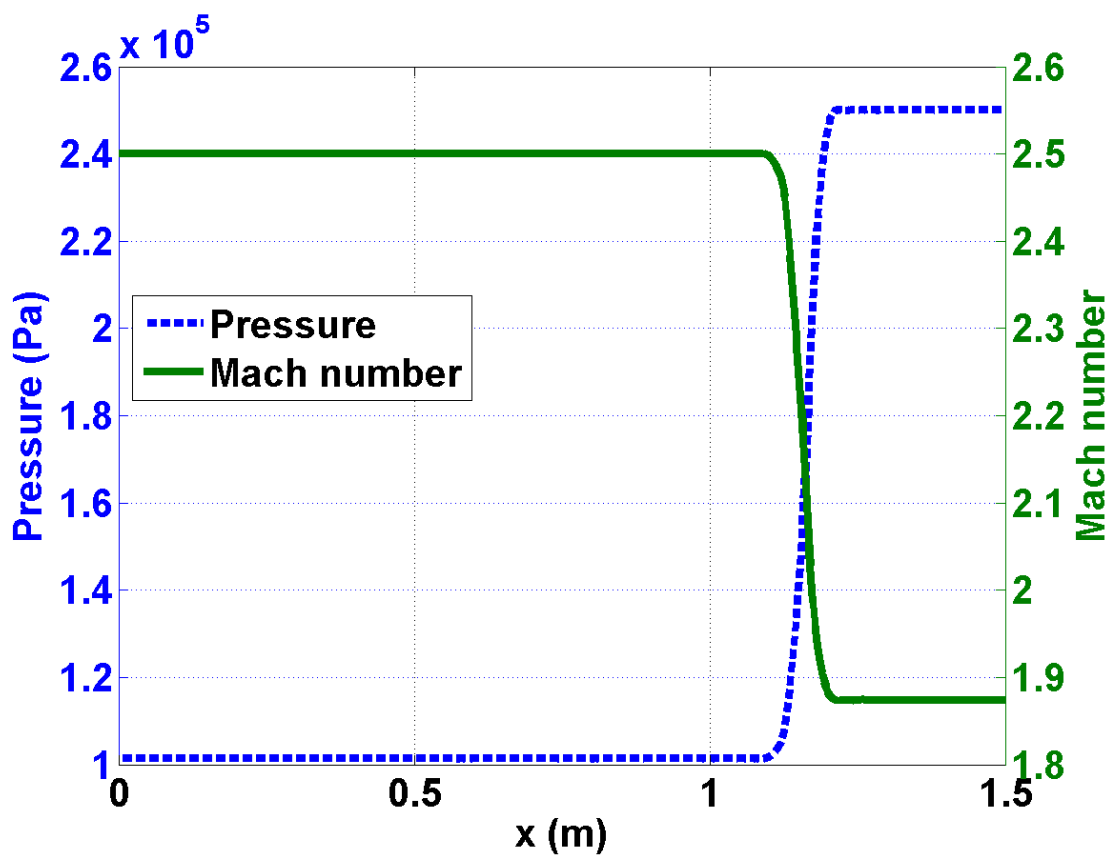


Figure 5.34: Supersonic flow in a compression corner: pressure and mach number profiles at steady-state

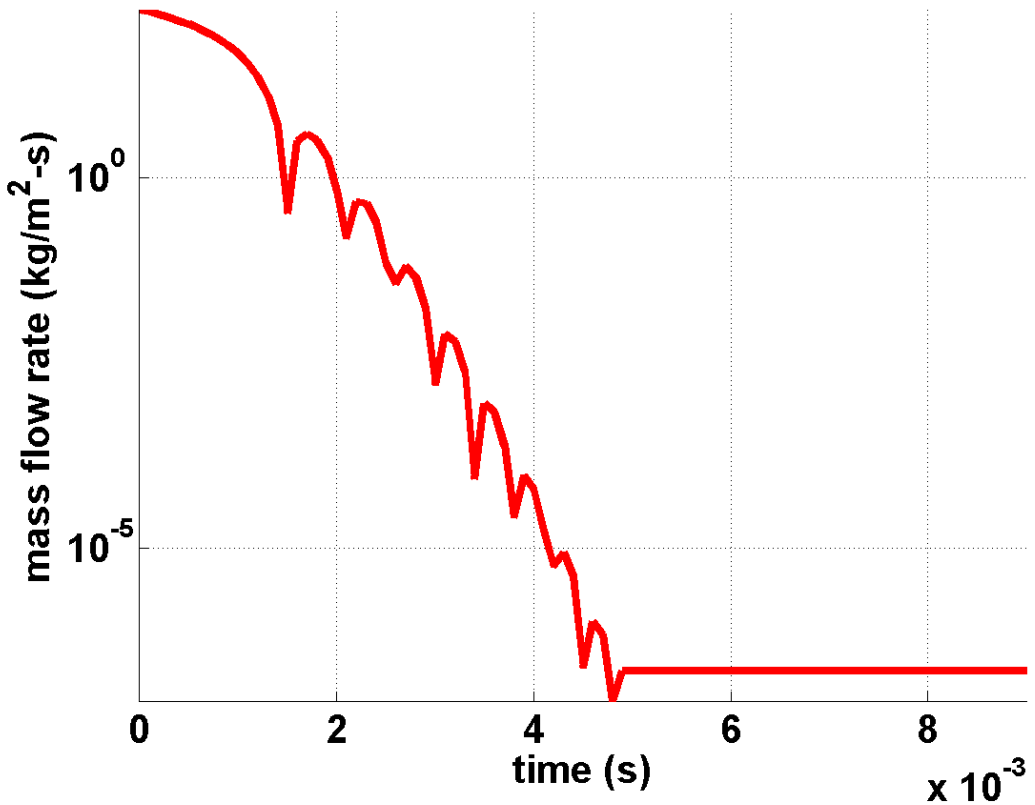


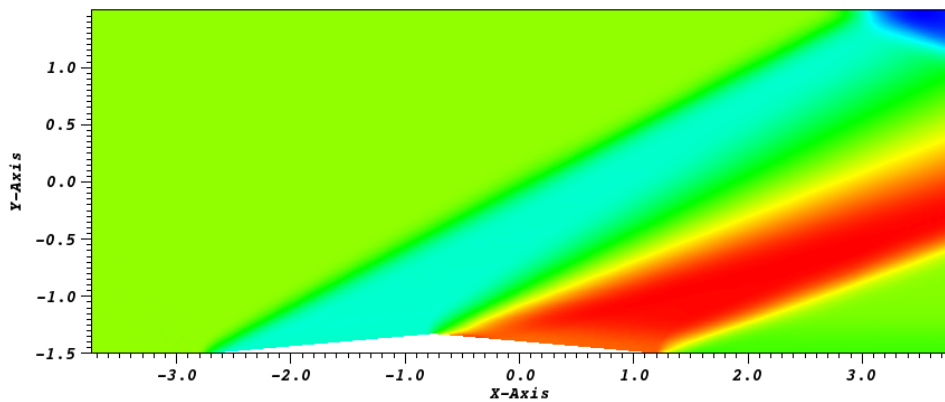
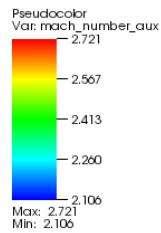
Figure 5.35: Supersonic flow in a compression corner: difference between inlet and outlet mass flow rates as a function of time.

The 1-D plots of the pressure and the mach number at  $y = 0$ , are also given in Fig. 5.34: the shock does not show any spurious oscillations and is well resolved. Finally, the difference between the inlet and outlet mass flow rates is plotted in Fig. 5.35 and show that a steady-state is reached. Overall, the numerical solution does not show any oscillations, match the analytical solution, and the shock is well resolved.

#### 5.7.4 Supersonic flow over a 5° double-wedge obstruction

The last of the 2-D supersonic example that is proposed to study is a Mach3 flow over a double-wedge obstruction located on the lower wall. The interesting feature of this test is that a steady-state is reached. The geometry was discretized with 4000  $Q_1$  elements. The double wedge extends on the bottom boundary from  $x = 1$  to  $x = 5 \text{ m}$ . The top wall is located at  $y = 5 \text{ m}$ . A supersonic inlet boundary condition was set at the inlet by specifying the pressure,  $P = 101,325 \text{ Pa}$ , the temperature,  $T = 300 \text{ K}$  and the vector velocity  $\mathbf{u} = (868.032, 0) \text{ m} \cdot \text{s}^{-1}$ . The wall-boundary and supersonic outlet boundary conditions were implemented following the method described in Section 5.5. The second-order temporal integrator *BDF2* was used with a *CFL* of 5 to reach the steady-state that was detected by monitoring the norm of the total residual. The Ideal gas equation of state was used with an adiabatic constant  $\gamma = 1.4$  and a volumetric heat capacity  $C_v = 716.7 \text{ J} \cdot \text{K}^{-1}$  (air properties). The Mach number and viscosity coefficients profiles at steady-state are given in Fig. 5.36 and Fig. 5.37, respectively.

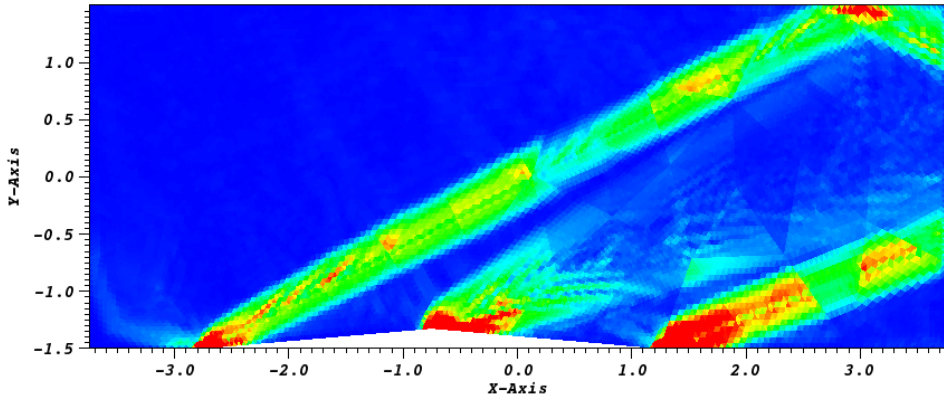
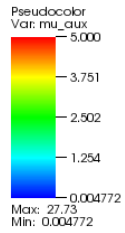
DB: DoubleWedgeObstruction\_out.e  
Time:0.1



user: delchini  
Wed May 14 17:16:17 2014

Figure 5.36: Supersonic flow over a  $5^\circ$  double-wedge obstruction: pressure solution at steady-state.

DB: DoubleWedgeObstruction\_out.e  
Time: 0.1



user: delchini  
Wed May 14 17:21:06 2014

Figure 5.37: Supersonic flow over a  $5^\circ$  double-wedge obstruction: viscosity coefficient at steady-state.

The steady-state solution consists of a two shocks that form because of the interaction of the flow with the double wedge. The first wedge generates a shock that reflects on the top wall and then exits the computational domain: the interaction of the shock with the wall close to the outlet boundary requires a robust implementation of the boundary conditions and the stabilization method. The second shock is generated by the trailing wedge. In between the two shock regions, an expansion fan is formed.

## 5.8 2-D numerical results for subsonic flows

### 5.8.1 Subsonic flow over a 2-D cylinder

Fluid flow over a 2-D cylinder is often used as a benchmark case to test numerical schemes in the low-mach regime [25, 68, 34]. For this test, an analytical solution is available in the incompressible limit or low-Mach limit and is often referred to as the potential flow solution. The main features of the potential flow are the following:

- The solution is symmetric: the iso-Mach contour lines are used to assess the symmetry of the numerical solution;
- The velocity at the top of the cylinder is twice the incoming velocity set at the inlet;
- The pressure fluctuations are proportional to the square of inlet Mach number, i.e.,

$$\delta P = \frac{\max(P(\mathbf{r})) - \min(P(\mathbf{r}))}{\max(P(\mathbf{r}))} \propto M_\infty^2 \quad (5.51)$$

where  $\delta P$  and  $M_\infty$  denote the pressure fluctuations and the inlet Mach number, respectively.

The computational domain consists of a  $1 \times 1$  square with a circular hole of radius 0.05 in its center. A  $\mathbb{P}_1$  triangular mesh with 4008 triangular elements was used to discretize the geometry. The ideal gas equation of state, with  $\gamma = 1.4$  is used. At the inlet, a subsonic stagnation boundary condition is used: the stagnation pressure and temperature are computed using the following relations:

$$\begin{cases} P_0 = P \left(1 + \frac{\gamma-1}{2} M^2\right)^{\frac{\gamma-1}{\gamma}} \\ T_0 = T \left(1 + \frac{\gamma-1}{2} M^2\right) \end{cases} \quad (5.52)$$

A static pressure boundary condition is used for the outlet boundary and the following static pressure  $P_s = 101,325 \text{ Pa}$  is set. The implementation of the pressure boundary conditions is based of [55]. A solid wall boundary condition is set for the top and bottom walls of the computational domain. The simulations are run until a steady state is reached with a  $CFL$  of 40. The steady state is considered reached when the residual norm (for all equations) is less than  $10^{-12}$ .

Several simulations are performed, with inlet Mach numbers  $M_{\text{inlet}}$  ranging from  $10^{-3}$  to  $10^{-7}$ , and are shown from Fig. 5.38 through Fig. 5.42. The iso-Mach contour lines are drawn using 30 equally-spaced intervals  $2 \cdot 10^{-10}$  to  $M_{\text{inlet}}$  and allow us to assess the symmetry of the numerical solution.

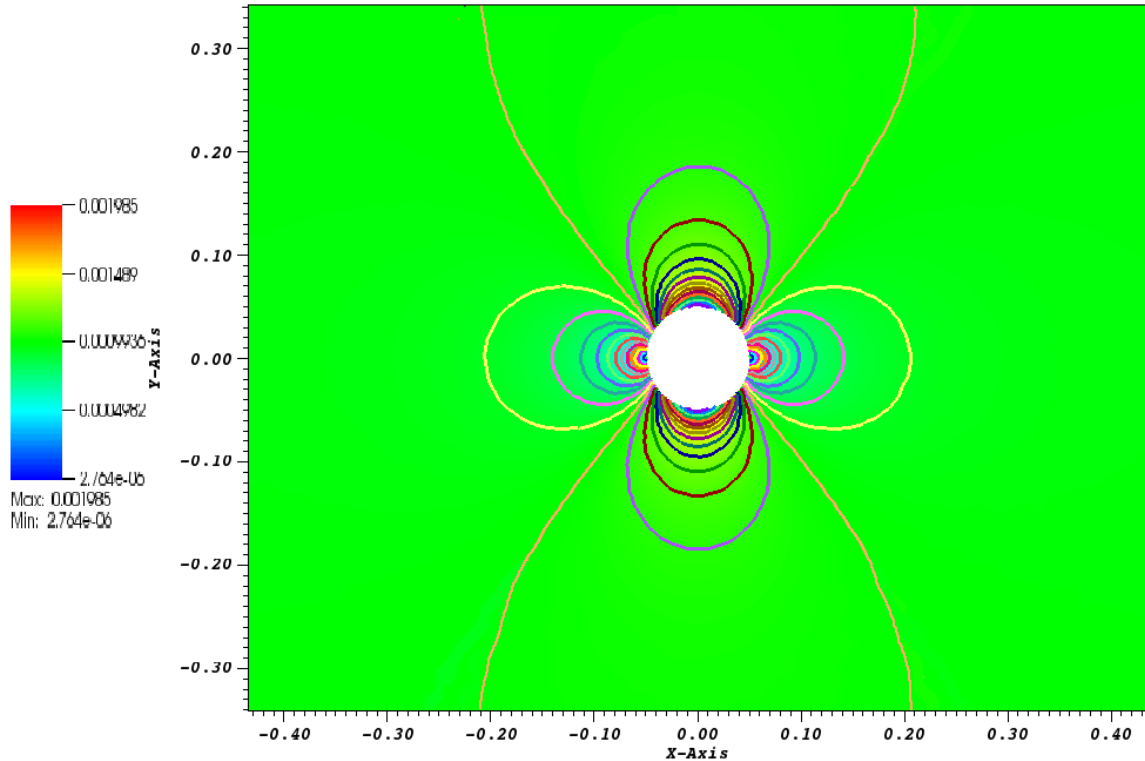


Figure 5.38: Subsonic flow over a 2-D cylinder:  $M_{\text{inlet}} = 10^{-3}$

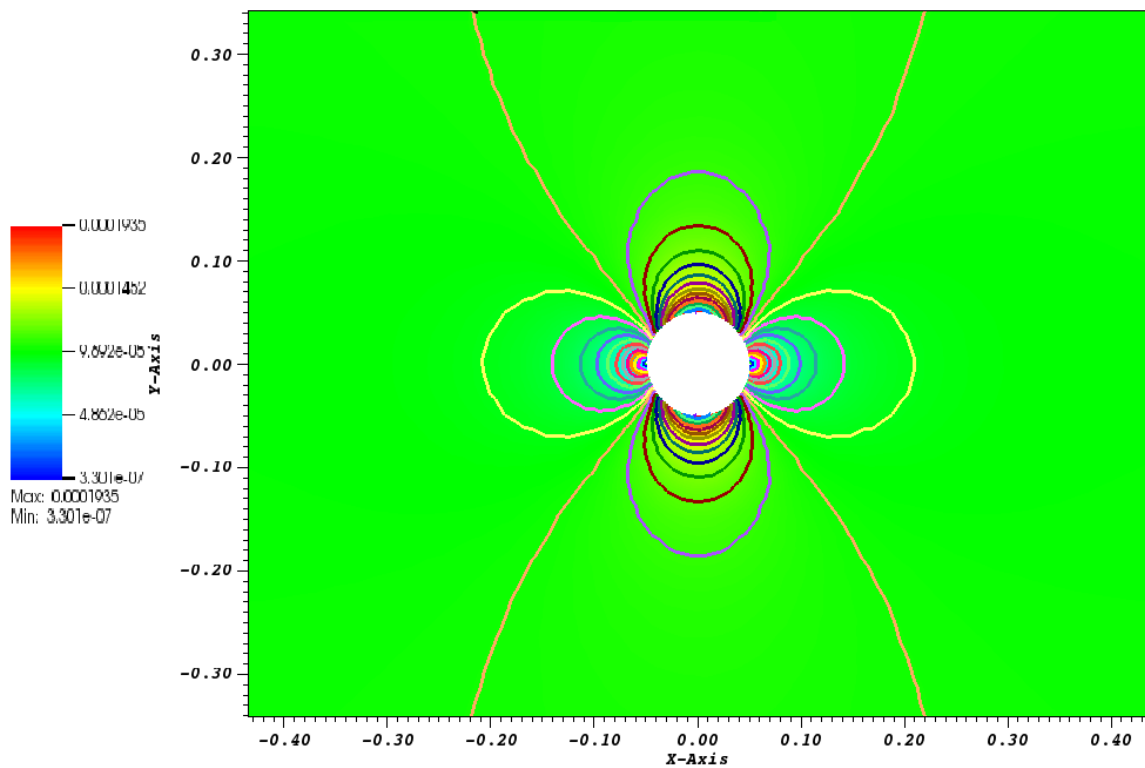


Figure 5.39: Subsonic flow over a 2-D cylinder:  $M_{\text{inlet}} = 10^{-4}$

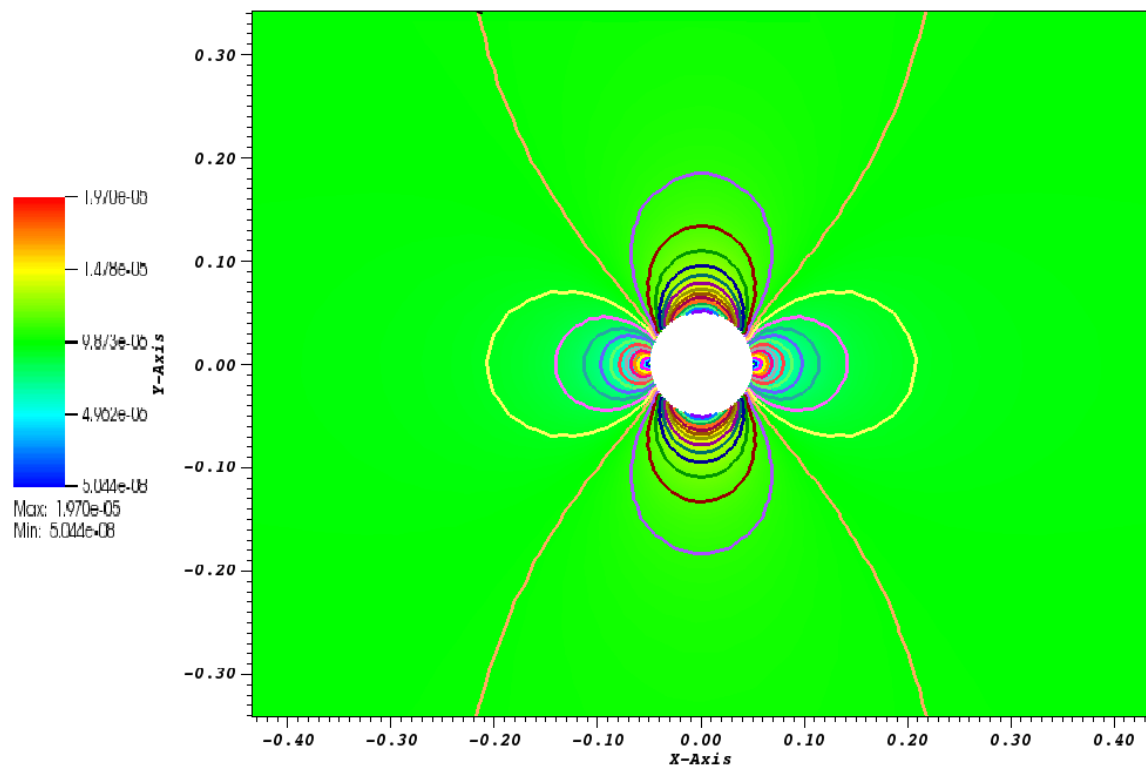


Figure 5.40: Subsonic flow over a 2-D cylinder:  $M_{\text{inlet}} = 10^{-5}$

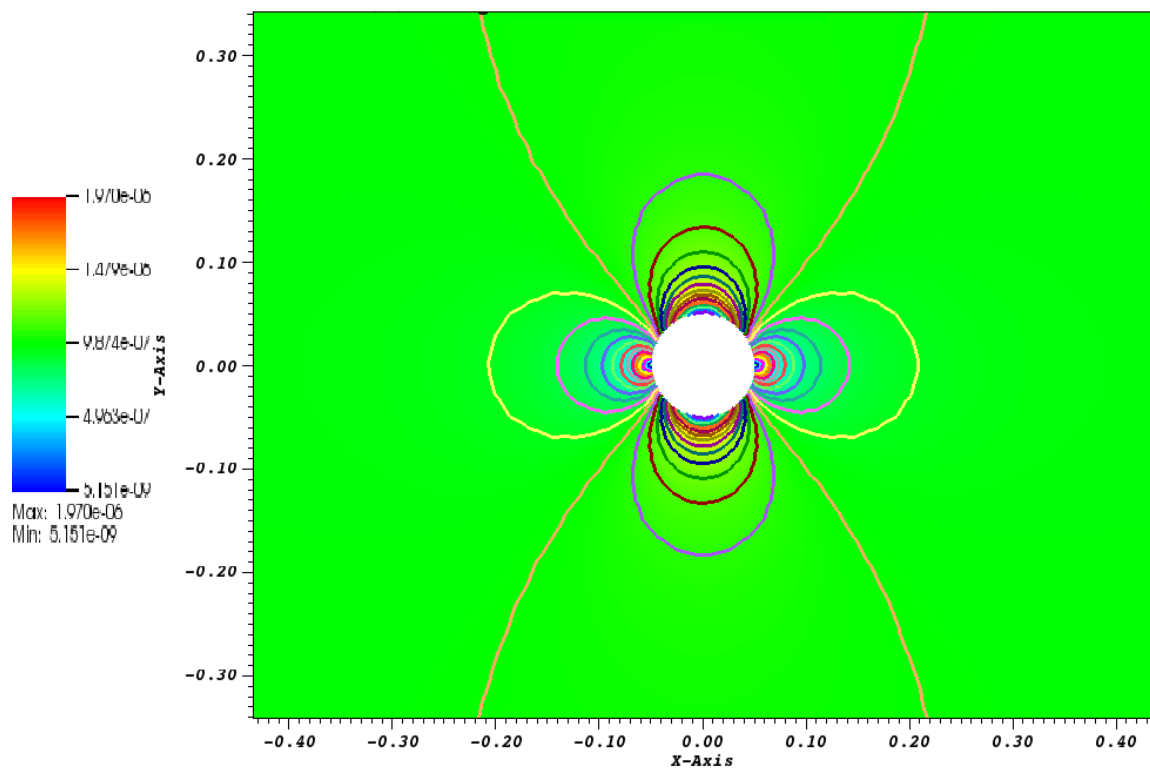


Figure 5.41: Subsonic flow over a 2-D cylinder:  $M_{\text{inlet}} = 10^{-6}$

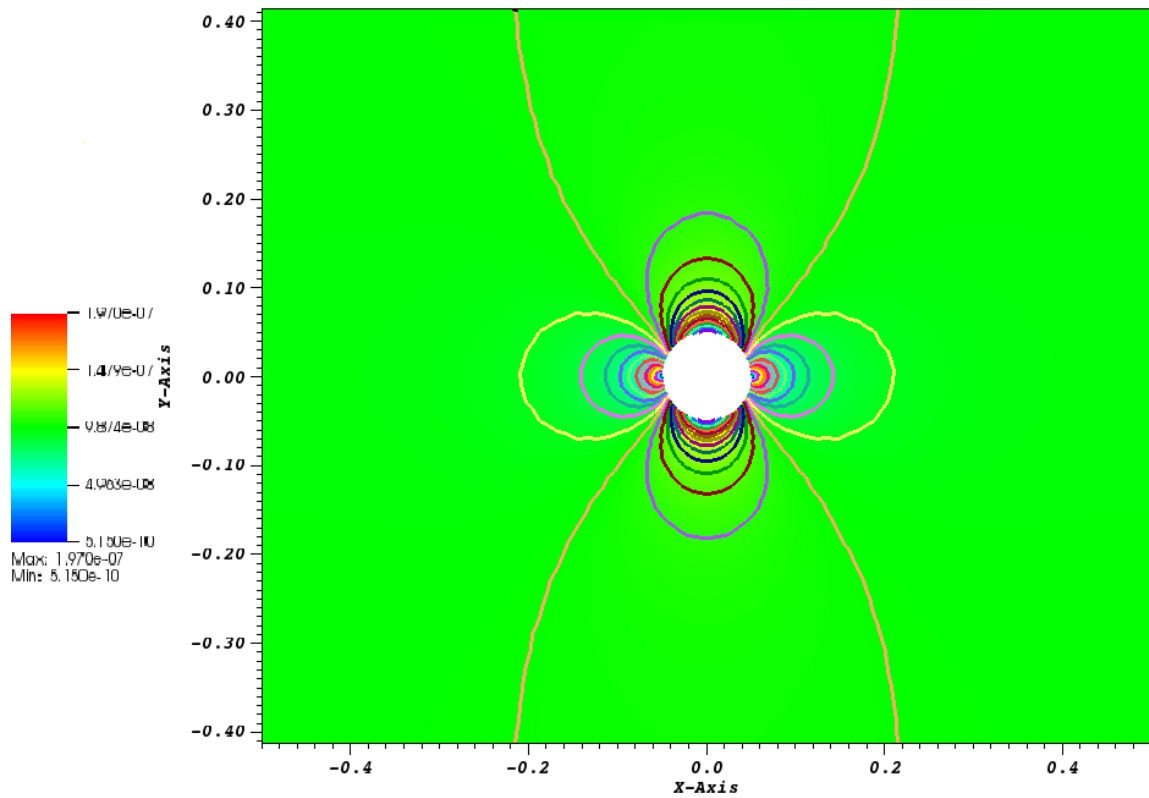


Figure 5.42: Subsonic flow over a 2-D cylinder:  $M_{\text{inlet}} = 10^{-7}$

The velocity at the top of the cylinder and at the inlet are given for different Mach-number values (ranging from  $10^{-3}$  to  $10^{-7}$ ) in Table 5.15. The ratio of the inlet velocity to the velocity at the top of cylinder is also computed and is very close to the theoretical value of 2 that is expected in the incompressible limit.

Table 5.15: Velocity ratio for different mach numbers.

Mach number	inlet velocity	velocity at the top of the cylinder	ratio
$10^{-3}$	$2.348 \cdot 10^{-3}$	$1.176 \cdot 10^{-3}$	1.99
$10^{-4}$	$2.285 \cdot 10^{-4}$	$1.145 \cdot 10^{-4}$	1.99
$10^{-5}$	$2.283 \cdot 10^{-5}$	$1.144 \cdot 10^{-5}$	1.99
$10^{-6}$	$2.283 \cdot 10^{-6}$	$1.144 \cdot 10^{-6}$	1.99
$10^{-7}$	$2.283 \cdot 10^{-7}$	$1.144 \cdot 10^{-7}$	1.99

In Fig. 5.43, the fluctuations in pressure and velocity are plotted as a function of the Mach number (on a log-log scale). The fluctuations are expected to be of the order of  $M^2$  and  $M$  for the pressure and velocity, respectively. It is known that some stabilization methods, e.g., [25, 68, 34], can produce pressure fluctuations with the wrong Mach-number order. Here, entropy viscosity method yields the correct order in the low-Mach limit. For ease of comparison, the reference lines with slope values of 1 and 2 are also plotted.

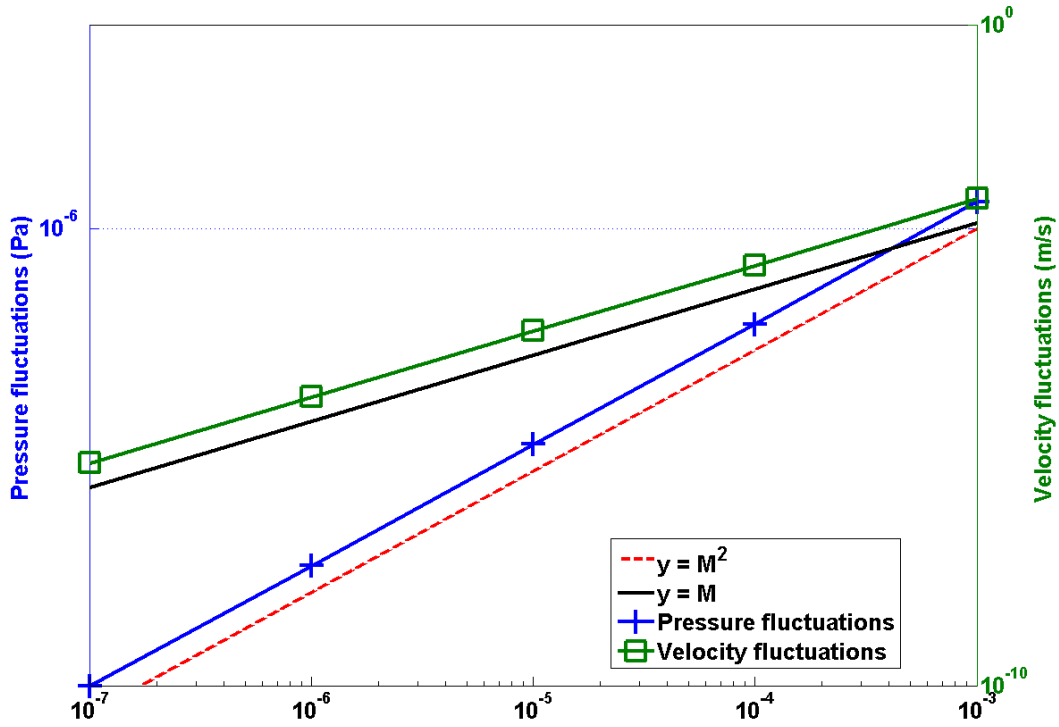


Figure 5.43: Log-log plot of the pressure and velocity fluctuations as a function of the far-field Mach number.

### 5.8.2 Subsonic flow over a 2-D hump

This is another example of an internal flow configuration. It consists of a channel of height  $L = 1 \text{ m}$  and length  $3L$ , with a circular bump of length  $L$  and thickness  $0.1L$ . The bump is located on the bottom wall at a distance  $L$  from the inlet. The system is initialized with an uniform pressure  $P = 101,325 \text{ Pa}$  and temperature  $T = 300 \text{ K}$ . The initial velocity is computed from the inlet Mach number, the pressure, the temperature and the ideal gas equation (with  $\gamma = 1.4$ ). Here,  $C_v = 717 \text{ J/kg - K}$ . At the inlet, a subsonic stagnation boundary condition is used and the stagnation pressure and temperature are computed using Eq. (5.52).

The static pressure  $P_s = 101,325 \text{ Pa}$  is set at the subsonic outlet. The results are shown in Fig. 5.44, Fig. 5.45, Fig. 5.46 and Fig. 5.47 for the inlet Mach numbers  $M_\infty = 0.7$ ,  $M_\infty = 0.01$ ,  $M_\infty = 10^{-4}$  and  $M_\infty = 10^{-7}$ , respectively. It is expected that, within the low Mach number range, the solution does not depend on the Mach number and is identical to the solution obtained with an incompressible flow code. On the other hand, for a flow at  $M = 0.7$ , the compressible effects become more important and a shock can form. An uniform grid of 3352  $Q_1$  elements was used to obtain the numerical solution for Mach numbers below  $M_\infty = 0.01$ . A once-refined mesh was employed for the  $M_\infty = 0.7$  simulation in order to better resolve the shock. A *CFL* of 20 was employed and the simulations were run until steady state.

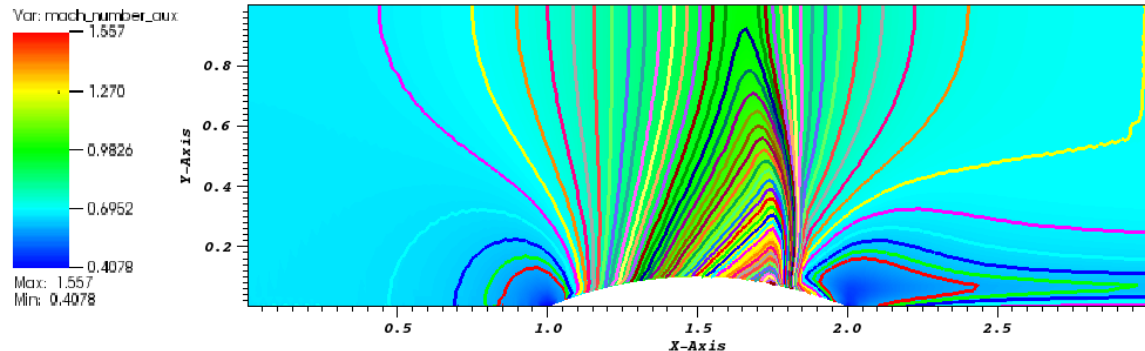


Figure 5.44: Subsonic flow over a 2-D hump: mach 0.7

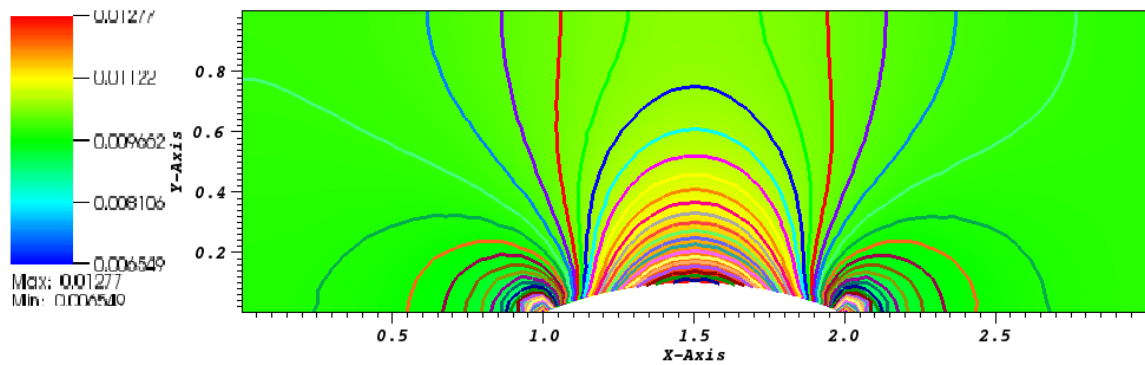


Figure 5.45: Subsonic flow over a 2-D hump: mach  $10^{-2}$

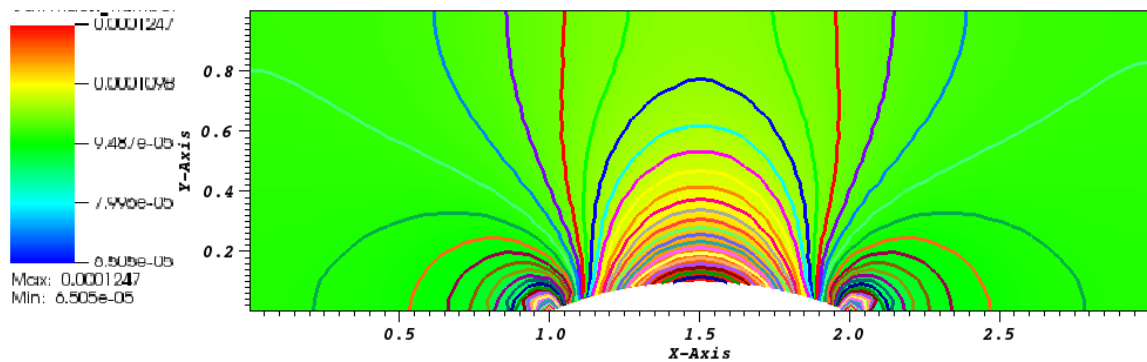


Figure 5.46: Subsonic flow over a 2-D hump: mach  $10^{-5}$

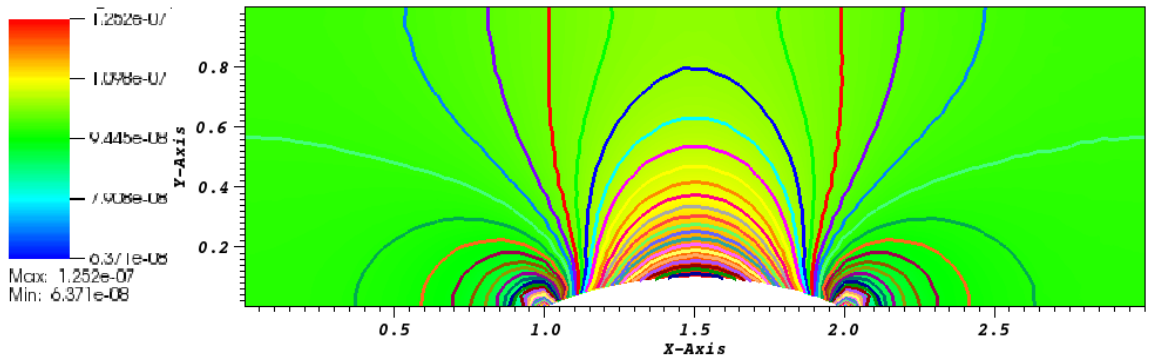


Figure 5.47: Subsonic flow over a 2-D hump:  $\text{mach } 10^{-7}$

The results showed in Fig. 5.45, Fig. 5.46 and Fig. 5.47 correspond to the low-Mach regime. The iso-Mach lines are drawn ranging from the minimum and the maximum values (provided in each legend) using 50 equally-spaced intervals. The steady-state solution is symmetric and does not depend on the value of the inlet Mach number, as expected in the incompressible limit.

In Fig. 5.44, the steady-state numerical solution develops a shock: the compressibility effect are no longer negligible. The iso-Mach lines are also plotted with 50 intervals and range from 0.4 to 1.6. The shock is well resolved and does not display any instabilities or spurious oscillations.

The results presented from Fig. 5.45 through Fig. 5.47 were obtained with the new definitions of the viscosity coefficients and illustrate the ability of the entropy viscosity method to correctly simulate several types of flows (subsonic and transonic flows) without tuning parameters.

## 6. APPLICATION OF THE ENTROPY VISCOSITY METHOD TO THE SEVEN-EQUATION MODEL

Compressible two-phase flows are found in numerous industrial applications and are an ongoing area of research in modeling and simulation over many years. A variety of models with different levels of complexity has been developed such as: five-equation model [32], six-equation model [66], and more recently the seven-equation model [55]. These models are all obtained by integrating the single-phase flow balance equations weighed by a characteristic or indicator function for each phase. The resulting system of equations contains non-conservative terms that describe the interaction between phases but also an equation for the volume fraction. Once a system of equations describing the physics is derived, the next challenging step is to develop a robust and accurate discretization to obtain a numerical solution. Assuming that the system of equations is hyperbolic under some conditions, a Riemann solver could be used but is often ruled out because of the complexity due to the number of equations involved. Furthermore, careless approximation for the treatment of the non-conservative terms can lead to failure in computing the numerical solution [1]. An alternative is to use an approximate Riemann solver, a well-established approach for single-phase flows, while deriving a consistent discretization scheme for the non-conservative terms.

This methodology was applied to the seven-equation model (SEM) introduced by Berry et al. in [55]. This model is known to be unconditionally hyperbolic which is highly desirable when working with approximate Riemann solvers and can treat a wide range of applications. Its particularity comes from the pressure and velocity relaxation terms in the volume fraction, momentum and energy equations

that can bring the two phases in equilibrium when using large values of the relaxation parameters. In other words, the seven-equation model can degenerate into the six- and five-equation models. Alike for the other two-phase flow models, solving for the seven-equation model requires a numerical solver and significant effort was dedicated to this task for spatially discontinuous schemes. Because each phase is assumed to obey the Euler equations, most of the numerical solvers are adapted from the single-phase approximate Riemann solvers. For example, Saurel et al. [59, 60] employed a HLL-type scheme to solve for the SEM but noted that excessive dissipation was added to the contact discontinuity. A more advanced HLLC-type scheme was developed in [40] but only for the subsonic case and then extended to supersonic flows in [72]. More recently, Ambroso et al. [3] proposed an approximate Riemann solver accounting for source terms such as gravity and drag forces, but with no interphase mass transfer.

We propose to investigate how the EVM applies to the seven-equation model when discretized with a CFEM. First, the multi-D seven-equation model is recalled and detailed in Section 6.1 and particular attention is given to the entropy equation. Then, the dissipative terms are derived using the entropy inequality, in Section 6.2, on the same principle of what was done in Section 5 for the multi-D Euler equations. In Section 6.3, a low-Mach asymptotic limit is performed in order to derive a definition for the viscosity coefficients consistent with the incompressible limit results. Lastly, 1-D numerical results are presented in Section 6.4.

## 6.1 Descriptions of the multi-D seven-equation model

The multi-D seven-equation model is obtained by assuming that each phase obeys the single-phase Euler equations (with phase-exchange terms) and by integrating over a control volume after multiplying by a characteristic function. The detailed derivation can be found in [55]. In this section, the governing equations are recalled

for each phase (liquid and vapor) and the source terms are described.

### 6.1.1 The system of equations for the liquid and vapor phases

The liquid phase obeys the following mass, momentum and energy balance equations, supplemented by a non-conservative volume-fraction equation:

$$\frac{\partial(\alpha\rho)_{liq} A}{\partial t} + \nabla \cdot (\alpha\rho \mathbf{u} A)_{liq} = -\Gamma A_{int} A \quad (6.1a)$$

$$\begin{aligned} \frac{\partial(\alpha\rho\mathbf{u})_{liq} A}{\partial t} + \nabla \cdot [\alpha_{liq} A (\rho\mathbf{u} \otimes \mathbf{u} + P\mathbb{I})_{liq}] &= P_{int} A \nabla \alpha_{liq} + P_{liq} \alpha_{liq} \nabla A \\ &+ A \lambda_u (\mathbf{u}_{vap} - \mathbf{u}_{liq}) - \Gamma A_{int} \mathbf{u}_{int} A \end{aligned} \quad (6.1b)$$

$$\begin{aligned} \frac{\partial(\alpha\rho E)_{liq} A}{\partial t} + \nabla \cdot [\alpha_{liq} \mathbf{u}_{liq} A (\rho E + P)_{liq}] &= P_{int} \mathbf{u}_{int} A \nabla \alpha_{liq} - \bar{P}_{int} A \mu_P (P_{liq} - P_{vap}) \\ &+ \bar{\mathbf{u}}_{int} A \lambda_u (\mathbf{u}_{vap} - \mathbf{u}_{liq}) + \Gamma A_{int} \left( \frac{P_{int}}{\rho_{int}} - H_{liq,int} \right) A \\ &+ Q_{wall,liq} + Q_{int,liq} \end{aligned} \quad (6.1c)$$

$$\frac{\partial \alpha_{liq} A}{\partial t} + A \mathbf{u}_{int} \cdot \nabla \alpha_{liq} = A \mu_P (P_{liq} - P_{vap}) - \frac{\Gamma A_{int} A}{\rho_{int}} \quad (6.1d)$$

On the same model, the equations for the vapor phase are:

$$\frac{\partial(\alpha\rho A)_{vap}}{\partial t} + \nabla \cdot (\alpha\rho \mathbf{u})_{vap} A = \Gamma A_{int} A \quad (6.2a)$$

$$\frac{\partial (\alpha \rho u)_{vap} A}{\partial t} + \nabla \cdot \left[ \alpha_{vap} A (\rho \mathbf{u} \otimes \mathbf{u} + P \mathbb{I})_{vap} \right] = P_{int} A \nabla \alpha_{vap} + P_{vap} \alpha_{vap} \nabla A \quad (6.2b)$$

$$+ A \lambda_u (\mathbf{u}_{liq} - \mathbf{u}_{vap}) + \Gamma A_{int} u_{int} A$$

$$\frac{\partial (\alpha \rho E)_{vap} A}{\partial t} + \nabla \cdot \left[ \alpha_{vap} \mathbf{u}_{vap} A (\rho E + P)_{vap} \right] = P_{int} \mathbf{u}_{int} A \nabla \alpha_{vap} - \bar{P}_{int} A \mu_P (P_{vap} - P_{liq})$$

$$+ \bar{\mathbf{u}}_{int} A \lambda_u (\mathbf{u}_{liq} - \mathbf{u}_{vap}) - \Gamma A_{int} \left( \frac{P_{int}}{\rho_{int}} - H_{vap,int} \right) A$$

$$+ Q_{wall,vap} + Q_{int,vap} \quad (6.2c)$$

$$\frac{\partial \alpha_{vap} A}{\partial t} + A \mathbf{u}_{int} \cdot \nabla \alpha_{vap} = A \mu_P (P_{vap} - P_{liq}) + \frac{\Gamma A_{int} A}{\rho_{int}} \quad (6.2d)$$

where  $\alpha_k$ ,  $\rho_k$ ,  $\mathbf{u}_k$  and  $E_k$  denote the volume fraction, the density, the velocity vector and the total specific energy of phase  $k = \{liq, vap\}$ , respectively. The phase pressure  $P_k$  is computed from an equation of state. The interfacial variables are denoted by the subscript *int* and their definition will be given in Section 6.1.2. The interfacial pressure and velocity and their corresponding average values are denoted by  $P_{int}$ ,  $\mathbf{u}_{int}$ ,  $\bar{P}_{int}$  and  $\bar{\mathbf{u}}_{int}$ , respectively.  $\Gamma$  is the net mass transfer rate per unit interfacial area from the liquid to the vapor phase and  $A_{int}$  is the interfacial area per unit volume of mixture. Also,  $H_{liq,int}$  and  $H_{vap,int}$  are the liquid and gas total specific enthalpies at the interface, respectively, with the following definition:  $H_k = h_k + 0.5 \|\mathbf{u}\|^2$ .  $\mu_P$  is the pressure relaxation coefficient and  $\lambda_u$  denotes the velocity relaxation coefficient. The wall and interfacial heat sources are denoted by  $Q_{wall,k}$  and  $Q_{int,k}$ , respectively, and are detailed in Section 6.1.2. Lastly, the cross section  $A$  is assumed spatially dependent. In the case of two-phase flows, the equation for the vapor volume fraction,

Eq. (6.2d), is simply replaced by the algebraic relation

$$\alpha_{vap} = 1 - \alpha_{liq} \quad (6.3)$$

The set of eight equations given in Eq. (6.1) and in Eq. (6.2) is now reduced to seven which yields the multi-D seven-equation model. A set of seven waves is present in such a model: two acoustic waves and a contact wave for each phase supplanted by a volume fraction wave propagating at the interfacial velocity  $\mathbf{u}_{int}$ . Considering a domain of dimension  $\mathbb{D}$ , the corresponding eigenvalues are the following for each phase  $k$ :

$$\begin{aligned}\lambda_1 &= \mathbf{u}_{int} \cdot \bar{\mathbf{n}} \\ \lambda_{2,k} &= \mathbf{u}_k \cdot \bar{\mathbf{n}} - c_k \\ \lambda_{3,k} &= \mathbf{u}_k \cdot \bar{\mathbf{n}} + c_k \\ \lambda_{d+3,k} &= \mathbf{u}_k \cdot \bar{\mathbf{n}} \text{ for } d = 1 \dots \mathbb{D},\end{aligned}$$

where  $\bar{\mathbf{n}}$  is a unit vector pointing to a given direction. For each phase  $k$ , an entropy equation can be derived when accounting only for the pressure and velocity relaxation terms (all of the terms proportional to the net mass transfer term  $\Gamma$  and the interfacial heat transfer  $Q_{int,k}$  are removed). The entropy function for a phase  $k$  is denoted by  $s_k$  and function of the density  $\rho_k$  and the internal energy  $e_k$ . The derivation is detailed in Appendix E and only the final result is recalled here when assuming that the

phase  $k$  is in interaction with a phase  $j$ :

$$(s_e)_k^{-1} \alpha_k \rho_k A \frac{Ds_k}{Dt} = \mu_P \frac{Z_k}{Z_k + Z_j} (P_j - P_k)^2 + \lambda_u \frac{Z_j}{Z_k + Z_j} (\mathbf{u}_j - \mathbf{u}_k)^2 \\ \frac{Z_k}{(Z_k + Z_j)^2} \left[ Z_j (\mathbf{u}_j - \mathbf{u}_k) + \frac{\nabla \alpha_k}{\|\nabla \alpha_k\|} (P_k - P_j) \right]^2, \quad (6.4)$$

where  $Z_k$  denotes the phasic acoustic impedance and is defined as the product of the density and the speed of sound:  $Z_k = \rho_k c_k$ . The partial derivative of the entropy function  $s_k$  with respect to the internal energy  $e_k$ ,  $(s_e)_k$ , is defined proportional to the inverse of the temperature of phase  $k$  as in Section 5 for the single phase Euler equations. The right hand-side of Eq. (6.4) is unconditionally positive since all terms are squared. Furthermore, Eq. (6.4) is valid for each phase  $k = \{liq, vap\}$  and ensures positivity of the total entropy equation that is obtained by summing over the phases:

$$\sum_k (s_e)_k^{-1} \alpha_k \rho_k A \frac{Ds_k}{Dt} = \sum_k (s_e)_k^{-1} \alpha_k \rho_k A (\partial_t s_k + \mathbf{u}_k \cdot \nabla s_k) \geq 0. \quad (6.5)$$

Note that when one phase disappears, Eq. (6.5) degenerates into the single phase entropy equation given in Eq. (5.9).

### 6.1.2 The source terms

In this section, insights about the relaxation terms, the net mass transfer term and the interfacial heat transfer terms are given.

#### 6.1.2.1 Interface pressure and velocity, mechanical relaxation coefficients

The mechanical relaxation terms are used to bring the two phases into equilibrium by making pressure and velocity equal. The mechanical relaxation coefficients  $\mu_P$  and  $\lambda_u$  can be seen as inverse relaxation times: the larger the relaxation coefficients, the faster the two phases will be brought to equilibrium. Derivation of the relaxation

terms is achieved by using rational thermodynamic to ensure consistency with the second thermodynamic law for the two-phase mixture [67]. The methodology is very similar to what is done for the derivation of the dissipative terms using the entropy inequality.

In the continuous limit of small mesh spacing and time steps along with employment of the Godunov weak wave limit, it can be shown that the pressure and velocity relaxation terms obeys the following relations [9, 11]:

$$P_{int} = \bar{P}_{int} + \frac{Z_{liq}Z_{vap}}{Z_{liq} + Z_{vap}} \frac{\nabla \alpha_{liq}}{||\nabla \alpha_{liq}||} \cdot (\mathbf{u}_{vap} - \mathbf{u}_{liq}) \quad (6.6)$$

$$\bar{P}_{int} = \frac{Z_{vap}P_{liq} + Z_{liq}P_{vap}}{Z_{liq} + Z_{vap}} \quad (6.7)$$

The interfacial velocities  $\mathbf{u}_{int}$  and its average value  $\bar{\mathbf{u}}_{int}$  are computed from:

$$\mathbf{u}_{int} = \bar{\mathbf{u}}_{int} + \frac{\nabla \alpha_{liq}}{||\nabla \alpha_{liq}||} \frac{P_{vap} - P_{liq}}{Z_{liq} + Z_{vap}} \quad (6.8)$$

$$\bar{\mathbf{u}}_{int} = \frac{Z_{liq}\mathbf{u}_{liq} + Z_{vap}\mathbf{u}_{vap}}{Z_{liq} + Z_{vap}}. \quad (6.9)$$

The pressure,  $\mu_P$ , and velocity,  $\lambda_u$ , relaxation coefficients are proportional to each other and function of the interfacial area  $A_{int}$ :

$$\lambda_u = \frac{1}{2} \mu_P Z_{liq} Z_{vap} \quad (6.10)$$

$$\mu_P = \frac{A_{int}}{Z_{liq} + Z_{vap}} \quad (6.11)$$

The specific interfacial area (i.e., the interfacial surface area per unit volume of two-phase mixture),  $A_{int}$ , must be specified from some type of flow regime map or function under the form of a correlation. In [55],  $A_{int}$  is chosen to be a function of

the liquid volume fraction:

$$A_{int} = A_{int}^{max} [6.75 (1 - \alpha_{liq})^2 \alpha_{liq}] , \quad (6.12)$$

where  $A_{int}^{max} = 5100 \text{ m}^2/\text{m}^3$ . With such definition, the interfacial area is zero in the limits  $\alpha_{liq} = 0$  and  $\alpha_{liq} = 1$ . To relax the seven-equation model to the ill-posed classical six-equation model, only the pressures should be relaxed toward a single pressure for both phases. This is accomplished by specifying the pressure relaxation coefficient to be very large, i.e., letting it approach infinity. But if the pressure relaxation coefficient goes to infinity, so does the velocity relaxation rate also approach infinity. This then relaxes the seven-equation model not to the classical six-equation model but to the mechanical equilibrium five-equation model of Kapila [32]. This reduced five-equation model is also hyperbolic and well-posed. The five-equation model provides a very useful starting point for constructing multi-dimensional interface resolving methods which dynamically captures evolving and spontaneously generated interfaces [62]. Thus the seven-equation model can be relaxed locally to couple seamlessly with such a multi-dimensional, interface resolving code.

Numerically, the mechanical relaxation coefficients  $\mu_P$  (pressure) and  $\lambda_u$  (velocity) can be relaxed independently to yield solutions to useful, reduced models (as explained previously). It is noted, however, that relaxation of pressure only by making  $\mu_P$  large without relaxing velocity will indeed give ill-posed and unstable numerical solutions, just as the classical six-equation two-phase model does, with sufficiently fine spatial resolution, as confirmed in [55, 27].

Even though the implementation of the seven-equation two-phase model does not use the generalized approach of DEM [55], the interfacial pressure and velocity closures as well as the pressure and velocity relaxation coefficients of Equations (6.6)

to (6.11) are utilized.

### *6.1.2.2 Interphase mass transfer*

For vapor to be formed from the liquid phase (vaporization) energy must be added to the liquid to produce vapor at nucleation sites; whether the liquid is heated directly or decompressed below its saturation pressure. A liquid to vapor phase change may occur based on two main mechanisms. The first is related to vaporization induced by external heating or heat transfer in a nearly constant pressure environment which is called heterogeneous boiling, or simply boiling. This heat input can occur through a solid/liquid interface with the solid typically hotter than the liquid, or through a liquid/gas interface with the gas being hotter than the liquid.

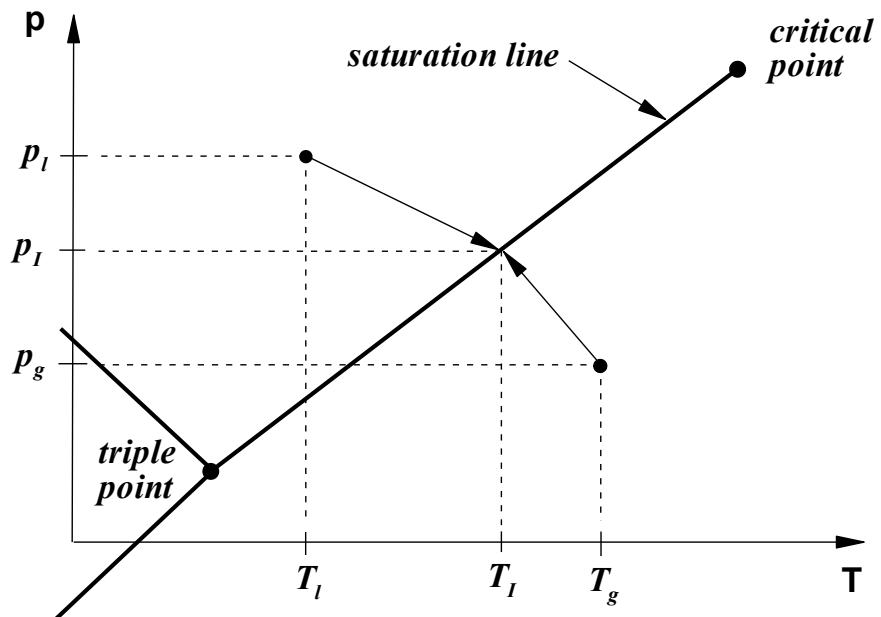
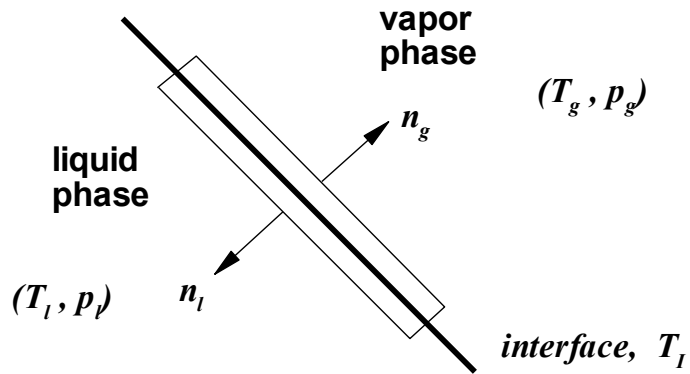


Figure 6.1: Interface control volume (top);  $T$ - $p$  state space around saturation line,  $T_{liq} < T_{vap}$ , (bottom) [55].

To examine the mass flow rate between phases, local mechanisms of the vaporization (condensation) process are considered between the liquid phase and its associated vapor in the presence of temperature gradients. The mechanisms of interest here are dominated by heat diffusion at the interface. The pertinent local equations

to consider are the mass and energy equations. As a vaporization front propagates slowly (on the order of 1 mm/s to 1 m/s) compared to acoustic waves present in the medium (which propagate with speeds of the order 1 km/s), acoustic propagation results in quasi-isobaric pressure evolution through vaporization fronts. The momentum equation is therefore not needed, because the quasi-isobaric assumption (neglecting the pressure and kinetic energy variations in the total energy equation) is made. A simple expression for the interphase mass flow rate is obtained from [55]:

$$\begin{aligned}\Gamma = \Gamma_{vap} &= \frac{h_{T,liq}(T_{liq} - T_{int}) + h_{T,vap}(T_{vap} - T_{int})}{h_{vap,int} - h_{liq,int}} \\ &= \frac{h_{T,liq}(T_{liq} - T_{int}) + h_{T,vap}(T_{vap} - T_{int})}{L_v(T_{int})}\end{aligned}\quad (6.13)$$

where  $L_v(T_{int}) = h_{vap,int} - h_{liq,int}$  represents the latent heat of vaporization. The interface temperature is determined by the saturation constraint  $T_{int} = T_{sat}(P)$  with the appropriate pressure  $P = \bar{P}_{int}$  determined above, the interphase mass flow rate is thus determined. The lower graphic of Figure 6.1 schematically shows the  $P$ - $T$  state space in the vicinity of the saturation line (shown for the case with  $T_{liq} < T_{vap}$ ).

To better illustrate the model for vaporization or condensation, Figure 6.2 shows pure liquid and pure vapor regions separated by an interface.

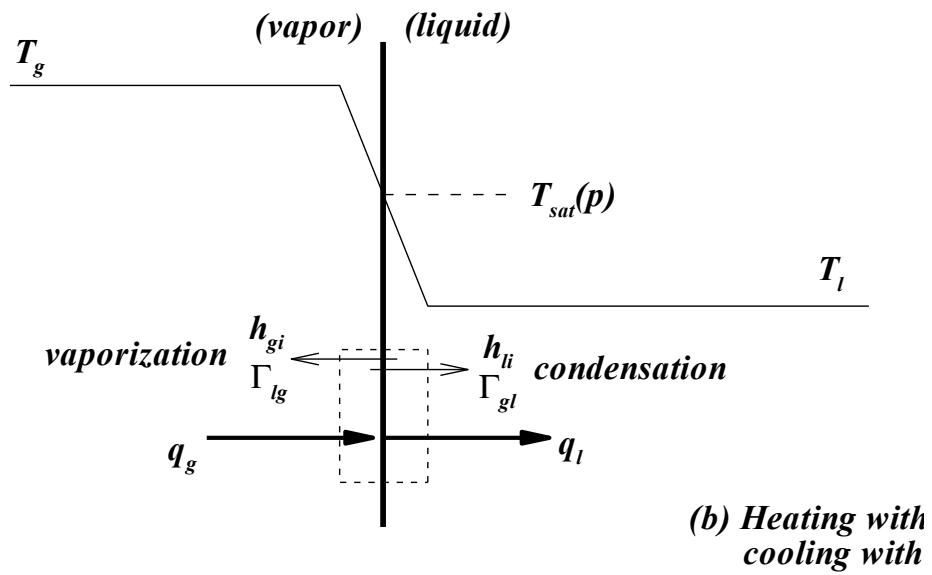
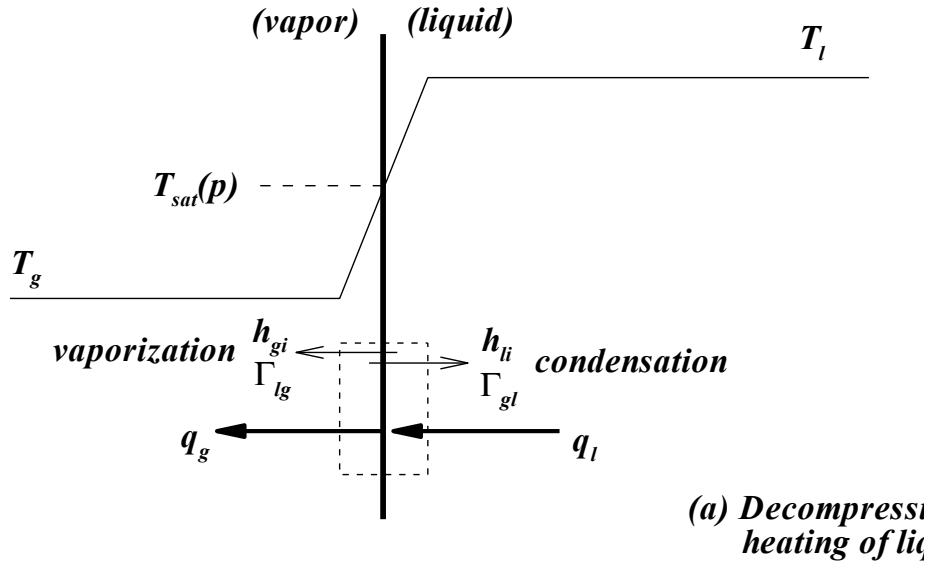


Figure 6.2: Vaporization and condensation at a liquid-vapor interface (after Moody [47]).

Representative temperature profiles are shown for heat transfer from vapor to liquid or liquid to vapor. As discussed by Moody [47], either vaporization or condensation can occur for both temperature profiles. The interphase mass transfer is determined by the net interfacial heat transfer: if net heat transfer is toward the

interface, vapor will form; conversely, if net heat transfer is away from the interface, liquid will condense. Figure 6.2 shows heat transfer rates  $q_{vap}$  and  $q_{liq}$  from the vapor and liquid sides of the interface. For bidirectional phase change (vaporization and condensation), mass transfer based on heat balance at the interface is adopted. When vaporization occurs, vapor is assumed to form at a saturated interface temperature  $T_{int} = T_{sat}(\bar{P}_{int})$ . If condensation occurs, liquid is assumed to form also at a saturated interface temperature  $T_{int} = T_{sat}(\bar{P}_{int})$ . The interfacial total enthalpies  $H_{k,int}$  correspond to the saturated values in order that the interphase mass transfer rate and conservation of total energy be compatible:

$$H_{k,int} = h_{k,int} + \frac{1}{2}u_{int}^2 \quad (6.14)$$

for phase  $k = (liq, vap)$ , where  $h_{k,int}$  is the phase  $k$  specific enthalpy evaluated at the interface condition. Phasic specific enthalpy depends upon the equation of state used and will be discussed with the equations of state. The interfacial density corresponds to the liquid saturated density  $\rho_{int} = \rho_{liq,sat}(P_{int})$ .

#### 6.1.2.3 Interface direct heat transfer

Without wall boiling, a simple model for the direct convective heat transfer  $Q_{wall}$  from the wall to fluid phase  $k$  will be the same as that of a single-phase except the duct wall area over which this heat transfer can occur is weighted by the wetted fraction of the phase. That is,

$$Q_{wall,k} = h_{w,k}P_w (T_k - T_{wall}) \alpha_k \quad (6.15)$$

for phase  $k = (liq, vap)$ , where  $h_{w,k}$  is the convective wall heat transfer coefficient associated with phase  $k$  and  $P_w$  is the wall-heated perimeter. Similarly, the direct

heat transfer from/to the interface to/from the phase  $k$ , which will also be used to determine the mass transfer between the phases, is

$$Q_{int,k} = h_{T,k} (T_{int} - T_k) A_{int} A \quad (6.16)$$

with  $h_{T,k}$  denoting the convective heat transfer coefficient between the interface and phase  $k$ . The phasic bulk temperature  $T_k$  is determined from the respective phase's equation of state.

#### 6.1.2.4 Stiffened Gas Equation of State (SGEOS) for two-phase flows

With the seven-equation two-phase model each phase is compressible and behaves with its own convex equation of state (EOS). For initial development purposes it was decided to use a simple form capable of capturing the essential physics. For this purpose the stiffened gas equation of state (SGEOS) [38] was selected (as it was also for single phase),

$$P_k(\rho_k, e_k) = (\gamma_k - 1)\rho_k(e_k - q_k) - \gamma P_{k,\infty} \quad (6.17)$$

where  $P_k$ ,  $\rho_k$ ,  $e_k$ , and  $q_k$  are the pressure, density, internal energy, and the binding energy of the fluid considered, respectively. The parameters  $\gamma_k$ ,  $q_k$ , and  $P_{k,\infty}$  are fluid-dependent coefficients. The first term on the right hand side is a repulsive effect that is present for any state (gas, liquid, or solid), and is due to molecular vibrations. The second term on the right represents the attractive molecular effect that guarantees the cohesion of matter in the liquid or solid phases. The parameters used in this SGEOS are determined by using a reference curve, usually in the  $(P_k, \frac{1}{\rho_k})$  plane.

To extend this equation of state for two phases, LeMetayer [38] uses the saturation curves as this reference curve to determine the stiffened gas parameters for liquid and vapor phases. The SGEOS is the simplest prototype that contains the main

physical properties of pure fluids, repulsive and attractive molecular effects, thereby facilitating the handling of the essential physics and thermodynamics with a simple analytical formulation. Thus each fluid has its own thermodynamics. For each phase the thermodynamic state is determined by the SGEOS:

$$e_k(P_k, \rho_k) = \frac{P_k + \gamma_k P_{k,\infty}}{(\gamma_k - 1)\rho_k} + q_k \quad (6.18)$$

$$\rho_k(P_k, T_k) = \frac{P_k + P_{k,\infty}}{(\gamma_k - 1)c_{k,v}T_k} \quad (6.19)$$

$$h_k(T_k) = \gamma_k c_{k,v} T_k + q_k \quad (6.20)$$

$$g_k(P_k, T_k) = \left( \gamma_k c_{k,v} - q'_k \right) T_k - c_{k,v} T_k \ln \frac{T_k^\gamma}{(P_k + P_{k,\infty})^{\gamma_k - 1}} + q_k \quad (6.21)$$

where  $T_k$ ,  $h_k$ , and  $g_k$  are the temperature, enthalpy, and Gibbs free enthalpy, respectively, of the phase considered. In addition to the three fluid parameters mentioned above, two additional constants have been introduced, the constant volume specific heat  $c_{k,v}$  and the parameter  $q'_k$ . The method to determine these parameters in liquid-vapor systems, and in particular the coupling of liquid and vapor parameters, is given in [38]. The values for water and its vapor from that reference are given in Table 2. These parameter values appear to yield reasonable approximations over a temperature range from 298K to 473K. For higher temperature range the parameters can easily be refit.

Unlike van der Waals type modeling where mass transfer is a thermodynamic path, with the seven-equation two-phase model the mass transfer modeling, which produces a relaxation toward thermodynamic equilibrium, is achieved by a kinetic process. Thus the seven-equation model preserves hyperbolicity during mass transfer. From equation (6.20) it is readily seen that the phase  $k$  specific enthalpy evaluated

at the interface condition from equation (6.14) is

$$h_{k,int} = c_{p,k} T_{int} + q_k \quad (6.22)$$

because  $c_{p,k} = \gamma_k c_{v,k}$ .

The bulk interphase mass transfer from the liquid phase to the vapor phase  $\Gamma$  is due to their difference in Gibb's free energy. At saturated conditions the Gibb's energies of the two phases are equal. It is necessary to determine the saturation temperature  $T_{sat}(P)$  for given pressure  $P = \bar{P}_{int}$  and the heat of vaporization  $L_v(T_{sat}(\bar{P}_{int}))$  at this saturation temperature with the SGEOS for each phase. For this calculation, the procedure of [38] is adopted. This procedure for the determination of SGEOS parameters can be made very accurate provided the two reference states are chosen sufficiently close to represent the experimental saturation curves as locally quasi-linear. Restrictions occur near the critical point, but away from this point, a wide range of temperatures and pressures can be considered. At thermodynamic equilibrium at the interface, the two phasic Gibbs free enthalpies must be equal,  $g_{vap} = g_{liq}$ , so the use of equation (6.21) yields

$$\ln(P + P_{\infty,vap}) = A + \frac{B}{T} + C \ln(T) + D \ln(P + P_{\infty,liq}) \quad (6.23)$$

where

$$A = \frac{c_{p,liq} - c_{p,vap} + q'_{vap} - q'_{liq}}{c_{p,vap} - c_{v,vap}} \quad (6.24)$$

$$B = \frac{q_{liq} - q_{vap}}{c_{p,vap} - c_{v,vap}} \quad (6.25)$$

$$C = \frac{c_{p,vap} - c_{p,liq}}{c_{p,vap} - c_{v,vap}} \quad (6.26)$$

$$D = \frac{c_{p,liq} - c_{v,liq}}{c_{p,vap} - c_{v,vap}} . \quad (6.27)$$

Relation (6.23) is nonlinear, but can be used to compute the theoretical curve  $T_{sat}(P)$ .

A simple Newton iterative numerical procedure is used. With  $T_{sat}(P)$  determined, the heat of vaporization is calculated as

$$\begin{aligned} L_v(T_{int}) &= h_{vap,int} - h_{liq,int} \\ &= h_{k,int} \\ &= (\gamma_{vap} c_{v,vap} T + q_{vap}) - (\gamma_{liq} c_{v,liq} T + q_{liq}) . \end{aligned} \quad (6.28)$$

## 6.2 A viscous regularization for the multi-D seven-equation model

In this section, the dissipative terms for the multi-D seven-equation model *with pressure and velocity relaxation source terms* are derived (the mass and energy transfer terms are omitted). The methodology proposed in Section 2 is followed. For clarity purpose, the seven-equation model with pressure and velocity relaxation terms is recalled when considering a phase  $k$  in interaction with a second phase  $j$ :

$$\partial_t (\alpha_k A) + A \mathbf{u}_{int} \cdot \nabla \alpha_k = A \mu_P (P_k - P_j) \quad (6.29a)$$

$$\partial_t (\alpha_k \rho_k A) + \nabla \cdot (\alpha_k \rho_k \mathbf{u}_k A) = 0 \quad (6.29b)$$

$$\begin{aligned} \partial_t (\alpha_k \rho_k u_k A) + \nabla \cdot [\alpha_k A (\rho_k \mathbf{u}_k \otimes \mathbf{u}_k + P_k \mathbb{I})] = \\ \alpha_k P_k \nabla A + P_{int} A \nabla \alpha_k + A \lambda_u (\mathbf{u}_j - \mathbf{u}_k) \end{aligned} \quad (6.29c)$$

$$\begin{aligned} \partial_t (\alpha_k \rho_k E_k A) + \nabla \cdot [\alpha_k A \mathbf{u}_k (\rho_k E_k + P_k)] = \\ A P_{int} \mathbf{u}_{int} \cdot \nabla \alpha_k - \mu_P \bar{P}_{int} (P_k - P_j) + A \lambda_u \bar{\mathbf{u}}_{int} \cdot (\mathbf{u}_j - \mathbf{u}_k) \end{aligned} \quad (6.29d)$$

In order to apply the EVM, dissipative terms are added to each equation of the system given in Eq. (6.29), which yields:

$$\partial_t (\alpha_k A) + \mathbf{u}_{int} A \nabla \alpha_k = A \mu_P (P_k - P_j) + \nabla \cdot \mathbf{l}_k \quad (6.30a)$$

$$\partial_t (\alpha_k \rho_k A) + \nabla \cdot (\alpha_k \rho_k \mathbf{u}_k A) = \nabla \cdot \mathbf{f}_k \quad (6.30b)$$

$$\begin{aligned} \partial_t (\alpha_k \rho_k \mathbf{u}_k A) + \nabla \cdot [\alpha_k A (\rho_k \mathbf{u}_k \otimes \mathbf{u}_k + P_k \mathbb{I})] = \\ \alpha_k P_k \nabla A + P_{int} A \nabla \alpha_k + A \lambda_u (\mathbf{u}_j - \mathbf{u}_k) + \nabla \cdot \mathbf{g}_k \end{aligned} \quad (6.30c)$$

$$\begin{aligned} \partial_t (\alpha_k \rho_k E_k A) + \nabla \cdot [\alpha_k A \mathbf{u}_k (\rho_k E_k + P_k)] = \\ P_{int} A \mathbf{u}_{int} \cdot \nabla \alpha_k - \mu_P \bar{P}_{int} (P_k - P_j) + A \lambda_u \bar{\mathbf{u}}_{int} \cdot (\mathbf{u}_j - \mathbf{u}_k) + \nabla \cdot (\mathbf{h}_k + \mathbf{u} \cdot \mathbf{g}_k) \end{aligned} \quad (6.30d)$$

where  $\mathbf{f}_k$ ,  $\mathbf{g}_k$ ,  $\mathbf{h}_k$  and  $\mathbf{l}_k$  are the dissipative terms. The next step consists of deriving the entropy equation for the phase  $k$ , on the same model as what is done in Appendix E. Extra terms will appear in the right-hand-side of the entropy equation due to the dissipative terms. By choosing properly the definition of the dissipative terms, the sign of these extra terms can be controlled in order to ensure positivity of the entropy residual:

1. recast the system of equation given in Eq. (6.30) in terms of the primitive variables  $(\alpha_k, \rho_k, \mathbf{u}_k, e_k)$ .
2. derive the entropy equation by using the chain rule:

$$\frac{Ds_k}{Dt} = (s_\rho)_k \frac{D\rho_k}{Dt} + (s_e)_k \frac{De_k}{Dt} \quad (6.31)$$

where  $\frac{D}{Dt}$  is the material derivative. The terms  $(s_e)_k$  and  $(s_\rho)_k$  denote the partial derivative of the entropy  $s_k$  with respect to  $e_k$  and  $\rho_k$ , respectively.

3. isolate the terms of interest and choose an appropriate expression for each of the dissipative terms in order to ensure positivity of the right-hand side.

We first recast Eq. (6.30) in terms of the primitive variables: the volume fraction equation remains unchanged. The equation for the primitive variable  $\rho_k$  is derived by combining Eq. (6.30a) and Eq. (6.30b):

$$\alpha_k A \left[ \partial_t \rho_k + \left( \mathbf{u}_k - \underline{\underline{\mathbf{u}_{int}}} \right) \cdot \nabla \rho_k \right] = \underline{\underline{A \rho_k \mu_P (P_k - P_j)}} + \nabla \cdot \mathbf{f}_k - \rho_k \nabla \cdot \mathbf{l}_k \quad (6.32)$$

The velocity equation is obtained by subtracting the density equation from the momentum equation:

$$\begin{aligned} \alpha_k \rho_k A [\partial_t \mathbf{u}_k + \mathbf{u}_k \cdot \nabla \cdot \mathbf{u}_k] + \nabla \cdot (\alpha_k \rho_k A P_k \mathbb{I}) = \\ \underline{\alpha_k P_k \nabla A + P_{int} A \nabla \alpha_k + A \lambda (\mathbf{u}_j - \mathbf{u}_k)} + \nabla \cdot \mathbf{g}_k - \mathbf{u}_k \otimes \mathbf{f}_k \end{aligned} \quad (6.33)$$

After multiplying Eq. (6.33) by the velocity vector  $\mathbf{u}_k$ , the resulting kinetic energy equation is subtracted from the total energy equation to obtain the internal energy equation for phase  $k$ :

$$\begin{aligned} \alpha_k \rho_k A [\partial_t \mathbf{e}_k + \mathbf{u}_k \cdot \nabla \cdot \mathbf{e}_k] + \alpha_k \rho_k A P_k \nabla \mathbf{u}_k = \\ \underline{\underline{P_{int} A (\mathbf{u}_{int} - \mathbf{u}_k) \cdot \nabla \alpha_k}} - \underline{\underline{\alpha_k P_k \mathbf{u}_k \nabla A}} \\ \underline{\underline{- \bar{P}_{int} A \mu_P (P_k - P_j)}} + \underline{\underline{A \lambda_u (\mathbf{u}_j - \mathbf{u}_k) \cdot (\bar{\mathbf{u}}_{int} - \mathbf{u}_k)}} \\ + \nabla \cdot \mathbf{h}_k + \mathbf{g}_k : \nabla \mathbf{u}_k + \|\mathbf{u}\|_k^2 \mathbf{f}_k \end{aligned} \quad (6.34)$$

The underline terms in Eq. (6.32) and Eq. (6.34) yield the positive terms in the right-hand-side of Eq. (6.4) and thus are ignored in the remaining of the derivation. The entropy equation is now obtained by combining the density equation (Eq. (6.32)) and the internal energy equation (Eq. (6.34)) through the chain rule given in Eq. (6.31) to yield:

$$\alpha_k \rho_k A \frac{D s_k}{D t} = (s_e)_k [\nabla \cdot \mathbf{h}_k + \mathbf{g}_k : \nabla \mathbf{u}_k + (\|\mathbf{u}\|_k^2 - e_k) \nabla \cdot \mathbf{f}_k] + (\rho s_\rho)_k [\nabla \cdot \mathbf{f}_k - \rho_k \nabla \cdot \mathbf{l}_k]. \quad (6.35)$$

where it was assumed that the entropy of phase  $k$  satisfies the second thermodynamic law:

$$T_k ds_k = de_k - P_k \frac{d\rho_k}{\rho_k^2}$$

which implies  $P_k(s_e)_k + \rho_k(s_\rho)_k = 0$ , (6.36)

$$(s_e)_k = T_k^{-1} \text{ and } (s_\rho)_k = -(s_e)_k P_k \frac{d\rho_k}{\rho_k^2}.$$

From this point, two options are available in order to derive the dissipative terms: either we consider the total entropy residual of the system by summing Eq. (6.35) over each phase, or we can consider each phase independently. This dilemma can be answered by remembering that the seven-equation model degenerates into the single phase flow equations in the limits  $\alpha_k = 0, 1$ . Thus, the dissipative terms also have to be consistent with the single-phase flow limits. As a result, it is chosen to derive the dissipative terms by considering each phase independently which will automatically ensure positivity of the total entropy residual as well.

The right-hand side of Eq. (6.35) can be further simplified by using the following expression for the dissipative terms  $\mathbf{f}_k$ ,  $\mathbf{g}_k$  and  $\mathbf{h}_k$ :

$$\mathbf{f}_k = \tilde{\mathbf{f}}_k + \rho_k \mathbf{l}_k \quad (6.37)$$

$$\mathbf{g}_k = \alpha_k \rho_k A \mu_k \mathbb{F}(\mathbf{u}_k) + \mathbf{f}_k \otimes \mathbf{u}_k \quad (6.38)$$

$$\mathbf{h}_k = \tilde{\mathbf{h}}_k - \frac{||\mathbf{u}||^2}{2} \mathbf{f}_k + (\rho e)_k \mathbf{l}_k. \quad (6.39)$$

Note the area function  $A$  in the definition of  $\mathbf{g}$ . It yields:

$$\begin{aligned} \alpha_k \rho_k A \frac{D s_k}{D t} = & \\ \underbrace{(s_e)_k \alpha_k \rho_k A \mu_k \mathbb{F}(\mathbf{u}_k) : \nabla \mathbf{u}_k}_{\mathcal{R}_1} + & \underbrace{\left[ \nabla \cdot \tilde{\mathbf{h}}_k - e_k \nabla \cdot \tilde{\mathbf{f}}_k \right] + (\rho s_\rho)_k \nabla \cdot \tilde{\mathbf{f}}_k}_{\mathcal{R}_2} + \\ \underbrace{(s_e)_k \nabla \cdot (\rho_k e_k \mathbf{l}_k) - (s_e)_k e_k \nabla \cdot (\rho_k \mathbf{l}_k) + \rho_k (s_\rho)_k \nabla \cdot (\rho_k \mathbf{l}_k) - \rho_k^2 (s_\rho)_k \nabla \cdot \mathbf{l}_k}_{\mathcal{R}_3}, & \quad (6.40) \end{aligned}$$

where  $\mu_k$  is a positive viscosity coefficient for phase  $k$ . For simplicity, the right-hand-side of Eq. (6.40) is split into three terms denoted by  $\mathcal{R}_1$ ,  $\mathcal{R}_2$  and  $\mathcal{R}_3$ . Since  $(s_e)_k$  is defined as the inverse of the temperature and thus positive, the sign of the first term,  $\mathcal{R}_1$ , is conditioned by the choice of the function  $\mathbb{F}(\mathbf{u}_k)$  so that the product with the tensor  $\nabla \mathbf{u}_k$  is positive. As in [24],  $\mathbb{F}(\mathbf{u}_k)$  is chosen proportional to the symmetric gradient of the velocity vector  $\nabla^s \mathbf{u}_k$ , whom entries are given by  $(\nabla^s \mathbf{u})_{i,j} = \frac{1}{2} (\partial_{x_i} u_j + \partial_{x_j} u_i)$ . Such a choice ensures the associated dissipative terms to be rotationally invariant and also positivity of  $\mathcal{R}_1$ . An other option would be to simply set  $\mathbb{F}(\mathbf{u}_k)$  proportional to  $\nabla \mathbf{u}_k$  which allows to recover the parabolic regularization.

After a few lines of algebra, the third term  $\mathcal{R}_3$  can be recast as a function of the gradient of the entropy as follows:

$$\mathcal{R}_3 = \rho_k A \mathbf{l}_k \cdot \nabla s_k. \quad (6.41)$$

One of the assumptions made in the entropy minimum principle is to that the entropy is at a minimum which implies that its gradient is null. Because of this, it follows that the term  $\mathcal{R}_3$  is zero at the minimum and thus, the entropy minimum principle is verified independently of the definition of the dissipative term  $\mathbf{l}_k$  used in the volume

fraction equation. It will be explained later in this section how to derive a definition for  $\mathbf{l}_k$ .

We now focus on the term denoted by  $\mathcal{R}_2$ , that is found identical to the right-hand-side of the single phase entropy equation obtained from the multi-D Euler equations (see Eq. (A.6) in Appendix A). Thus, following [24] and also Appendix A, the term  $\mathcal{R}_2$  is known to be positive when (i) assuming concavity of the entropy function  $s_k$  with respect to the internal energy  $e_k$  and the specific volume  $1/\rho_k$  (or convexity of  $-s_k$ ) and (ii) choosing the following definitions for the dissipative terms  $\tilde{h}_k$  and  $\tilde{f}_k$ :

$$\tilde{\mathbf{f}}_k = \alpha_k A \kappa_k \nabla \rho_k \quad (6.42)$$

$$\tilde{\mathbf{h}}_k = \alpha_k A \kappa_k \nabla (\rho e)_k, \quad (6.43)$$

where  $\kappa_k$  is another positive viscosity coefficient. The entropy equation can now be written in its final form:

$$\begin{aligned} \alpha_k \rho_k A \frac{D s_k}{D t} - \mathbf{f}_k \cdot \nabla s_k - \nabla \cdot (\alpha_k \rho_k A \nabla s_k) = \\ - \alpha_k A \kappa_k \mathbf{Q}_k + (s_e)_k \alpha_k A \rho_k \mu_k \nabla^s \mathbf{u}_k : \nabla \mathbf{u}_k, \end{aligned} \quad (6.44)$$

where  $\mathbf{Q}_k$  is a negative semi-definite quadratic form defined as:

$$\begin{aligned} \mathbf{Q}_k &= X_k^t \Sigma_k X_k \\ \text{with } X_k &= \begin{bmatrix} \nabla \rho_k \\ \nabla e_k \end{bmatrix} \text{ and } \Sigma_k = \begin{bmatrix} \partial_{\rho_k} (\rho_k^2 \partial_{\rho_k} s_k) & \partial_{\rho_k, e_k} s_k \\ \partial_{\rho_k, e_k} s_k & \partial_{e_k, e_k} s_k \end{bmatrix}. \end{aligned}$$

Eq. (6.44) is used to prove the entropy minimum principle: assuming that  $s_k$  reaches its minimum value in  $\mathbf{r}_{min}(t)$  at each time  $t$ , the gradient,  $\nabla s_k$ , and Laplacian,  $\Delta s_k$ , of the entropy are null and positive at this particular point, respectively. Furthermore, it is recalled that the viscosity coefficients  $\mu_k$  and  $\kappa_k$  are positive by definition. Then, because the right-hand-side of Eq. (6.44) is proven positive, the entropy minimum principle holds for each phase  $k$ , **independently of the definition of the dissipative term  $\mathbf{l}_k$** , such as:

$$\alpha_k \rho_k A \partial_t s_k(\mathbf{r}_{min}, t) \geq 0 \Rightarrow \partial_t s_k(\mathbf{r}_{min}, t) \geq 0$$

It remains to obtain a definition for the dissipative term  $\mathbf{l}_k$  used in the volume fraction equation. A way to achieve this is to consider the volume fraction equation, Eq. (6.30a), by itself and notice that it is an hyperbolic equation with eigenvalue  $\mathbf{u}_{int}$ . An entropy equation can be derived and used to prove the entropy minimum principle by properly choosing the dissipative term. The objective is to ensure positivity of the volume fraction and also uniqueness of the weak solution. Following the work of Guermond et al. in [29, 30] and by analogy with Burger's equation described in Section 4, it can be shown that a dissipative term ensuring positivity and uniqueness of the weak solution for the volume fraction equation, is of the form  $\mathbf{l}_k = \beta_k A \nabla \alpha_k$  where  $\beta_k$  is a positive viscosity coefficient.

All of the dissipative terms are now defined and recalled here:

$$\mathbf{l}_k = \beta_k A \nabla \alpha_k \quad (6.45a)$$

$$\mathbf{f}_k = \alpha_k A \kappa_k \nabla \rho_k + \rho_k A \mathbf{l}_k \quad (6.45b)$$

$$\mathbf{g}_k = \alpha_k A \mu_k \rho \nabla^s \mathbf{u}_k \quad (6.45c)$$

$$\mathbf{h}_k = \alpha_k A \kappa_k \nabla (\rho e)_k + \mathbf{u}_k : \mathbf{g}_k - \frac{\|\mathbf{u}_k\|^2}{2} \mathbf{f}_k + (\rho e)_k \mathbf{l}_k \quad (6.45d)$$

At this point, some remarks are in order:

1. The viscous regularization given in Eq. (6.45) for the multi-D seven-equation model, is equivalent to the parabolic regularization [51] when assuming  $\beta_k = \kappa_k$  and  $\mathbb{F}(\mathbf{u}_k) = \alpha_k \rho_k \kappa_k \nabla \mathbf{u}_k$ . However, decoupling between the regularization on the velocity and on the density in the momentum equation is important to make the regularization rotation invariant but also to ensure well-scaled dissipative terms for a wide range of Mach number as was shown in Section 5 for the multi-D Euler equations.
2. The dissipative term  $\mathbf{l}_k$  requires the definition of a new viscosity coefficient  $\beta_k$ . It was shown that this viscosity coefficient is independent of the other viscosity coefficients  $\mu_k$  and  $\kappa_k$ . Its definition should account for the eigenvalue associated with the void fraction equation  $\mathbf{u}_{int}$ . In addition, an entropy residual can be determined by analogy to Burger's equation.
3. The dissipative term  $\mathbf{f}_k$  is a function of  $\mathbf{l}_k$ . Thus, all of the other dissipative terms are also functions of  $\mathbf{l}_k$ .
4. The partial derivatives  $(s_e)_k$  and  $(s_{\rho_k})_k$  can be computed using the definition provided in Eq. (6.36) and are functions of the thermodynamic variables: pressure, temperature and density.

5. All of the dissipative terms are chosen to be proportional to the void fraction  $\alpha_k$  and the cross-sectional area  $A$ , but the one in the volume fraction equation that is only proportional to  $A$ . For instance,  $\alpha_k A \nabla \rho_k$  is the flux of the dissipative term in the continuity equation through the area seen by the phase  $\alpha_k A$ . When one of the phases disappears, the dissipative terms must go to zero for consistency. On the other hand, when  $\alpha_k$  goes to one, the single-phase equation must be recovered.
6. Compatibility of the viscous regularization proposed in Eq. (6.45) with the generalized entropies identified in Harten et al. [26] has not been investigated yet. However, it is believed that the entropy inequalities still holds because of the similarities of the entropy residual for the multi-D seven-equation model with the entropy residual derived in the single phase flow case [24].

Through the derivations of the viscous regularization, it was noted that another set of dissipative terms  $\mathbf{f}_k$  and  $\mathbf{l}_k$  would also ensure positivity of the entropy residual:

$$\mathbf{l}_k = \beta_k T_k \left[ \frac{\rho_k}{P_k + \rho_k e_k} \nabla \left( \frac{P_k}{\rho_k e_k} \right) - \frac{1}{P_k} \nabla \rho_k \right] \quad (6.46a)$$

$$\mathbf{f}_k = \kappa_k \nabla \rho_k + \frac{\rho_k^2 (s_\rho)_k}{(\rho s_\rho - e s_e)_k} \mathbf{l}_k \quad (6.46b)$$

However, the definition of  $\mathbf{l}_k$  proposed in Eq. (6.46a) was not considered as valid for the following reasons: positivity of the volume fraction cannot be achieved and the parabolic regularization is not retrieved.

A rotation invariant viscous regularization for the multi-D seven-equation model is now available involving three viscosity coefficients  $\beta_k$ ,  $\mu_k$  and  $\kappa_k$ , for each phase  $k$ . Definition of these viscosity coefficients is the purpose of the next section (Sec-

tion 6.3).

### 6.3 Low-mach asymptotic limit and viscosity coefficients

This section aims at deriving a definition of the viscosity coefficients involved in the viscous regularization for the multi-D seven-equation model. We propose to follow the same methodology as in Section 5 for the multi-D Euler equations: after obtaining the non-dimensional equations, a definition for the viscosity coefficients is derived based on the entropy residual and consistent with the low-Mach asymptotic limit. Particular attention is paid to the definition of the viscosity coefficient  $\beta_k$  used in the volume fraction equation.

Using the EVM to define the viscosity coefficients is not the unique option here. Other numerical methods initially developed for single-phase flows, such as pressure-based and Lapidus viscosity methods, could be used as a starting point and adapted to the seven-equation model. Such a reasoning is motivated by one of the initial assumptions of the seven-equation model that assumes each phase verifies the Euler equations.

#### 6.3.1 *Definition of the viscosity coefficients*

The viscous regularization derived in Section 6.2 for the multi-D SEM requires three viscosity coefficients for each phase  $k$  denoted by  $\beta_k$ ,  $\mu_k$  and  $\kappa_k$ . Following the methodology detailed in Section 2.2, for each viscosity coefficient an upper bound, denoted by the subscript  $max$ , is defined and referred to as the first-order viscosity coefficient, along with a entropy viscosity coefficient that is set proportional to an

entropy residual and denoted by the subscript  $e$ :

$$\beta_k(\mathbf{r}, t) = \min(\beta_{e,k}(\mathbf{r}, t), \beta_{max,k}(\mathbf{r}, t)),$$

$$\mu_k(\mathbf{r}, t) = \min(\mu_{e,k}(\mathbf{r}, t), \mu_{max,k}(\mathbf{r}, t)),$$

$$\kappa_k(\mathbf{r}, t) = \min(\kappa_{e,k}(\mathbf{r}, t), \kappa_{max,k}(\mathbf{r}, t)).$$

where all of the variables are locally defined. As for the multi-D single-phase Euler equations and for the same reasons, the entropy residual for each phase  $k$  is recast as a function of the pressure, the velocity, the density and the speed of sound as follows:

$$R_k(\mathbf{r}, t) := \partial_t s_k + \mathbf{u}_k \cdot \nabla s_k = \frac{Ds_k}{Dt} = \frac{(s_e)_k}{(P_e)_k} \left( \underbrace{\frac{DP_k}{Dt} - c_k^2 \frac{D\rho_k}{Dt}}_{\tilde{R}_k(\mathbf{r}, t)} \right), \quad (6.47)$$

where  $\tilde{R}_k(\mathbf{r}, t)$  is the new entropy residual of phase  $k$  and will experience the same variations as  $R_k(\mathbf{r}, t)$ .

We first choose to investigate the definitions of the high and first-order viscosity coefficients for  $\mu_k$  and  $\kappa_k$ . It is noted that the dissipative terms function of  $\mu_k$  and  $\kappa_k$  are the same as the ones for the single-phase Euler equation when considering  $\tilde{A} = \alpha_k A$  as a pseudo cross section. Furthermore, we need to ensure consistency with the single-phase Euler equation in the limits  $\alpha_k \rightarrow 1$ . Thus, based on the work done in Section 5.2.1, the first order viscosity coefficients are set proportional to the local maximum eigenvalue  $\lambda_k$ ,

$$\kappa_{max,k}(\mathbf{r}, t) = \mu_{max,k}(\mathbf{r}, t) = \frac{h}{2} (||\mathbf{u}_k|| + c_k) \quad (6.48)$$

and the entropy viscosity viscosity coefficients are defined as

$$\mu_{e,k}(\mathbf{r}, t) = h^2 \frac{\max \left( |\tilde{R}_k(\mathbf{r}_q, t)|, \|\mathbf{u}_k(\mathbf{r}_q, t)\| J[P_k](t), \|\mathbf{u}_k(\mathbf{r}_q, t)\| c_k^2(\mathbf{r}_q, t) J[\rho_k](t) \right)}{\text{norm}_{P,k}^\mu}, \quad (6.49a)$$

and

$$\kappa_{e,k}(\mathbf{r}, t) = h^2 \frac{\max \left( |\tilde{R}_k(\mathbf{r}_q, t)|, \|\mathbf{u}_k(\mathbf{r}_q, t)\| J[P_k](t), \|\mathbf{u}_k(\mathbf{r}_q, t)\| c_k^2(\mathbf{r}_q, t) J[\rho_k](t) \right)}{\text{norm}_{P,k}^\kappa}. \quad (6.49b)$$

where  $h$  is the grid size and  $J[x](t)$  denotes the jump of the quantity  $x$  and was defined in Section 3. The normalization parameters  $\text{norm}_{P,k}^\mu$  and  $\text{norm}_{P,k}^\kappa$  will be determined later in this section by inspecting the non-dimensional version of the seven-equation model.

It remains to specify the viscosity coefficients  $\beta_e$  and  $\beta_{max}$ . For the purpose of this paragraph, let us consider the scalar volume fraction equation and assume that the interface velocity  $\mathbf{u}_{int}$  is given. Because it is a scalar hyperbolic equation, it is proposed to define the high and first-order viscosity coefficients on the same model as Burger's equation. Thus,  $\beta_{max}$  is set proportional to the eigenvalue that is the interface velocity  $\mathbf{u}_{int}$ ,

$$\beta_{max,k}(\mathbf{r}, t) = \frac{h}{2} \|\mathbf{u}_{int}\|, \quad (6.50)$$

whereas the entropy viscosity viscosity coefficient  $\beta_e$  is function of an entropy residual,  $R_{\alpha,k}$ , derived from the volume fraction equation for phase  $k$  as follows:

$$\beta_{e,k}(\mathbf{r}, t) = h^2 \frac{\max (|R_{\alpha,k}(\mathbf{r}_q, t)|, \|\mathbf{u}_{int}(\mathbf{r}_q, t)\| J[\alpha_k](t))}{\text{norm}_k^\beta} \quad (6.51)$$

where  $\text{norm}_k^\beta$  denotes a normalization parameters whom definition will be further

investigated. To derive the entropy residual  $R_{\alpha,k}$ , we consider the volume fraction equation for phase  $k$  with its viscous regularization and assume the existence of a mathematical entropy denoted by  $\eta(\alpha_k)$ :

$$\partial_t (A\alpha_k) + A\mathbf{u}_{int} \cdot \nabla \alpha_k = \nabla \cdot (\beta_k A \nabla \alpha_k) \quad (6.52)$$

After multiplying by  $\frac{d\eta(\alpha_k)}{d\alpha_k}$  and using the chain rule, an expression for the entropy residual  $R_{\alpha,k}$  is obtained:

$$R_{\alpha,k} = \partial_t (A\eta(\alpha_k)) + A\mathbf{u}_{int} \cdot \nabla \eta(\alpha_k) = \frac{d\eta(\alpha_k)}{d\alpha_k} \nabla \cdot (\beta_k A \nabla \alpha_k) \quad (6.53)$$

Because Eq. (6.53) is identical to Eq. (2.27), it is concluded that  $R_{\alpha,k} \geq 0$  when assuming  $\eta$  convex with respect to  $\alpha_k$ , which justifies the definition of the entropy viscosity viscosity coefficient  $\beta_{e,k}$  given in Eq. (6.51) based on Eq. (2.1.4). The entropy function is taken equal to  $\eta(\alpha_k) = \frac{\alpha_k^2}{2}$  which is convex.

### 6.3.2 Low-mach asymptotic limit of the seven-equation model

In order to have a complete definition for the viscosity coefficients  $\beta_k$ ,  $\mu_k$  and  $\kappa_k$ , the normalization parameters introduced in the definition of the entropy viscosity coefficients  $\beta_{e,k}$ ,  $\mu_{e,k}$  and  $\kappa_{e,k}$  have to be determined. In Section 5, the normalization parameters were derived from the non-dimensionalized multi-D Euler equations in order to obtain well-scaled dissipative terms. Thus, it is proposed to follow the same method to derive the three normalization parameters  $\text{norm}_{P,k}^\mu$ ,  $\text{norm}_{P,k}^\kappa$  and  $\text{norm}_k^\beta$  used in the definition of the viscosity coefficients involved in the viscous regularization of the seven-equation model. For simplicity, the Ideal Gas equation of state is considered through the derivations.

For now, the definition of the viscosity coefficients is simply derived by analogy

to Section 5.2.2. First, we define the far-field or stagnation coefficients for each phase as it is done in Eq. (5.11) by adding the subscript  $k$  to  $\infty$ . Then, the scaled equations are derived for each phase which leads to the definition of a phasic Péclet and Reynolds numbers referred to as  $\text{Pé}_k$  and  $\text{Re}_k$ , respectively, that are tied to the far-field or stagnation quantities of the viscosity coefficients  $\mu_{k,\infty}$  and  $\kappa_{k,\infty}$  as shown in Eq. (6.54):

$$\text{Re}_{k,\infty} = \frac{u_{k,\infty} L_\infty}{\mu_{k,\infty}} \text{ and } \text{Pé}_{k,\infty} = \frac{u_{k,\infty} L_\infty}{\kappa_{k,\infty}}. \quad (6.54)$$

Because the viscous regularization derived previously in Section 6.2 requires an extra viscosity coefficient  $\beta_k$  for the volume fraction equation, a new Péclet number,  $\text{Pé}_{k,\infty}^\beta$  is also defined as follows,

$$\text{Pé}_{k,\infty}^\beta = \frac{u_{int,\infty} L_\infty}{\beta_{k,\infty}} \quad (6.55)$$

that will allow us to derive the proper scaling for  $\beta_{k,\infty}$ . Once the scaled equations are obtained, the scaling of the numerical numbers can be chosen in order to meet the different criteria already listed in Section 5.2.2. The scaling of the new Péclet number we defined,  $\text{Pé}_{k,\infty}^\beta$ , is derived from the scaled volume fraction equation that does not contain any term weighted by the reference Mach number  $M_\infty$ , which yields  $\text{Pé}_{k,\infty}^\beta = 1$  to have a well-scaled dissipative term. This scaling is the same as for  $\text{Pé}_{k,\infty}$  from the continuity equation: the volume fraction and continuity equations have similar behavior since they are both advection-type equations. Thus, based on the reasoning used in Section 6.2, the following definitions for the viscosity coefficients is proposed in Eq. (6.56):

$$\mu_k(\mathbf{r}, t) = \min \left( \mu_{\max,k}(\mathbf{r}, t), \mu_{e,k}(\mathbf{r}, t) \right) \text{ and } \kappa_k(\mathbf{r}, t) = \min \left( \kappa_{\max,k}(\mathbf{r}, t), \kappa_{e,k}(\mathbf{r}, t) \right) \quad (6.56a)$$

where the first-order viscosity is given by

$$\kappa_{\max,k}(\mathbf{r}, t) = \mu_{\max,k}(\mathbf{r}, t) = \frac{h}{2} \left( \|\mathbf{u}_k\| + c_k \right) \quad (6.56b)$$

and the entropy viscosity coefficients by

$$\kappa_{e,k}(\mathbf{r}, t) = \frac{h^2 \max(\tilde{R}_k, J_k)}{\rho_k c_k^2} \text{ and } \mu_{e,k}(\mathbf{r}, t) = \frac{h^2 \max(\tilde{R}_k, J_k)}{\text{norm}_{P,k}^\mu} \quad (6.56c)$$

with the jumps given by

$$J_k = \max \left( \|\mathbf{u}_k\| [[\nabla P_k \cdot \mathbf{n}]], \|\mathbf{u}_k\| c_k^2 [[\nabla \rho_k \cdot \mathbf{n}]] \right) \quad (6.56d)$$

where  $\text{norm}_{P,k}^\kappa$  is computed from Eq. (6.57).

$$\text{norm}_P^\mu = (1 - \sigma(M))\rho c^2 + \sigma(M)\rho \|\mathbf{u}\|^2 \quad (6.57)$$

where  $M_k$  is the local Mach number for phase  $k$ . The function  $\sigma(M)$  is taken from Eq. (5.28) with the same parameters as for the single-phase flow equations:  $a = 3$  and  $M^{thres} = 0.05$ . The jump  $J_k$  is a function of the jump of pressure and density gradients across the face with respect to its normal vector  $\mathbf{n}$ . Then, the largest value over all faces is determined and used in the definition of the viscosity coefficients. Lastly, the viscosity coefficient for the volume fraction equation is given by:

$$\beta_k(\mathbf{r}, t) = \min \left( \beta_{\max,k}(\mathbf{r}, t), \beta_{e,k}(\mathbf{r}, t) \right) \quad (6.58)$$

where the first-order viscosity is given by

$$\beta_{\max,k}(\mathbf{r}, t) = \frac{h}{2} \|\mathbf{u}_{int}\| \quad (6.59)$$

and the corresponding entropy viscosity coefficient,  $\beta_{e,k}$ , by

$$\beta_{e,k}(\mathbf{r}, t) = \frac{h^2 \max(R_{\alpha,k}, J_{\alpha,k})}{\|\alpha_k - \bar{\alpha}_k\|_{\infty}}, \quad (6.60)$$

where  $\bar{\alpha}_k$  is the average value of the volume fraction over the entire computational domain, and  $\|\cdot\|_{\infty}$  denotes the infinite norm. The definition of the  $\beta_{e,k}$  is consistent with the scaling of  $\text{P\'{e}}_{k,\infty}^{\beta} = 1$ . The jump is given by:

$$J_{\alpha,k} = \|\mathbf{u}_{int}\| \cdot [[\nabla \alpha_k \cdot \mathbf{n}]]. \quad (6.61)$$

With the definition of the viscosity coefficients  $\mu_k$  and  $\kappa_k$  proposed in Eq. (5.30), the low-Mach asymptotic limit is ensured for isentropic flow, and transonic flows with shocks will be correctly resolved for each phase  $k$ . Furthermore, the definition of the viscosity coefficient  $\beta_k$  is consistent with the EVM used for the scalar hyperbolic equations and thus should efficiently stabilize shocks forming in the volume fraction profile. Plus, it is noted that the viscous regularization and the definition of the viscosity coefficients proposed for the seven-equation two-phase flow model degenerates into the EVM used for the single-phase Euler equations. In order to validate the proposed definition of the viscosity coefficients, 1-D numerical simulations are performed in Section 6.4.

## 6.4 Numerical results

1-D numerical tests are presented in this section. The objective is to test the viscous regularization derived in Section 6.2 and the definition of the viscosity coefficients proposed in Section 6.3 for the 1-D seven-equation model. The first test, presented in Section 6.4.1, consists of a pure advection of a volume fraction discontinuity. In Section 6.4.2, a standard shock tube filled with two independent fluids is presented. The same shock tube is considered in Section 6.4.3 but with pressure and velocity relaxation terms. Then in Section 6.4.4, numerical solutions for a 1-D converging-diverging nozzle are presented for the 1-D seven-equation model with relaxation and exchange terms. Lastly, simulation of a two-phase flow in a 1-D straight pipe with friction and wall-heat source is considered in Section 6.4.5. For each test, information relative to the mesh, the CFL number and the boundary conditions are given.

### 6.4.1 1-D advection test: uniform velocity and pressure flow with a volume fraction discontinuity

We consider a 1-D straight pipe of length  $L = 1 \text{ m}$  filled with two gas phases in equilibrium (same pressure and velocity) described by the Ideal Gas equation of state with  $\gamma_1 = 3$  and  $\gamma_2 = 1.4$ . This basic test has a trivial solution which corresponds to the pure advection of the volume fraction discontinuity. The viscous regularization for the SEM is quite complex and it is important to check that it can give the correct solution of a simple advection test. The objective is to make sure that the numerical stabilization method is not responsible for the apparition of an artificial mixture zone. The geometry is discretized with an uniform mesh of 100 cells. The initial conditions consist of a uniform pressure  $P_1 = P_2 = 0.1 \text{ MPa}$  and a uniform velocity  $u_1 = u_2 = 100 \text{ m/s}$ . The density of the phase 1 and 2 are set to 10 and  $1 \text{ kg/m}^3$ ,

respectively. On the left part of the tube, the liquid volume fraction is  $\alpha_1 = 0.9$ , while on the right part of the tube it is  $\alpha_1 = 0.1$ . The numerical solution is run with a *CFL* of 1 until the final time  $t_{final} = 1703 \mu s$ . The numerical solutions are given from Fig. 6.3 to 6.6.

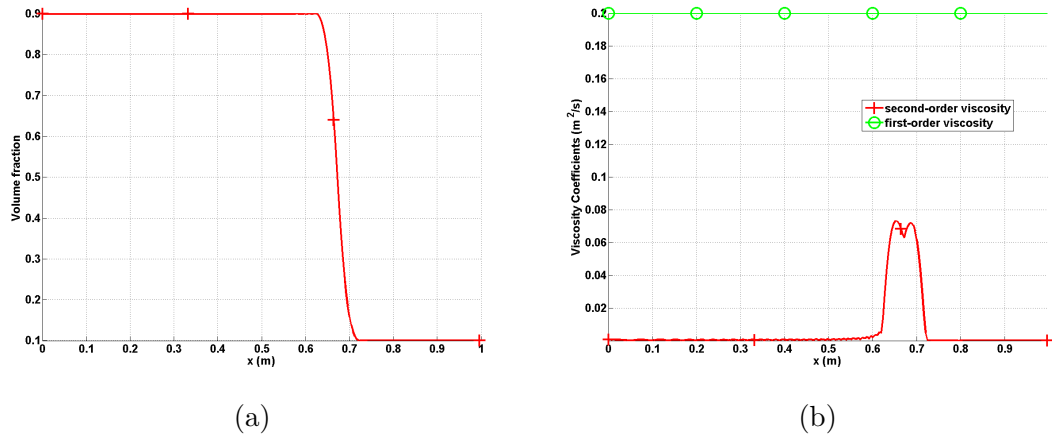


Figure 6.3: 1-D advection test: volume fraction (left) and viscosity coefficients for volume fraction equation (right) of phase 1

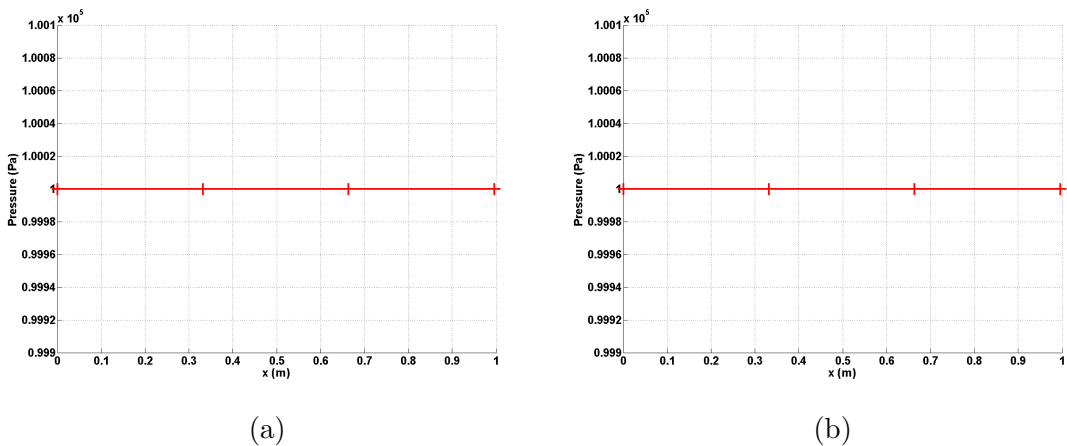


Figure 6.4: 1-D advection test: pressure profiles of phase 1 (left) and 2 (right)

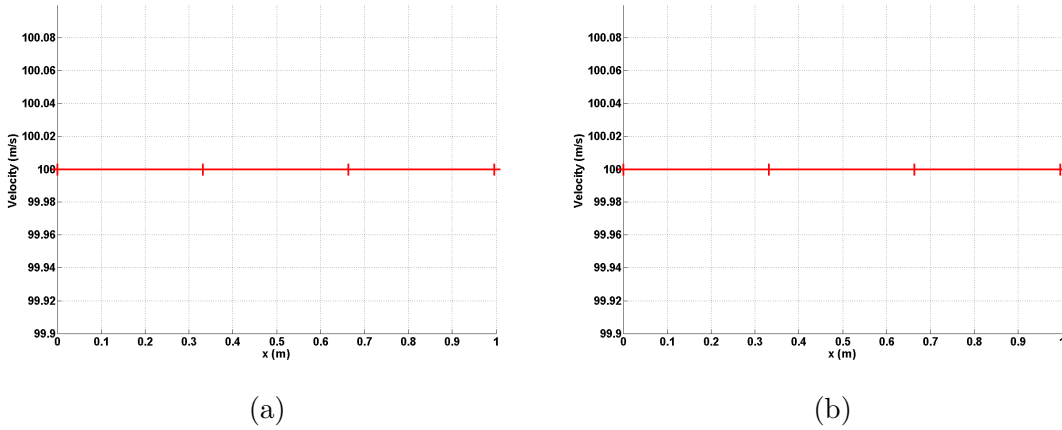


Figure 6.5: 1-D advection test:: velocity profiles of phase 1 (left) and 2 (right)

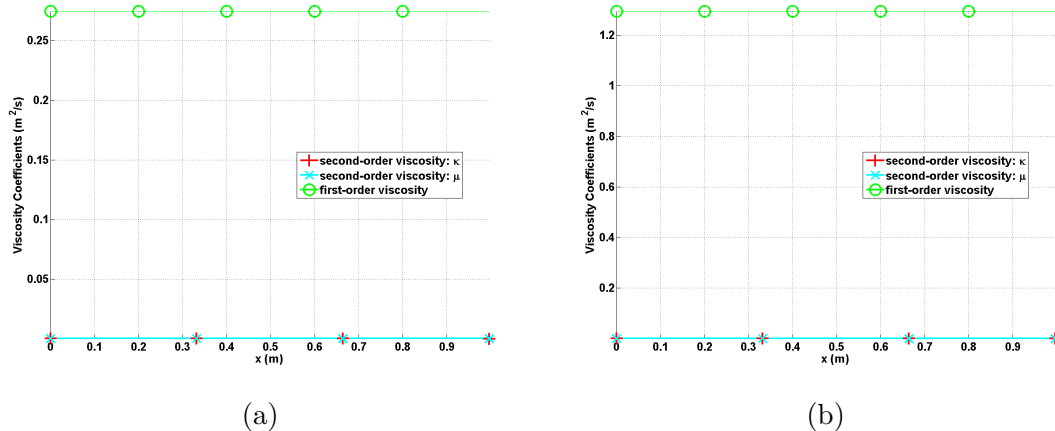


Figure 6.6: 1-D advection test: viscosity coefficient profiles of phase 1 (left) and 2 (right)

The stabilization numerical method preserves the uniform pressure (Fig. 6.4) and velocity (Fig. 6.5) flow conditions while correctly resolving the discontinuity in the volume fraction profile as shown in Fig. 6.3a. The viscosity coefficients  $\mu_k$  and  $\kappa_k$  are equal to zero for both phases as shown in Fig. 6.6, since the flow conditions are

uniform. However, the viscosity coefficient  $\beta_k$  is peaked in the discontinuity region as expected. This test clearly shows that the stabilization method does not induce any artificial waves due to the smearing of the discontinuity in the volume fraction profile.

#### 6.4.2 1-D shock tube for two independent fluids

We still consider a 1-D straight pipe of length  $L = 1 \text{ m}$  filled with the same fluids as in Section 6.4.1. The membrane separates the pipe in two chambers with a high pressure ( $P_{left} = 1 \text{ MPa}$ ) on the left side and a low pressure ( $P_{left} = 0.1 \text{ MPa}$ ) in the right side. Both fluids are initially at rest. The volume fraction is set to 0.5 which means each side of the chamber contains a mixture of two fluids with different equation of state parameters. Since the velocity and pressure relaxation coefficients  $\mu_P$  and  $\lambda_u$  are set to zero, the two fluids will behave independently to each other and the volume fraction is expected to remain uniform during the simulation. An exact solution is available for each fluid which simply corresponds to the single-phase exact solution obtained from a Riemann solver. The geometry is discretized with an uniform mesh of 500 cells and run with a  $CFL$  of one until  $t_{final} = 305 \text{ } \mu\text{s}$ . The numerical and exact solutions are given from Fig. 6.7 to 6.13.

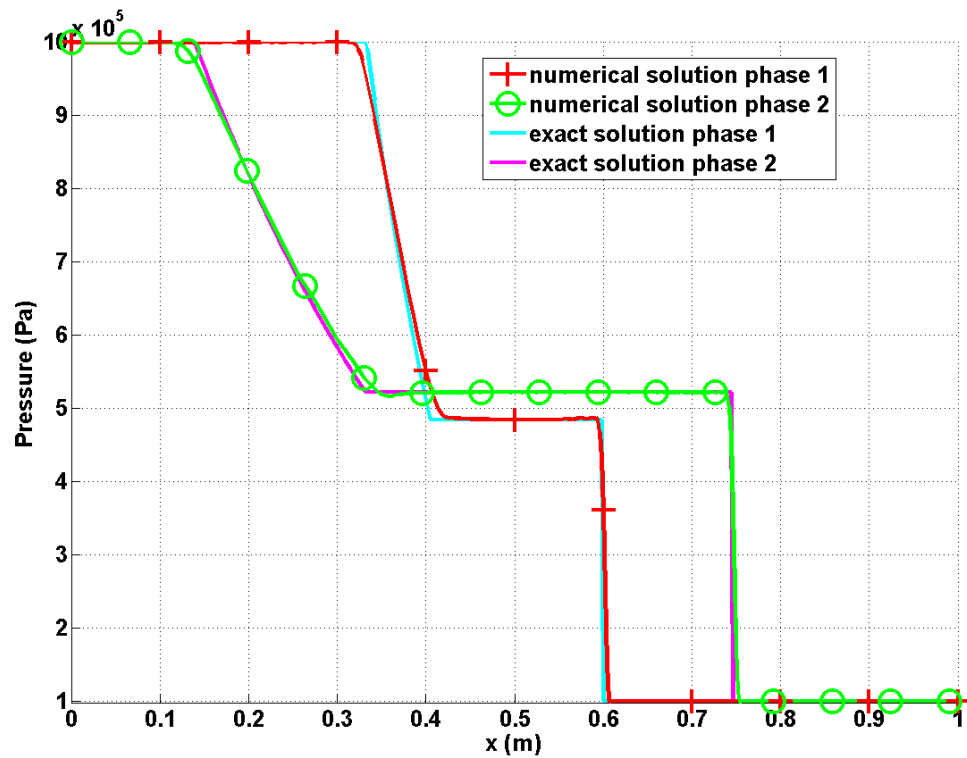


Figure 6.7: 1-D shock tube for two independent fluids: pressure profiles at  $t = 305 \mu s$ .

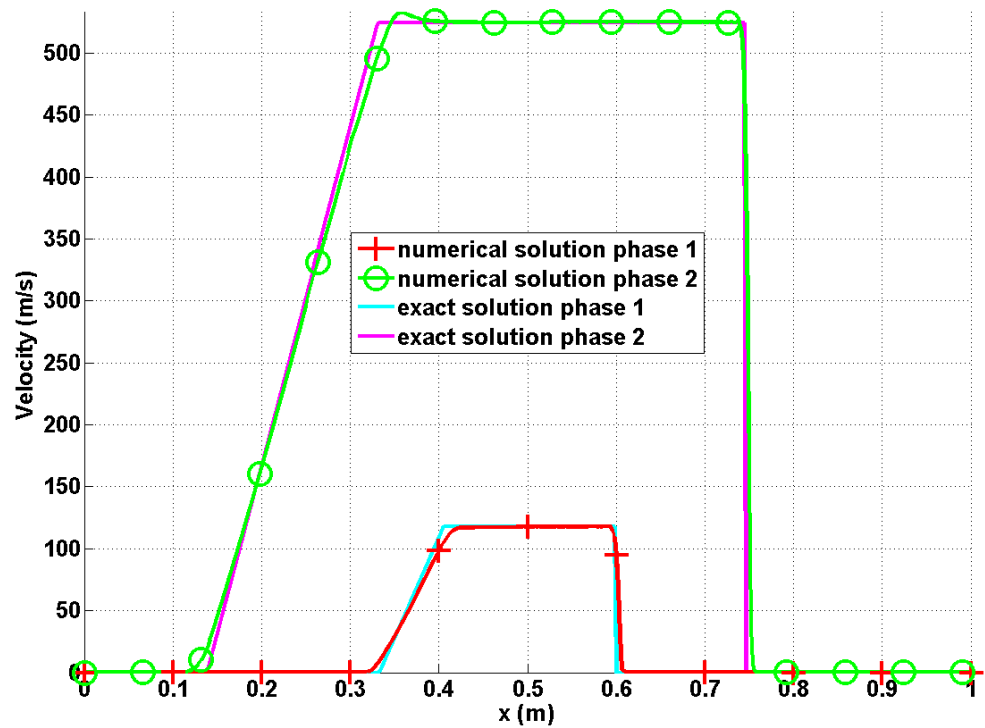


Figure 6.8: 1-D shock tube for two independent fluids: velocity profiles at  $t = 305 \mu s$ .

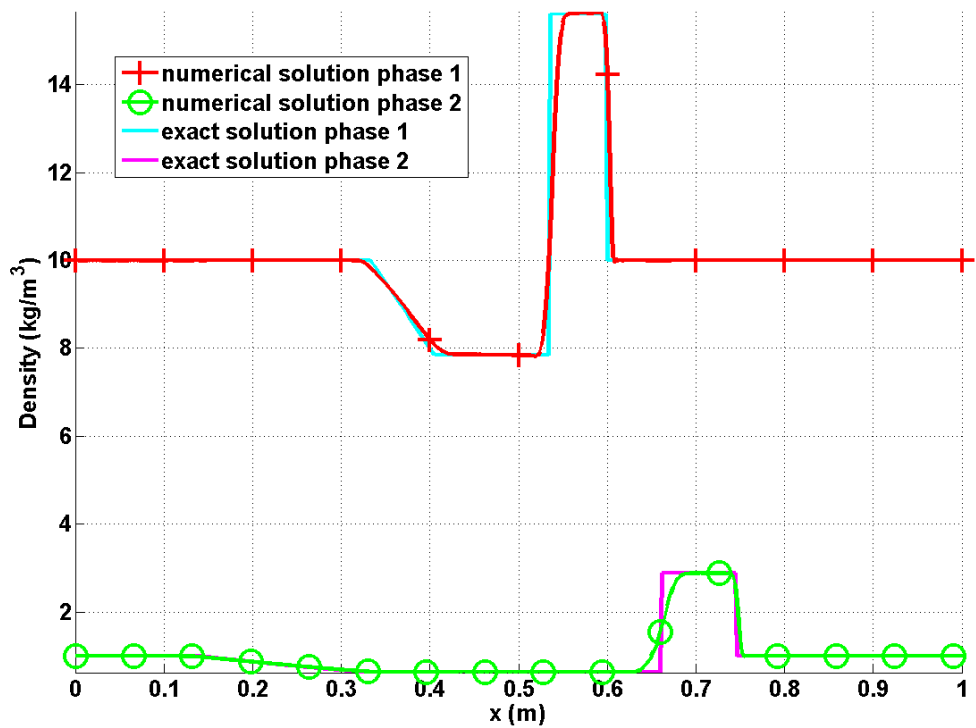


Figure 6.9: 1-D shock tube for two independent fluids: density profiles at  $t = 305 \mu s$ .

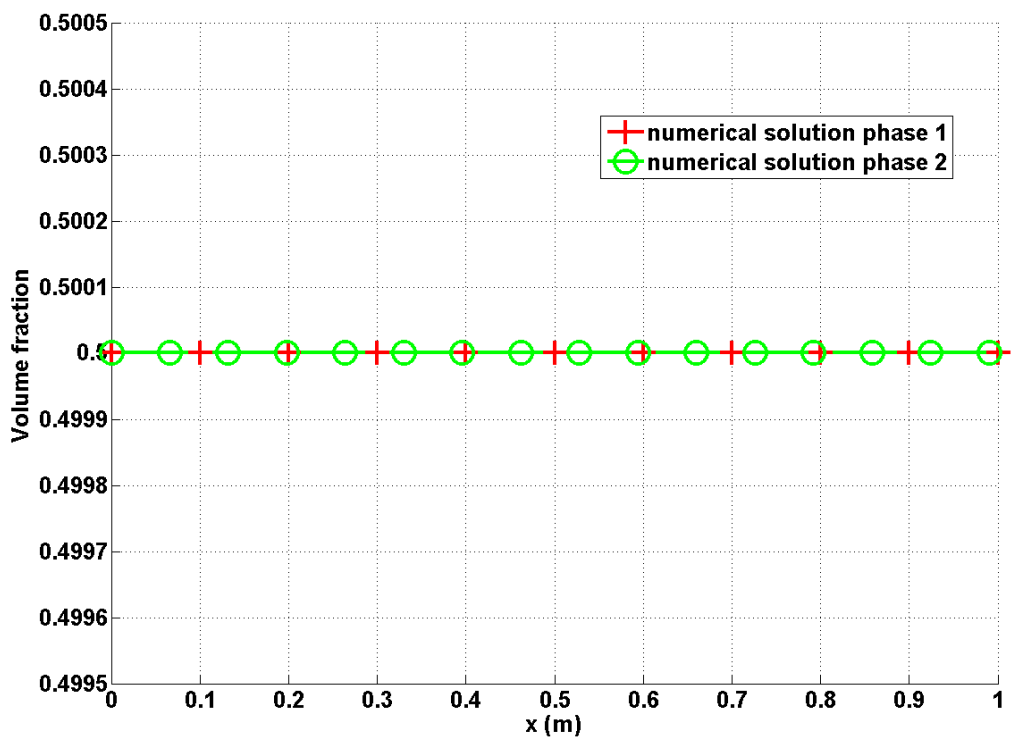


Figure 6.10: 1-D shock tube for two independent fluids: volume fraction profiles at  $t = 305 \mu s$ .

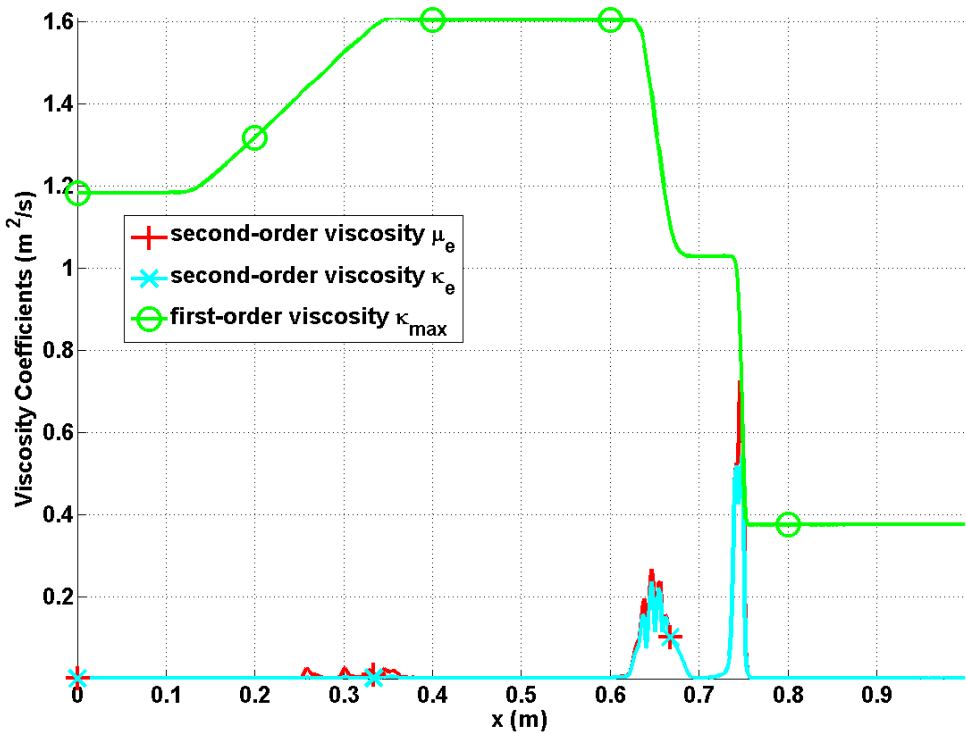


Figure 6.11: 1-D shock tube for two independent fluids: viscosity coefficient profiles for phase 2 at  $t = 305 \mu s$ .

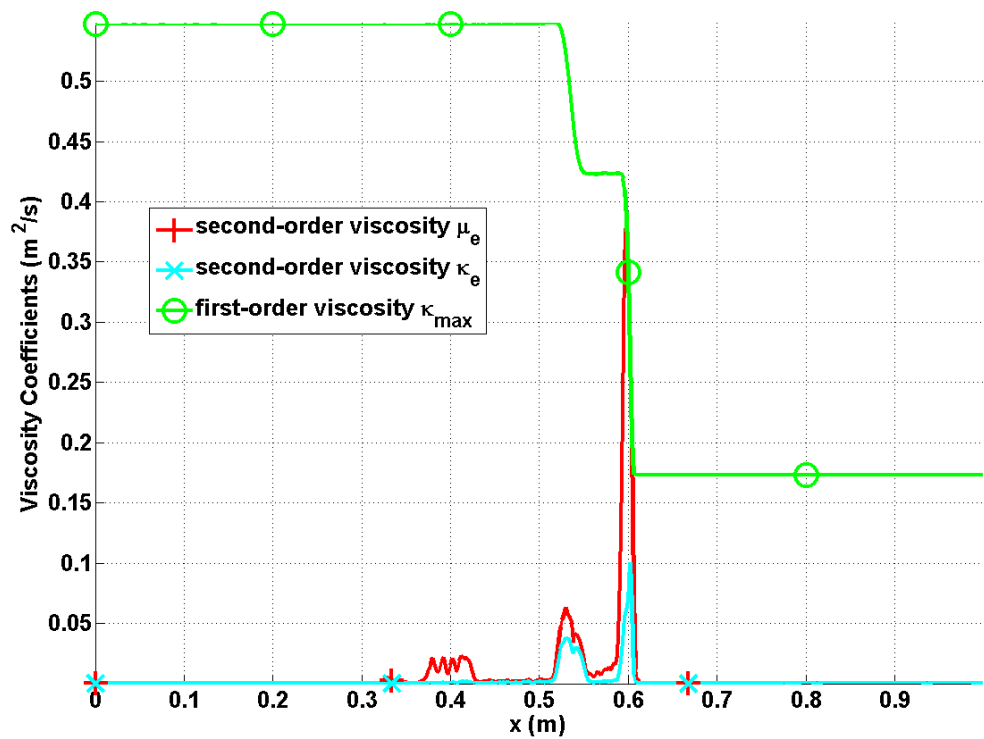


Figure 6.12: 1-D shock tube for two independent fluids: viscosity coefficient profiles for phase 1 at  $t = 305 \mu s$ .

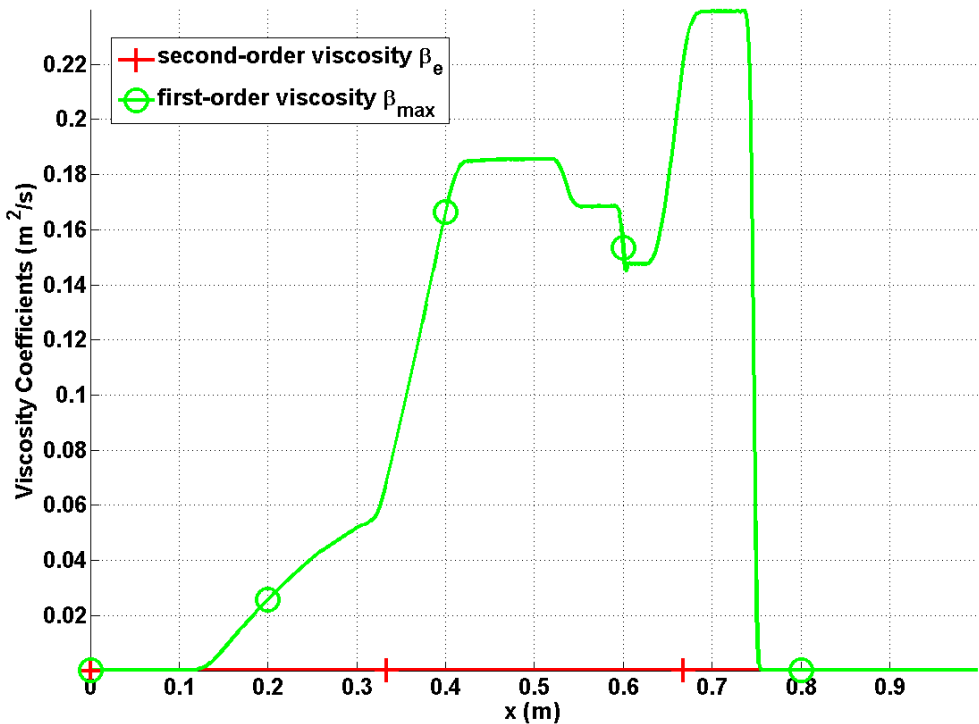


Figure 6.13: 1-D shock tube for two independent fluids: viscosity coefficient profiles for volume fraction equation of phase 1 at  $t = 305 \mu s$ .

The pressure, velocity and density profiles given in Fig. 6.7, Fig. 6.8 and Fig. 6.9, respectively, show good agreement with the exact solutions for both phases. The fluid 2 is lighter and thus experiences stronger variations: its velocity is larger and the shock moves faster. The viscosity coefficients shown in Fig. 6.11 and Fig. 6.12 for both phases have similar profiles: they are peaked in the shock regions and also display a bump in the contact wave. In Fig. 6.10, it is noted that the volume fraction profiles remain uniform and are not altered by the variations in the other variables. The viscosity coefficient  $\beta_k$  used in the volume fraction equation is zero (Fig. 6.13) as expected since the volume fraction profile is uniform.

### 6.4.3 1-D shock tube for two fluids with pressure and velocity relaxation terms

Once again, we consider a 1-D shock tube with the same initial conditions and the same fluids as in Section 6.4.2. The pressure and velocity relaxation coefficients are no longer set to zero but computed from Eq. (6.10) and Eq. (6.11) with  $A_{int,max} = 10^4$   $m^{-1}$ :  $\mu_P \sim 4$  and  $\lambda_u \sim 5 \times 10^5$   $s^{-1}$ . The values of the relaxation coefficients are large enough to make the relaxation terms dominant in the momentum and energy equations of each phase (see Eq. (6.1) and Eq. (6.2)). Thus, the two fluids will exhibit the same pressure and velocity. The volume fraction will not remain uniform but is expected to vary due to the pressure relaxation source term (Eq. (6.1d)). For this test, an exact solution is not available but the reader can refer to [61] for a comparison. An uniform mesh of 500 cells is used. The code is run until  $t_{final} = 305$   $\mu s$  with a  $CFL$  of one. The numerical solutions are presented in Fig. 6.14 to 6.20.

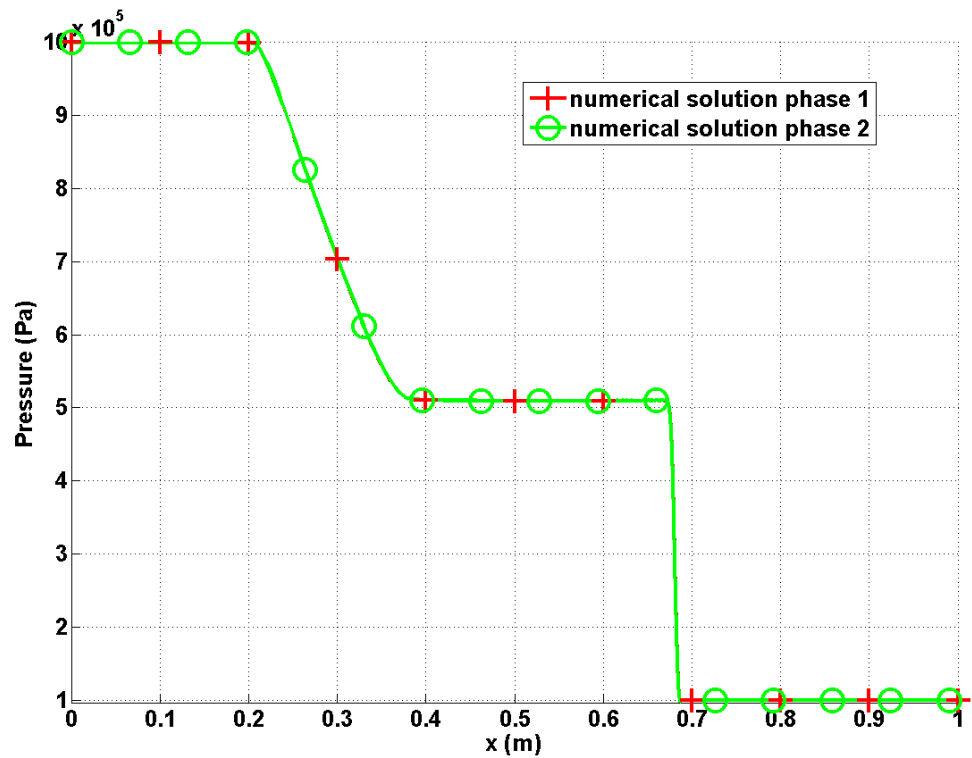


Figure 6.14: 1-D shock tube for two fluids with relaxation terms: pressure profiles at  $t = 305 \mu s$ .

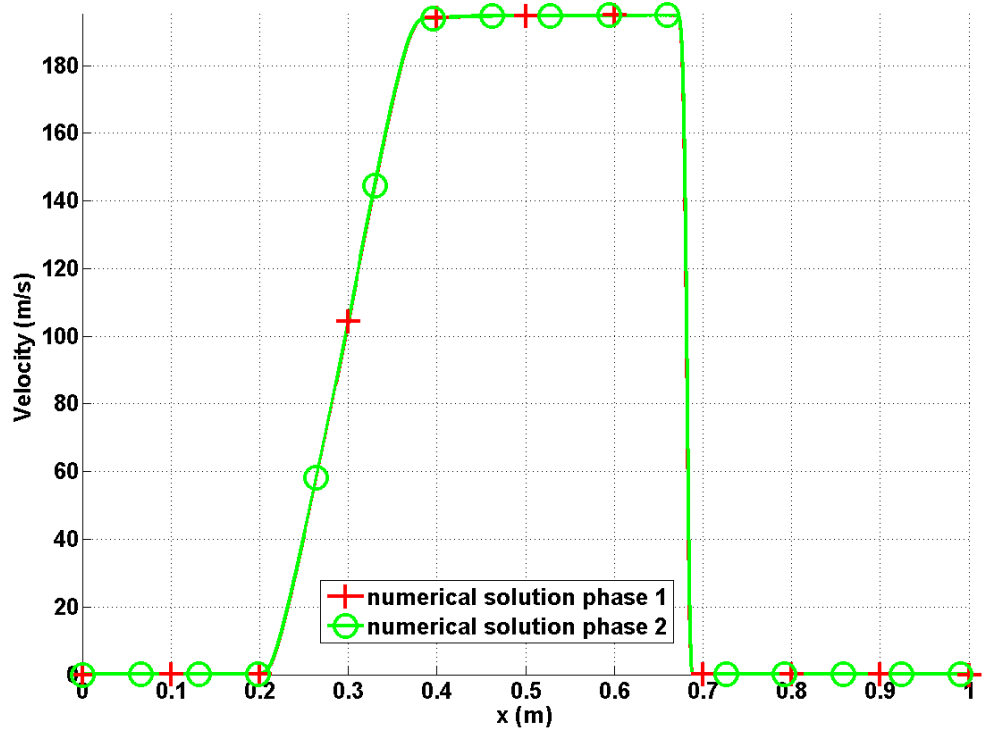


Figure 6.15: 1-D shock tube for two fluids with relaxation terms: velocity profiles at  $t = 305 \mu s$ .

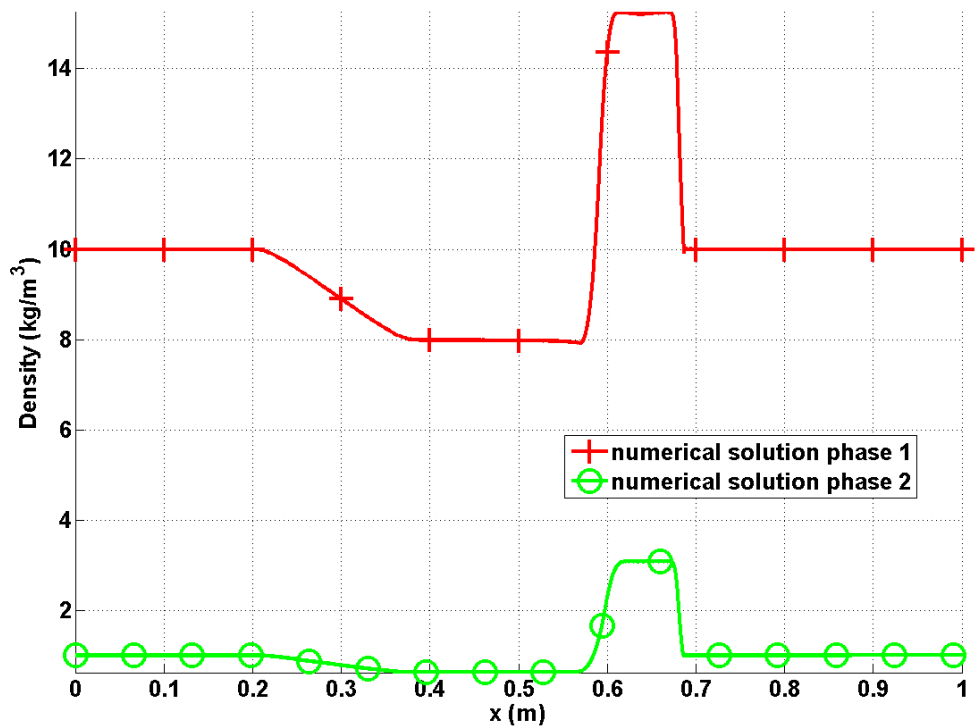


Figure 6.16: 1-D shock tube for two fluids with relaxation terms: density profiles at  $t = 305 \mu s$ .

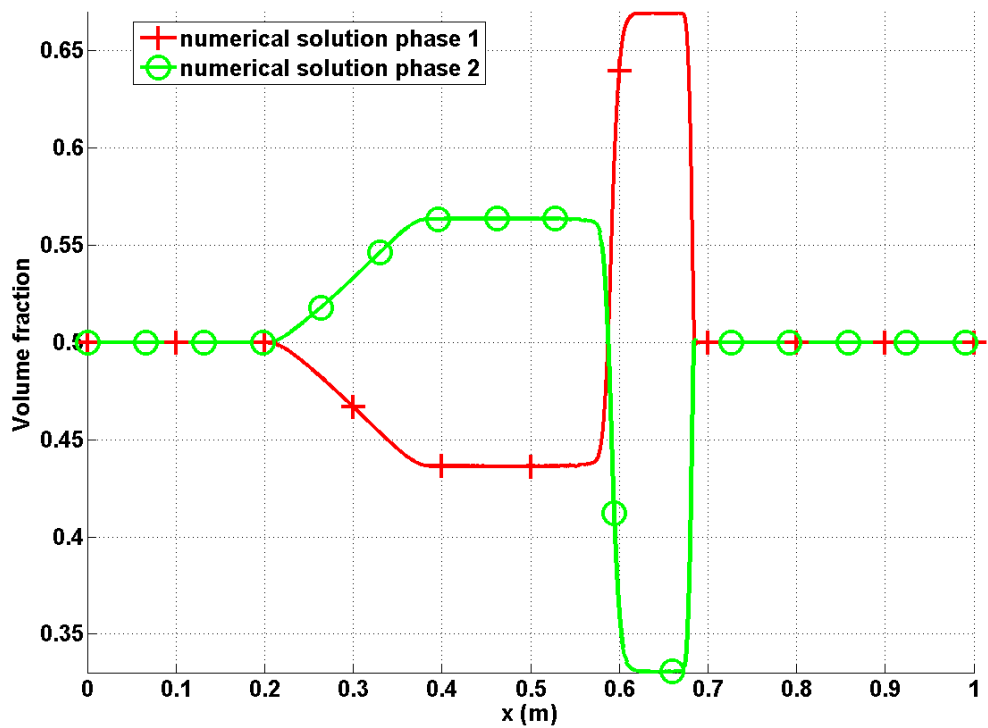


Figure 6.17: 1-D shock tube for two fluids with relaxation terms: volume fraction profiles at  $t = 305 \mu s$ .

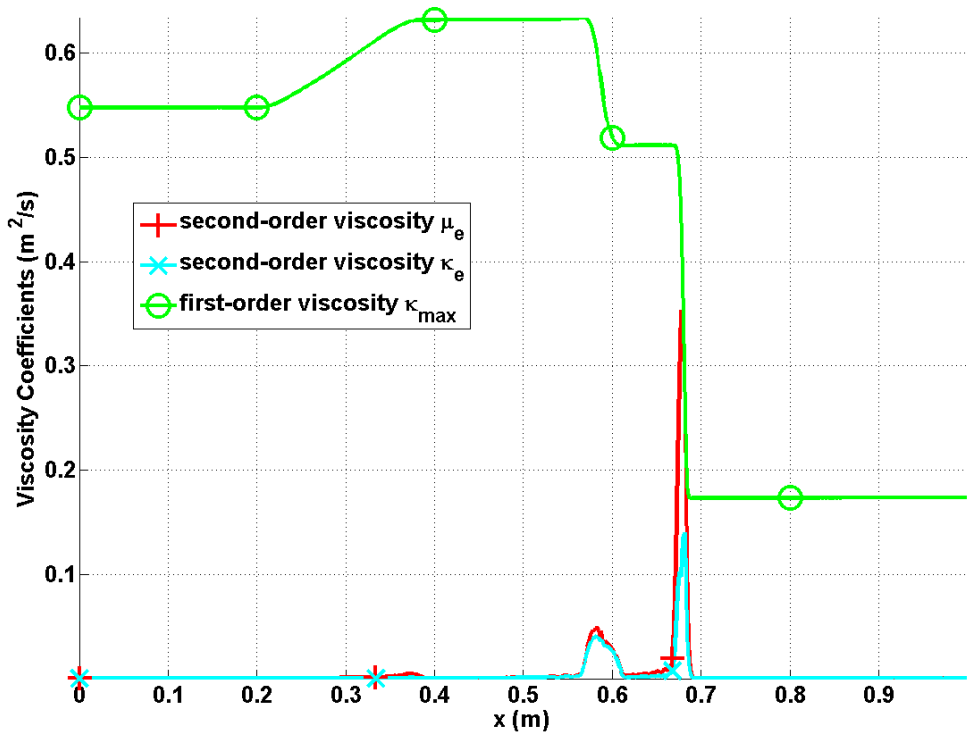


Figure 6.18: 1-D shock tube for two fluids with relaxation terms: viscosity coefficient profiles for phase 1 at  $t = 305 \mu s$ .

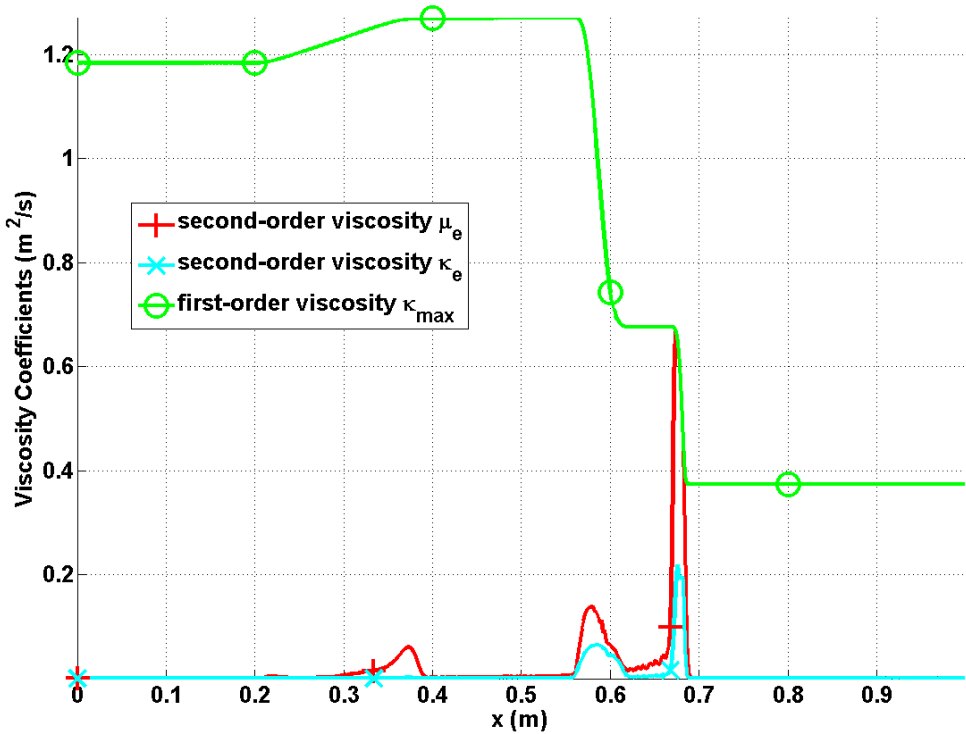


Figure 6.19: 1-D shock tube for two fluids with relaxation terms: viscosity coefficient profiles for phase 2 at  $t = 305 \mu s$ .

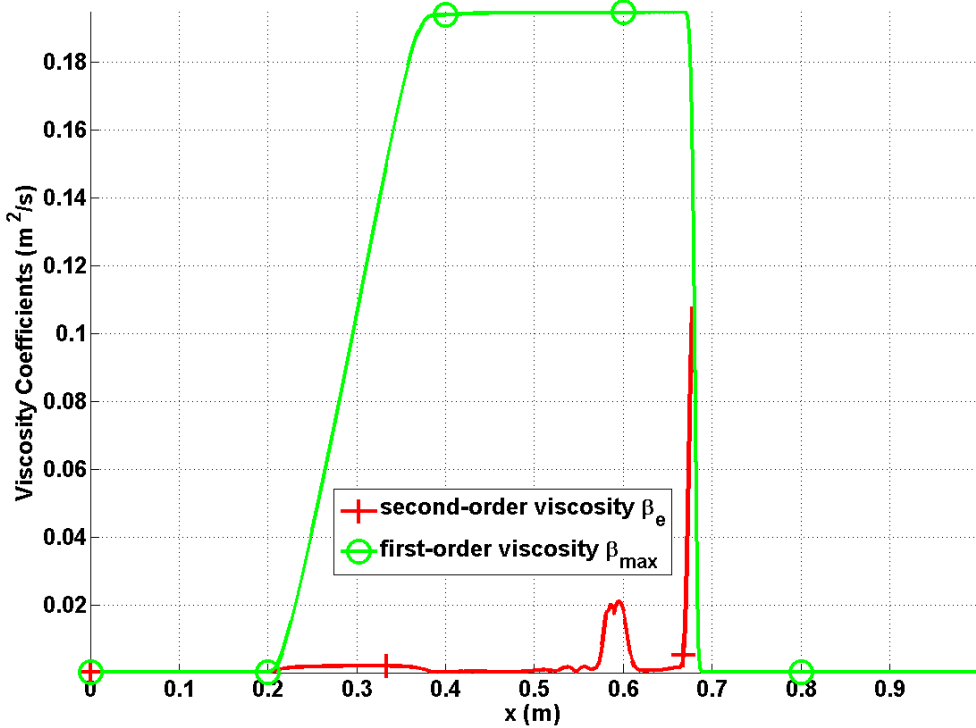


Figure 6.20: 1-D shock tube for two fluids with relaxation terms: viscosity coefficient profiles for volume fraction equation of phase 1 at  $t = 305 \mu s$ .

As expected, the two fluids have the same pressure and velocity profiles as shown in Fig. 6.14 and Fig. 6.15, respectively. The shock is well resolved and does not display any instability. The main difference with the numerical results obtained in Section 6.4.2 lies in the volume fraction profiles that are no longer uniform but display a shock wave around  $x = 0.7 m$  as shown in Fig. 6.17. Consequently, the viscosity coefficient  $\beta_k$  is peaked in the same region.

#### 6.4.4 1-D converging-diverging nozzle test

In this test, we propose to investigate the behavior of two fluids in a one meter long 1-D converging-diverging nozzle with  $A(x) = 1 + 0.5 \cos(2\pi x)$ . This test was

first introduced by Saurel et al. in [55] for the 1-D seven-equation model and consists of a mixture of liquid water and vapor described by the SGEOS with the parameters given in Table 6.1.

Table 6.1: Stiffened Gas Equation of State (SGEOS) parameters for steam and liquid water.

fluid	$\gamma$	$C_v \text{ (J.kg}^{-1}.\text{K}^{-1}\text{)}$	$P_\infty \text{ (Pa)}$	$q \text{ (J.kg}^{-1}\text{)}$
liquid water	2.35	1816	$10^9$	$-1167 \cdot 10^3$
steam	1.43	1040	0	$2030 \cdot 10^3$

Stagnation boundary conditions are specified on the left of the nozzle (inlet) for both phases with a stagnation temperature  $T_0 = 453 \text{ K}$  and a stagnation pressure  $P_0 = 1 \text{ MPa}$  (the stagnation density can be computed from  $T_0$  and  $P_0$  and the equation of state). At the outlet, a static pressure boundary condition is specified with  $P = 0.5 \text{ MPa}$  for both phases. The volume fraction is set to  $\alpha_k = 0.5$  at the inlet. The initial conditions are computed from the boundary conditions by assuming the two fluids at rest and linearly interpolating the pressure and temperature between the boundary values. The geometry is discretized with an uniform mesh of 100 cells and run until steady-state. The pressure and velocity relaxation coefficients are computed from Eq. (6.10) and Eq. (6.11) and the use of Eq. (6.12) for different values of  $A_{int,max}$  that will be specified. The reader can refer to Section 5.6.1 and Section 5.6.2 for numerical solutions in a 1-D nozzle when considering two independent fluids (i.e., without relaxation source terms). First numerical results are presented when considering only the pressure and velocity relaxation terms for different values of  $A_{int,max}$ .

Then, the same simulation is run when adding the mass and energy exchange source terms.

We first consider the 1-D seven-equation model with the relaxation source terms for different values of  $A_{int,max} = 10^2, 10^3$  and  $10^4 \text{ m}^{-1}$ . The pressure profiles are given for all of the value of  $A_{int,max}$  for comparison. The density, velocity, volume fraction and viscosity coefficients are only given for  $A_{int,max} = 10^4 \text{ m}^{-1}$ . The numerical results are presented from Fig. 6.23 to 6.29.

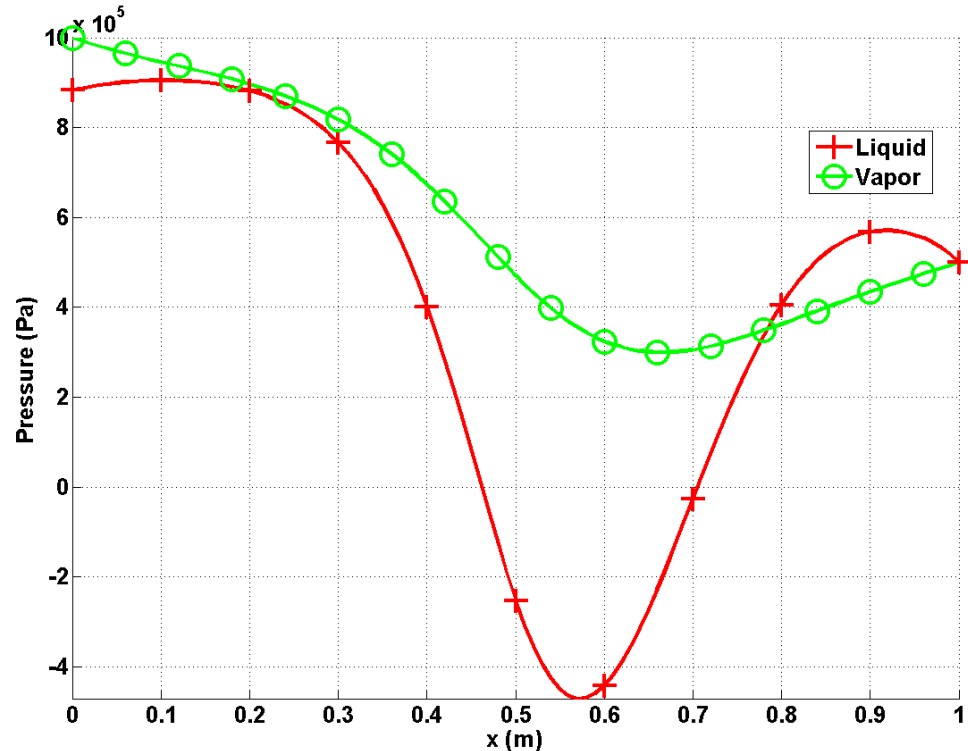


Figure 6.21: 1-D converging-diverging nozzle test: pressure profiles at steady state with  $A_{int,max} = 10^2$ .

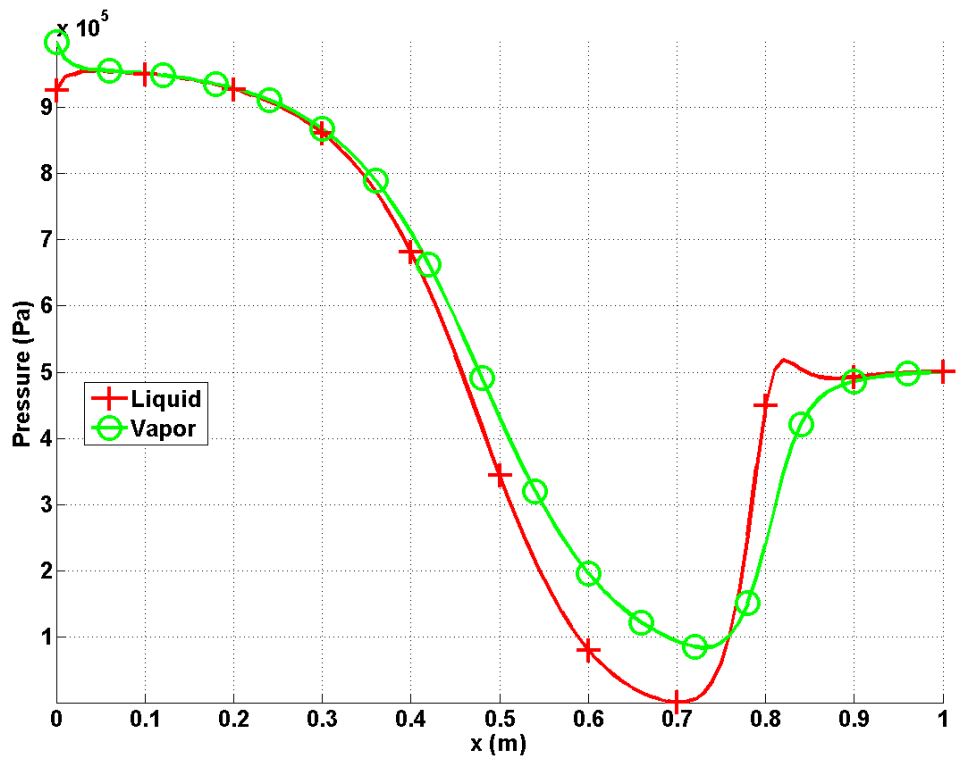


Figure 6.22: 1-D converging-diverging nozzle test: pressure profiles at steady state with  $A_{int,max} = 10^3$ .

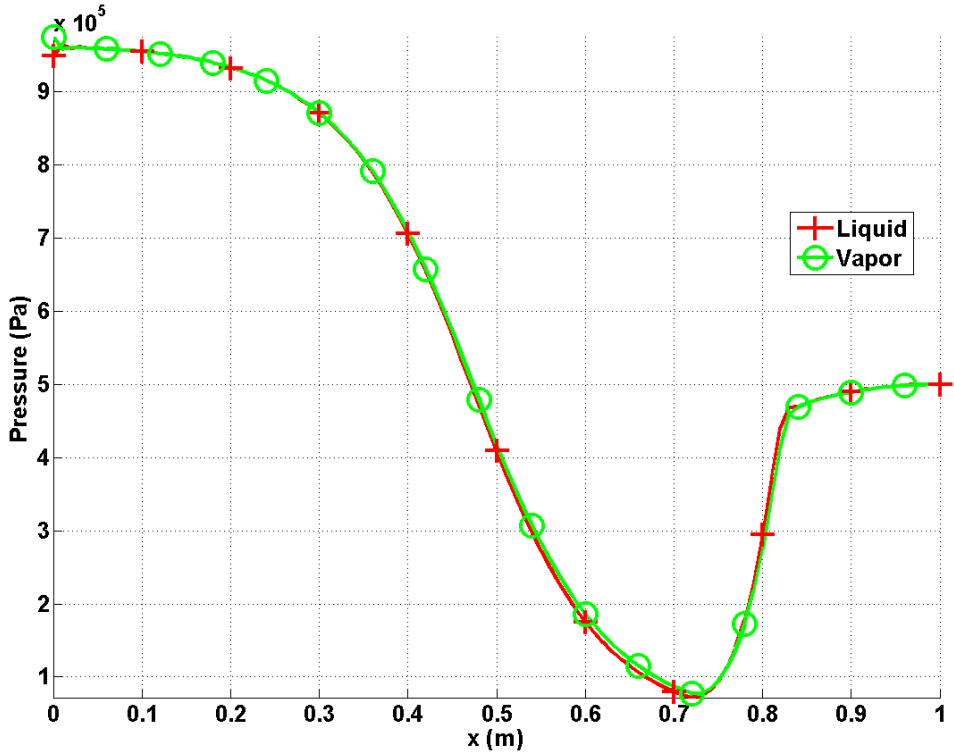


Figure 6.23: 1-D converging-diverging nozzle test: pressure profiles at steady state with  $A_{int,max} = 10^4$ .

The pressure profiles for  $A_{int,max} = 10^2, 10^3$  and  $10^4 \text{ m}^{-1}$  are given in Fig. 6.21, Fig. 6.22 and Fig. 6.23, respectively. As the value of  $A_{int,max}$  increases, the liquid pressure becomes positive and matches the vapor pressure variations. The static pressure outlet boundary holds for both phases. At the inlet, the liquid and vapor pressures are not equal since the implementation of the boundary condition does not account for the relaxation terms: the static pressure is computed from the stagnation pressure using entropy and enthalpy conservation relations.

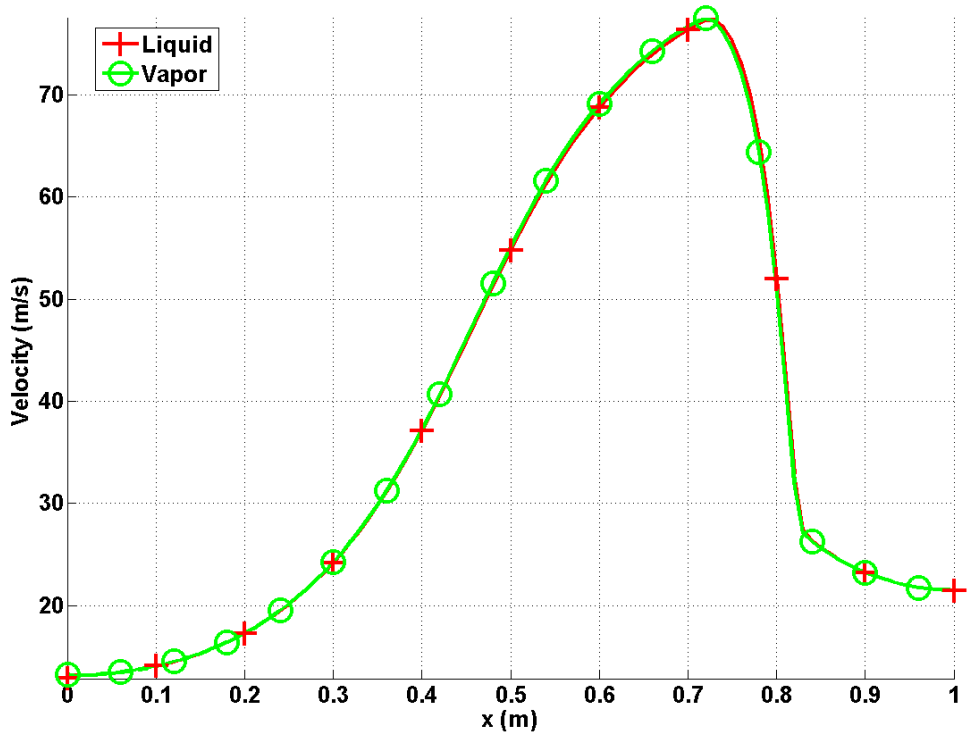


Figure 6.24: 1-D converging-diverging nozzle test: velocity profiles at steady state.

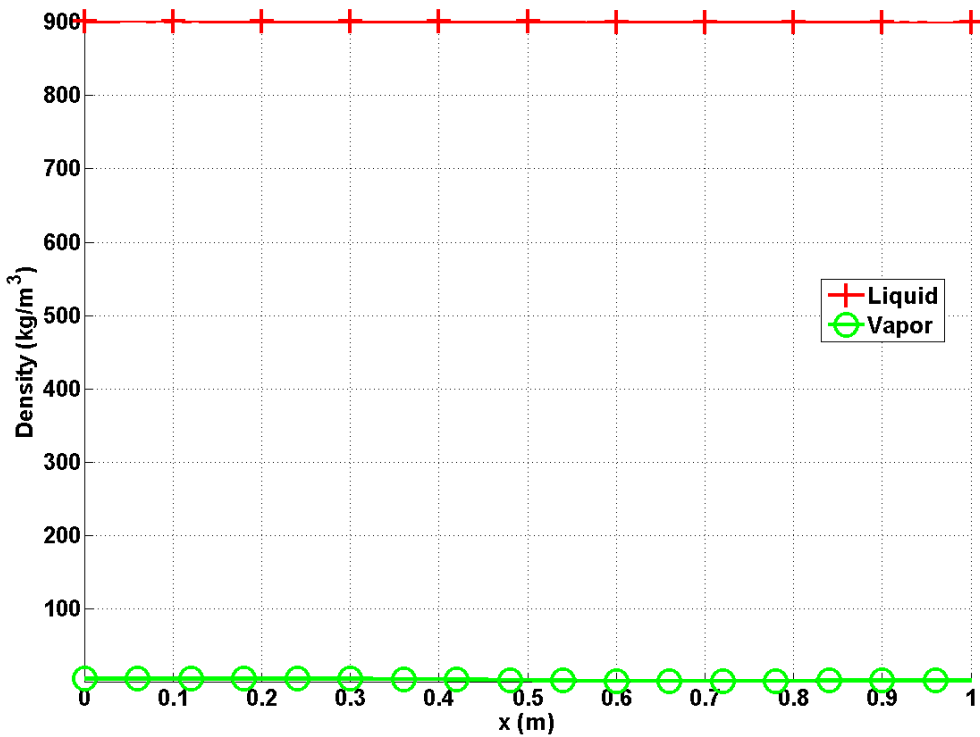


Figure 6.25: 1-D converging-diverging nozzle test: density profiles at steady state.

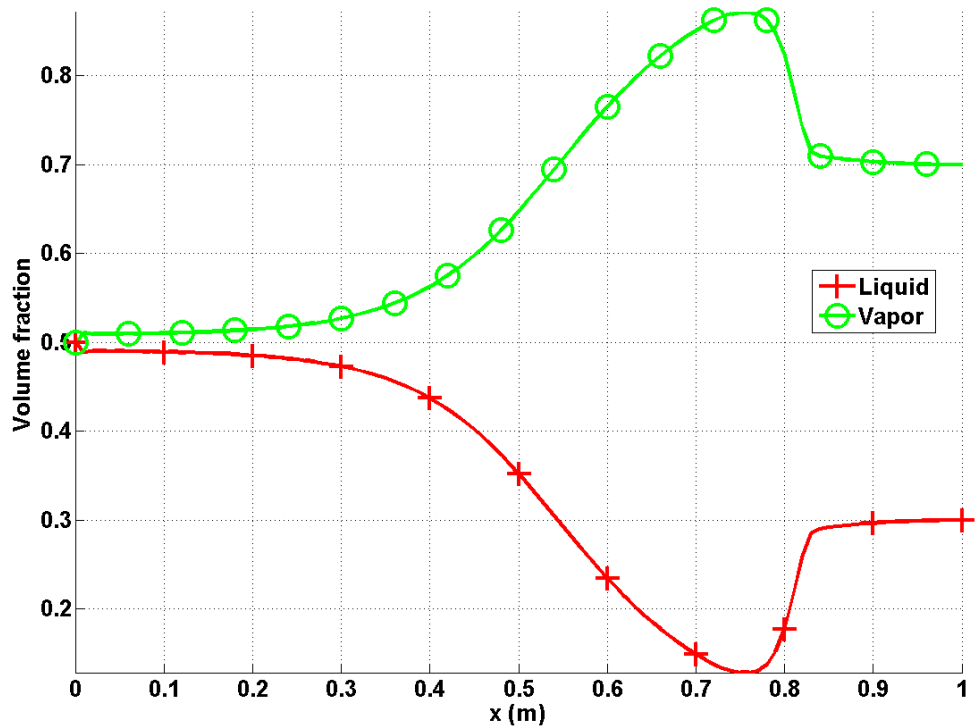


Figure 6.26: 1-D converging-diverging nozzle test: volume fraction profiles at steady state.

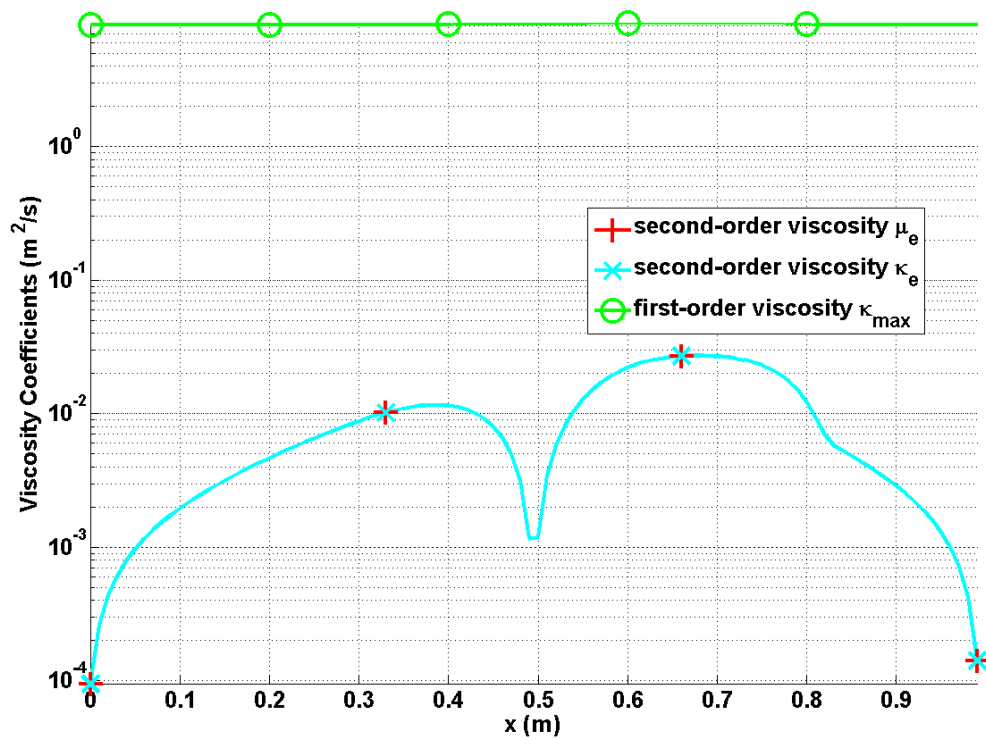


Figure 6.27: 1-D converging-diverging nozzle test: viscosity coefficients profiles for liquid phase at steady state.

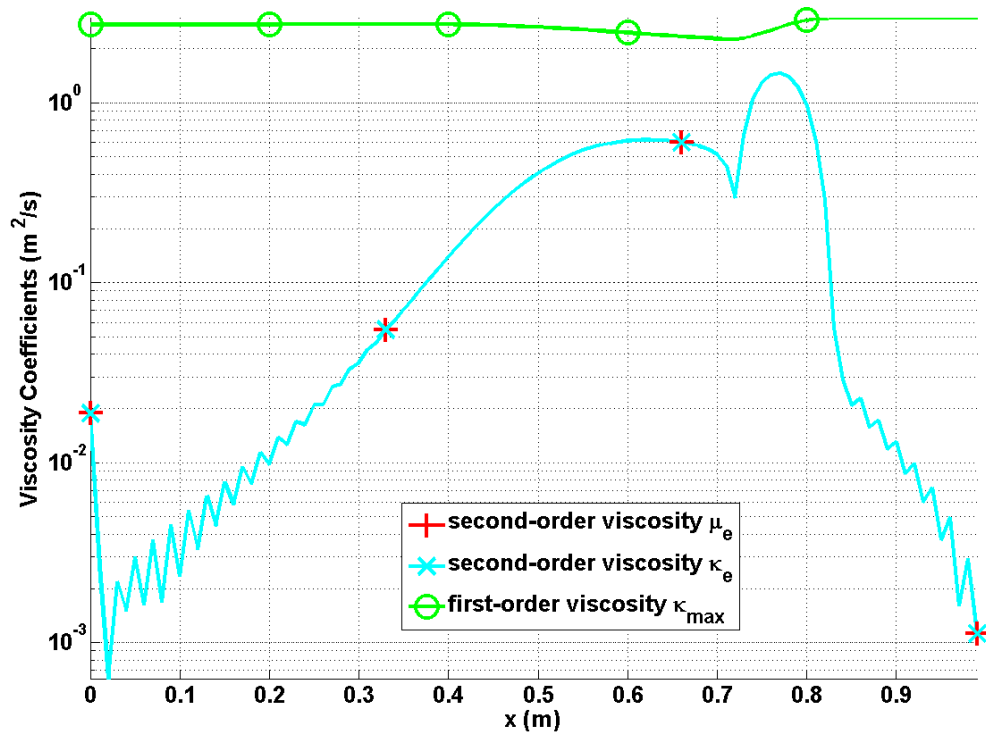


Figure 6.28: 1-D converging-diverging nozzle test: viscosity coefficients profiles for vapor phase at steady state.

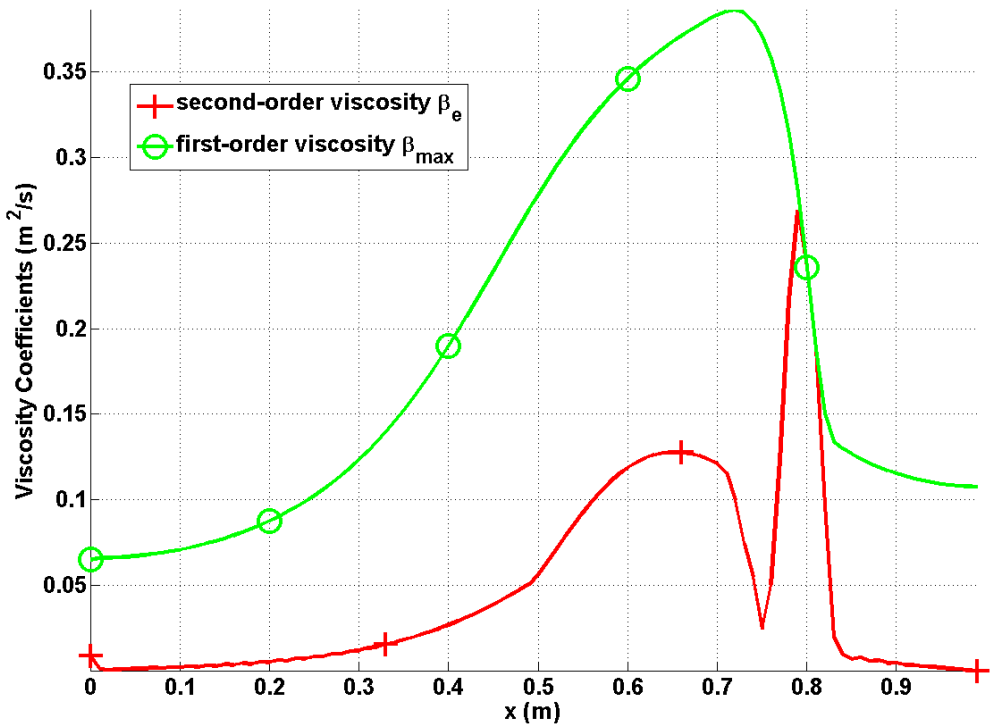


Figure 6.29: 1-D converging-diverging nozzle test: viscosity coefficients profiles for liquid volume fraction phase at steady state.

The velocity, density, volume fraction and viscosity coefficients profiles are plotted from Fig. 6.24 to 6.29 in the case  $A_{int,max} = 10^4 \text{ m}^{-1}$ . Because of the velocity relaxation source terms, velocity equilibrium holds between the liquid and vapor phases. The liquid and vapor density profiles are different by two order of magnitude. The volume fraction of both phases varies throughout the nozzle as a consequence of the pressure equilibrium. The viscosity coefficients  $\mu_k$  and  $\kappa_k$  are equal to each other since there are no shock waves and are large enough to stabilize the strong variations in the pressure and velocity profiles. Lastly, the viscosity coefficient  $\beta_k$  follows the variations of the volume fraction for both phases. It is interesting to note that the

fast vapor flow yields strong variations in the divergent part of the nozzle. Overall, the viscosity coefficients are large enough to prevent the formation of any numerical instability without altering the physical solution.

Next, the same converging-diverging nozzle is run with mass and energy exchange source terms. The code is run until steady-state with  $A_{int,max} = 10^3 \text{ m}^{-1}$ . The corresponding numerical results are shown from Fig. 6.30 to 6.36.

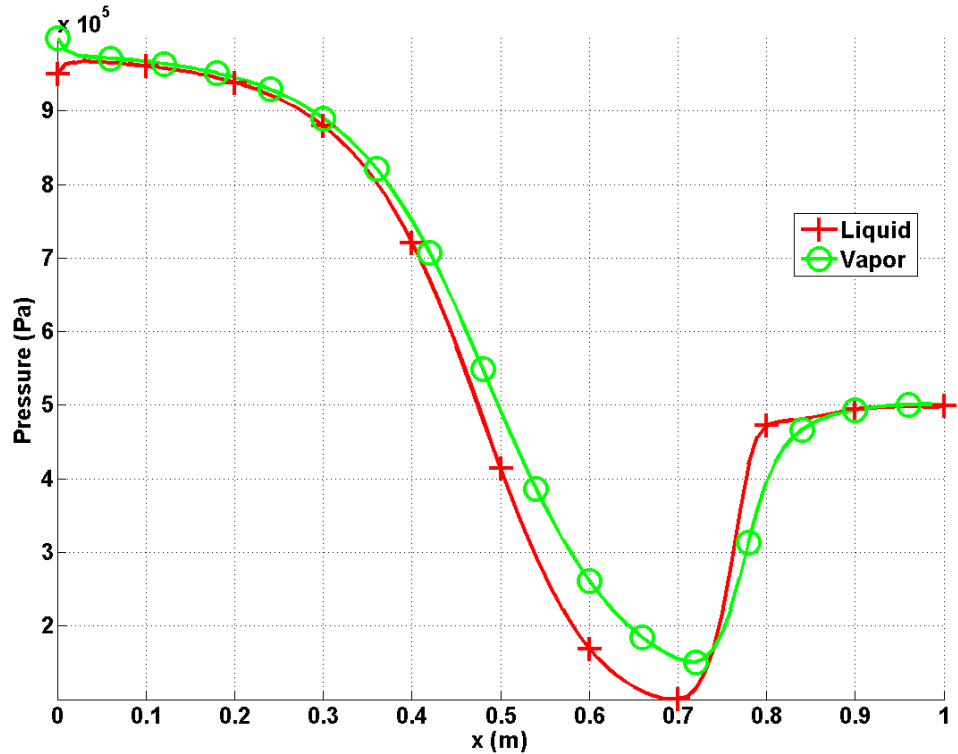


Figure 6.30: 1-D converging-diverging nozzle test: pressure profiles at steady state with thermodynamic relaxations and mass and heat exchange terms.

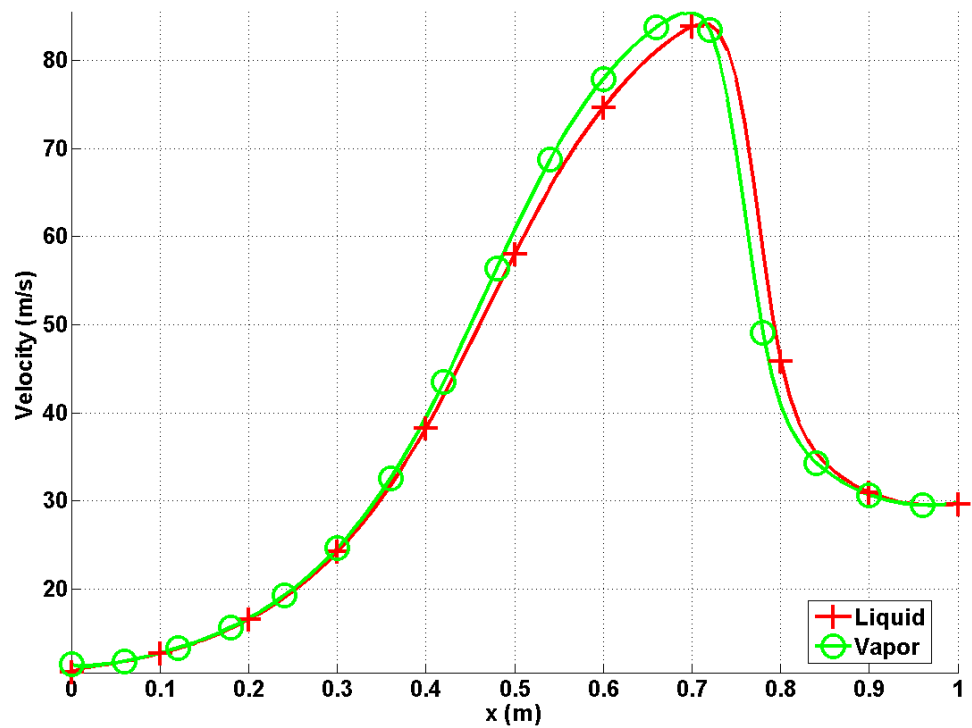


Figure 6.31: 1-D converging-diverging nozzle test: velocity profiles at steady state with thermodynamic relaxations and mass and heat exchange terms.

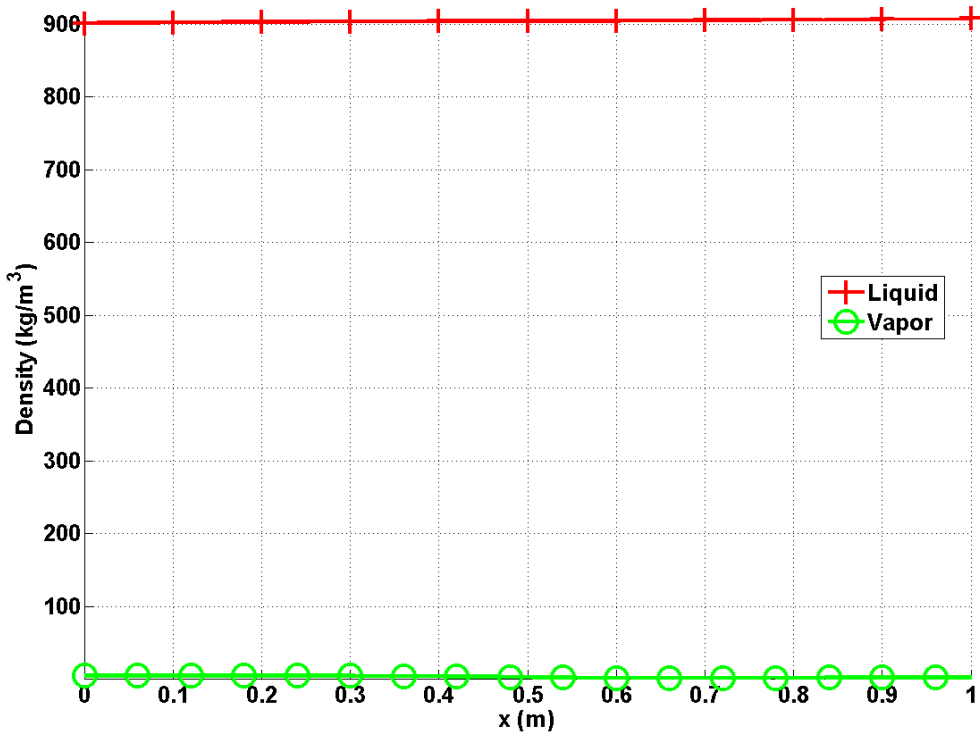


Figure 6.32: 1-D converging-diverging nozzle test: density profiles at steady state with thermodynamic relaxations and mass and heat exchange terms

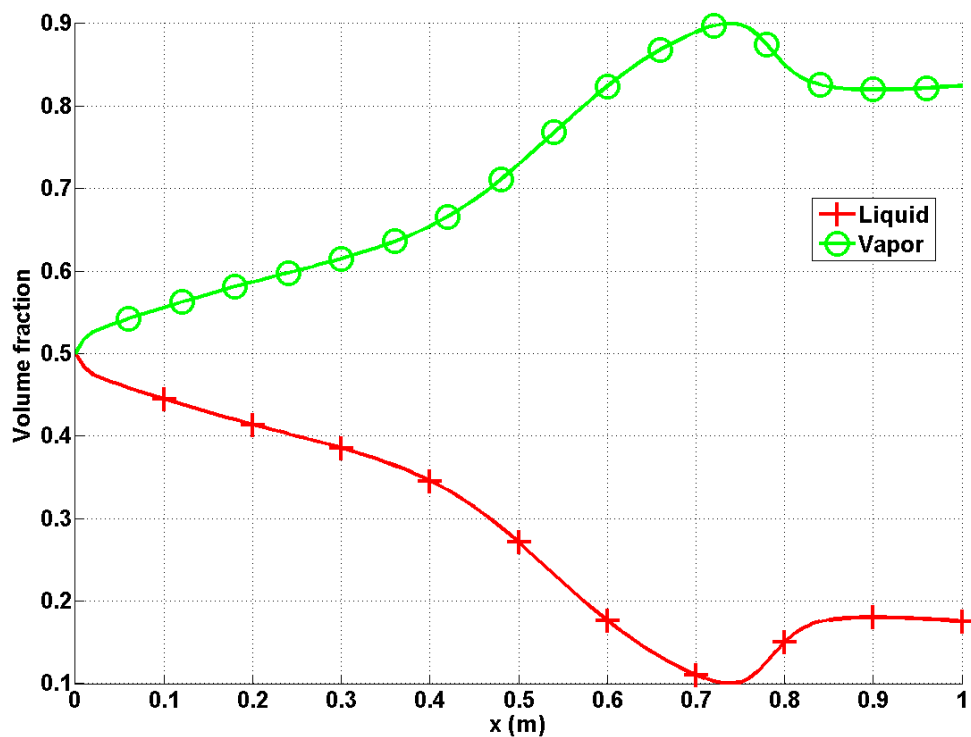


Figure 6.33: 1-D converging-diverging nozzle test: volume fraction profiles at steady state with thermodynamic relaxations and mass and heat exchange terms.

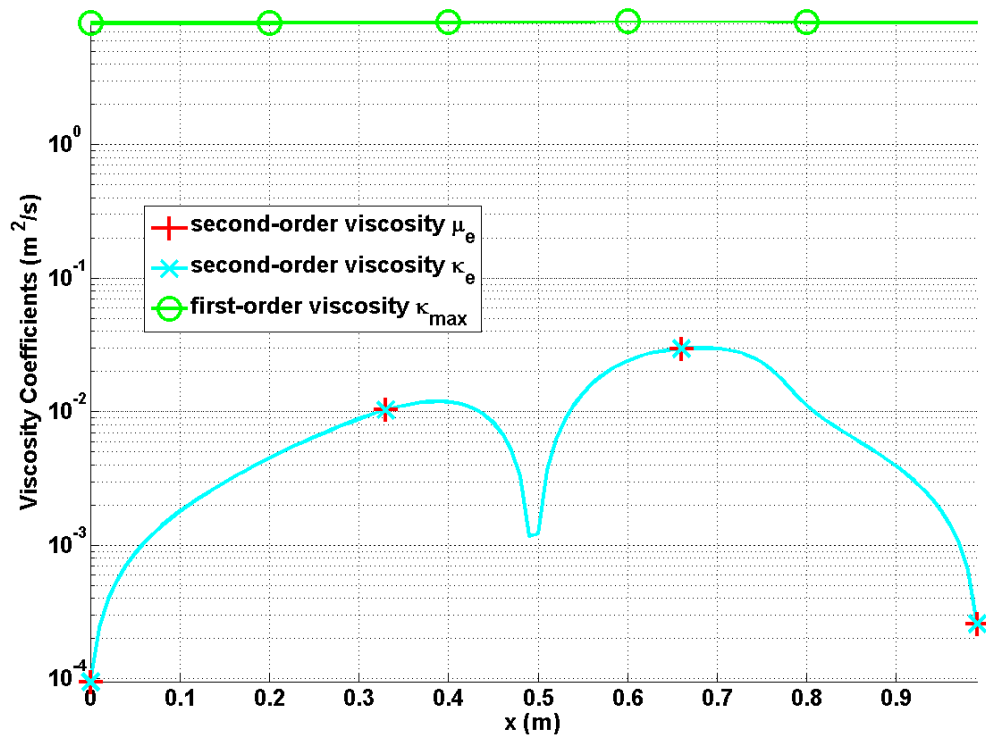


Figure 6.34: 1-D converging-diverging nozzle test: viscosity coefficients profiles for liquid phase at steady state with thermodynamic relaxations and mass and heat exchange terms.

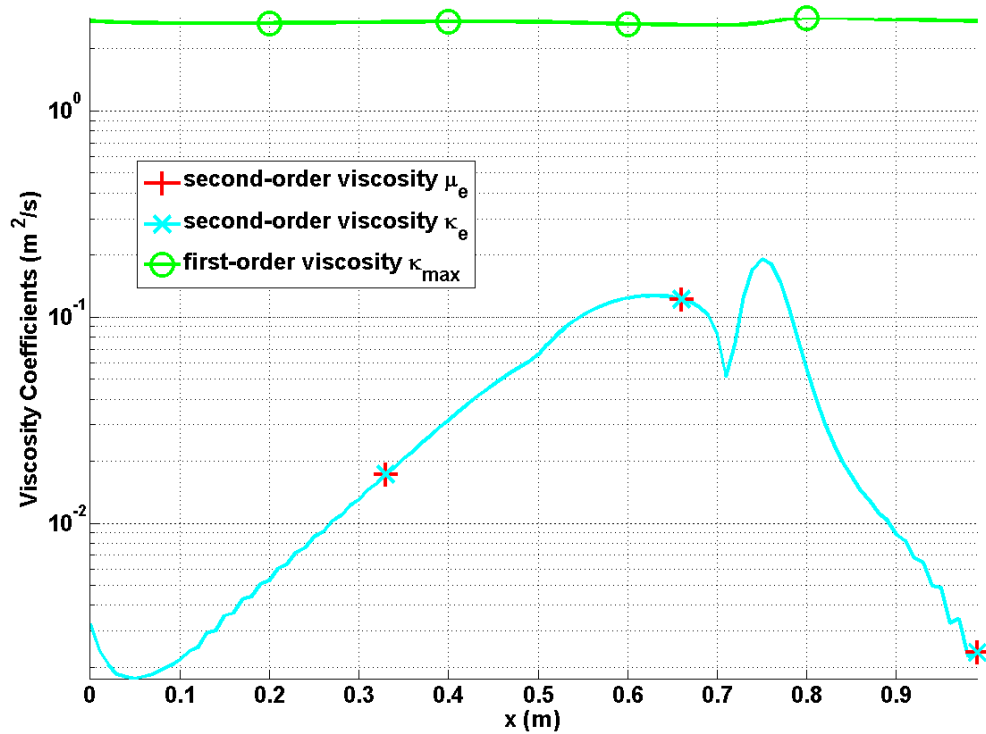


Figure 6.35: 1-D converging-diverging nozzle test: viscosity coefficients profiles for vapor phase at steady state with thermodynamic relaxations and mass and heat exchange terms.

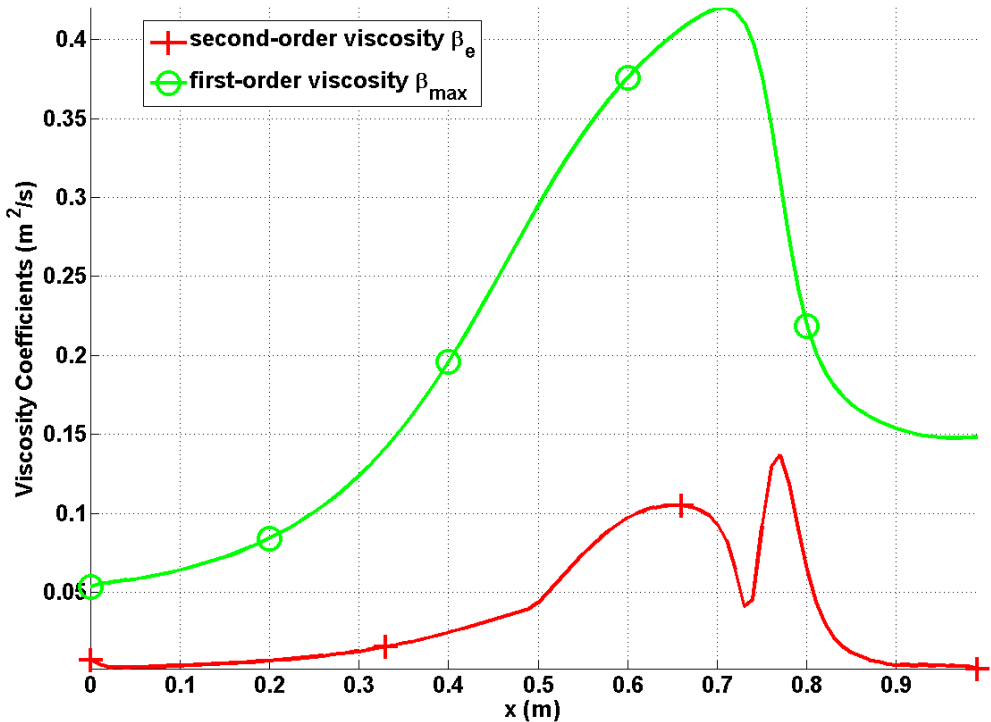


Figure 6.36: 1-D converging-diverging nozzle test: viscosity coefficients profiles for liquid volume fraction at steady state with thermodynamic relaxations and mass and heat exchange terms.

Because of the mass and heat transfers between phases, the flow variations are smoother than in the previous case. Consequently, the viscosity coefficients are also smoother while effectively stabilizing the scheme.

#### 6.4.5 1-D straight pipe with wall-friction force, wall heat source and exchange terms (mass and energy)

We present one sample result for a 1-D straight pipe of constant area  $A = 10^{-4} \text{ m}^2$  with a wall heat source (the wall temperature is constant:  $T_w = 550 \text{ K}$ ). The stiffened gas equation of state is used to model the liquid and vapor phases with the

parameters taken from [38] for each phase. A static pressure of  $P = 7.1 \text{ MPa}$  is set at the outlet. The volume fraction, the enthalpy and the mass flow rate are specified at the inlet for each phase. The wall friction coefficient is constant and the same for the two phases,  $f_w = 4 \times 10^{-2}$ . The interfacial area  $A_{int}$  is set to a large value to equalize the pressure and velocity of the two phases. The initial conditions are uniform. The geometry is discretized with a uniform mesh of 100 elements and the simulation is run with  $\text{CFL} = 100$  until a steady state is obtained.

The pressure, temperature, velocity, volume fraction and viscosity coefficients profiles are plotted from Fig. 6.37 through Fig. 6.41. As expected, the liquid and vapor pressure profiles are identical (Fig. 6.37) and decrease throughout the domain because of wall friction. The liquid and velocity profiles are also identical as shown in Fig. 6.39 and increase due to the wall friction force and the heat addition. In Fig. 6.38, the liquid and vapor temperature profiles are distinct and have the same variation: the temperature rises since energy is added to the flow by the wall heat source. The variations of the vapor and liquid volume fractions are opposite: vapor is produced since the liquid temperature is larger than the saturation temperature. All of the profiles are smooth and do not display any spurious oscillations: the entropy viscosity coefficients shown in Fig. 6.41,  $\kappa_{e,k}$  and  $\beta_{e,k}$ , are well-scaled and large enough to stabilize the numerical solution without altering it (only  $\beta_{e,liquid}$  is plotted since  $\beta_{e,liquid} = \beta_{e,vapor}$ ). It is also noted the difference of several order of magnitude between the entropy viscosity and first-order viscosity coefficients denoted by the subscript *max*. The first-order viscosity coefficients are over-dissipative and ill-scaled in the low Mach regime.

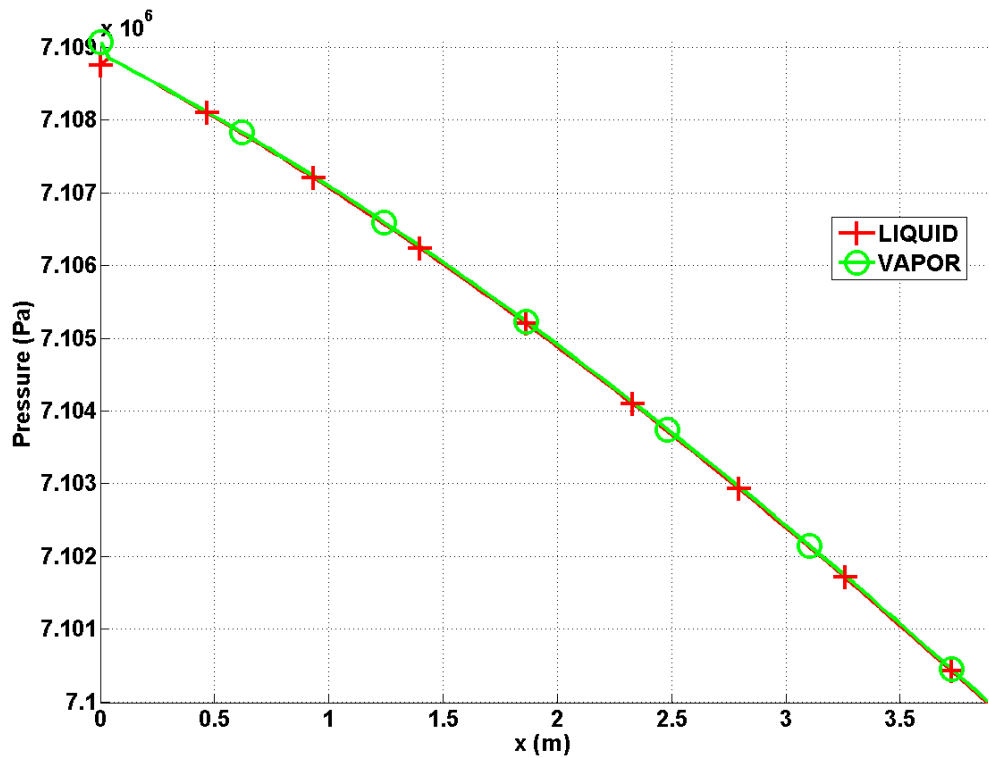


Figure 6.37: 1-D straight pipe with source terms: pressure profiles at steady-state

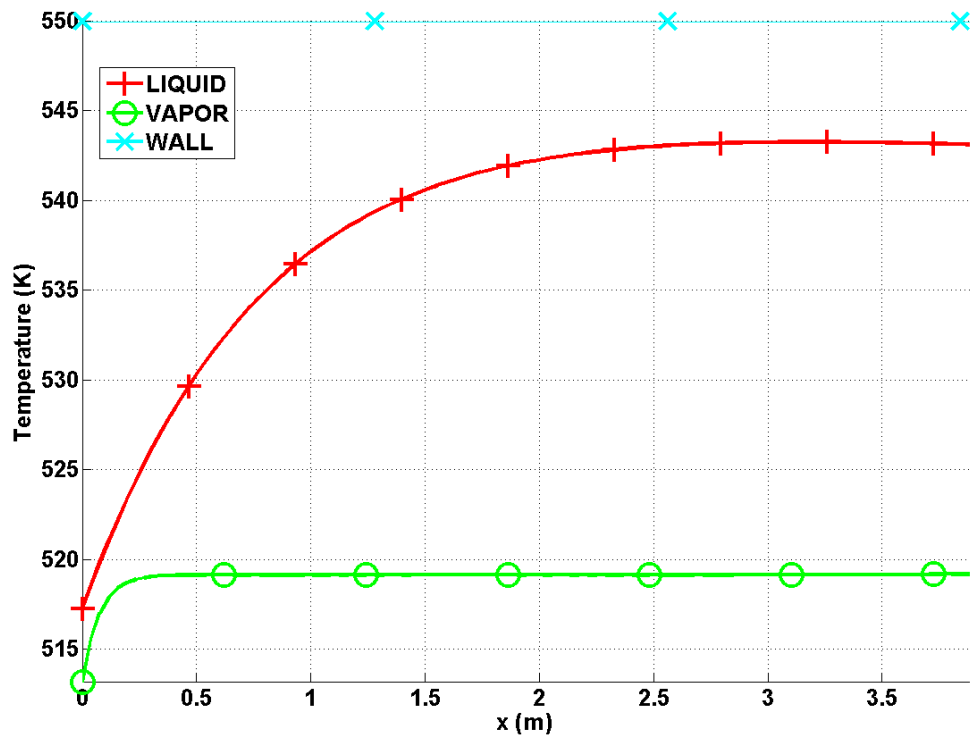


Figure 6.38: 1-D straight pipe with source terms: temperature profiles at steady-state

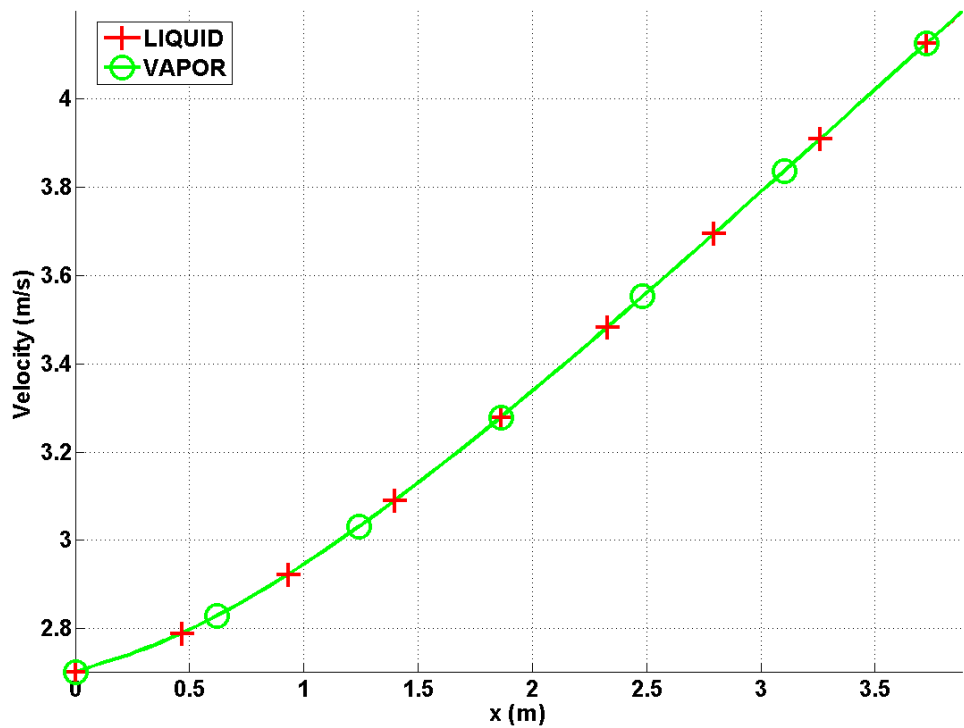


Figure 6.39: 1-D straight pipe with source terms: velocity profiles at steady-state

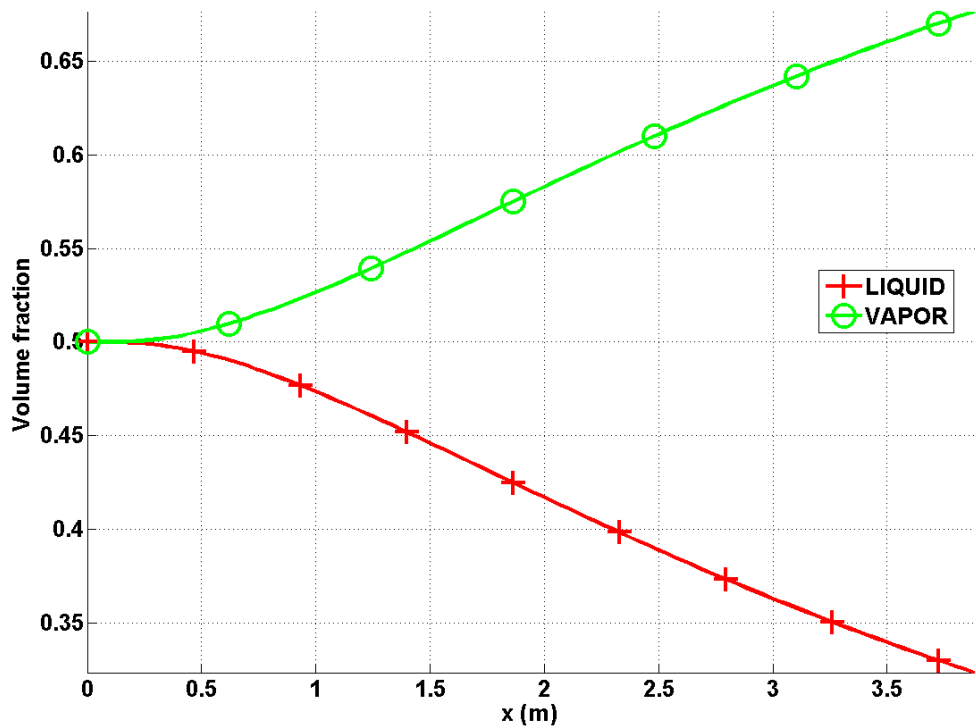


Figure 6.40: 1-D straight pipe with source terms: volume fraction profiles at steady-state

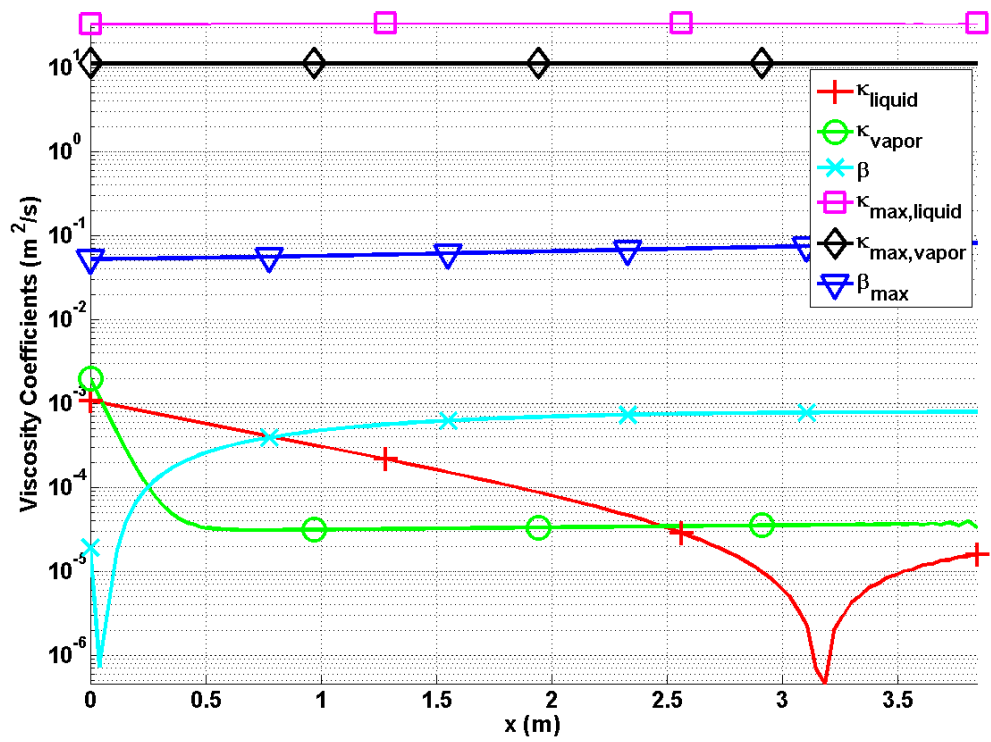


Figure 6.41: 1-D straight pipe with source terms: viscosity coefficients profiles at steady-state

## 7. APPLICATION OF THE ENTROPY VISCOSITY METHOD TO THE 1-D GREY RADIATION-HYDRODYNAMIC EQUATIONS

### 7.1 Backgrounds

Solving the radiation hydrodynamic equations is a challenging task for multiple reasons. First, the characteristic time scales between the radiation and hydrodynamics are different by several orders of magnitude which often requires the radiation part to be solved implicitly to ensure stability. Second, as with any wave-dominated problems, high resolution schemes are needed to accurately resolve shocks. Third, achieving high-order accuracy is challenging but some recent developments provided high-order accuracy results both in time and space when discretizing either the Euler equations [49, 29, 30, 39] or the radiation equation independently from each other.

Significant effort has been put into developing Riemann solvers for both the radiation and hydrodynamic equations. Balsara [7] developed a Riemann solver for the radiation-hydrodynamic equations by considering the frozen approximation that decouples the two physics components. However, such an approach may be questionable in the equilibrium diffusion limit. In this case, the coupling terms drive the physics and have to be accounted for. A *generalized Riemann solver* that accounts exactly for the relaxation terms was developed in [7]. Another approach assumes the strong equilibrium diffusion limit in which radiation diffusion is negligible and the radiation simply advects at the material velocity [71]. In this limit, the radiation hydrodynamics equation can be expressed in the form of the Euler equations with a radiation-modified equation of state (REOS) . Any solution technique for the Euler equations may be applied to these equations. Thus, one may develop approximate Riemann solvers for these equations and applied them in a general context.

Edwards and al. [28] proposed a two-stage semi-implicit IMEX scheme to solve the coupled radiation-hydrodynamic equations. They applied a Trapezoidal/BDF2 temporal discretization scheme to the nonlinear grey radiation diffusion. The radiation and hydrodynamic equations are solved implicitly and explicitly, respectively. A Riemann solver along with a flux limiter is used to resolve shocks and other waves. Their results show good agreement with semi-analytical solutions.

In this chapter we propose to solve the 1-D radiation-hydrodynamics equations by using *the entropy viscosity method*. The methodology proposed in Section 2.2 will be applied. Because of the similarity between Euler equations and the radiation hydrodynamic equations, it is conjectured that the entropy viscosity method may be a good candidate for resolving shocks occurring in radiation-hydrodynamic phenomena.

The 1-D grey radiation-hydrodynamic (GRH) equations are recalled in Eq. (7.1):

$$\begin{cases} \partial_t(\rho) + \partial_x(\rho u) = 0 \\ \partial_t(\rho u) + \partial_x(\rho u^2 + P + \frac{\epsilon}{3}) = 0 \\ \partial_t(\rho E) + \partial_x[u(\rho E + P)] = -\frac{u}{3}\partial_x\epsilon - \sigma_a c(aT^4 - \epsilon) \\ \partial_t\epsilon + \frac{4}{3}\partial_x(u\epsilon) = \frac{u}{3}\partial_x\epsilon + \partial_x\left(\frac{c}{3\sigma_t}\partial_x\epsilon\right) + \sigma_a c(aT^4 - \epsilon) \end{cases}, \quad (7.1)$$

where  $\rho$ ,  $u$ ,  $E$ ,  $\epsilon$ ,  $P$  and  $T$  are the material density, material velocity, material specific total energy, radiation energy density, material pressure and temperature, respectively. The total and absorption cross sections,  $\sigma_t$  and  $\sigma_a$ , are either constant or density- and temperature-dependent. The variables  $a$  and  $c$  are the Boltzman constant and the speed of light, respectively. Lastly, the symbols  $\partial_t$  and  $\partial_x$  denote the temporal and spatial partial derivatives, respectively. The material temperature

and pressure are computed with the Ideal Gas equation of state (IGEOS):

$$\begin{cases} P = (\gamma - 1)C_v \rho T \\ e = C_v T \end{cases}, \quad (7.2)$$

where  $e$  is the specific internal energy and is obtained from the expression  $e = E - 0.5u^2$ . The heat capacity  $C_v$  and the heat ratio coefficient  $\gamma$  are assumed constant.

The objective of this paper is to extend the entropy-based viscosity method to the 1-D grey radiation-hydrodynamic equations. The approach followed in this paper is similar to those of [7, 54]: an infinite opacity is assumed and the relaxation terms are ignored in order to make Eq. (7.1) hyperbolic. Then, an entropy equation is derived and used to obtain the functional forms of the viscous stabilization terms. Definitions for the viscosity coefficients are provided.

This chapter is organized as follows. In Section 7.2, the entropy viscosity method is extended to the grey radiation-hydrodynamic equations; details regarding the derivation of the adequate dissipative terms and definitions for the new viscosity coefficients are provided. Numerical results are presented in Section 7.3 where the second-order accuracy of the scheme is demonstrated in both the equilibrium diffusion and streaming limits, using the method of manufactured solutions applied to the GRH equations. Then, several numerical test cases, taken from the published literature, are provided; in these simulations, the Mach number varies from 1.05 to 50 [53].

## 7.2 The Entropy Viscosity Method applied to the 1-D radiation-hydrodynamic equations

In this section, we extend the entropy viscosity method [29, 30, 69] to the 1-D radiation-hydrodynamic equations in a staged process. First, the reader is guided

through the main steps that lead to the derivation of the dissipative terms, using the entropy minimum principle [63]. Then, a definition for the entropy viscosity coefficient based upon the entropy production is given.

We recall that the entropy viscosity method was developed for hyperbolic system of equations. However, the radiation hydrodynamic equations are not strictly hyperbolic but several numerical techniques are based on the study of their hyperbolic parts [7, 54]. Thus, following the same rationale, the system of equations given in Eq. (7.1) is made hyperbolic by assuming an infinite opacity (the frozen approximation) and by ignoring the relaxation terms. These two assumptions yield the following system of equations:

$$\begin{cases} \partial_t(\rho) + \partial_x(\rho u) = 0 \\ \partial_t(\rho u) + \partial_x(\rho u^2 + P + \frac{\epsilon}{3}) = 0 \\ \partial_t(\rho E) + \partial_x[u(\rho E + P)] = -\frac{u}{3}\partial_x\epsilon \\ \partial_t\epsilon + \frac{4}{3}\partial_x(u\epsilon) = \frac{u}{3}\partial_x\epsilon \end{cases} \quad (7.3)$$

The jacobian matrix of the hyperbolic terms can be computed to derive the eigenvalues:

$$\lambda_1 = u - c_m, \lambda_{2,3} = u \text{ and } \lambda_4 = u + c_m, \quad (7.4)$$

where  $c_m$  is the radiation-modified material speed of sound and is defined as follows:

$$c_m^2 = \underbrace{P_\rho + \frac{P}{\rho^2}P_e}_{c_{Euler}^2} + \frac{4\epsilon}{9\rho} \quad (7.5)$$

with  $P_x$  the standard shorthand notation for  $\partial_x P$ , and  $c_{Euler}^2$  denotes the definition of the speed of sound when considering only the 1-D Euler equations. The above hyperbolic system of equations can be recast in a conservative form. This allows us

to assume the existence of an entropy function  $s$  [36] that depends upon the internal energy  $e$ , the density  $\rho$ , and the radiation energy density  $\epsilon$ . Following some algebra given in Appendix D, an equation satisfied by the entropy  $s$  is obtained:

$$\rho \frac{Ds}{Dt} = \rho (\partial_t s + u \partial_x s) = 0, \quad (7.6)$$

where  $\frac{Ds}{Dt}$  denotes the total or material derivative. Eq. (7.6) is referred to as the entropy residual and is used to prove the entropy minimum principle,  $\frac{Ds}{Dt} \geq 0$ , [63].

When adding dissipative terms to each equation of Eq. (7.3) as required in the entropy viscosity method, the entropy residual equation is modified and some additional terms will appear in the right-hand side of Eq. (7.6). The sign of these extra terms needs to be studied for the entropy minimum principle to hold. As such, the entropy minimum principle is invoked to guide in the derivation of appropriate expressions for each of the dissipative terms. Obtaining the final expression of the dissipative terms is a lengthy process and only the final result along with the key assumptions are stated here. The reader is referred to Appendix D for the details of the derivation. The system of equations with the dissipative terms is as follows:

$$\left\{ \begin{array}{l} \partial_t (\rho) + \partial_x (\rho u) = \partial_x (\kappa \partial_x \rho) \\ \partial_t (\rho u) + \partial_x (\rho u^2 + P + \frac{\epsilon}{3}) = \partial_x (\kappa \partial_x \rho u) \\ \partial_t (\rho E) + \partial_x [u (\rho E + P)] + \frac{u}{3} \partial_x \epsilon = \partial_x (\kappa \partial_x (\rho E)) \\ \partial_t \epsilon + \frac{4}{3} \partial_x (u \epsilon) - \frac{u}{3} \partial_x \epsilon = \partial_x (\kappa \partial_x \epsilon) \end{array} \right. , \quad (7.7)$$

where  $\kappa$  is a locally defined positive viscosity coefficient. It was assumed the following conditions hold:

$$\left\{ \begin{array}{l} P \frac{\partial s}{\partial e} + \rho^2 \frac{\partial s}{\partial \rho} + \frac{4}{3} \rho \epsilon \frac{\partial s}{\partial \epsilon} = 0 \\ s(\rho, e, \epsilon) = \hat{s}(\rho, e) + \frac{\rho_0}{\rho} \tilde{s}(\epsilon) \end{array} \right. \quad (7.8)$$

where  $\tilde{s}$  is concave with respect to the radiation energy density  $\epsilon$  and  $\hat{s}$  is concave with respect to the internal energy  $e$  and the specific volume  $\rho^{-1}$ . The constant  $\rho_0$  is of order one and appears only for dimensionality purposes. The function  $\hat{s}$  and  $\tilde{s}$  are both physical entropy functions.

Once the dissipative terms are obtained, it remains to define the local viscosity coefficient  $\kappa(x, t)$ . Note that at the difference of the multi-D Euler equations of Section 5, only one viscosity coefficient is required since the low Mach asymptotic limit is not investigated in this chapter. In other word, it is assumed that  $\mu(x, t) = \kappa(x, t)$  following the notations used in Section 5. We require the following to hold in the prescription for  $\kappa$ :

- Since the entropy residual is a measure of the entropy production that occurs in shock regions, it is natural to define a viscosity coefficient proportional to the entropy residual. This will enable shock detection and tracking and will also provide a measure of the viscosity required to stabilize the scheme. This viscosity coefficient is referred to as the *entropy viscosity coefficient* or *second-order viscosity coefficient* and is denoted by  $\kappa_e(x, t)$ .
- An upper bound on  $\kappa$  is to be set since entropy production can be very large in shocks. For explicit time integration, the maximum value of the viscosity coefficient is related to the Courant-Friedrichs-Lowy number (CFL). The upper bound on  $\kappa$  is defined by analogy to the standard upwind (Godunov) scheme that is known to efficiently smooth out oscillations (but is only first-order accurate). With implicit temporal integrators, the same reasoning is used even if the CFL number may not need to be strictly respected. This upper bound will be referred to as the *first-order viscosity*, denoted by  $\kappa_{max}(x, t)$ .
- The viscosity coefficient  $\kappa$  that is actually used in the dissipative terms of

Eq. (7.3) is defined as follows:  $\kappa(x, t) = \min(\kappa_e(x, t), \kappa_{max}(x, t))$ . With such a definition, the viscosity added to the system of equations will saturate to the first order viscosity in the shock regions. Elsewhere, the entropy production and thus the viscosity coefficient  $\kappa$  are expected to be small.

Next, we define the local first- and second-order viscosity coefficients  $\kappa_{max}(x, t)$  and  $\kappa_e(x, t)$ , respectively. Following the work of Zingan et al. [69], the first-order viscosity definition is based on the local largest eigenvalue that is known to be  $|u| + c_m$  in 1-D:

$$\kappa_{max} = \frac{h}{2} (|u| + c_m) \quad (7.9)$$

where  $h$  is the local grid size. This definition is derived based on the upwind scheme and a simple derivation can be found in [29] in the case of a scalar hyperbolic equation. Through the definition of the radiation-modified speed of sound  $c_m$ , both the material and radiation properties are accounted for in the definition of the first-order viscosity coefficient.

The definition of the second order viscosity coefficient  $\kappa_e(x, t)$  is based upon the entropy residual (Eq. (7.6)) recast as a function of pressure  $P$ , density  $\rho$  and radiation energy density  $\epsilon$ :

$$R(x, t) = \frac{s_e}{P_e} \underbrace{\left( \frac{dP}{dt} - c_{Euler}^2 \frac{d\rho}{dt} \right)}_{\hat{R}(x, t)} \quad (7.10)$$

The term  $s_e$  is the inverse of the material temperature (Appendix D) and  $P_e$  is computed from the IGEOS. These two terms are positive so that the sign of the entropy residual  $R(x, t)$  can be determined by simply inspecting the terms inside the parentheses, denoted by  $\hat{R}(x, t)$ . Such an expression is easier to compute than the one given in Eq. (7.6) which required an analytical expression for the entropy function. In addition to the entropy residual, inter-element jumps in the pressure

and density gradients,  $J$ , are also accounted for. The objective is to be able to also detect discontinuities that are not shocks, such as contact waves (there is no entropy production in a contact wave), in order to stabilize them as well.

Thus, the entropy viscosity coefficient  $\kappa_e(x, t)$  is set to be proportional to  $\hat{R}(x, t)$  and  $J$  with the following form:

$$\kappa_e(x, t) = h^2 \frac{\max(|\hat{R}(x, t)|, J)}{n_P} \quad (7.11)$$

where  $J = \max_i(J(x_i, t))$ , and  $J(x_i, t)$  is the jump of a given quantity at cell interface  $x_i$ , and  $n_P$  is a normalization function (of the same units as pressure) that has to be chosen so that the viscosity coefficient  $\kappa$  has units of  $m^2/s$ . The following definition for the normalization function has been chosen:  $n_P = \rho c_m^2$ . Thus, the final definition for the viscosity coefficient  $\kappa$  is the following:

$$\kappa_e(x, t) = h^2 \frac{\max(|\hat{R}(x, t)|, J)}{\rho c_m^2} \quad (7.12)$$

The jump  $J$  in the definition of  $\kappa(x, t)$  is piecewise-constant. Its definition is discretization-dependent and defined as follows for Continuous Galerkin FEM:

$$\begin{cases} J_P(x_i, t) = |u|[[\partial_x P]] \\ J_\rho(x_i, t) = c_m^2 |u|[[\partial_x \rho]] \\ J(x_i, t) = \max(J_\rho(x_i, t), J_P(x_i, t)) \end{cases} \quad (7.13)$$

The symbol  $[[\cdot]]$  denotes the jump at the cell interface.

The entropy viscosity method is now well defined for the hyperbolic system given in Eq. (7.3) and will be used to solve for the grey radiation-hydrodynamic equations given in Eq. (7.1). However, one may question how the relaxation source terms,

$\sigma_a c(aT^4 - \epsilon)$  and the physical diffusion term,  $\partial_x(D\partial_x\epsilon)$ , may affect the entropy viscosity method. When applying the entropy viscosity method, the radiation energy density equation will now contain a diffusive term and a numerical dissipative term with a vanishing viscosity coefficient  $\kappa$ . As long as the diffusive coefficient  $D = \frac{c}{3\sigma_t}$  is larger than the viscosity coefficient  $\kappa$ , the numerical dissipative term should not be required. A way to ensure consistency and prevent the formation of oscillations in the frozen limit is to merge the two second-order derivative terms into one as follows:

$$\partial_x \left( \frac{c}{3\sigma_t} \partial_x \epsilon \right) + \partial_x (\kappa \partial_x \epsilon) \implies \partial_x \left[ \max \left( \frac{c}{3\sigma_t}, \kappa \right) \partial_x \epsilon \right] \quad (7.14)$$

Thus, as long as the artificial viscosity coefficient  $\kappa$  is locally smaller than the physical diffusive coefficient  $D = \frac{c}{3\sigma_t}$ , no artificial viscosity is required to ensure stability of the numerical scheme. As the diffusive coefficient  $D$  goes to zero, shocks can form in the radiation energy density profile and will require a certain amount of viscosity in order to prevent oscillations from appearing.

The effect of the relaxation source terms onto the entropy viscosity method can become problematic in the equilibrium diffusion limit ( $\sigma_a c \rightarrow \infty$ ): the relaxation source terms behave as dissipative terms and make the system parabolic [39]. In [31], a study on the impact of various artificial viscosity methods onto hyperbolic systems with relaxation terms was carried out. It was shown that high-order viscosity coefficients are more suitable since they do not alter the physical solution as much as first-order viscosity terms (upwind scheme). A manufactured solution is employed in Section 7.3.1 to test the convergence of the numerical solution in the equilibrium-diffusion limit. The normalization factor has to be larger than  $h$  in order to conserve high-order accuracy.

The reader will notice that, except for the definition of the jumps, the whole

method is independent of the spatial discretization employed. The technique could be used with discontinuous Galerkin finite element or finite volume methods. In both cases, an adequate definition of the jump terms can be found in [69].

### 7.3 Numerical results

In this section, numerical results using the entropy viscosity method are presented for the dimensional 1-D grey radiation-hydrodynamic equations. First, second-order accuracy of the method is demonstrated using the method of manufactured solution (MMS). Then, results for some standard radiation-hydrodynamic test cases are given. Details of the temporal and spatial discretizations for a the CGFEM employed in the multi physics MOOSE framework [17] are given in Section 3.1.

#### 7.3.1 *Space/time accuracy*

The same manufactured solution as in [28] is used in order to test both the diffusive and streaming limit solutions in a slab of thickness  $L = 2\pi \text{ cm}$ . The manufactured solutions are composed of trigonometric functions. Periodic boundary conditions are used for all of the variables. The  $L_2$  norm of the error between the numerical and exact solutions are computed for density, momentum, total material energy, and radiation energy density. For each new simulation, the time step is divided by two and the number of spatial degrees of freedom is doubled. With such settings, the error is expected to decrease by a factor 4 if second-order convergence is achieved.

The first manufactured solution is designed to test the equilibrium-diffusion limit. In that case, the radiation energy is in equilibrium with the material temperature and the opacity is large which means that the radiation mean-free path is not resolved

but the variation of the solution is resolved. The following exact solution was used:

$$\begin{cases} \rho = \sin(x - t) + 2 \\ u = \cos(x - t) + 2 \\ T = \frac{0.5\gamma(\cos(x-t)+2)}{\sin(x-t)+2} \\ \epsilon = aT^4 \end{cases} . \quad (7.15)$$

The cross sections  $\sigma_a$  and  $\sigma_t$  are assumed constant and set to the same value  $1000 \text{ cm}^{-1}$ . The simulation is run until  $t = 3 \text{ sh}$  ( $1 \text{ sh} = 10^{-8} \text{ sec}$ ). The  $L_2$  error norm along with its ratio between consecutive simulations are given in Table 7.1 for the equilibrium diffusion limit case.

Table 7.1:  $L_2$  norms of the error for the equilibrium diffusion limit case using a manufactured solution.

# of cells	time step size ( $sh$ )	$\rho$	ratio	$\rho\mathbf{E}$	ratio
20	$10^{-1}$	0.590766	NA	1.333774	NA
40	$5 \cdot 10^{-1}$	0.290626	2.03	0.478819	2.79
80	$2.5 \cdot 10^{-2}$	0.0959801	3.021	0.154119	3.11
160	$1.25 \cdot 10^{-2}$	0.02593738	3.70	0.0405175	3.80
320	$6.25 \cdot 10^{-3}$	$6.471444 \cdot 10^{-3}$	4.00	$9.90446 \cdot 10^{-3}$	4.09
640	$3.125 \cdot 10^{-3}$	$1.584158 \cdot 10^{-3}$	4.01	$2.44727 \cdot 10^{-3}$	4.04
# of cells	time step size ( $sh$ )	$\epsilon$	ratio	$\rho\mathbf{u}$	ratio
20	$10^{-1}$	0.00650085	NA	0.910998	NA
40	$5 \cdot 10^{-1}$	0.00124983	5.20	0.4090946	2.23
80	$2.5 \cdot 10^{-2}$	0.000262797	4.76	0.125943	3.25
160	$1.25 \cdot 10^{-2}$	$6.17726 \cdot 10^{-5}$	4.25	$3.381042 \cdot 10^{-3}$	3.72
320	$6.25 \cdot 10^{-3}$	$1.509184 \cdot 10^{-5}$	4.09	$8.373657 \cdot 10^{-3}$	4.04
640	$3.125 \cdot 10^{-3}$	$3.72548 \cdot 10^{-6}$	4.05	$2.070538 \cdot 10^{-3}$	4.04

The second manufactured solution is used to test the method in the streaming limit: the radiation streaming dominates the absorption/re-emission term and

evolves at a fast time scale. The exact solution used is as follows :

$$\begin{cases} \rho = \sin(x - t) + 2 \\ u = (\sin(x - t) + 2)^{-1} \\ T = 0.5\gamma \\ \epsilon = \sin(x - 1000t) + 2 \end{cases} \quad (7.16)$$

For this manufactured solution, the cross sections are still assumed constant and set to the same value  $1 \text{ cm}^{-1}$ . The final time is  $t_{final} = 3 \text{ sh}$ . Once again, the  $L_2$  error norm is given in Table 7.2 for the density, momentum, material total energy and radiation energy density.

Table 7.2:  $L_2$  norms of the error for the streaming limit case using a manufactured solution.

# of cells	time step size ( $sh$ )	$\rho$	ratio	$\rho\mathbf{E}$	ratio
20	$10^{-1}$	$1.4373 \cdot 10^{-2}$	NA	$5.88521 \cdot 10^{-1}$	NA
40	$5 \cdot 10^{-2}$	$3.760208 \cdot 10^{-3}$	3.82	$1.4244 \cdot 10^{-1}$	4.13
80	$2.5 \cdot 10^{-2}$	$9.91724 \cdot 10^{-4}$	3.79	$3.2047 \cdot 10^{-2}$	4.44
160	$1.25 \cdot 10^{-2}$	$2.4455 \cdot 10^{-4}$	4.06	$7.4886 \cdot 10^{-3}$	4.28
320	$6.25 \cdot 10^{-3}$	$6.280715 \cdot 10^{-5}$	3.89	$1.82327 \cdot 10^{-3}$	4.11
640	$3.125 \cdot 10^{-3}$	$1.57920 \cdot 10^{-5}$	3.98	$4.50463 \cdot 10^{-4}$	4.05
1280	$1.5625 \cdot 10^{-4}$	$3.96096 \cdot 10^{-6}$	3.99	$1.12061 \cdot 10^{-4}$	4.02
# of cells	time step size ( $sh$ )	$\epsilon$	ratio	$\rho\mathbf{u}$	ratio
20	$10^{-1}$	$3.82001 \cdot 10^{-1}$	NA	$2.354671 \cdot 10^{-3}$	NA
40	$5 \cdot 10^{-2}$	$1.21500 \cdot 10^{-1}$	3.14	$6.138814 \cdot 10^{-4}$	3.84
80	$2.5 \cdot 10^{-2}$	$3.27966 \cdot 10^{-2}$	3.70	$1.74974 \cdot 10^{-4}$	3.51
160	$1.25 \cdot 10^{-2}$	$8.38153 \cdot 10^{-3}$	3.91	$3.61297 \cdot 10^{-5}$	4.84
320	$6.25 \cdot 10^{-3}$	$2.10925 \cdot 10^{-3}$	3.97	$9.03866 \cdot 10^{-6}$	3.99
640	$3.125 \cdot 10^{-3}$	$5.28472 \cdot 10^{-4}$	3.99	$2.25649 \cdot 10^{-6}$	4.01
1280	$1.5625 \cdot 10^{-4}$	$1.322268 \cdot 10^{-4}$	3.99	$5.69984 \cdot 10^{-7}$	3.95

For both manufactured solutions the error is divided by four as the time step and the spatial mesh are reduced by a factor two. Thus, we conclude that GRH equations can be numerically solved with second-order accuracy using the entropy viscosity method when the exact solution is smooth.

### 7.3.2 Radiation shock simulations

The purpose of this section is to show that the entropy-based viscosity method (Section 7.2) can accurately resolve shocks occurring in radiation-hydrodynamic simulations. Multiple test cases are considered, with Mach numbers of 1.05, 1.2, 2, 5 and 50 [53]. All of the simulations are run with 500 spatial cells and with a Courant-Friedrichs-Lowy (CFL number) of 10 until steady-state (even if the scheme employed here is fully implicit, a CFL number can still be computed and is a good reference for comparison against semi-implicit or fully explicit codes). Linear Lagrange polynomials and the second-order temporal integrator BDF2 are once again used. For clarity, the initial conditions for each test case will be recalled in a table and plots of the density,  $\rho(x)$ , the radiation temperature,  $\theta(x)$ , and material temperature,  $T(x)$ , at steady-state will be given as well as those of the viscosity coefficients,  $\kappa(x)$  and  $\kappa_{max}(x)$ . The computational domain consists of a 1-D slab of thickness  $L$ . The initial discontinuity between the left and right states is located at  $x_0$  and will be specified for all test cases. For all of the test cases presented in this paper, the cross sections  $\sigma_a$  and  $\sigma_t$  are assumed constant and set to  $853.144 \text{ cm}^{-1}$  and  $390.711 \text{ cm}^{-1}$ , respectively, if not otherwise specified. The heat capacity at constant specific volume is set to  $C_v = 0.12348 \text{ jerks}/(g - \text{keV})$ .

For the Mach 2 simulation, results will also be shown when employing only the first-order viscosity ( $\kappa(x, t) = \kappa_{max}(x, t)$ ) in order to show the benefits of using a high-order viscosity coefficient.

The inlet and outlet boundary conditions (BCs) are given next. The Euler equations and radiation equation are considered independently since the latter one is parabolic. At the inlet, the flow is supersonic and, therefore, no physical information exits the system. Thus, Dirichlet boundary condition can be used. At the outlet,

the flow become subsonic which requires a particular treatment. Following the work from [55], a static boundary condition is implemented. Only the back pressure is provided and the other variables are computed using the characteristic equations. For the radiation equation, vacuum boundary conditions are used at both inlet and outlet.

#### 7.3.2.1 An equilibrium diffusion test

For this test, the inlet Mach number is set to 1.05. The radiation field and material are in equilibrium. The initial conditions are given in Table 7.3.

Table 7.3: Initial conditions for mach 1.05.

	left	right
$\rho (g/cm^3)$	1.	1.0749588
$u (cm/sh)$	0.1228902	0.1144127
$T (keV)$	0.1	0.1049454
$\epsilon (jerks/cm^3)$	$1.372 \cdot 10^{-6}$	$1.6642117 \cdot 10^{-6}$

The computational domain is of size  $L = 0.08 \text{ cm}$  and the initial step is at  $x_0 = 0.015 \text{ cm}$ . The numerical solutions at steady state are given in Fig. 7.1, Fig. 7.2 and Fig. 7.3.

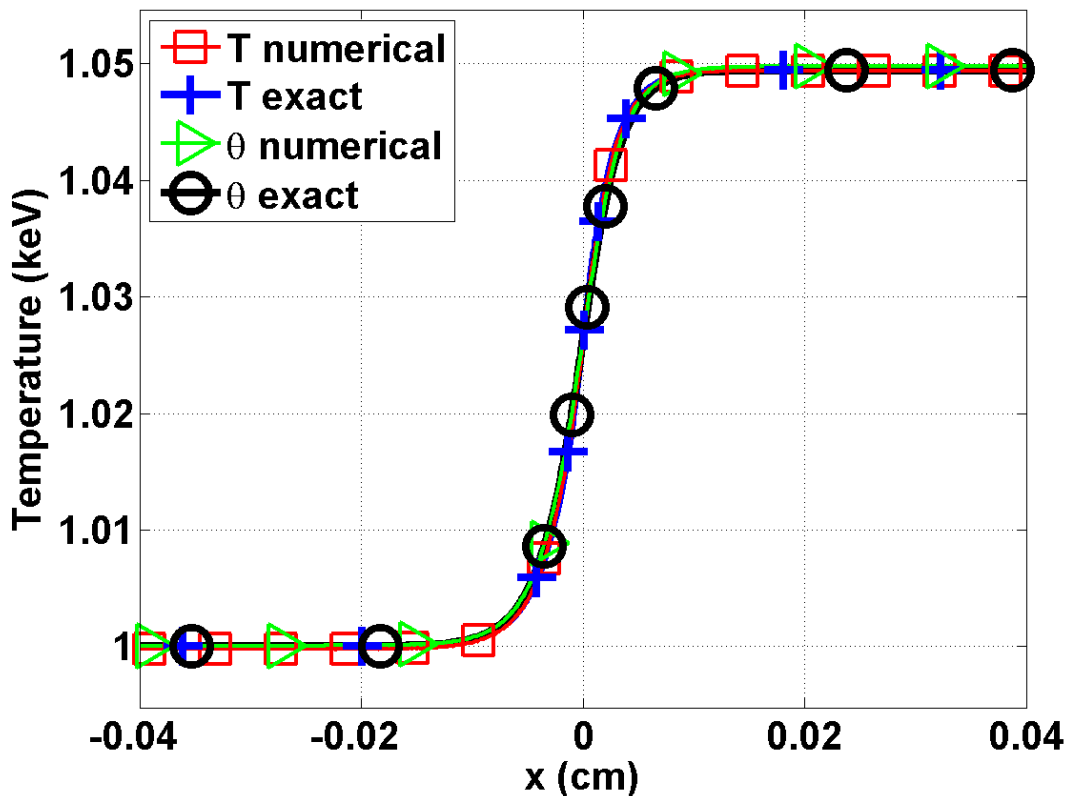


Figure 7.1: Material and radiation temperature profiles at steady state for Mach 1.05 test.

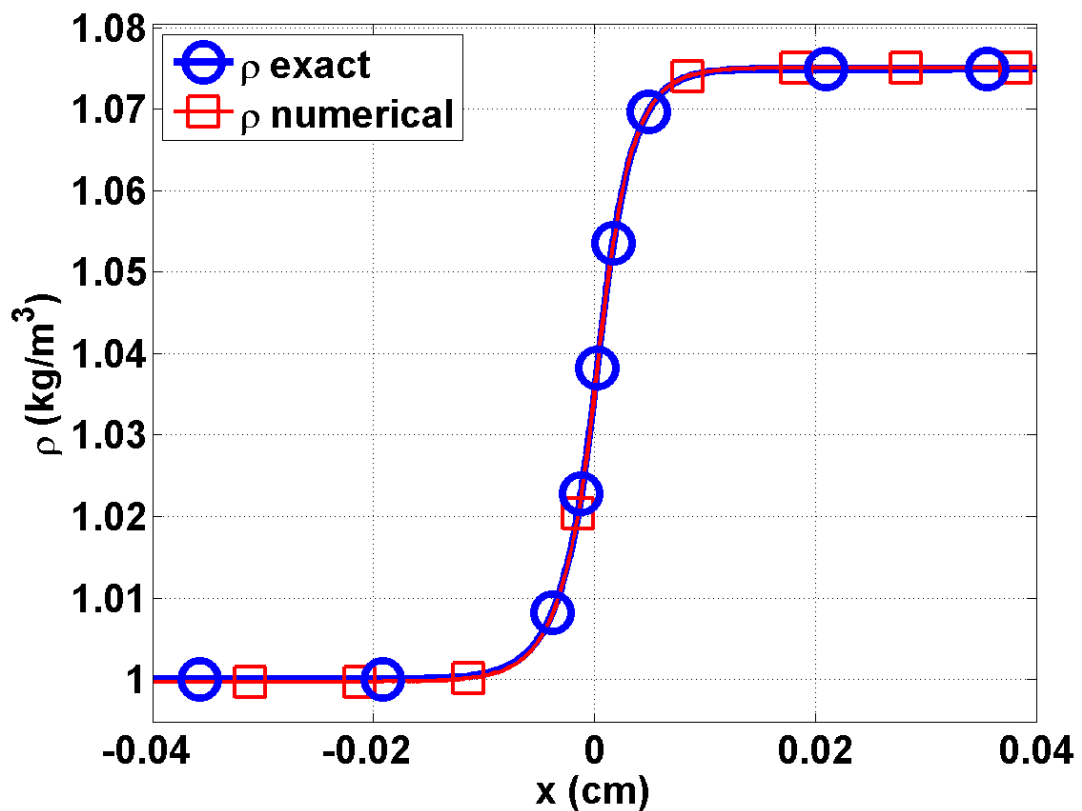


Figure 7.2: Material density profile at steady state for Mach 1.05 test.

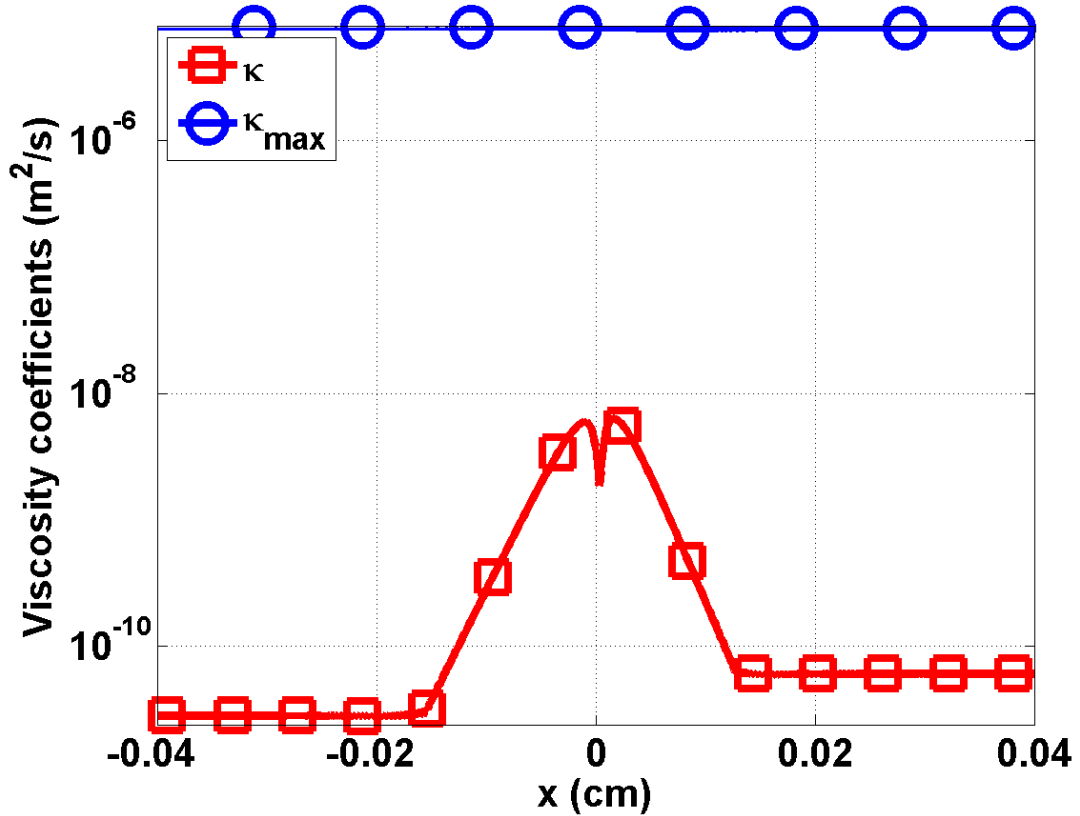


Figure 7.3: First-order viscosity  $\kappa_{max}$  and second-order viscosity  $\kappa$  profiles at steady state for Mach 1.05 test (logarithm scale).

The energy transfer between the material and radiation fields is not large enough to form a shock in the material. Thus, all of the material variables are smooth (Fig. 7.1 and Fig. 7.2) as well as the radiation temperature  $\theta$ . Because of the smoothness of the solution, the viscosity coefficient  $\kappa$  is three order of magnitude smaller than the first-order viscosity coefficient  $\kappa_{max}$  (Fig. 7.3).

#### 7.3.2.2 A 1.2 mach hydrodynamic shock

In this test, the material experiences a shock and the radiation energy density remains smooth. The initial conditions, corresponding to a Mach number of 1.2 at

the inlet, are as follows:

Table 7.4: Initial conditions for mach 1.2.

	left	right
$\rho$ ( $g/cm^3$ )	1.	1.0749588
$u$ ( $cm/sh$ )	0.1405588	0.1083456
$T$ ( $keV$ )	0.1	0.1194751
$\epsilon$ ( $jerks/cm^3$ )	$1.372 \ 10^{-6}$	$2.7955320 \ 10^{-6}$

The slab thickness is set to  $L = 0.045 \ cm$  and the initial step was located at  $x_0 = 0 \ cm$ .

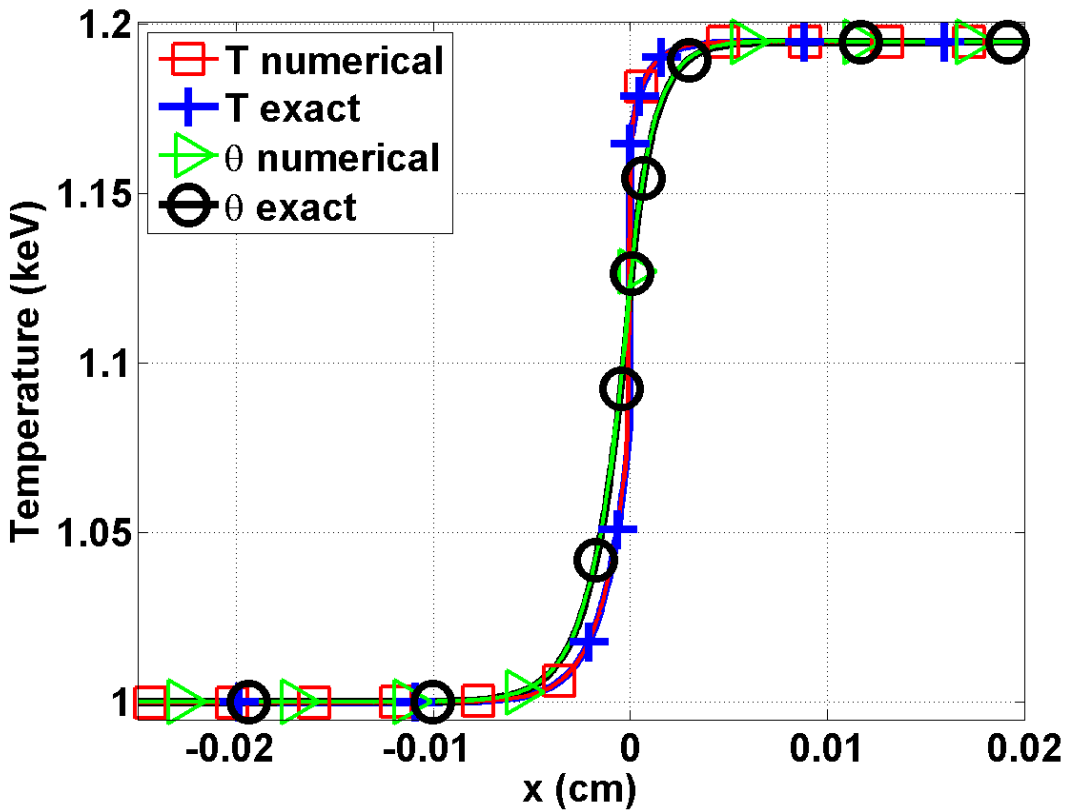


Figure 7.4: Material and radiation temperature profiles at steady state for Mach 1.2 test.

The radiation and material temperatures have two different behaviors (Fig. 7.4): the later experiences an embedded hydrodynamic shock, whereas the radiation temperature is smooth because of the diffusion term. The material temperature profile does not show any pre- and post-shock oscillations. In Fig. 7.5, the material density profile has a shock as well. The viscosity coefficient (Fig. 7.6) is peaked in the shock as expected but does not saturate to the first-order viscosity. It is conjectured that the diffusion term in the radiation equation brings extra stability to the system. Overall, the numerical solution behaves as expected in the shock and the entropy-based viscosity method seems to efficiently stabilize the numerical scheme.

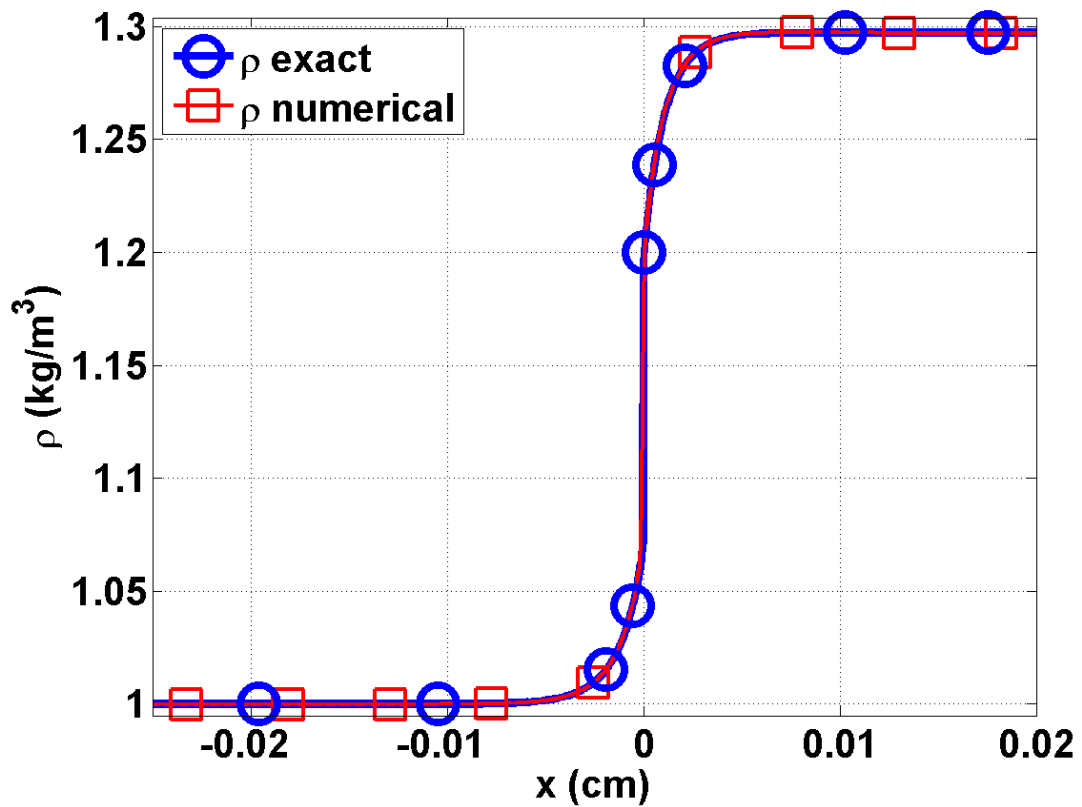


Figure 7.5: Material density profile at steady state for Mach 1.2 test.

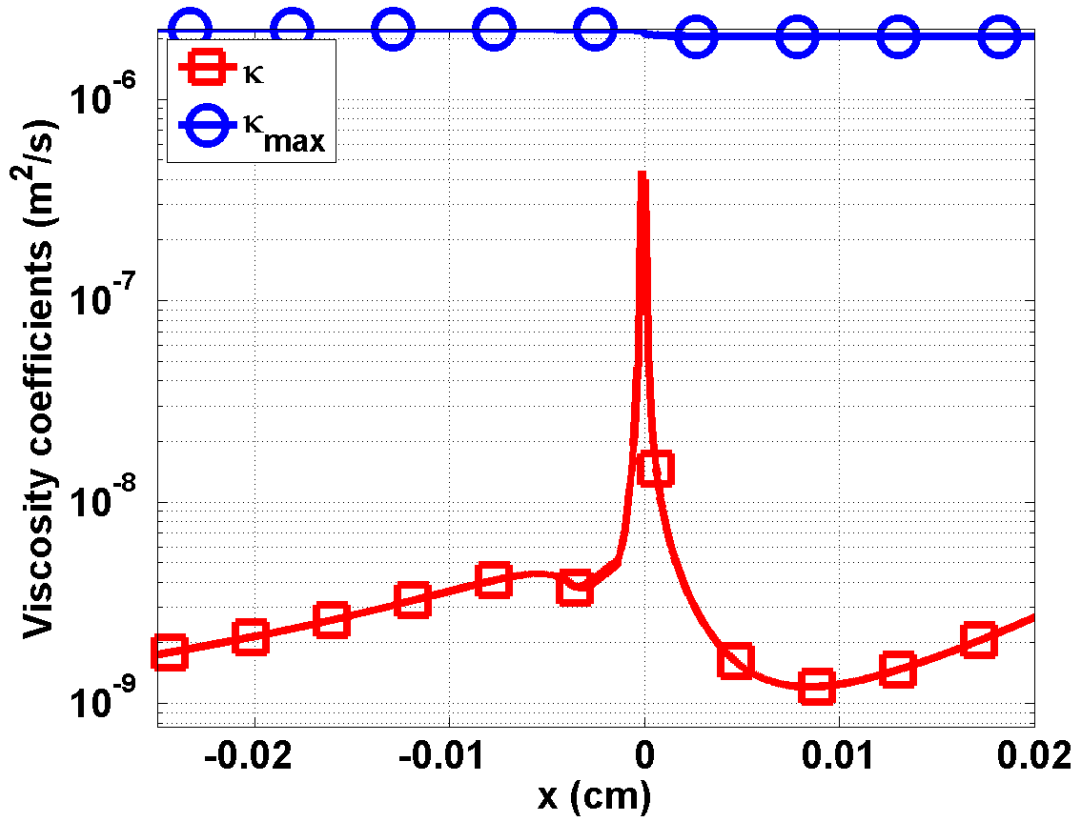


Figure 7.6: First-order viscosity  $\kappa_{max}$  and second-order viscosity  $\kappa$  profiles at steady state for Mach 1.2 test (logarithm scale).

### 7.3.2.3 A mach 2 shock

The Mach 2 shock test has two features: a hydrodynamic shock and a Zeldovich spike, which make it interesting for testing the robustness of the entropy-based viscosity method. The initial conditions are specified in Table 7.5 for a slab of length  $L = 0.04 \text{ cm}$  with  $x_0 = 0. \text{ cm}$ .

Table 7.5: Initial conditions for mach 2.

	left	right
$\rho$ ( $g/cm^3$ )	1.	1.0749588
$u$ ( $cm/sh$ )	0.1405588	0.1083456
$T$ ( $keV$ )	0.1	0.1194751
$\epsilon$ ( $jerks/cm^3$ )	$1.372 \ 10^{-6}$	$2.7955320 \ 10^{-6}$

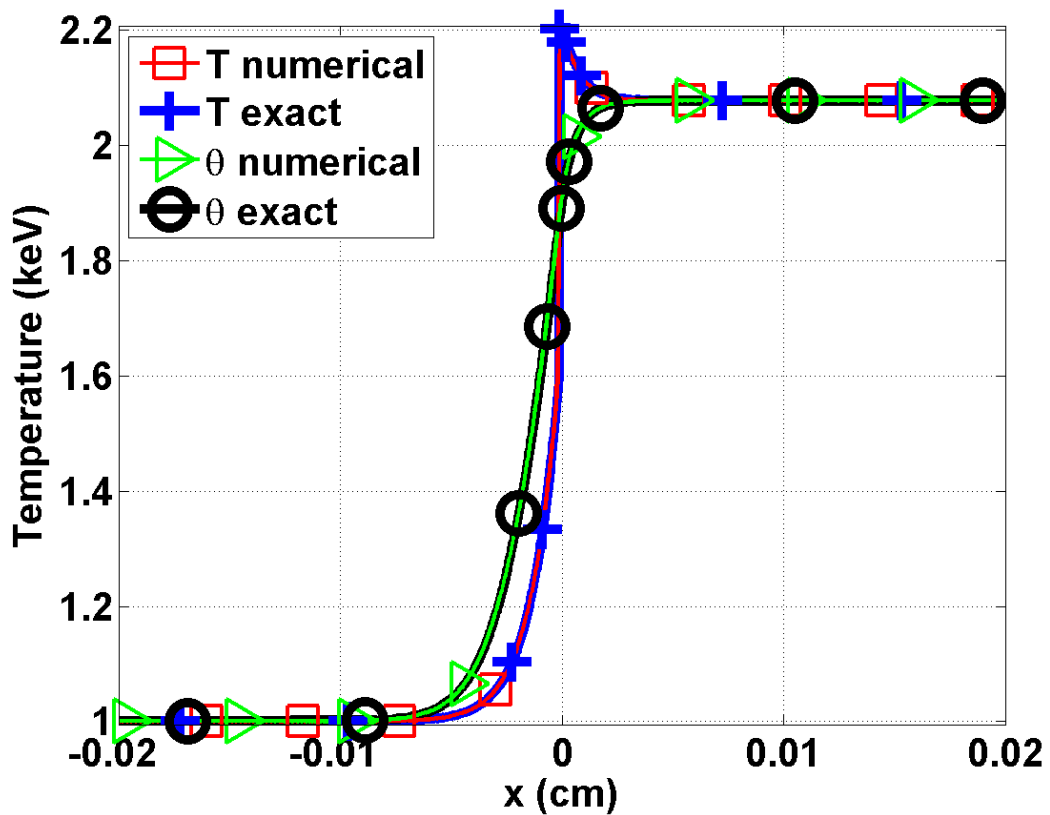


Figure 7.7: Material and radiation temperature profiles at steady-state for Mach 2 test.

Once again, the radiation temperature profile is smooth and the material temperature experiences an embedded hydrodynamic shock and a peak as shown in Fig. 7.7. In Fig. 7.8, the shock is well resolved. The viscosity coefficient profile is given in Fig. 7.9 and is peaked, once again, in the shock region.

For comparison purpose, the same simulation was run with the first-order viscosity only, i.e.,  $\kappa$  was set equal to  $\kappa_{max}$  for the whole domain in order to see the advantage of using a second-order viscosity coefficient. The results are given in Fig. 7.10 for the material density and temperature. Numerical solutions with first- and second-order viscosity coefficients are graphed. The radiation temperature profile (not shown here) is not affected much by the first-order viscosity and the curves are coincident. This is expected because of the way the artificial viscosity term is treated in the radiation equation (Section 7.2). However, on the same figure, the shock and peak in the material temperature profile are smoothed out: the shock is not as sharp and the peak amplitude is reduced because of the larger amount of viscosity added to the system. This test shows the benefits of using a high-order viscosity coefficient in order to avoid over-dissipation.

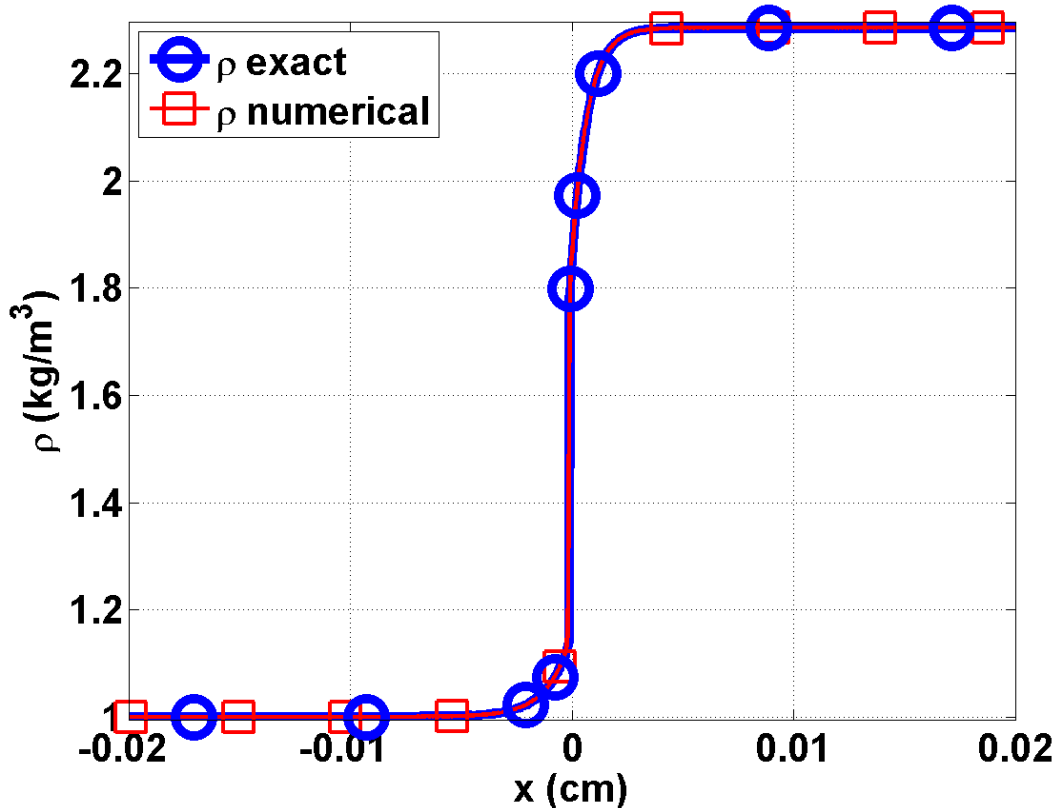


Figure 7.8: Material density profile at steady-state for Mach 2 test.

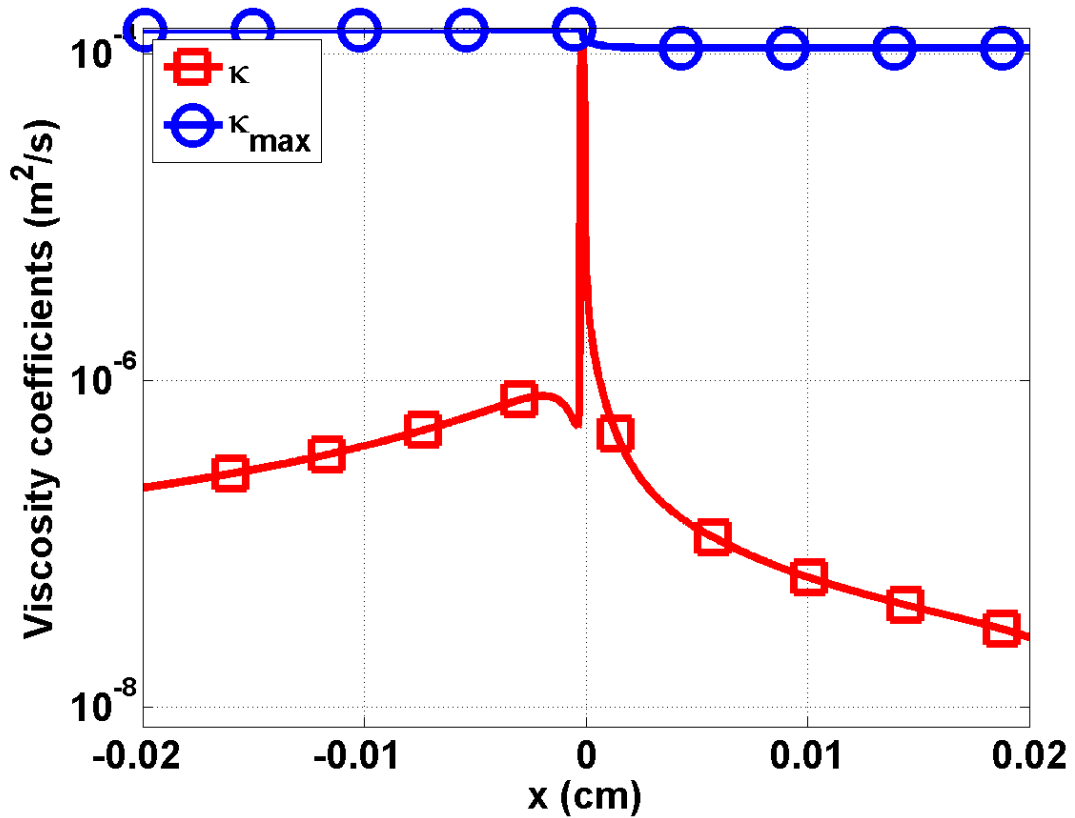


Figure 7.9: First-order viscosity  $\kappa_{max}$  and second-order viscosity  $\kappa$  profiles at steady state for Mach 2 test.

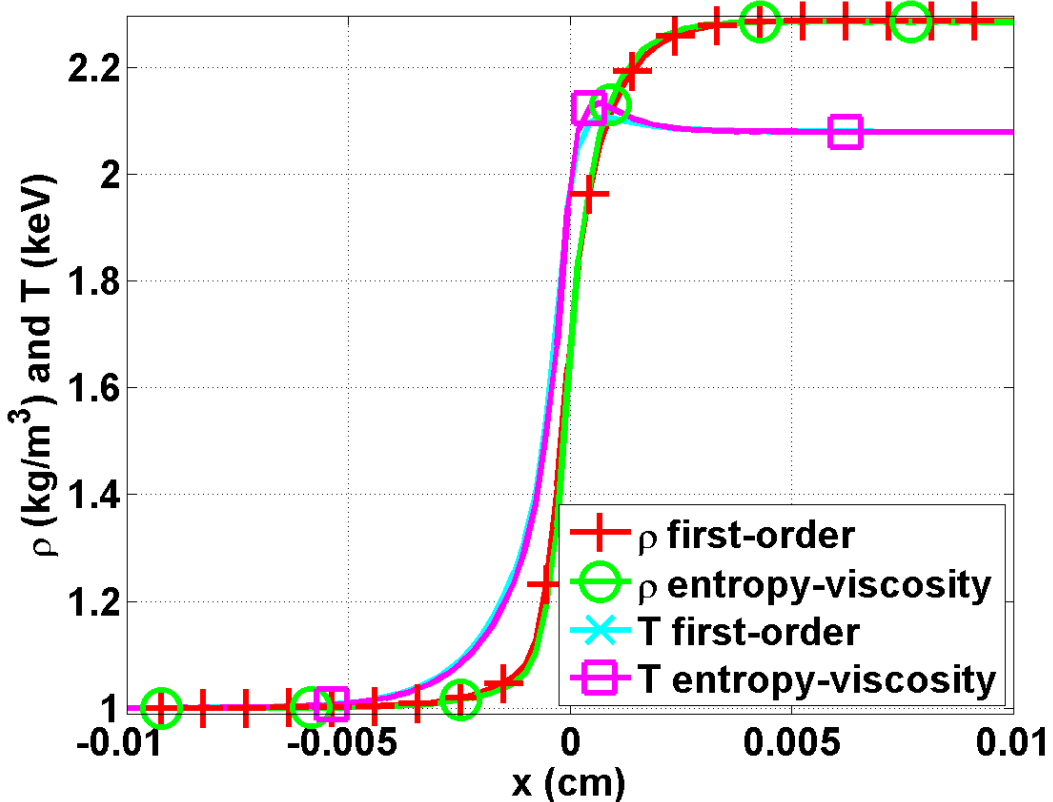


Figure 7.10: Comparison between the material density and temperature profiles run with the high-order and first-order viscosity coefficients.

#### 7.3.2.4 mach 5 shock

A Mach 5 test is run with the initial conditions of Table 7.6 on a computational domain of length  $L = 0.05 \text{ cm}$  ( $x_0 = 0 \text{ cm}$ ). Steady-state results are shown in Fig. 7.11, Fig. 7.13, and Fig. 7.14 for the material and radiation temperatures, the density and the viscosity coefficients, respectively.

Table 7.6: Initial conditions for mach 5.

	left	right
$\rho$ ( $g/cm^3$ )	1.	1.0749588
$u$ ( $cm/sh$ )	0.1405588	0.1083456
$T$ ( $keV$ )	0.1	0.1194751
$\epsilon$ ( $jerks/cm^3$ )	$1.372 \ 10^{-6}$	$2.7955320 \ 10^{-6}$

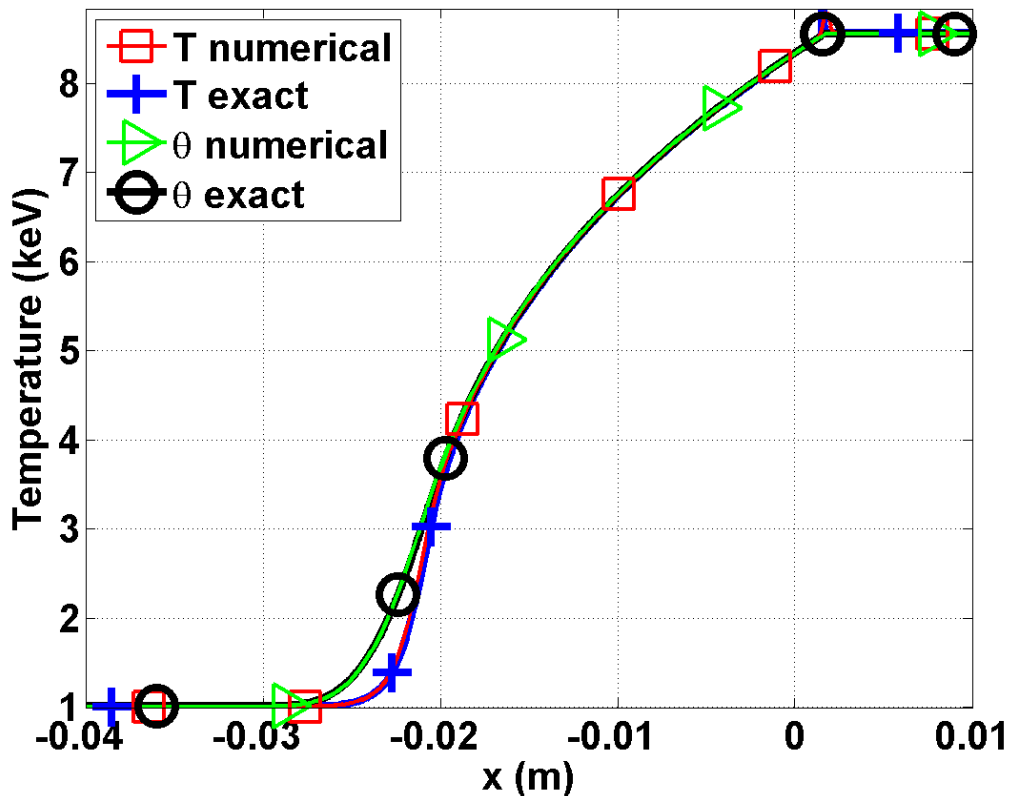


Figure 7.11: Material and radiation temperature profiles at steady state for Mach 5 test. Zoom at the location go the peak using different mesh resolutions.

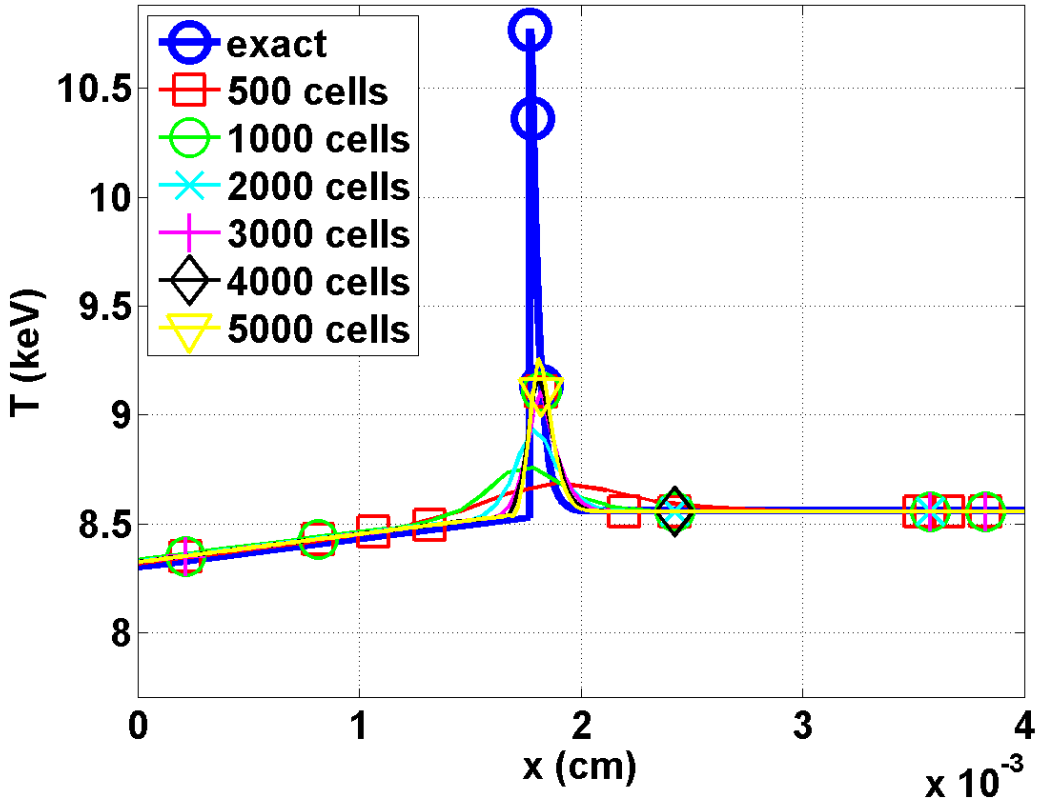


Figure 7.12: Material temperature profiles at steady state for the Mach 5 test in the neighborhood spike.

In Fig. 7.11, the radiation temperature profile is smooth. The material temperature no longer exhibits an embedded hydrodynamic shock but shows a Zeldovich spike. The mesh with 500 elements is not fine enough to correctly resolve the Zeldovich spike. In Fig. 7.12, the Zeldovich spike region is plotted for different mesh resolutions, using from 500 to 5000 elements: the peak is better resolved when using large numbers of elements and its position seems to be independent of the mesh size when appropriately refined. The density profile, Fig. 7.13, shows a shock located at the same position as the Zeldovich spike of the material temperature profile. The viscosity coefficient  $\kappa$  is also peaked in the shock region, as expected. The material

and radiation variables do not present any numerical oscillations.

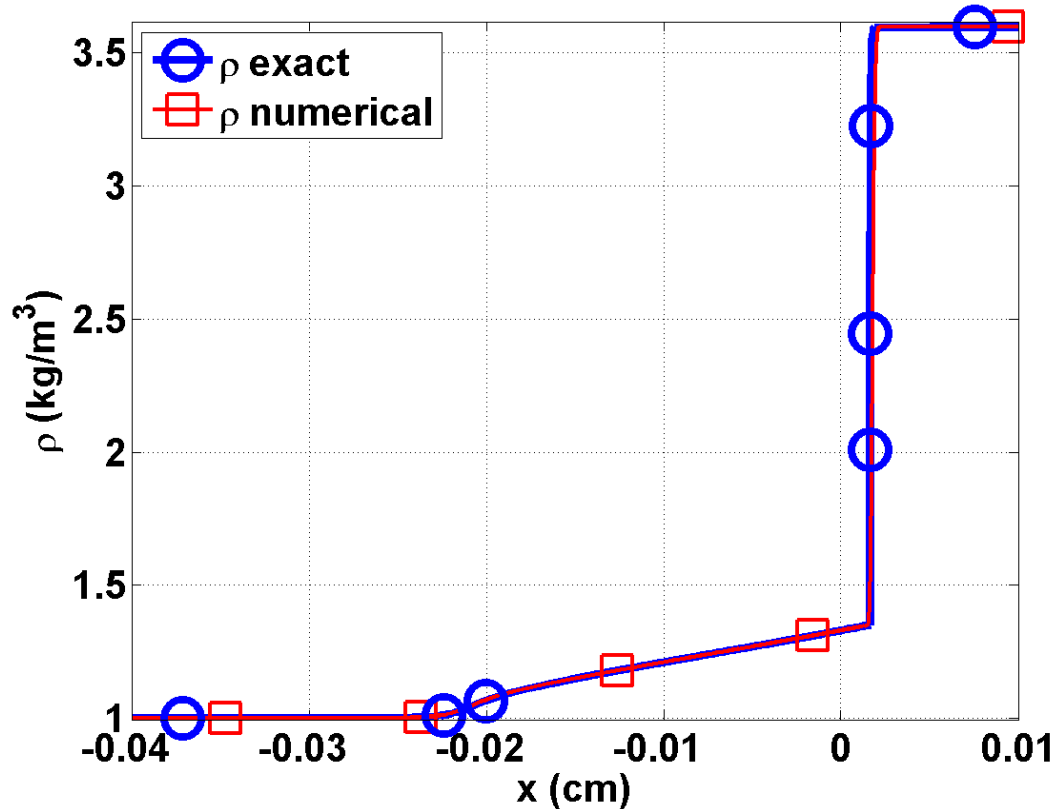


Figure 7.13: Material density profile at steady state for Mach 5 test.

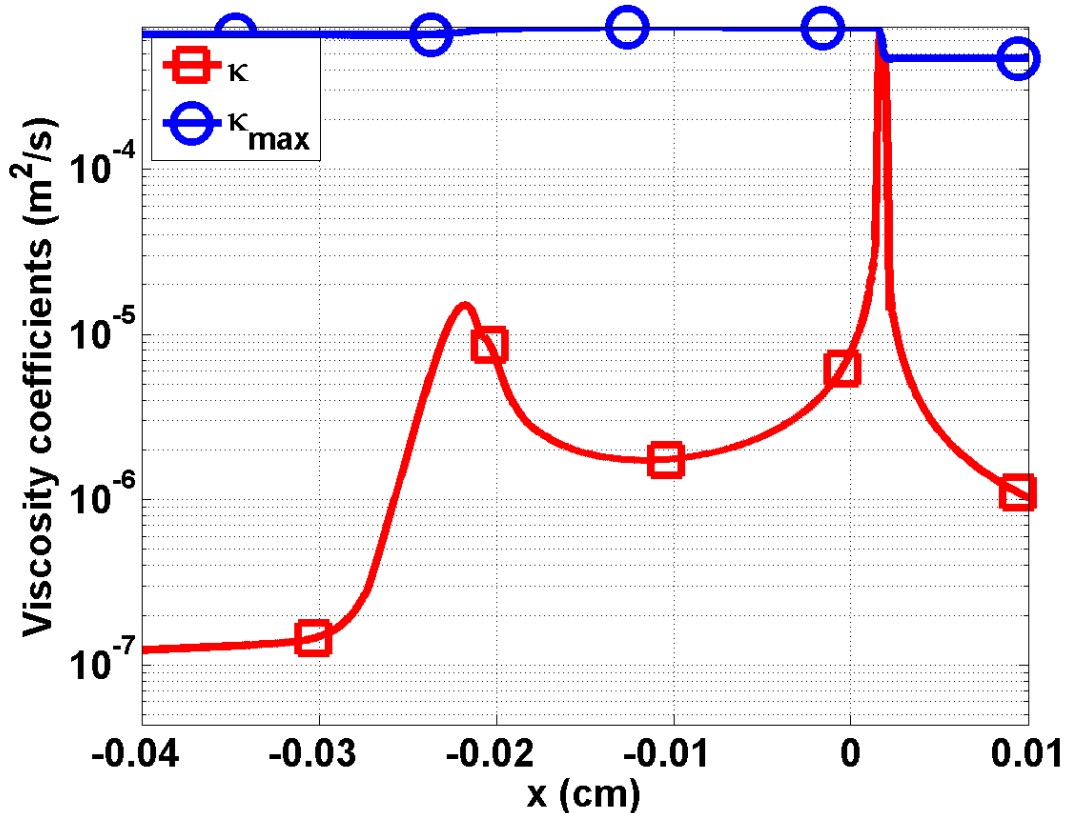


Figure 7.14: First-order viscosity  $\kappa_{max}$  and second-order viscosity  $\kappa$  profiles at steady state for Mach 5 test.

#### 7.3.2.5 mach 50 shock

The Mach 50 test is known to be challenging. The initial conditions are given in Table 7.7. The computational domain is of length  $L = 0.2 \text{ cm}$ . Results are once again given at steady state.

Table 7.7: Initial conditions for mach 50.

	left	right
$\rho$ ( $g/cm^3$ )	1.	6.5189217
$u$ ( $cm/sh$ )	585.6620	89.84031
$T$ ( $keV$ )	1.0	85.51552
$\epsilon$ ( $jerks/cm^3$ )	$1.372 \ 10^{-2}$	$7.33726 \ 10^5$

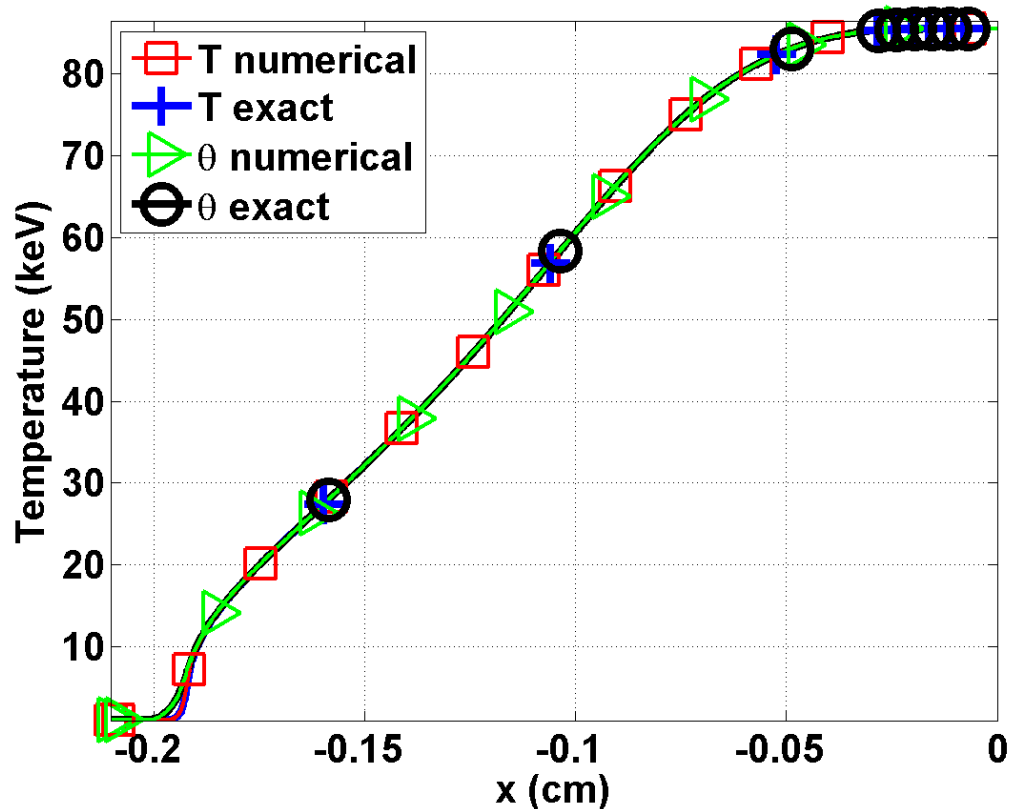


Figure 7.15: Material and radiation temperature profiles at steady state for Mach 50 test.

At Mach 50, there is no embedded hydrodynamic shock forming as shown in Fig. 7.15. The density profile is smooth as shown in Fig. 7.16. In Fig. 7.15, the material and radiation temperatures overlap on all of the computational domain except for a small region located between  $x = -0.2$  and  $x = -0.18$  cm. In this particular region, the viscosity coefficient saturates to the first-order viscosity (see Fig. 7.17) because of the inflection point in the material temperature profile. The artificial dissipative terms correctly stabilize the material temperature profile without altering the physical solution: the radiation temperature is expected to increase ahead of the material temperature.

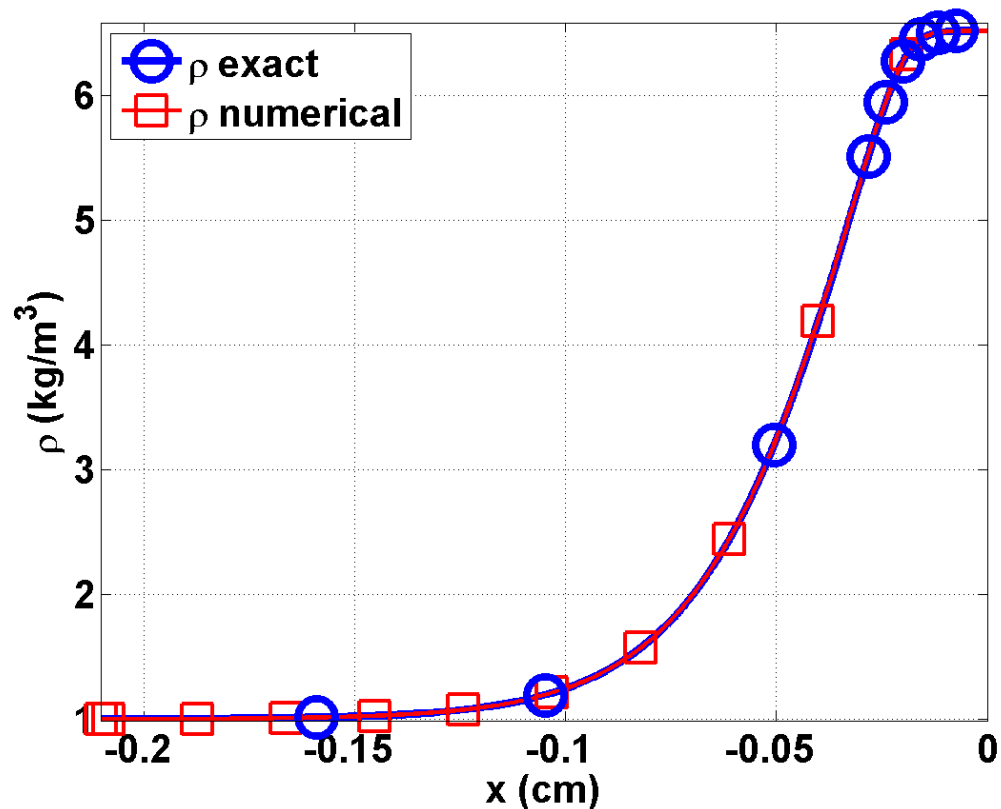


Figure 7.16: Material density profile at steady-state for Mach 50 test.

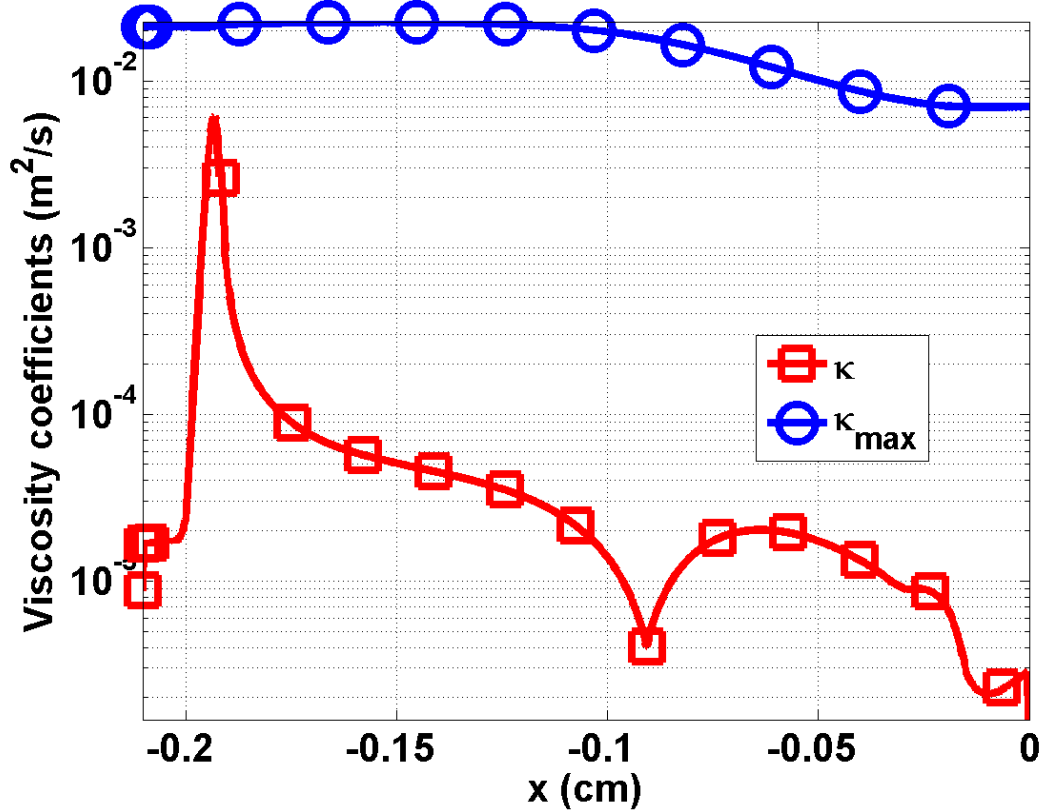


Figure 7.17: First-order viscosity  $\kappa_{max}$  and second-order viscosity  $\kappa$  profiles at steady-state for Mach 50 test.

## 8. CONCLUSIONS.

The entropy viscosity method has been successfully applied to three hyperbolic system of equations: the multi-D Euler equations, the 1-D seven-equation two-phase model and the 1-D grey radiation-hydrodynamic equations. The numerical method was implemented using a continuous Galerkin finite element method and a second-order implicit temporal solver. The method relies on the derivation of dissipative terms consistent with the entropy inequality in order to ensure uniqueness of the numerical solution and on the definition of smart viscosity coefficients that are able to detect shock waves and discontinuities, allowing second-order accuracy when the numerical solution is smooth. More precisely, the viscosity coefficients are defined proportional to the entropy residual that is known to be peaked in the shock region, and also to the inter-element jumps that will allow detection of other discontinuities. The definition of the viscosity coefficients also requires a normalization parameter that is derived using the non-dimensionalized form of the hyperbolic system of equations under consideration, in order to have well-scaled dissipative terms.

This approach allowed us to derive and present a new version of the entropy viscosity method valid for a wide range of Mach number when applying the entropy viscosity method to the multi-D Euler equations. The definition of the viscosity coefficients is now consistent with the low-Mach asymptotic limit, does not require an analytical expression for the entropy function, and is therefore applicable to a larger variety of flow regimes, from very low-Mach flows to supersonic flows. The method has also been extended to Euler equation with variable area to solve nozzle flow problems. In 1-D, convergence of the numerical solution to the exact solution was demonstrated by computing the convergence rates of the  $L_1$  and  $L_2$  norms for flows

in a converging-diverging nozzle and in straight pipes. For smooth solutions, second-order convergence was verified; solutions with shocks converged with the expected theoretical rates of 1 ( $L_1$ -norm) and 0.5 ( $L_2$ -norm).

The effectiveness of the method was also demonstrated in 2-D using a series of benchmark problems for both subsonic and supersonic flows in various geometries, with Mach numbers ranging from  $10^{-7}$  to 2.5. For very low-Mach flows, we numerically verified that the pressure fluctuations were proportional to the square of the Mach number, as expected in the incompressible limit.

The effect of source terms onto the entropy viscosity method was also investigated and justifications were provided on how to account for the source terms in the definition of the viscosity coefficients. 1-D tests were performed for a simple model of a PWR using RELAP-7, and showed promising results.

The entropy-viscosity method was also applied to the 1-D seven-equation two-phase model through the same theoretical approach as for the multi-D Euler equation. After deriving the viscous regularization using the entropy minimum principle for each phase, a definition for the viscosity coefficients was derived consistent with the low-Mach asymptotic limit and also with the single-phase limit cases  $\alpha \rightarrow 0$  and  $\alpha \rightarrow 1$  for the multi-D seven-equation model. Particular attention was given to the volume fraction equation whom dissipative term and the associated viscosity coefficient were determined by analogy with Burger's equation. Numerical tests showed that the numerical method behaves as expected for various 1-D shock tubes and also various geometries. The stabilization method does not create any artificial mixture waves and can effectively resolve shocks and other discontinuities in the two limit cases: with and without relaxation terms. The numerical solutions compared well against either the exact solution when available, or solutions from other numerical methods.

Furthermore, we have also shown that the entropy-based viscosity method is a valid candidate for solving the 1-D radiation-hydrodynamic equations. A theoretical derivation is given for the derivation of the dissipative terms that are consistent with the entropy minimum principle. The viscosity coefficient  $\kappa$  is defined proportional to the entropy residual that measures the local entropy production allowing detection of shocks. Through the manufactured solution method, it is demonstrated, firstly, that second-order accuracy is achieved when the solution is smooth, and secondly, that the artificial dissipative terms do not affect the physical solution in the equilibrium-diffusion limit. The entropy-based numerical scheme also behaves well in the tests performed for Mach numbers ranging from 1.05 to 50. The main features such as the embedded hydrodynamic shock and the Zeldovich spike are resolved accurately without spurious oscillations. The viscosity coefficient is peaked in the shock region only and behaves as expected. All of these results were obtained by using an unique definition of the viscosity coefficient that is computed on the fly. The addition of dissipative terms to the set of equations requires more computational work but is rather simple to implement.

As future work, extension to multi-dimensional geometries tests should be considered for both the seven-equation model and the radiation-hydrodynamic equations. All of the derivations presented in this dissertation hold. The definition of the viscosity coefficients do not need to be modified and the viscous regularizations were derived in the multi-D case for both system of equations. The multi-D seven equation model will require a preconditioner accounting for the relaxation terms when using a non-linear solver. As for the radiation-hydrodynamic equations, it would also be interesting to model the radiation equation with an  $S_n$  transport approximation and apply the entropy based artificial viscosity to the resultant radiation-hydrodynamics equations. Given the advective nature of the  $S_n$  equations, dissipation would need

to be added to these equations.

## REFERENCES

- [1] R Abgrall. How to prevent pressure oscillations in multicomponent flow calculations: a quasi conservative approach. *Journal of Comput Phys*, 60:125–150, 2002.
- [2] R Abgrall and R Saurel. Discrete equations for physical and numerical compressible multiphase mixtures. *Journal of Comput Phys*, 186:361–396, 2003.
- [3] A Ambroso, C Chalons, and P-A Raviart. A godunov-type method for the seven-equation model of compressible multiphase mixtures. *Comput Fluids*, 54:67–91, 2012.
- [4] D Anders, R Berry, D Gaston, R Martineau, J Peterson, H Zhang, H Zhao, and L Zou. Relap-7 level 2 milestone report: demonstration of a steady-state single phase pwr simulation with relap-7. Technical Report INL/EXT-12-25924, Idaho National Laboratory, USA, 2014.
- [5] J Anderson. *Modern Compressible Flow: With Historical Perspective*. McGraw-Hill Science Engineering, Columbus, OH, 1982.
- [6] U M Ascher and L R Petzold. *Computer Methods for Ordinary Differential Equations and Differential-Algebraic Equations*. SIAM, Philadelphia, Ph, 1998.
- [7] D Balsara. An analysis of the hyperbolic nature of the equations of radiation hydrodynamics. *J. Quant. Spectrosc. Radiat. Transfer*, 61:617–627, 1999.
- [8] G E Barter and D L Darmofal. Shock capturing with pde-based artificial viscosity for dgfem: Part i. formulation. *Journal of Comput Phys*, 229:1810–1827, 1979.

- [9] R A Berry, R Saurel, F Petitpas, E Daniel, O LeMetayer, S Gavrilyuk, N Dovetta, and R C Martineau. Progress in the development of compressible, multiphase flow modeling capability for nuclear reactor flow applications. Technical Report INL/EXT-08-15002, Idaho National Laboratory, U. S. A., 2008.
- [10] J C Butcher. *Numerical Methods for Ordinary Differential Equations*. John Wiley & Sons, New York, NY, 2003.
- [11] A Chinnayya, E Daniel, and R Saurel. Modelling detonation waves in heterogeneous energetic materials. *Journal of Comput Phys*, 196:490–538, 2004.
- [12] I Christov and B Popov. New non-oscillatory central schemes on unstructured triangulations for hyperbolic systems of conservation laws. *Journal of Comput Phys*, 227:5736–5757, 2008.
- [13] B Cockburn, C Johnson, C Shu, and E Tadmor. *Advanced Numerical Approximation of Nonlinear Hyperbolic Equations*. Springer, Berlin, Germany, 1998.
- [14] B Cockburn, G Karniadakis, and C Shu. Discontinuous galerkin methods: theory, computation and applications. *Lecture Notes in Computer Science and Engineering*, 11:97–109, 2000.
- [15] B Cockburn and C Shu. The local discontinuous galerkin method for time-dependent convection-diffusion systems. *Numer. Anal.*, 35:2440–2463, 1998.
- [16] B Cockburn and C Shu. The runge-kutta discontinuous galerkin method for conservation laws. *Journal of Comput Phys*, 2:199–224, 1998.
- [17] G Hansen D Gaston, C Newsman and D Lebrun-Grandie. A parallel computational framework for coupled systems of nonlinear equations. *Nucl. Eng. Design*, 239:1768–1778, 2009.

- [18] D L Darmofal and K Siu. A robust multigrid algorithm for the euler equations with local preconditioning and semi-coarsening. *Journal of Comput Phys*, 151:728–756, 1999.
- [19] R A DeVore and G G Lorentz. *Constructive Approximation*. Springer-Verlag, Berlin, Germany, 1991.
- [20] J Donea and A Huerta. *Finite Element Methods for Flow Problems*. Wiley, Oxford, England, 2003.
- [21] A F Emery. Finite element formulations for convection dominated flows with particular emphasis on the compressible euler equations. *Proceedings of the AIAA 21st Aerospace Sciences Meeting AIAA Paper*, pages 83–125, 1983.
- [22] E Godlewski and P-A Raviart. *Numerical Approximations of Hyperbolic Systems of Conservation Laws*. Springer, New-York, New-York, 1996.
- [23] J-L Guermond and R Pasquetti. Entropy-based nonlinear viscosity for fourier approximations of conservation laws. In *C.R. Math. Acad. Sci.*, volume 326, pages 801–806, Paris, 2008.
- [24] J-L Guermond and B Popov. Viscous regularization of the euler equations and entropy principles. *SIAM Journal on Applied Mathematics*, 74 (2):284–305, 2012.
- [25] H Guillard and C Viozat. On the behavior of upwind schemes in the low mach number limit. *Comput Fluids*, 28:63–86, 1999.
- [26] A Harten, L P Franca, and M Mallet. Convex entropies and hyperbolicity for general euler equations. *SIAM J Numer Anal*, 6:2117–2127, 1998.
- [27] J M Herrard and O Hurisse. A simple method to compute standard two-fluid models. *Int J of Computational Fluid Dynamics*, 19:475–482, 2005.

- [28] R Lowrie J D Edwards, J E Morel. Second-order discretization in space and time for radiation hydrodynamics. In *International Conference on Mathematics and Computational Methods Applied to Nuclear Science & Engineering (M&C 2013)*, Sun Valley, Idaho, USA, 2013.
- [29] B Popov J-L Guermond, R Pasquetti. Entropy viscosity method for nonlinear conservation laws. *Journal Comput Phys*, 230:4248–4267, 2011.
- [30] R Pasquetti J-L Guermond. Entropy viscosity method for high-order approximations of conservation laws. *Lecture Notes in Computational Science and Engineering*, 76:411–418, 2011.
- [31] S Jin and C Levermore. Numerical schemes for hyperbolic conservation laws with stiff relaxation terms. *Journal of Comput Phys*, 126:449–467, 1996.
- [32] A K Kapila, R Menikoff, J B Bdil S F Son, and D S Stewart. Two-phase modeling of deflagration-to-detonation transition in granular materials. *Phys Fluids*, 13:3002–3024, 2001.
- [33] D A Knoll and D E Keyes. Jacobian-free Newton-Krylov methods: a survey of approaches and applications. *Journal of Comput Phys*, 193(2):357–397, January 2004.
- [34] J S Wong D L, Darmofal, and J Peraire. The solution of the compressible euler equations at low mach numbers using a stabilized finite element algorithm. *Comput Methods Appl Mech Engrg*, 190:5719–5737, 2001.
- [35] A Lapidus. A detached shock calculation by second order finite differences. *Journal Comput Phys*, 2:154–177, 1967.
- [36] P Lax. Weak solutions of nonlinear hyperbolic equations and their numerical computation. *Comm. Pure Appl. Math.*, 7:159–193, 1954.

- [37] S LeMartelot, B Nkonga, and R Saurel. Liquid and liquid-gas flows at all speeds: Reference solutions and numerical schemes. *Research report*, 7935:97–109, 2012.
- [38] O LeMetayer, J Massoni, and R Saurel. Elaborating equation of state for a liquid and its vapor for two-phase flow models. *International Journal of Thermal Science*, 43:265–276, 2004.
- [39] R Leveque. *Numerical Methods for Conservation Laws*. Birkhäuser Basel, Zurich, Switzerland, 1990.
- [40] Q Li, H Feng, T Cai, and C Hu. Difference scheme for two-phase flow. *Appl Math Mech*, 25:536, 2004.
- [41] X-S Li and C-W Gu. An all-speed roe-type scheme and its asymptotic analysis of low mach number behavior. *Journal of Comput Phys*, 227:5144–5159, 2008.
- [42] R Liska and B Wendroff. Comparison of several difference schemes on 1d and 2d test problems for the euler equations. *SIAM Journal Sci. Comput.*, 25:995–1017, 2003.
- [43] R Lohner. *Applied CFD Techniques: an Introduction Based on Finite Element Methods*. Wiley, Oxford, England, 2003.
- [44] R Lohner, K Morgan, and J Peraire. A simple extension to multidimensional problems of the artificial viscosity due to lapidus. *Commun. Numer. Methods Eng.*, 1(14):141–147, 1985.
- [45] R Loubere. Validation test case suite for compressible hydrodynamics computation. *Theoretical Division T-7 Los Alamos National Laboratory*, 2005.
- [46] R Martineau and R Berry. An efficient, semi-implicit pressure-based scheme employing a high-resolution finite element method for simulating transient and

steady, inviscid and viscous, compressible flows on unstructured grids. Technical Report INEEL-EXT-03-00490, Idaho National Laboratory, USA, 2003.

- [47] F J Moody. *Introduction to Unsteady Thermofluid Mechanics*. Wiley, Oxford, England, 1990.
- [48] B Muller. Low-mach number asymptotes of the navier-stokes equations. *Journal of Engineering Mathematics*, 34:97–109, 1998.
- [49] J Van Rosendale MY Hussaini, B van Leer. *Upwind and High-Resolution Schemes*, volume 1. Springer Berlin Heidelberg, Berlin, Germany, 1997.
- [50] P Perrot. *A to Z of Thermodynamics*. Oxford University Press, Oxford, England, 1998.
- [51] B Perthame and C-W Shu. On positivity preserving finite volume schemes for euler equations. *Numer. Math.*, 73:119–130, 1996.
- [52] J J Quirk. A contribution to the great riemann solver debate. *NASA Contractor Report 191409*, ICASE Report No.:92–64, 1992.
- [53] J D Edwards R B Lowrie. Radiative shock solutions with grey non equilibrium diffusion. *Journal of Comput Phys*, 18:129–143, 2008.
- [54] J E Morel R B Lowrie. Issues with high-resolution godunov methods for radiation hydrodynamics. *Journal of Quantitative Spectroscopy & Radiative Transfer*, 69:475–489, 2001.
- [55] O LeMetayer R Berry, R Saurel. The discrete equation method (dem) for fully compressible, two-phase flows in ducts of spatially varying cross-section. *Nuclear Engineering and Design*, 240:3797–3818, 2010.
- [56] J Hittinger R Lowrie, J Morel. Coupling radiation and hydrodynamics. *Journal Quant. Spectrosc. Radiat. Transfer*, 61:432–500, 1999.

- [57] J Reisner, J Serencsa, and Shkoller S. A space-time smooth artificial viscosity method for nonlinear conservation laws. *Journal of Comput Phys*, 253:912–933, 2013.
- [58] T W Roberts. The behavior of flux difference splitting schemes near slowly moving shock waves. *Journal of Comput Phys*, 90:141–160, 1990.
- [59] R Saurel and R Abgrall. A multiphase godunov method for compressible multifluid and multiphase flows. *Journal of Comput Phys*, 150:425–267, 2001.
- [60] R Saurel and O Lemetayer. A multiphase model for compressible flows with interfaces, shocks, detonation waves and cavitation. *Journal of Comput Phys*, 431:239–271, 2001.
- [61] R Saurel, J Massoni, and F Renaud. A numerical method for one-dimensional compressible multiphase flows on moving meshes. *Intern Journ for Num Methods in Fluids*, 54:1425–1450, 2007.
- [62] R Saurel, F Petitpas, and R A Berry. Simple and efficient relaxation methods for interfaces separating compressible fluids, cavitating flows and shocks in multiphase mixtures. *Journal of Comput Phys*, 228:1678–1712, 2009.
- [63] E Tadmor. A minimum entropy principle in the gas dynamics equations. *Appl. Numer. Math.*, 2:211–219, 1986.
- [64] T E Tezduyar and T J R Hughes. An evaluation of several differencing methods for inviscid fluid flow problems. *Journal of Comput Phys*, 2:306–331, 1968.
- [65] E F Toro. *Riemann Solvers and Numerical Methods for Fluid Dynamics*. 2<sup>nd</sup> Edition, Springer Berlin Heidelberg, Berlin, Germany, 1999.
- [66] I Toumi. An upwind numerical method for two-fluids two-phases flow models. *Nucl Sci Eng*, 123:147–168, 1996.

- [67] C Truesdell and C Wang. *Rational Thermodynamics*. Graw-Hill Book Company, New-York, NY, 1969.
- [68] E Turkel. Preconditioned techniques in computational fluid dynamics. *Annu Rev Fluid Mech*, 31:385–416, 1999.
- [69] J Morel V Zingan, J-L Guermond and B Popov. Implementation of the entropy viscosity method with the discontinuous galerkin method. *Journal of Comput Phys*, 253:479–490, 2013.
- [70] J von Neumann and R D Richtmyer. A method for the numerical calculation of hydrodynamic shocks. *J Appl Phys*, 190:232–237, 1950.
- [71] P R Woodward W Dai. Numerical simulations for radiation hydrodynamics. i. diffusion limit. *Journal of Comput Phys*, 142:182–207, 1998.
- [72] A Zein, M Hantke, and G Warnecke. Modeling phase transition for compressible two-phase flows applied to metastable liquids. *Journal of Comput Phys*, 229:2964–2998, 2010.

## APPENDIX A

### DERIVATION OF THE DISSIPATIVE TERMS FOR THE EULER EQUATIONS WITH VARIABLE AREA USING THE ENTROPY MINIMUM PRINCIPLE

Euler equations (without viscous regularization) with variable area are recalled here

$$\partial_t (\rho A) + \nabla \cdot (\rho \mathbf{u} A) = 0 \quad (\text{A.1a})$$

$$\partial_t (\rho \mathbf{u} A) + \nabla \cdot [A (\rho \mathbf{u} \otimes \mathbf{u} + P \mathbf{I})] = P \nabla A \quad (\text{A.1b})$$

$$\partial_t (\rho E A) + \nabla \cdot [\mathbf{u} A (\rho E + P)] = 0. \quad (\text{A.1c})$$

The specific entropy is a function of the density  $\rho$  and the internal energy  $e$ , i.e.,  $s(e, \rho)$ , the above system of equations satisfies the minimum entropy principle [39],

$$A \rho (\partial_t s + \mathbf{u} \cdot \nabla \cdot s) \geq 0. \quad (\text{A.2})$$

The entropy function  $s$  satisfies the second law of thermodynamics,  $T ds = de - \frac{P}{\rho^2} d\rho$ , which implies  $s_e := T^{-1}$  and  $s_\rho := -PT^{-1}\rho^{-2}$ . One can show that [24]

$$s_e = T^{-1} \geq 0 \text{ and } P s_e + \rho^2 s_\rho = 0 \quad (\text{A.3})$$

In order to apply the entropy viscosity method to the variable-area Euler equations, dissipative terms need to be added to each equation in Eq. (A.1). The functional forms of these terms need to be such that the entropy residual derived with these terms present also satisfies the minimum entropy principle. To prove the minimum entropy principle, the extra terms appearing in the entropy residual are either recast

as conservative terms or shown to be positive. The rest of this appendix presents this demonstration. Following [24], we first write the variable-area equation with dissipative terms.

$$\partial_t (\rho A) + \nabla \cdot (\rho \mathbf{u} A) = \nabla \cdot \mathbf{f} \quad (\text{A.4a})$$

$$\partial_t (\rho \mathbf{u} A) + \nabla \cdot [A (\rho \mathbf{u} \otimes \mathbf{u} + P \mathbf{I})] = P \nabla A + \nabla \cdot \mathbf{g} \quad (\text{A.4b})$$

$$\partial_t (\rho E A) + \nabla \cdot [\mathbf{u} A (\rho E + P)] = \nabla \cdot (\mathbf{h} + \mathbf{u} \cdot \mathbf{g}). \quad (\text{A.4c})$$

where  $\mathbf{f}$ ,  $\mathbf{g}$  and  $\mathbf{h}$  are dissipative fluxes to be determined. Starting from the modified system of equations given in Eq. (A.4), the entropy residual is derived again. The derivation requires the following steps : express the governing laws in terms of primitive variables  $(\rho, \mathbf{u}, e)$ , multiply the continuity equation by  $\rho s_\rho$  and the internal energy equation by  $s_e$ , and invoke multivariate chain rule, e.g.,  $\partial s / \partial x = s_e \partial e / \partial x + s_\rho \partial \rho / \partial x$ . These steps are similar to the ones from the standard Euler equations [24]. Some of the lengthy algebra is omitted here. The above steps yield:

$$A \rho (\partial_t s + \mathbf{u} \cdot \nabla s) = s_e \left[ \nabla \cdot \mathbf{h} + \mathbf{g} : \nabla \mathbf{u} + \left( \frac{u^2}{2} - e \right) \nabla \cdot \mathbf{f} \right] + \rho s_\rho \nabla \cdot \mathbf{f} \quad (\text{A.5})$$

The next step consists of choosing a definition for each of the dissipative terms so that the left hand-side is positive. The right hand-side of Eq. (A.5) can be simplified using the following relations,  $\mathbf{g} = A \mu \nabla^s \mathbf{u} + \mathbf{f} \otimes \mathbf{u}$  and  $\mathbf{h} = \tilde{\mathbf{h}} - 0.5 \|\mathbf{u}\|^2 \mathbf{f}$ , which yields:

$$A \rho (\partial_t s + \mathbf{u} \cdot \nabla s) = s_e \left[ \nabla \cdot \tilde{\mathbf{h}} - e \nabla \cdot \mathbf{f} \right] + \rho s_\rho \nabla \cdot \mathbf{f} + A s_e \mu \nabla^s \mathbf{u} : \nabla \mathbf{u}$$

The right hand-side is now integrated by parts:

$$\begin{aligned} A\rho(\partial_t s + \mathbf{u} \cdot \nabla \cdot s) &= \nabla \cdot \left[ s_e \tilde{\mathbf{h}} - s_e e \mathbf{f} + \rho s_\rho \mathbf{f} \right] - \\ &\quad \nabla \cdot \tilde{\mathbf{h}} \nabla s_e + \mathbf{f} \cdot \nabla (es_e) - \mathbf{f} \cdot \nabla (\rho s_\rho) + As_e \mu \nabla^s \mathbf{u} : \nabla \mathbf{u} \end{aligned}$$

where  $\nabla^s$  is the symmetric gradient. The term  $As_e \mu \nabla^s \mathbf{u} : \nabla \mathbf{u}$  is positive and thus, does not need any further modification. It remains to treat the other terms of the right hand-side that we now call *rhs*:

$$rhs = \nabla \cdot \left[ s_e \tilde{\mathbf{h}} - s_e e \mathbf{f} + \rho s_\rho \mathbf{f} \right] - \tilde{\mathbf{h}} \cdot \nabla s_e + \mathbf{f} \cdot \nabla (es_e) - \mathbf{f} \cdot \nabla (\rho s_\rho)$$

The first term of *rhs* is a conservative term. By choosing carefully a definition for  $\tilde{\mathbf{h}}$  and  $\mathbf{f}$ , the conservative term can be expressed as a function of the entropy  $s$ . It is also required to include the variable area in the choice of the dissipative terms so that when assuming constant area, the regular multi-D Euler equations are recovered. The following definitions for  $\tilde{\mathbf{h}}$  and  $\mathbf{f}$  are chosen:

$$\tilde{\mathbf{h}} = A\kappa \nabla(\rho e) \text{ and } \mathbf{f} = A\kappa \nabla\rho,$$

which yields, using the chain rule:

$$rhs = \nabla \cdot (\rho A\kappa \nabla s) - A\kappa \underbrace{[\nabla(\rho e) \nabla s_e - \nabla\rho \nabla(es_e) + \nabla\rho \nabla(\rho s_\rho)]}_{\mathbf{Q}}$$

It remains to treat the term  $\mathbf{Q}$  that can be recast under a quadratic form, following the work done in [24]:

$$\begin{aligned}\mathbf{Q} &= X^t \Sigma X \\ \text{with } X &= \begin{bmatrix} \nabla \rho \\ \nabla e \end{bmatrix} \text{ and } \Sigma = \begin{bmatrix} \partial_\rho(\rho^2 \partial_\rho s) & \partial_{\rho,e}s \\ \partial_{\rho,e}s & \partial_{e,e}s \end{bmatrix}\end{aligned}$$

The matrix  $\Sigma$  is symmetric and identical to the matrix obtained in [24]. The sign of the quadratic form can be simply determined by studying the positiveness of the matrix  $\Sigma$ . In this particular case, it is required to prove that the matrix is negative definite: the quadratic form is in the right hand-side and is preceded of a negative sign. According to [24], the convexity of the opposite of the entropy function  $s$  with respect to the internal energy  $e$  and the specific volume  $1/\rho$  is sufficient to ensure that the matrix  $\Sigma$  is negative definite.

Thus, the right hand-side of the entropy residual Eq. (A.5), are now either recast as conservative terms, or known to be positive. Following the work done by [24], the entropy minimum principle holds.

## APPENDIX B

### DERIVATION OF THE ENTROPY RESIDUAL AS A FUNCTION OF DENSITY, PRESSURE AND SPEED OF SOUND

The entropy residual is as follows:

$$R(\vec{r}, t) = \partial_t s(\vec{r}, t) + \vec{u} \cdot \nabla s(\vec{r}, t),$$

where all variables were defined previously. This form of the entropy residual is not suitable for the low-Mach limit as explained in Section 5.1.1. In this appendix, we recast the entropy residual  $R(\vec{r}, t)$  as a function of the primitive variables (pressure, velocity and density) and the speed of sound. The first step of this derivation is to use the chain rule, recalling that the entropy is a function of the internal energy  $e$  and the density  $\rho$ , yielding

$$R(\vec{r}, t) = s_e \frac{D e}{D t} + s_\rho \frac{D \rho}{D t},$$

where  $s_e$  denotes the partial derivative of  $s$  with respect to the variable  $e$ . We recall that  $\frac{D}{D t}$  denotes the material derivative. Since the internal energy  $e$  is a function of pressure  $P$  and density  $\rho$  (through the equation of state), we use again the chain rule to re-express the previous equation as a function of the material derivatives in  $P$

and  $\rho$ :

$$\begin{aligned}
R(\vec{r}, t) &= s_e e_P \frac{DP}{Dt} + (s_e e_\rho + s_\rho) \frac{D\rho}{Dt} \\
&= s_e e_P \left( \frac{DP}{Dt} + \frac{1}{s_e e_P} (s_e e_\rho + s_\rho) \frac{D\rho}{Dt} \right) \\
&= s_e e_P \left( \frac{DP}{Dt} + \left( \frac{e_\rho}{e_P} + \frac{s_\rho}{s_e e_P} \right) \frac{D\rho}{Dt} \right).
\end{aligned}$$

We are now close to the final result (see Eq. (5.9)). To prove that the term multiplying the material derivative of the density is indeed equal to the square of the speed of sound, we recall that the speed of sound is defined as the partial derivative of pressure with respect to density at constant entropy, which can be recast as a function of the entropy as follows (see Appendix A.2 of [24]):

$$c^2 := \left. \frac{\partial P}{\partial \rho} \right|_{s=cst} = P_\rho - \frac{s_\rho}{s_e} P_e.$$

Using the following relations (see Appendix A.1 of [24])

$$P_e = \frac{1}{e_P} \text{ and } P_\rho = -\frac{e_\rho}{e_P},$$

Eq. (5.9) is obtained and recalled below for completeness:

$$R(\vec{r}, t) := \partial_t s + \vec{u} \cdot \nabla s = \frac{Ds}{Dt} = \frac{s_e}{P_e} \left( \underbrace{\frac{DP}{Dt} - c^2 \frac{D\rho}{Dt}}_{\tilde{R}(\vec{r}, t)} \right).$$

## APPENDIX C

### ENTROPY RESIDUAL FOR AN ISENTROPIC FLOW

This appendix aims at showing that the entropy residual is null when assuming an isentropic flow.

The entropy residual as a function of the pressure, the density, the velocity and the speed of sound is recalled here:

$$\tilde{R} = \frac{dP}{dt} - c^2 \frac{d\rho}{dt}. \quad (\text{C.1})$$

Assuming an isentropic flow, the pressure is only a function of the density as follows:  $P = f(\rho)$  or  $\rho = f^{-1}(P)$ . Using the definition of the speed of sound  $c^2 = \left. \frac{\partial P}{\partial \rho} \right)_s$  and the above form the equation of state, the following relation is derived:

$$c^2 = \left. \frac{\partial P}{\partial \rho} \right)_s = \frac{dP}{d\rho} = \frac{df(\rho)}{d\rho}. \quad (\text{C.2})$$

Using the chain rule, the entropy residual of Eq. (C.1) can be recast as a function of the density, the velocity and the speed of sound, and proven equal to zero:

$$\begin{aligned} \tilde{R} &= \frac{df(\rho)}{d\rho} \frac{d\rho}{dt} - c^2 \frac{d\rho}{dt} \\ &= c^2 \frac{d\rho}{dt} - c^2 \frac{d\rho}{dt} \\ &= 0 \end{aligned}$$

## APPENDIX D

### PROOF OF THE ENTROPY MINIMUM PRINCIPLE FOR THE RADIATION-HYDRODYNAMIC EQUATIONS WITH DISSIPATIVE TERMS

In this appendix, a demonstration of the entropy minimum principle for the system of equations Eq. (7.7) is given. This proof, inspired by [24], details the steps that lead to the derivation of the dissipative terms for the multi-D Euler equations by using the entropy minimum principle.

We start with the hyperbolic system given in Eq. (7.3) and add dissipative terms to each equation as follows:

$$\begin{cases} \frac{d\rho}{dt} + \rho \partial_x u = \partial_x f \\ \partial_t(\rho u) + \partial_x \left( \rho u^2 + P + \frac{\epsilon}{3} \right) = \partial_x g \\ \partial_t(\rho E) + \partial_x [u(\rho E + P)] = \partial_x (h + ug) \\ \partial_t \epsilon + u \partial_x \epsilon + \frac{4}{3} \epsilon \partial_x u = \partial_x l \end{cases} \quad (D.1)$$

where  $f$ ,  $g$ ,  $h$  and  $l$  are dissipative terms to be determined. Eq. (D.1) is then recast as a function of the primitive variables  $(\rho, u, e, \epsilon)$  to yield:

$$\begin{cases} \frac{d\rho}{dt} + \rho \partial_x u = \partial_x f \\ \rho \frac{du}{dt} + \partial_x \left( P + \frac{\epsilon}{3} \right) = \partial_x g - u \partial_x f \\ \rho \frac{de}{dt} + P \partial_x u = \partial_x h + g \partial_x u + (0.5u^2 - e) \partial_x f \\ \frac{d\epsilon}{dt} + \frac{4}{3} \epsilon \partial_x u = \partial_x l \end{cases} \quad (D.2)$$

The right-hand side of the internal energy equation can be simplified by choosing the dissipative terms  $g$  and  $h$  as follows:  $h = \tilde{h} - 0.5u^2 f$  and  $g = \rho \mu \partial_x u + u f$  where

$\mu \geq 0$  is a dissipative coefficient. Using these definitions, the system of equation given in Eq. (D.2) becomes:

$$\begin{cases} \frac{d\rho}{dt} + \rho \partial_x u = \partial_x f \\ \rho \frac{du}{dt} + \partial_x \left( P + \frac{\epsilon}{3} \right) = \partial_x g - u \partial_x f \\ \rho \frac{de}{dt} + P \partial_x u = \rho \mu (\partial_x u)^2 + \partial_x \tilde{h} - e \partial_x f \\ \frac{d\epsilon}{dt} + \frac{4}{3} \epsilon \partial_x u = \partial_x l \end{cases} \quad (\text{D.3})$$

This system of equation admits an entropy function  $s$  that depends on density  $\rho$ , internal energy  $e$  and radiation energy density  $\epsilon$ . In order to prove the entropy minimum principle, a conservation statement satisfied by the entropy is needed. This equation which is referred to as an entropy residual  $D_e(x, t)$ , can be obtained by a combination of the equations given in Eq. (D.3). This process is motivated by the following (chain rule)

$$\partial_\alpha s = \partial_\rho s \partial_\alpha \rho + \partial_e s \partial_\alpha e + \partial_\epsilon s \partial_\alpha \epsilon, \quad (\text{D.4})$$

which holds for any independent variable  $\alpha = x, t$ . It is also required to define the dissipative terms  $\tilde{h}$ ,  $f$  and  $l$ . The following definitions are chosen:

$$\begin{cases} f = \kappa \partial_x \rho \\ \tilde{h} = \kappa \partial_x (\rho e) \\ l = \kappa \partial_x \epsilon \end{cases} \quad (\text{D.5})$$

where  $\kappa$  is another positive dissipative coefficient.

Thus, using the continuity, the internal energy and the radiation equations of Eq. (D.3) and using Eq. (D.4) along with the definition of the dissipative terms, a conservation

statement satisfied by the entropy  $s$  is obtained:

$$\frac{ds}{dt} + \underbrace{\left( P\partial_e s + \rho^2\partial_\rho s + \frac{4}{3}\rho\epsilon\partial_\epsilon s \right) \partial_x u }_{(a)} = \partial_x (\rho\kappa\partial_x s) + \kappa\partial_e s\partial_x s - \rho\kappa \underbrace{XAX^t}_{(b)} + \underbrace{s_e\rho\mu(\partial_x u)^2}_{(c)} \quad (\text{D.6})$$

where  $X$  is a row vector defined as  $X = (\rho, e, \epsilon)$  and  $A$  is the 3x3 symmetric matrix:

$$A = \begin{bmatrix} \partial_\rho (\rho^2\partial_\rho s) & \partial_{\rho,e}s & \partial_\rho (\rho\partial_\epsilon s) \\ \partial_{\rho,e}s & \partial_{e,e}s & \partial_{e,\epsilon}s \\ \partial_\rho (\rho\partial_\epsilon s) & \partial_{e,\epsilon}s & \partial_{\epsilon,\epsilon}s \end{bmatrix} \quad (\text{D.7})$$

In order to show that an entropy minimum principle holds, the signs of the terms (a), (b) and (c) in Eq. (D.6) need to be studied.

Regarding (a), it is assumed that  $P\partial_e s + \rho^2\partial_\rho s + \frac{4}{3}\rho\epsilon\partial_\epsilon s = 0$ . The motivation for this is two-fold: First, in order to have a negative sign for the term (a), it would require  $P\partial_e s + \rho^2\partial_\rho s + \frac{4}{3}\rho\epsilon\partial_\epsilon s$  to have a sign of opposite to that  $\partial_x u$ . The thermodynamic variables cannot be a function of the material velocity or its derivative under a non-relativistic assumption. Such a statement would not be true when dealing with relativistic equations of state. Second, a similar assumption was made in [24] for multi-D Euler equations (without the radiation energy):  $P\partial_e s + \rho^2\partial_\rho s = 0$ .

The term (b),  $XAX^t$ , is a quadratic form and its sign is determined by simply looking at the positiveness of the matrix  $A$  [22]. Here we need to prove that  $A$  is

negative-definite which is equivalent to showing the three following inequalities:

$$\left\{ \begin{array}{l} A_1 \geq 0 \\ A_2 \leq 0 \\ A_3 = A \geq 0 \end{array} \right. \quad (\text{D.8})$$

where  $A_k$  is the  $k^{th}$  order leading principle minor. Determining the sign of the last inequality that corresponds to the determinant of the 3 by 3 matrix  $A$  can be difficult and needs to be simplified. Zeroing out the off-diagonal entries of the last row or column would simplify the expression for the determinant of  $A$ . This can be achieved by assuming  $\partial_\rho(\rho\partial_\epsilon s)$  and  $\partial_{e,\epsilon}s$  are zero, which requires the following form for the entropy function:

$$s(\rho, e, \epsilon) = \tilde{s}(\rho, e) + \frac{\rho_0}{\rho} \hat{s}(\epsilon). \quad (\text{D.9})$$

where  $\tilde{s}$  and  $\hat{s}$  are two functions whose properties will be provided later. The constant  $\rho_0$  is used for a dimensionality purpose. Next, using the expression of the entropy given in Eq. (D.9), matrix  $A$  becomes:

$$A = \begin{bmatrix} \partial_\rho(\rho^2\partial_\rho \tilde{s}) & \partial_{\rho,e}\tilde{s} & 0 \\ \partial_{\rho,e}\tilde{s} & \partial_{e,e}\tilde{s} & 0 \\ 0 & 0 & \rho^{-1}\partial_{e,\epsilon}\hat{s} \end{bmatrix}$$

Proving that the matrix  $A$  is negative-definite is now straightforward by inspecting the sign of the leading principal minors:

$$\left\{ \begin{array}{l} A_1 = \partial_\rho(\rho^2\partial_\rho \tilde{s}) \leq 0 \\ A_2 = \partial_\rho(\rho^2\partial_\rho \tilde{s})\partial_{e,e}\tilde{s} - (\partial_{\rho,e}\tilde{s})^2 \geq 0 \\ A_3 = \rho^{-1}\partial_{e,\epsilon}\hat{s}A_2 \leq 0 \end{array} \right. \quad (\text{D.10})$$

This is easily achieved when assuming that the functions  $-\tilde{s}$  and  $-\hat{s}$  are convex.

Thus, the sign of (b) is now determined.

Finally, it remains to determine the sign of the term  $(c) = \partial_e s \rho \mu (\partial_x u)^2$ . The density  $\rho$  and the viscosity coefficient  $\mu$  are both positive: the latest proof for positivity of the density can be found in [24]. Then, only the sign of  $\partial_e s$  remains unknown but it can be determined by studying (a). It was assumed earlier in this appendix that  $P\partial_e s + \rho^2 \partial_\rho s + \frac{4}{3}\rho\epsilon\partial_e s = 0$ . This equation is now recast and split into two equations using Eq. (D.9). Separation of variables yields:

$$P\partial_e \tilde{s} + \rho^2 \partial_\rho \tilde{s} = \alpha \text{ and } \hat{s} - \frac{4\epsilon}{3}\partial_e \hat{s} = \alpha$$

where  $\alpha$  is a constant to determine. If one sets  $\alpha = 0$ , then the two physics are decoupled, which allows us to reconnect to the result derived in [24] for the multi-D Euler equations:  $P\partial_e \tilde{s} + \rho^2 \partial_\rho \tilde{s} = 0$ . Then, following [24], definitions for  $\partial_e \tilde{s}$  and  $\partial_\rho \tilde{s}$  are obtained:

$$\begin{cases} \partial_e s = \partial_e \tilde{s} = T^{-1} \\ \partial_\rho \tilde{s} = -\frac{P}{\rho^2} \partial_e \tilde{s} \end{cases}$$

where  $T$  is the material temperature which ensures positivity of  $\partial_e s$ . Thus, (c) is positive.

From the above results, the entropy minimum principle follows, so that the sign of the entropy residual is known:

$$\boxed{\partial_t s + u \partial_x s \geq 0} \quad (\text{D.11})$$

**Remark.** By assuming  $\alpha = 0$ , an expression for the  $\hat{s}$  can be derived by solving the ODE,  $\hat{s} - \frac{4\epsilon}{3}\partial_e \hat{s} = 0$ , which yields:  $\hat{s}(\epsilon) = \beta \exp\left(\frac{4\epsilon^2}{3}\right)$ , where  $\beta$  is a constant.

The sign of  $\beta$  is determined by using the condition,  $\partial_{\epsilon,\epsilon}\hat{s} \leq 0$ , derived above, so that  $\beta \leq 0$ .

**Remark.** The viscous regularization derived in this appendix, has two viscosity coefficients:  $\mu$  and  $\kappa$ . For the purpose of this paper, these coefficients are set equal. Under this assumption, the above viscous regularization is equivalent to the parabolic regularization of [51].

## APPENDIX E

### ENTROPY EQUATION FOR THE MULTI-D SEVEN EQUATION MODEL WITHOUT VISCOUS REGULARIZATION

This appendix provides the steps that lead to the derivation of the phasic entropy equation of the seven-equation model [55]. For the purpose of this dissertation, two phases are considered and denoted by the indexes  $j$  and  $k$ . In the seven-equation model, each phase obeys to the following set of equations (*Eq. (E.1)*):

$$\partial_t (\alpha_k A) + A \mathbf{u}_{int} \cdot \nabla \alpha_k = A \mu (P_k - P_j) \quad (\text{E.1a})$$

$$\partial_t (\alpha_k \rho_k A) + \nabla \cdot (\alpha_k \rho_k \mathbf{u}_k A) = 0 \quad (\text{E.1b})$$

$$\begin{aligned} \partial_t (\alpha_k \rho_k \mathbf{u}_k A) + \nabla \cdot [\alpha_k A (\rho_k \mathbf{u}_k \otimes \mathbf{u}_k + P_k \mathbb{I})] = \\ \alpha_k P_k \nabla A + P_{int} A \nabla \alpha_k + A \lambda (\mathbf{u}_j - \mathbf{u}_k) \end{aligned} \quad (\text{E.1c})$$

$$\begin{aligned} \partial_t (\alpha_k \rho_k E_k A) + \nabla \cdot [\alpha_k A \mathbf{u}_k (\rho_k E_k + P_k)] = \\ P_{int} A \mathbf{u}_{int} \cdot \nabla \alpha_k - \mu \bar{P}_{int} (P_k - P_j) + \bar{\mathbf{u}}_{int} A \lambda (\mathbf{u}_j - \mathbf{u}_k) \end{aligned} \quad (\text{E.1d})$$

where  $\rho_k$ ,  $\mathbf{u}_k$ ,  $E_k$  and  $P_k$  are the density, the velocity, the specific total energy and the pressure of  $k^{th}$  phase, respectively. The pressure and velocity relaxation parameters are denoted by  $\mu_P$  and  $\lambda_u$ , respectively. The variables with index  $_{int}$  correspond to

the interfacial variables and a definition is given in Eq. (E.2). The cross section  $A$  is only function of space:  $\partial_t A = 0$ .

$$\left\{ \begin{array}{l} P_{int} = \bar{P}_{int} - \frac{\nabla \alpha_k}{\|\nabla \alpha_k\|} \frac{Z_k Z_j}{Z_k + Z_j} (\mathbf{u}_k - \mathbf{u}_j) \\ \bar{P}_{int} = \frac{Z_k P_j + Z_j P_k}{Z_k + Z_j} \\ \mathbf{u}_{int} = \bar{\mathbf{u}}_{int} - \frac{\nabla \alpha_k}{\|\nabla \alpha_k\|} \frac{P_k - P_j}{Z_k + Z_j} \\ \bar{\mathbf{u}}_{int} = \frac{Z_k \mathbf{u}_k + Z_j \mathbf{u}_j}{Z_k + Z_j} \end{array} \right. \quad (\text{E.2})$$

where  $Z_k = \rho_k c_k$  and  $Z_j = \rho_j c_j$  are the impedance of the phase  $k$  and  $j$ , respectively. The speed of sound is denoted by the variable  $c$ . The function  $sgn(x)$  returns the sign of the variable  $x$ .

The first step consists of rearranging the equations given in Eq. (E.2) using the primitive variables  $(\alpha_k, \rho_k, \mathbf{u}_k, e_k)$ , where  $e_k$  is the specific internal energy of  $k^{th}$  phase. We introduce the material derivative  $\frac{D(\cdot)}{Dt} = \partial_t(\cdot) + \mathbf{u}_k \cdot \nabla(\cdot)$  for simplicity.

The void fraction is unchanged. The continuity equation is modified as follows:

$$\alpha_k A \frac{D \rho_k}{Dt} + \rho_k A \mu (P_k - P_j) + \rho_k A (\mathbf{u}_k - \mathbf{u}_j) \cdot \nabla \alpha_k + \rho_k \alpha_k \nabla \cdot (A \mathbf{u}_k) = 0 \quad (\text{E.3})$$

The momentum and continuity equations are combined to yield the velocity equation:

$$\alpha_k \rho_k A \frac{D \mathbf{u}_k}{Dt} + \partial_x (\alpha_k A P_k) = \alpha_k P_k \nabla A + P_{int} A \nabla \alpha_k + A \lambda_u (\mathbf{u}_j - \mathbf{u}_k) \quad (\text{E.4})$$

The internal energy is obtained from the total energy and the kinetic equation ( $\mathbf{u}_k$ \*Eq. (E.4)):

$$\begin{aligned} \alpha_k \rho_k A \frac{D e_k}{Dt} + \nabla \cdot (\alpha_k \mathbf{u}_k A P_k) - \mathbf{u}_k \cdot \nabla (\alpha_k A P_k) &= P_{int} A (\mathbf{u}_{int} - \mathbf{u}_k) \cdot \nabla \alpha_k \\ -\alpha_k P_k \mathbf{u}_k \cdot \nabla A - \bar{P}_{int} A \mu_P (P_k - P_j) + A \lambda_u (\mathbf{u}_j - \mathbf{u}_k) \cdot (\bar{\mathbf{u}}_{int} - \mathbf{u}_k) \end{aligned} \quad (\text{E.5})$$

In the next step, we assume the existence of a phase wise entropy  $s_k$  function of the density  $\rho_k$  and the internal energy  $e_k$ . Using the chain rule,

$$\frac{Ds_k}{Dt} = (s_\rho)_k \frac{D\rho_k}{Dt} + (s_e)_k \frac{De_k}{Dt}, \quad (\text{E.6})$$

along with the internal energy and the continuity equations, the following entropy equation is obtained:

$$\begin{aligned} \alpha_k \rho_k A \frac{Ds_k}{Dt} + A \underbrace{\left( P_k (s_e)_k + \rho_k^2 (s_\rho)_k \right) \mathbf{u}_k \cdot \nabla \alpha_k + \alpha_k \left( P_k (s_e)_k + \rho_k^2 (s_\rho)_k \right) \mathbf{u}_k \cdot \nabla A}_{(\text{a})} &= \\ (s_e)_k P_{int} A \left[ (\mathbf{u}_{int} - \mathbf{u}_k) \cdot \nabla \alpha_k - \bar{P}_{int} A \mu_P (P_k - P_j) + A \lambda_u (\bar{\mathbf{u}}_{int} - \mathbf{u}_k) \cdot (\mathbf{u}_j - \mathbf{u}_k) \right] &- \\ \rho^2 (s_\rho)_k \left[ \mu_P A (P_k - P_j) + A (\mathbf{u}_k - \mathbf{u}_{int}) \cdot \nabla \alpha_k \right] & \quad (\text{E.7}) \end{aligned}$$

where  $(s_e)_k$  and  $(s_\rho)_k$  denote the partial derivatives of the entropy  $s_k$  with respect to the internal energy  $e_k$  and the density  $\rho_k$ , respectively. The second term, (a), in the left hand side of Eq. (E.7) can be set to zero by assuming the following relation between the partial derivatives of the entropy  $s_k$ :

$$P_k (s_e)_k + \rho_k^2 (s_\rho)_k = 0. \quad (\text{E.8})$$

The above equation is equivalent to the application of the second thermodynamic law when assuming reversibility:

$$T_k ds_k = de_k - \frac{P_k}{\rho_k^2} d\rho_k \text{ with } (s_e)_k = \frac{1}{T_k} \text{ and } (s_\rho)_k = -\frac{P_k}{\rho_k^2} (s_e)_k \quad (\text{E.9})$$

Thus, equation Eq. (E.7) can be rearranged using the relation  $(s_\rho)_k = -\frac{P_k}{\rho_k^2}(s_e)_k$ :

$$((s_e)_k)^{-1} \alpha_k \rho_k \frac{Ds}{Dt} = \underbrace{[P_{int}(\mathbf{u}_{int} - \mathbf{u}_k) + P_k(\mathbf{u}_k - \mathbf{u}_{int})] \cdot \nabla \alpha_k}_{(b)} + \underbrace{\mu(P_k - P_j)(P_k - \bar{P}_{int})}_{(c)} + \underbrace{\lambda(\mathbf{u}_j - \mathbf{u}_k) \cdot (\bar{\mathbf{u}}_{int} - \mathbf{u}_k)}_{(d)} \quad (\text{E.10})$$

The right hand side of equation Eq. (E.10) is split into three terms (b), (c) and (d) that will be treated independently from each other. The terms (c) and (d) are simpler to start with and can be easily recast by using the definitions of  $\bar{\mathbf{u}}_{int}$  and  $\bar{P}_{int}$  given in equation Eq. (E.2):

$$\begin{aligned} \mu(P_k - P_j)(P_k - \bar{P}_{int}) &= \mu_P \frac{Z_k}{Z_k + Z_j} (P_j - P_k)^2 \\ \lambda(\mathbf{u}_j - \mathbf{u}_k) \cdot (\bar{\mathbf{u}}_{int} - \mathbf{u}_k) &= \lambda_u \frac{Z_j}{Z_k + Z_j} (\mathbf{u}_j - \mathbf{u}_k)^2 \end{aligned} \quad (\text{E.11})$$

By definition,  $\mu_P$ ,  $\lambda_u$  and  $Z_k$  are all positive. Thus, the above terms are unconditionally positive.

It remains to look at the last term (b). Once again, by using the definition of  $P_{int}$  and  $\mathbf{u}_{int}$ , and the following relations:

$$\begin{aligned} \mathbf{u}_{int} - \mathbf{u}_k &= \frac{Z_j}{Z_k + Z_j} (\mathbf{u}_j - \mathbf{u}_k) - \frac{\nabla \alpha_k}{\|\nabla \alpha_k\|} \frac{P_k - P_j}{Z_k + Z_j} \\ P_{int} - P_k &= \frac{Z_k}{Z_k + Z_j} (P_j - P_k) - \frac{\nabla \alpha_k}{\|\nabla \alpha_k\|} \frac{Z_k Z_j}{Z_k + Z_j} (\mathbf{u}_k - \mathbf{u}_j), \end{aligned}$$

(b) yields:

$$\begin{aligned}
[P_{int}(\mathbf{u}_{int} - \mathbf{u}_k) + P_k(\mathbf{u}_k - \mathbf{u}_{int})] \cdot \nabla \alpha_k &= (P_{int} - P_k)(\mathbf{u}_{int} - \mathbf{u}_k) \cdot \nabla \alpha_k = \\
&= \frac{Z_k}{(Z_k + Z_j)^2} \nabla \alpha_k \cdot \left[ Z_j(\mathbf{u}_j - \mathbf{u}_k)(P_j - P_k) + \frac{\nabla \alpha_k}{\|\nabla \alpha_k\|} Z_j^2 (\mathbf{u}_j - \mathbf{u}_k)^2 + \right. \\
&\quad \left. \frac{\nabla \alpha_k}{\|\nabla \alpha_k\|} (P_k - P_j)^2 + \frac{\nabla \alpha_k \cdot \nabla \alpha_k}{\|\nabla \alpha_k\|^2} (P_k - P_j) Z_j (\mathbf{u}_k - \mathbf{u}_j) \right] \quad (\text{E.12})
\end{aligned}$$

The above equation is factorized by  $\|\nabla \alpha_k\|$  and then recast under a quadratic form when noticing that  $\frac{\nabla \alpha_k \cdot \nabla \alpha_k}{\|\nabla \alpha_k\|^2} = 1$ , which yields:

$$\begin{aligned}
[(\mathbf{u}_{int} - \mathbf{u}_k)P_{int} + (\mathbf{u}_k - \mathbf{u}_{int})P_k] \nabla \alpha_k &= \\
\|\nabla \alpha_k\| \frac{Z_k}{(Z_k + Z_j)^2} \left[ Z_j(\mathbf{u}_j - \mathbf{u}_k) + \frac{\nabla \alpha_k}{\|\nabla \alpha_k\|} (P_k - P_j) \right]^2 & \quad (\text{E.13})
\end{aligned}$$

Thus, using results from Eq. (E.10), Eq. (E.11), Eq. (E.12) and Eq. (E.13), the entropy equation obtained in [55] holds and is recalled here for convenience:

$$\begin{aligned}
(s_e)_k^{-1} \alpha_k \rho_k A \frac{Ds_k}{Dt} &= \mu_P \frac{Z_k}{Z_k + Z_j} (P_j - P_k)^2 + \lambda_u \frac{Z_j}{Z_k + Z_j} (\mathbf{u}_j - \mathbf{u}_k)^2 \\
&\quad + \frac{Z_k}{(Z_k + Z_j)^2} \left[ Z_j(\mathbf{u}_j - \mathbf{u}_k) + \frac{\nabla \alpha_k}{\|\nabla \alpha_k\|} (P_k - P_j) \right]^2.
\end{aligned}$$